

Development of experimental and analytical/modelling methods for the investigation of biomass pyrolysis and gasification in a novel indirect fluidized bed reactor

Tsekos, C.

DOI

[10.4233/uuid:7660e4df-420c-4283-ab05-fd5ea6ec5a1b](https://doi.org/10.4233/uuid:7660e4df-420c-4283-ab05-fd5ea6ec5a1b)

Publication date

2024

Document Version

Final published version

Citation (APA)

Tsekos, C. (2024). *Development of experimental and analytical/modelling methods for the investigation of biomass pyrolysis and gasification in a novel indirect fluidized bed reactor*. [Dissertation (TU Delft), Delft University of Technology]. <https://doi.org/10.4233/uuid:7660e4df-420c-4283-ab05-fd5ea6ec5a1b>

Important note

To cite this publication, please use the final published version (if applicable). Please check the document version above.

Copyright

Other than for strictly personal use, it is not permitted to download, forward or distribute the text or part of it, without the consent of the author(s) and/or copyright holder(s), unless the work is under an open content license such as Creative Commons.

Takedown policy

Please contact us and provide details if you believe this document breaches copyrights. We will remove access to the work immediately and investigate your claim.

Development of experimental and analytical/modelling methods for the investigation of biomass pyrolysis and gasification in a novel indirect fluidized bed reactor

Dissertation

for the purpose of obtaining the degree of doctor
at Delft University of Technology
by the authority of the Rector Magnificus prof. dr. ir. T.H.J.J van der Hagen,
chair of the Board for Doctorates

to be defended publicly on
Monday 18 March 2024 at 10:00 o'clock

By

Christos TSEKOS

Master of Science in Sustainable Energy Technology
Delft University of Technology, the Netherlands
born in Marousi, Greece

This dissertation has been approved by the promotor:

Prof. dr. ir. W. de Jong and Prof. dr. ir. J.T. Padding

Composition of the doctoral committee:

Rector Magnificus

Prof. dr. ir. W. de Jong

Prof. dr. ir. J.T. Padding

Chairperson

Delft University of Technology, promotor

Delft University of Technology, promotor

Independent members:

Prof. Dr. Ir. A.A. Kiss

Prof. Dr. Ir. H.J. Heeres

Prof. Dr. Ir. G. Brem

Prof. dr. D. Roekaerts

Dr. Ir. J. Kiel

Delft University of Technology

University of Groningen

University of Twente

Delft University of Technology

Netherlands Organization for Applied
Scientific Research (TNO)



This research was performed within the context and with the support of the European project Biofuels Research Infrastructure (BRISK) 2 funded by EU Horizon 2020 (Grant Agreement Number: 731101).

ISBN: 978-94-6496-063-1

Copyright © 2024 by C. Tsekos. All rights reserved.

An electronic version of this dissertation is available at:

<http://repository.tudelft.nl/>

Contents

List of Figures	iv
List of Tables	ix
Summary	xi
Samenvatting	xiii
1. Introduction	1
1.1 Climate concerns and global energy crisis.....	2
1.2 The role of bioenergy	6
1.3 Biomass gasification and pyrolysis	9
1.3.1 Pyrolysis.....	9
1.3.2 Gasification	11
1.4 Scope and research questions.....	20
1.5 Thesis outline.....	21
2. PAH sampling and quantification from woody biomass fast pyrolysis in a Pyroprobe reactor with a modified tar sampling system	25
2.1 Introduction.....	26
2.2 Materials & methods.....	29
2.2.1 Proximate and ultimate analysis of the fuels	29
2.2.2 Apparatus and experimental procedure	29
2.2.3 Analysis of the products	32
2.3 Results & discussion	34
2.3.1 Influence of pyrolysis temperature on PAH evolution	34
2.3.2 Gravimetric liquid and char from PP and HF reactors.....	38
2.3.3 Analysis of the product gas	40
2.3.4 Overall mass balance of the experiments	41
2.4 Conclusions.....	41
3. Biomass pyrolysis TGA assessment with an international round robin	47
3.1 Introduction.....	48
3.2 Materials and methods	50
3.2.1 TGA experiments	50
3.2.2 Kinetic analysis	53
3.3 Results and discussion.....	53

3.3.1 Cellulose pyrolysis	53
3.3.2 Beech wood pyrolysis	57
3.4 Conclusions.....	71
4. Estimation of lignocellulosic biomass pyrolysis product yields using artificial neural networks	75
4.1 Introduction.....	76
4.2 Methods	80
4.2.1 Database development	80
4.2.2 ANN development	82
4.3 Results and discussion.....	85
4.3.1 Analysis of literature data	85
4.3.2 ANN results.....	86
4.4 Conclusions.....	92
5. Gasification of woody biomass in a novel indirectly heated bubbling fluidized bed steam reformer.....	99
5.1 Introduction.....	100
5.2 The Indirectly Heated Bubbling Fluidized Bed Steam Reformer (IHFBSR)	102
5.3 Materials and Methods	104
5.3.1 Feedstocks, bed material and analytical equipment.....	104
5.3.2 Definition of main process parameters.....	105
5.3.3 Experimental procedure and overview	106
5.3.4 Experimental matrix	107
5.4 Experimental results and discussion	108
5.4.1 Effect of STBR and bed material particle size.....	108
5.4.2 Effect of λ – high temperature (HT) versus low temperature (LT) experiments	113
5.4.3 Effect of secondary air injection.....	116
5.4.4 Effect of steam/air gasification duration.....	121
5.4.5 Comparison of IHFBFSR with other allothermal gasification concepts.....	125
5.5 Conclusions.....	126
6. Two phase modelling of Geldart B particles in a novel indirectly heated bubbling fluidized bed biomass steam reformer	133
6.1 Introduction.....	134
6.2 Experimental setup.....	136
6.2.1 Reactor description	136

6.2.2 Hydrodynamics experiments.....	138
6.3 Numerical model	140
6.4 Computational Fluid Dynamics.....	142
6.5 Results	143
6.5.1 Mesh and time step independence (without side-flow).....	143
6.5.2 Restitution coefficient (without side-flow)	148
6.5.3 IHBFSR simulation results (without side-flow).....	151
6.5.4 Effect of the N ₂ purge side-flow on the IHBFSR fluidization behaviour	153
6.6 Conclusions.....	159
7. Conclusions & Recommendations	165
7.1 Conclusions.....	166
7.2 Recommendations.....	168
A. Appendix – Tar sampling in a Pyroprobe reactor.....	171
B. Appendix - Estimation of lignocellulosic biomass pyrolysis product yields using artificial neural networks.....	179
C. Appendix - Indirectly heated bubbling fluidized bed steam reformer	187
D. Appendix - Two phase modelling of Geldart B particles in the IHBFSR ..	209
Curriculum Vitae	211
List of Publications	213

List of Figures

Figure 1.1: Global GHG emissions of modelled pathways (Panel a) and projected emission outcomes from near-term policy assessments for 2030 (Panel b). Reprinted from [1].	2
Figure 1.2: Comparison of EU imports of natural gas, petroleum oils, LNG and coal before and after the sanctions imposed to Russia according to the Eurostat database (Comext) and Eurostat Estimates [7].	4
Figure 1.3: Global renewable generation capacity growth from 2016 to 2022 [14].	5
Figure 1.4: Share of renewables in global total final energy consumption in 2019 (top) and share of global bioenergy consumption by end use in 2020 (bottom) [21].	7
Figure 1.5: Overview of some biomass conversion technologies and derived products [27-29].	8
Figure 1.6: Applications of pyrolysis products [38].	11
Figure 1.7: Biomass gasification pathway (adapted from [40]).	12
Figure 1.8: Schematic representation of bubbling (a) and circulating (b) fluidized bed gasification concepts (adapted from [51]).	17
Figure 1.9: Simplified schematic of the working principle of an entrained flow reactor [30].	18
Figure 1.10: Syngas from biomass gasification utilization pathways (adapted from [53]).	19
Figure 1.11: Overview of main syngas conversion pathways and final products (adapted from [61]).	20
Figure 2.1: CDS Pyroprobe 5200 setup during a fast pyrolysis experiment.	30
Figure 2.2: A schematic overview of the experimental procedure and product sampling methods that were followed in the conduction of the pyrolysis experiments.	30
Figure 2.3: Diagram of the pyroprobe reactor and purge flow pathway.	31
Figure 2.4: PAH evolution during pyrolysis (600 °C/s, 10 s holding time) of wood at different temperatures, comparison between pyroprobe and heated foil (HF).	35
Figure 2.5: PAH condensation on quartz and liquid traps from wood pyrolysis on PP (600 °C/s, 10 s holding time) at (a) 800 °C and (b) 1000 °C.	38
Figure 2.6: Effect of pyrolysis (600 °C/s, 10 s holding time) temperature on (a) char and (b) gravimetric liquid (condensables on quartz trap) yields.	39
Figure 2.7: Gas evolution over temperature during pyrolysis (600 °C/s, 10 s holding time) of wood: (a) CO ₂ , (b) CO, (c) CH ₄ and (d) H ₂ . Comparison between pyroprobe and heated foil.	40
Figure 3.1: Activation energies reported in literature for pure biomass components pyrolysis using several kinetic analysis methods [17-29]. Box plots indicate the median and interquartile ranges.	49
Figure 3.2: Activation energies reported in literature for pseudo-components in biomass pyrolysis using several kinetic analysis methods [30-47]. The values denoted with a * are mean values obtained from experiments performed under various heating rates or with different biomass species. For cases with 4 components, the 4th is either extractives [45, 46] or a second hemicellulose component [44]. Boxplots indicate the median and interquartile ranges.	50
Figure 3.3: TG (left) and DTG (right) curves for cellulose pyrolysis at 5 K/min.	54
Figure 3.4: Char yield as a function of initial sample mass for commercial Avicel® PH-101 cellulose pyrolysis at a heating rate of 5 K/min for partners #1 to #7.	55
Figure 3.5: Comparison of DTG experiment (circles) and model fitting (line) profiles for Avicel® PH-101 cellulose pyrolysis at a heating rate of 5 K/min with one first order reaction for the #1 (left) and #3 (right) cases.	55
Figure 3.6: TG curves for beech wood pyrolysis at heating rates of 1, 5, 10 and 20 K/min for partners #1 to #7.	57

Figure 3.7: DTG curves for beech wood pyrolysis at heating rates of 1, 5, 10 and 20 K/min for partners #1 to #7.	58
Figure 3.8: Arrhenius plots from the KAS method for conversions from 0.1 to 0.9 for beech wood pyrolysis at heating rates of 1, 5, 10 and 20 K/min for partners #1 to #7.	61
Figure 3.9: Activation energies along conversion (KAS method) for all experiments (top) and for experiments without outliers (#2 at 1 K/min and #5 at 20 K/min – bottom) for beech wood pyrolysis.	63
Figure 3.10: DTG experiments (circles) and model fitting (line) for beech wood at heating rates of 1, 5, 10 and 20 K/min for case #1.	65
Figure 3.11: DTG experiments (circles) and model fitting (line) for beech wood at a heating rate of 5 K/min for cases #2 to #7.	66
Figure 3.12: Activation energies along conversion (KAS method) for selected cases #1, #2 (without 1K/min), #4 and #6.	69
Figure 4.1: Char yield (left), gas yield (middle) and liquid yield (right) over temperature for the pyrolysis experiments database, excluding reference with ID 34 for the liquid product. Linear regression along with 95 % confidence interval is shown for char and gas ($R = 0.5226$ and $R = 0.5376$ respectively) and a locally weighed linear regression for the liquid.	85
Figure 4.2; Logarithmic plot of sample size over heating rate. Linear regression along with 95 % confidence interval is shown ($R = 0.9293$).	86
Figure 4.3: Performance of the reduced char ANN over the test set. Predictions of the networks are shown alongside the targets for each single sample in the test set. Indicative boundary lines are shown ± 5 wt% ar around the zero line.	87
Figure 4.4: Predictions of the reduced char ANN for varying values of lignin (a), ash (b), heating rate (c), temperature (d) and average particle size (e) for specific test samples.	88
Figure 4.5: Performance of the full liquid ANN over the test set. Predictions of the networks are shown alongside the targets for each single sample in the test set. Indicative boundary lines are shown ± 5 wt% ar around the zero line.	89
Figure 4.6: Predictions of the full liquid ANN for varying values temperature (a) and heating rate (b) for specific test samples.	89
Figure 4.7: Performance of the reduced gas ANN over the test set. Predictions of the networks are shown alongside the targets for each single sample in the test set. Indicative boundary lines are shown ± 5 wt% ar around the zero line.	90
Figure 4.8: Predictions of the reduced gas ANN for varying values temperature (a) and heating rate (b) for specific test samples.	90
Figure 4.9: Predictions of the full liquid (left) reduced gas (right) ANN for varying char values for specific test samples.	92
Figure 5.1: Conceptual design of the indirectly heated bubbling fluidized bed steam reformer (IHFBSR).	102
Figure 5.2: IHFBFSR simplified process flow chart (left)/ Basic dimensions and main sensors location in the IHFBFSR reactor chamber. P: pressure gauge, TC: thermocouple (right)	103
Figure 5.3: Effect of STBR and bed material particle size on the CCE (top left), CGE (top right), OE (bottom left) and tar content (including benzene) in the product gas for PG steam/air gasification with $\lambda = 0.2$ at temperatures between 830 °C and 840 °C in the IHFBFSR. Corresponding experimental indexes: 1,2,3,4 and 5 (SP2).	109
Figure 5.4: Effect of STBR and bed material particle size on the composition of gas produced from PG steam/air gasification with $\lambda = 0.2$ at temperatures between 830 °C and 840 °C in the IHFBFSR. Corresponding experimental indexes: 1,2,3,4 and 5 (SP2).	111

Figure 5.5: Effect of STBR and bed material particle size on the benzene and tar compounds production per kg of d.a.f. PG feed, for steam/air gasification with $\lambda = 0.2$ at temperatures between 830 °C and 840 °C in the IHBFBRSR. Corresponding experimental indexes: 1,2,3,4 and 5 (SP2)...	112
Figure 5.6: Effect of lambda (λ) on the CCE (top left), CGE (top right), OE (bottom left) and tar content (including benzene) in the product gas for ExR steam/air gasification with STBR = 1.2 in the IHBFBRSR. Corresponding experimental indexes: 7 and 8 (SP2).	114
Figure 5.7: Product gas composition (top left), N ₂ yield (top right), tar yield (bottom left) and benzene yield (bottom right) for steam/air gasification of ExR with STBR = 1.2 in the IHBFBRSR for different values of lambda (λ). Corresponding experimental indexes: 7 and 8 (SP2).....	115
Figure 5.8: Effect of secondary air injection and bed material particle size on the CCE (top left), CGE (top right), OE (bottom left) and tar content (including benzene) in the product gas for ExR steam/air gasification with $\lambda = 0.04$ and STBR = 1.2 in the IHBFBRSR. Corresponding experimental indexes: 8, 9, 10, 11 and 12 (SP2).....	117
Figure 5.9: Effect of secondary air injection and bed material particle size on the composition of gas produced from ExR steam/air gasification with $\lambda = 0.04$ and STBR = 1.2 in the IHBFBRSR. Corresponding experimental indexes: 8, 9, 10, 11 and 12 (SP2).....	118
Figure 5.10: Effect of secondary air injection and bed material particle size on the benzene and tar compounds production per kg of d.a.f. ExR feed for steam/air gasification with $\lambda = 0.04$ and STBR = 1.2 in the IHBFBRSR. Corresponding experimental indexes: 8, 9, 10, 11 and 12 (SP2).....	119
Figure 6.1: Conceptual design of the indirectly heated bubbling fluidized bed steam reformer (IHBFBRSR).....	136
Figure 6.2: Basic dimensions of IHBFBRSR and instrumentation (thermocouples – TC and pressure gauges – P locations)	137
Figure 6.3: Top: Air and N ₂ flow rates and temperature profile of the IHBFBRSR bed zone (TC01-TC05) with the bed height reduction (BHR) points marked during the fluidization experiment conducted in the IHBFBRSR. Bottom: Pressure drop over the bed during the fluidization experiment conducted in the IHBFBRSR.	139
Figure 6.4: Pressure drop over the bed area for different grid size and CFL combinations from the IHBFBRSR hydrodynamics simulations without a side-flow.	144
Figure 6.5: Power spectrum of pressure drop over the bed area for the simulations of the IHBFBRSR without side-flow for different mesh densities and CFL = 0.2 (left) and CFL = 0.4 (right). With the dotted line, the corresponding Savitzky – Golay filtered spectrum (polynomial order: 1, frame length: 9).	145
Figure 6.6: Instantaneous void fraction contours, showing the movement of bubbles (light orange) that tend to emerge at the inner wall at a dominant frequency of 4 Hz for the 15×d _p – CFL = 0.2 case. Time starts at 2.25 s at a step of 0.0317 s moving from (a) to (f).	147
Figure 6.7: Bed height for different mesh density and CFL combinations for the simulations of the IHBFBRSR without side-flow.	148
Figure 6.8: Time averaged void fraction contours of the IHBFBRSR bed area for different values of the restitution coefficient: (a) e=0.8, (b) e=0.85, (c) e=0.9, (d) e=0.95 and (e) e=0.99. The simulations were performed with a 15×d _p grid and a CFL of 0.4.	150
Figure 6.9: Void fraction contours of the IHBFBRSR bed area at t = 1.26 s (a), t = 1.89 s (b), t = 2.52 s (c), and t = 3.16 s (d). The simulation was performed with a 15×d _p grid and a CFL of 0.4.....	152
Figure 6.10: Gas volume fraction (left) and velocity vector field (right) from the final time step of the IHBFBRSR bed area simulation without side-flow. The simulation was performed with a 15×d _p grid and a CFL of 0.4.	153
Figure 6.11: Void fraction contours of the IHBFBRSR bed area at t = 0.92 s (a), t = 1.84 s (b), t = 2.76 s (c) and t = 3.69 s (d). In (e) and (f) the time averaged void fraction contours for the side-flow and	

no side-flow cases, respectively. The simulation was performed with a $15 \times d_p$ grid and a CFL of 0.2. The feeder side-flow is located at the outer wall at a dimensionless height of 0.2025.	155
Figure 6.12: Comparison of the bed height (left), pressure drop over the bed (right) and power spectrum of pressure drop over the bed area (bottom) from the simulations of the IHBFBSR with (blue) and without (red lines) side-flow. The simulation was performed with a $15 \times d_p$ grid and a CFL of 0.2. In the power spectrum graph (bottom), with the dotted line, the corresponding Savitzky – Golay filtered spectra (polynomial order: 1, frame length: 9).	157
Figure 6.13: Velocity vectors of the gas phase from the simulations of the IHBFBSR with side-flow. The simulation was performed with a $15 \times d_p$ grid and a CFL of 0.2.	158
Figure A.1: Plot of the measured temperature inside the holder versus the set temperature of the filament coil.	171
Figure A.2: On the left the isopropanol filled condenser before the initiation of a Miscanthus fast pyrolysis experiment at 900 °C. On the right the condenser after the completion of the same experiment	174
Figure A.3: Product yields from fast pyrolysis of Miscanthus in Pyroprobe for different liquid product sampling configurations.	175
Figure A.4: Tar yield of impinger condenser after the evaporation of IPA, collected from fast pyrolysis of Miscanthus at 600 °C/min in the Pyroprobe.	176
Figure A.5: Miscanthus fast pyrolysis product yields for different N ₂ purge mass flow rates (600 °C/s heating rate, 10 s holding time)	177
Figure B.1: Performance of the full char ANN over the test set. Predictions of the networks are shown alongside the targets for each single sample in the test set. Indicative boundary lines are shown ± 5 wt% ar around the zero line.	181
Figure B.2: Performance of the reduced liquid ANN over the test set. Predictions of the networks are shown alongside the targets for each single sample in the test set. Indicative boundary lines are shown ± 5 wt% ar around the zero line.	181
Figure B.3: Performance of the full gas ANN over the test set. Predictions of the networks are shown alongside the targets for each single sample in the test set. Indicative boundary lines are shown ± 5 wt% ar around the zero line.	182
Figure B.4: Performance of the full liquid ANN with char as an input over the test set. Predictions of the networks are shown alongside the targets for each single sample in the test set. Indicative boundary lines are shown ± 5 wt% ar around the zero line.	182
Figure B.5: Performance of the reduced gas ANN with char as an input over the test set. Predictions of the networks are shown alongside the targets for each single sample in the test set. Indicative boundary lines are shown ± 5 wt% ar around the zero line.	183
Figure B.6: Performance of the liquid, char and gas ANN over the test set for reference 34. Predictions of the networks are shown alongside the targets for each single sample in the test set. Indicative boundary lines are shown ± 5 wt% ar around the zero line.	184
Figure B.7: Performance of the char and gas ANN over the test set for reference 12. Predictions of the networks are shown alongside the targets for each single sample in the test set. Indicative boundary lines are shown ± 5 wt% ar around the zero line.	184
Figure C.1: Conceptual design of the indirectly heated bubbling fluidized bed steam reformer (IHBFBSR)	187
Figure C.2: IHBFBSR simplified process flow chart	188
Figure C.3: Basic dimensions and main sensors location in the IHBFBSR reactor chamber. PG: pressure gauge, TC: thermocouple	190
Figure C.4: Temperature of the N ₂ – air flow after the second preheater and in the windbox for three different experimental regimes.	193

Figure C.5: Temperature of the air – steam flow after the second preheater (EH02) and in the windbox for a high total flowrate (air = 11 kg/h and steam = 10 kg/h) and a low total flowrate (air = 1.9 kg/h and steam = 8.7 kg/h).....	194
Figure C.6: Temperature profile of the IHBFBRSR bed zone (thermocouples: TC01-TC05) for a high temperature (HT) steam gasification experiment with ExR as a feedstock and corundum F046 as bed material. The heating rate moving average refers to the average bed temperature heating rate with a period of 20.....	196
Figure C.7: Temperature profile of the IHBFBRSR bed zone (thermocouples: TC01-TC05) for a low temperature (LT) steam gasification experiment with ExR as a feedstock and corundum F046 as bed material. The heating rate moving average refers to the average bed temperature heating rate with a period of 20.....	197
Figure C.8: Temperature profile of the IHBFBRSR bed zone (thermocouples: TC01-TC05) for a high temperature (HT) steam gasification experiment with PG as a feedstock and corundum F046 as bed material. The heating rate moving average refers to the average bed temperature heating rate with a period of 20.....	199
Figure C.9: Temperature profile of the freeboard zone of the IHBFBRSR (TC06 – TC07) for a high (HT) and a low (LT) temperature steam gasification experiment with ExR and a HT with PG as a feedstock and corundum F046 as bed material (left) with STBR = 1.2. On the right, again the temperature profile of the freeboard zone of the IHBFBRSR (TC06 – TC07) for LT experiments in which various amounts of secondary air were injected (0, 4 and 8 kg/h) with ExR as a feedstock and corundum F046 as bed material under $\lambda = 0.04$ and STBR = 1.2. The LT experiment on the left is the same as the 0 kg/h one on the right.....	200
Figure C.10: Differential pressure drops over the distributor plate, the bed area and the freeboard during a HT steam gasification experiment with ExR as a feedstock and corundum F046 as bed material.	202
Figure C.11: Differential pressure drops over the distributor plate and the bed area during two LT steam gasification experiments with different amounts of secondary air injected (0 and 8 kg/h). ExR was employed as a feedstock and corundum F046 as the bed material. The red dotted line denotes the time were combustion was initiated for both experiments. The initiation of the steam gasification regime is marked with the green and the black line for the 0 kg/h and 8 kg/h experiments respectively.	203
Figure C.12: Differential pressure drops over the distributor plate and the bed area during LT (left) and HT (right) steam gasification experiments with corundum F054 and F046 used as bed material. ExR (left) and PG (right) was used as feedstock for the LT and HT respectively.	204

List of Tables

Table 1.1: Typical gasification reactions (adapted from [39, 41]).....	13
Table 1.2: Main tar decomposition reactions during tar reforming (adapted from [44]).....	15
Table 2.1: PAH capturing and analysis methods from pyrolysis reactors reported in literature...	28
Table 2.2: Proximate and ultimate analysis of waste softwood	29
Table 3.1: TGA instruments list and characteristics as well as employed initial mass and nitrogen purge flow for partners #1 to #7.	51
Table 3.2: Proximate, ultimate and elemental analysis of Beech wood. ^{a)} Calculated by difference.	52
Table 3.3: Temperature of the peak in reaction rate (DTG), char yield, averaged heating rate, kinetic parameters and error in the fitting for the cellulose pyrolysis experiments at 5 K/min....	54
Table 3.4: Average heating rate (K/min or °C/min – equivalent units), temperature of the peak and shoulder in DTG curve (°C) and char yield (%) for beech wood pyrolysis experiments at heating rates of 1, 5, 10 and 20 K/min (* result at 2 K/min, not considered for the mean).....	59
Table 3.5: Activation energies (kJ/mol) along conversion from KAS method for beech wood pyrolysis – data of #2 and #5 presented as well without outliers (#2 at 1K/min and #5 at 20 K/min).	62
Table 3.6: R-squared values from KAS method for beech wood pyrolysis – data of #2 and #5 presented as well without outliers (#2 at 1K/min and #5 at 20 K/min).....	62
Table 3.7: Kinetic parameters from model fitting method for beech wood pyrolysis for hemicellulose (HC), cellulose (CEL) and lignin (LIG).	64
Table 3.8: Comparison of activation energies in kJ/mol with fitting method for cellulose (CEL), hemicellulose (HC) and lignin (LIG) and KAS isoconversional method at selected points.	67
Table 3.9: Averaged kinetic parameters from model fitting method and comparison of activation energies to from fitting and isoconversional KAS method for selected cases #1, #2 (without 1K/min), #4 and #6.	68
Table 4.1: Implementation of ANNs for the description of biomass thermochemical conversion processes in literature	78
Table 4.2: Biomass pyrolysis experimental parameters obtained from literature sources, which were included in the database, serving as inputs and outputs of the developed ANN model respectively.....	80
Table 4.3: Results of the sequential test. The parameters are reported in descendent order of strength as predictors.	84
Table 5.1: Proximate analysis, ultimate analysis and Lower heating Value (LHV) for the two woody biomass feedstocks (PG and ExR) employed in the IHBFBRS commissioning experiments.....	104
Table 5.2: Experimental matrix for the PG and ExR steam gasification experiments conducted in the IHBFBRS	107
Table 5.3: Percentage of actual operating time for the bottom and top IHBFBRS burner for the various STBR steam/air gasification experiments conducted with PG as feedstock.	110
Table 5.4: Comparison of the effect of the total amount of air introduced and the respective introduction method for steam/air gasification experiments in the IHBFBRS, with a STBR of 1.2, ExR as a feedstock and corundum F046 as a bed material.	120
Table 5.5: Effect of steam/air gasification duration in the IHBFBRS on various process parameters and product yields (experiments 5 – 8).....	123

Table 5.6: Process conditions, working principles, performances and main gas compositions of Milena (ECN part of TNO), FICFB (TU Vienna), SilvaGas, Battelle (USA) and HPR (TU Munich) allothermal gasifiers	125
Table 6.1: Fluidization data obtained from the corresponding experiment in the IHBFSR	140
Table 6.2: Average pressure drop (dp), dominant frequency (Savitzky-Golay filter) and bed height derived from simulations with different values of the restitution coefficient. The average pressure drop was calculated in the 0.75 – 3.5 s interval and the bed height from 2.5 to 3.5 s, both after stabilization.	149
Table A.1: Correspondence between set filament temperature, actual sample temperature and holding time.....	172
Table A.2: Proximate, ultimate, elemental analysis and LHV of Miscanthus feedstock utilized in the fast pyrolysis experimental campaign.	172
Table B.1: Studies from literature included in the database, along with the amount of data points	179
Table B.2: Hyperparameter values used in the powerset and sequential tests	180
Table B.3: Hyperparameter values for the ANN models developed in the present study.....	180
Table B.4: Correspondence between RMSE and R ² values for the ANN models developed within the present study	180
Table C.1: Temperature at the circumference of various heights of the bottom and top radiant tube burners.	191
Table D.1: Ansys Fluent species property settings	209
Table D.2: Ansys Fluent simulations settings	209
Table D.3: Pressure drop over the bed (dp) (mean, maximum and minimum) and dominant frequency values calculated between 1 and 3 s of the simulation and bed height (from 2.5 to 3.5 s) for the mesh density/CFL combinations used in the independence tests without side-flow. .	210

Summary

The modern world is faced with a multitude of environmental and socio-economic issues, stemming from the way that energy is used and converted. Climate change due to anthropogenic activities (use of fossil fuel resources and its associated CO₂ equivalent emissions), has greatly affected humankind and nature in general, by leading to extreme weather phenomena and reducing the quality of life especially of people belonging to vulnerable communities. The unsustainable practices of the energy sector and the increased energy and materials needs of the public, have brought the situation to a point where immediate action is required to mitigate the effects of climate change. Furthermore, as became apparent by studying the impact of the COVID-19 pandemic and the Russo-Ukrainian war, the global energy market is heavily exposed to price and availability shocks that have a significant negative impact on the quality of life of people globally also in the very short term. Overall, the transition of the energy sector to a green and renewable alternative is essential and bioenergy constitutes a crucial piece of the puzzle of such a sustainable future.

In general, a wide range of bioenergy technologies have been or are being developed, that offer a significant range of feedstock – product possibilities to contribute in the global energy mix. Biomass feedstocks can be utilized in a variety of thermochemical or biochemical conversion methods to produce renewable electricity, heat, fuels, chemicals, or other intermediate products. Biomass pyrolysis and gasification constitute two of the most important thermochemical conversion technologies that have been attracting significant interest from the scientific and industrial communities and will certainly impact the formation and outlook of the future renewable energy mix.

The present work is focused initially on the exploration and development of experimental and analytical methods, as well as relevant models for the investigation of biomass pyrolysis. Pyrolysis, apart from a stand-alone process aimed at the valorisation of biomass feedstocks, also constitutes a crucial step in a biomass gasification process and a method for fuels characterization in general. Therein lies the two-fold purpose of this endeavour, since the methods and models developed for biomass pyrolysis also constitute a significant input for the field of biomass gasification. Characterization of biomass feedstocks in terms of their devolatilization behaviour and expected product composition during thermochemical conversion, is essential for the design of a biomass conversion process. For this purpose, the fast pyrolysis of woody biomass in a Pyroprobe reactor was examined and presented in Chapter 2, focusing on polycyclic aromatic hydrocarbons (PAH) formation at high pyrolysis temperatures, thus being relevant also to gasification processes. The goal of this work was to develop a method for the successful quantification of PAHs produced from biomass fast pyrolysis, with high reproducibility and minimal complexity. The flexibility of the proposed method allows the efficient conduction of multiple experiments, with minimal complexity in terms of sampling, while specific tar compounds can be targeted (PAH, sugars, acids, phenolics, etc.), depending on the experimental conditions.

Another important aspect of biomass feedstock characterization lies within the investigation of their mass loss behaviour and the derivation of the respective kinetics. Therefore, in Chapter 3, an international round robin of TGA pyrolysis experiments with pure cellulose and beech wood conducted by seven participants is presented. Within this work, a method was developed to increase the reliability of the determination of biomass pyrolysis kinetics. This method suggests the conduction of pure cellulose pyrolysis experiments at a heating rate of 5 K/min, to assess the employed TGA device and methods in comparison to relevant literature, as well as the employment of various heating rates and the utilization of isoconversional methods. While this method does not completely guarantee the error-free derivation of kinetics, it ensures that they are chemically meaningful. Such an approach can assist the reduction of the variability in biomass kinetics determination, which can be attributed significantly to the lack of consistency in data acquisition and kinetic analysis of TGA experiments.

The relevance of “big data” and the immense opportunities offered through machine learning applications are becoming increasingly interesting for most scientific fields, including biomass thermochemical conversion. The Artificial Neural Network (ANN) models proposed in Chapter 4 for the prediction of the pyrolysis product yields focus on generalizability, to achieve the best possible results for a variety of biomass feedstocks, reactor types and process conditions. A large database consisting of a variety of small-scale experimental pyrolysis studies was built, constituting a first-of-its-kind attempt in terms of employing ANN models for such a wide range of literature data. Overall, the implementation of the ANN models was successful, as shown by the reasonable RMSE values obtained. The derived models were able to reproduce the expected trends in relation to temperature variation. However, other parameters such as residence and holding time did not appear to have any particular effect.

One of the main goals of this PhD work was to investigate a novel type of indirect/allothermal gasifier, namely the Indirectly Heated Bubbling Fluidized Bed Steam Reformer (IHFBSR). The scientific and technical effort was focused on the commissioning of a 50 kW_{th} pilot unit and the conduction of experimental work in order to explore its operational characteristics and behaviour, while evaluating the industrial relevance of the proposed system in the field of biomass gasification (Chapter 5). Through the conduction of these experimental campaigns it was found that char accumulating in the bed area for the overall process promotes H₂ formation and in-situ tar destruction. Furthermore, it was found that by injecting moderate amounts of air in the freeboard, tar reduction and carbon conversion can be improved without compromising H₂ production. Finally, the product gas composition and overall system efficiency obtained compare favourably to similar allothermal gasification systems, while carbon conversion can still be improved.

Finally, an important step during the investigation of a new reactor system, such as the IHFBFSR, is gaining an understanding into the governing hydrodynamic phenomena during its operation. As shown in Chapter 6, CFD – TFM simulations were employed for this purpose, which were successfully verified with the corresponding experimental results obtained from fluidization experiments. The simulation of the reactor’s hydrodynamic behaviour showcased small deviations compared to the experimental and computational values of the global hydrodynamic metrics (bed height and pressure drop). Through the simulations, it was observed that for realistic values of the particle restitution coefficient the gas flow forms channels near the reactor wall. Overall, the present work constitutes the first step to study the fluidization behaviour of the novel IHFBFSR reactor and offers significant feedback for potential improvements on its design.

Samenvatting

De moderne wereld heeft momenteel te maken met een veelheid aan uitdagingen die liggen op het vlak van milieu en sociaal-economische problematiek, welke voortkomt uit de manier waarop energie wordt gebruikt en omgezet. Klimaatverandering als gevolg van menselijke activiteiten (het gebruik van fossiele brandstoffen en hun gerelateerde CO₂-equivalente emissies), heeft al de mensheid en de natuur in het algemeen enorm getroffen door extreme weerverschijnselen en het reduceren van de kwaliteit van leven, in het bijzonder van de mensen die al behoren tot kwetsbare gemeenschappen. Niet-duurzame praktijken van de energiesector en de toegenomen vraag naar energie en materialen hebben een situatie veroorzaakt waardoor onmiddellijke actie nodig is om de effecten van klimaatverandering om te buigen. Voorts wordt, zoals duidelijk werd door te kijken naar de impact van de COVID-19 pandemie en de oorlog in Oekraïne, de wereld energiemarkt fors blootgesteld aan prijs- en beschikbaarheidsfluctuaties die een significant negatieve invloed hebben op de kwaliteit van leven van mensen wereldwijd, ook op de zeer korte termijn. Kortom, de transitie van de energiesector naar een groen en hernieuwbaar alternatief is essentieel en bio-energie vormt een cruciaal stuk van de puzzel van zo'n duurzame toekomst.

In het algemeen is er al – of wordt er verder – een breed spectrum aan bio-energie technologieën ontwikkeld die een significante range aan voeding – product ketens mogelijk maken om bij te dragen aan de wereld energiemarkt. Biomassavoedingen kunnen worden ingezet in een verscheidenheid aan thermochemische of biochemische conversietechnieken om hernieuwbare elektriciteit, warmte, brandstoffen, chemicaliën, of andere tussenproducten te produceren. Biomassapyrolyse en -vergassing zijn twee van de meest belangrijke thermochemische conversietechnologieën die in de belangstelling staan van wetenschappelijke en industriële gemeenschappen en deze zullen zeker de samenstelling en het vooruitzicht van de toekomstige hernieuwbare energieportfolio bepalen.

Deze studie is in eerste instantie gericht op de verkenning en ontwikkeling van experimentele en analytische methoden en verder op relevante modellen voor de bestudering van biomassa pyrolyse. Pyrolyse is, naast dat het een apart op zichzelf staand proces is voor de valorisatie van biomassavoedingen, ook een cruciale stap in een biomassavergassingproces alsmede een methode voor brandstofkarakterisering in het algemeen. Daarin ligt het tweeledige doel van deze studie, aangezien de methoden en modellen die ontwikkeld worden voor biomassapyrolyse ook een belangrijke input vormen op het gebied van biomassavergassing. De karakterisering van biomassavoedingen in termen van hun ontvluchtigingsgedrag en de verwachte productsamenstelling tijdens het thermochemische conversieproces is essentieel voor het ontwerp van een biomassaconversieproces. Met dit doel voor ogen zijn de snelle pyrolyse van houtachtige biomassa in een Pyroprobe reactor bestudeerd en gepresenteerd in Hoofdstuk 2, dat gericht is op polycyclische aromatische koolwaterstoffen (PAK) vorming bij hoge pyrolysetemperaturen, hetgeen dus belangrijk is ook voor vergassingsprocessen. Het doel van dit werk was het ontwikkelen van een methode voor de succesvolle kwantificering van PAKs gegenereerd door snelle pyrolyse van biomassa met een hoge mate van reproduceerbaarheid en minimale complexiteit. De flexibiliteit van de voorgestelde methode faciliteert het efficiënt uitvoeren van meerdere experimenten met minimale complexiteit in termen van bemonstering, terwijl ook specifieke teercomponenten kunnen worden geanalyseerd (PAK, suikers, zuren, fenol-achtige componenten, etc.), afhankelijk van de experimentele condities.

Een ander belangrijk aspect van biomassavoedingskarakterisering ligt in de bestudering van hun gedrag met betrekking tot massa afname en de afleiding van de conversiekinetiek. Daarom wordt in Hoofdstuk 3 een beschrijving gegeven van een internationale "round robin" studie van TGA pyrolyse met pure cellulose en beukenhout, uitgevoerd door zeven participanten. In deze studie werd een methode ontwikkeld om de betrouwbaarheid te vergroten van de bepaling van de kinetiek van biomassapyrolyse. Deze methode beveelt aan om pyrolyse experimenten met pure cellulose uit te

voeren met een verwarmingssnelheid van 5 K/min om het gebruikte TGA apparaat en methoden te beoordelen in vergelijking met relevante literatuur, alsmede het toepassen van verschillende verwarmingssnelheden en het gebruik van "isoconversie" methoden. Hoewel deze methode niet volledig de foutenvrije afleiding van kinetiek garandeert, verzekert deze wel dat ze in chemisch opzicht van praktische betekenis is. Een dergelijke benadering kan helpen bij het reduceren van de variabiliteit in de bepaling van de kinetiek van biomassaconversie, welke significant het gevolg is van het gebrek aan consistentie in data acquisitie en kinetiek analyse van TGA experimenten.

De relevantie van "big data" en de immense mogelijkheden geboden door "machine learning" toepassingen worden in toenemende mate interessant voor de meeste wetenschappelijke terreinen, inclusief de thermochemische conversie van biomassa. De "Artificial Neural Network" (ANN) modellen voorgesteld in Hoofdstuk 4 voor de voorspelling van de pyrolyse product opbrengsten zijn gericht op generaliseerbaarheid om de best mogelijke resultaten te bereiken voor een variëteit aan biomassavoedingen, reactor types en procescondities. Een uitgebreide database met een variëteit aan kleinschalige experimentele pyrolyse studies is opgebouwd, en dit is een unieke poging in termen van het toepassen van ANN modellen voor een dergelijk breed spectrum aan literatuurdatabank. In het algemeen was de implementatie van de ANN modellen succesvol, zoals aangetoond door de verkregen tamelijk goede RMSE waarden. De afgeleide modellen waren in staat om de verwachte trends met betrekking tot de temperatuur variatie te reproduceren. Echter, andere parameters zoals de verblijftijd en de "holding time" bleken geen bijzondere effecten te vertonen.

Een van de belangrijkste doelen van dit promotiewerk was het bestuderen van een nieuw type indirecte/allotherme vergasser, namelijk de "Indirectly Heated Bubbling Fluidized Bed Steam Reformer" (IHBFSR). Het wetenschappelijke en technische werk was gericht op de oplevering van een 50 kWth proefopstelling en het doorvoeren van een experimenteel programma om de operationele karakteristieken te verkennen alsmede het reactorgedrag, tezamen met het evalueren van de industriële relevantie van het voorgestelde systeem op het gebied van biomassavergassing (Hoofdstuk 5). Door middel van het uitvoeren van deze experimentele campagnes is gebleken dat bio-cokes ("char") accumulatie in het bed de H₂-vorming bevordert alsmede in-situ teerafbreek. Verder is gevonden dat door het injecteren van beperkte hoeveelheden lucht in het vrijboord teerreductie en koolstofconversie kan worden verbeterd zonder afbreuk te doen aan H₂ productie. Tenslotte zijn de gerealiseerde productgas samenstelling en de algehele systeemefficiëntie goed vergelijkbaar met andere allotherme vergassingsystemen, hoewel de koolstofconversie nog kan worden verbeterd.

Tenslotte is een belangrijke stap gedurende het onderzoek naar een nieuw reactorsysteem, zoals de IHBFSR, het verkrijgen van een beter begrip van de hydrodynamica gedurende de bedrijfsvoering. Zoals beschreven in Hoofdstuk 6, werden CFD – TFM simulaties uitgevoerd voor dit doel en deze konden succesvol worden geverifieerd met overeenkomstige experimentele resultaten verkregen met fluïdisatie experimenten. De simulatie van het hydrodynamische gedrag van de reactor vertoonde geringe afwijkingen vergeleken met experimentele en berekende waarden van de globale hydrodynamische grootheden (bedhoogte and drukval). In de simulaties werd duidelijk dat voor realistische waarden van de deeltjesrestitutiecoëfficiënt de gasstroming kanalen vormt nabij de reactorwand. Kortom, het huidige werk omvat de eerste stap naar bestudering van het fluïdisatiegedrag van de nieuwe IHBFSR reactor en biedt een significante feedback voor potentiële verbeteringen van het ontwerp.

1. Introduction

1.1 Climate concerns and global energy crisis

Climate change is one of the greatest challenges that mankind is currently facing, posing a threat to human well-being and planetary health. According to the Intergovernmental Panel on Climate Change (IPCC), human activities, mostly through emissions of greenhouse gases, are responsible for the increase of the global surface temperature by 1.1 °C above the 1850 – 1900 levels, between 2011 – 2020 [1]. A multitude of reasons for this effect can be identified in unsustainable energy and land use, land-use change, lifestyles and patterns of consumption and production across regions, countries and individuals. The impact of climate change has been rapid and widespread, affecting the atmosphere, oceans, cryosphere and biosphere, leading to many weather and climate extremes throughout the world. These adverse impacts and losses to nature and people, have been disproportionately affecting vulnerable communities who have historically contributed less to climate change. Perhaps the most important conclusion derived from the AR6 Synthesis report of the IPCC, was that the global greenhouse gases (GHG) emissions in 2030, according to the nationally determined contributions announced in 2021, suggest that warming will exceed 1.5 °C during the 21st century while making the 2 °C threshold harder to achieve (Figure 1.1). Overall, the window of opportunity for a liveable and sustainable future for mankind is closing and the necessary sustainable developments can only be achieved through international cooperation, financial support and governance/policy actions [1].

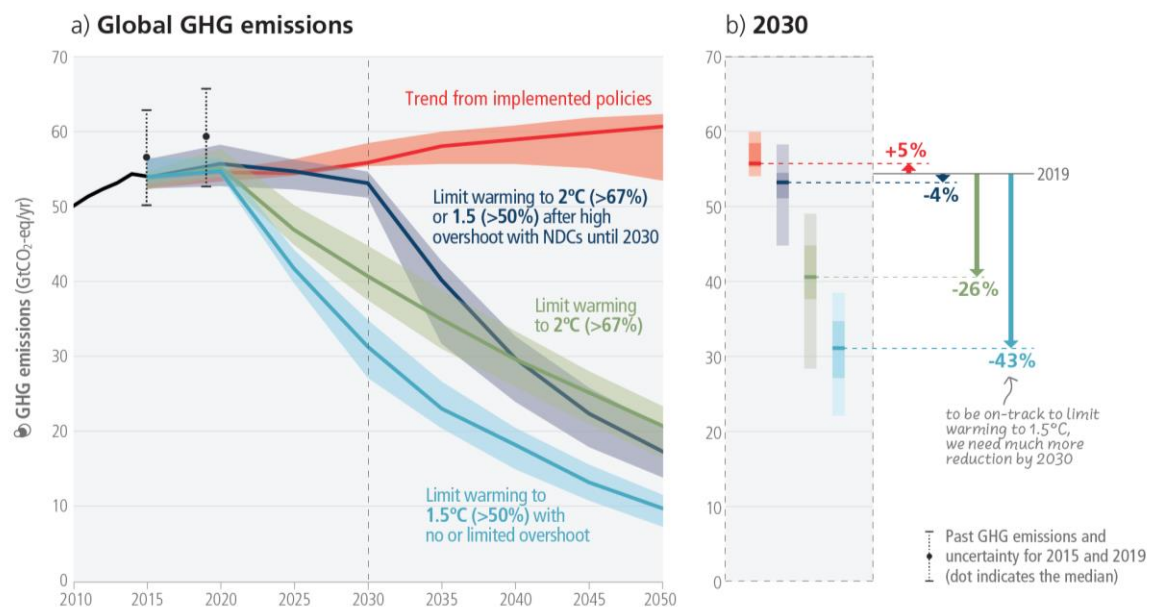


Figure 1.1: Global GHG emissions of modelled pathways (Panel a) and projected emission outcomes from near-term policy assessments for 2030 (Panel b). Reprinted from [1].

The concerns regarding climate change highlight the importance of a global transition towards a “green future” where fossil fuel consumption and GHG emissions will be lower. Despite the steady progress achieved in energy transition, with the renewable energy installation capacity increasing by more than 200 GW in 2019 [2], the COVID-19 pandemic significantly hindered the developments. The unprecedented shock imposed by the pandemic and the resulting lockdown had a significant effect on the entirety of the energy sector and correspondingly the energy transition efforts. The disruption of the business and economic activities led to a nearly 5 % decrease in global energy demand in 2020 and a 7 % decline in global emissions, weakening the oil-producing countries’ grip on the energy

market, causing a significant drop in oil prices. This drop led to a further loss of the competitive edge of renewable energy technologies versus traditional technologies, while the drastic reduction of international trade also caused a setback on the corresponding supply chains. Furthermore, funds from renewable energy projects and tax deductions were withdrawn in favour of much needed support for medical and health expenditures, while many countries focused more on economy recovery by further promoting conventional fuel domination (e.g. new routes for fossil fuel supply, nuclear extensions, coal revival) on their energy investment structure [3]. Once the lockdown measures were lifted in the beginning of 2021, the industrial activities were resumed and the demand for energy carriers was increased, leading to a surge in energy prices. The increased demand for natural gas initially in Asia and then in Europe, caused electricity and natural gas price hikes in 2021. Some EU Member States even introduced support mechanisms (e.g. tax exemptions) to lower the burden on low-income consumers which were already heavily hit by the pandemic, while the European Commission introduced a toolkit focused on facilitating the renewable energy transition and increasing energy efficiency, in order to tackle the crisis [4]. The price shocks faced, raised the debates around the issue of whether the European energy and climate policy is successful in increasing security of energy supply, by promoting the use of natural gas as a “bridge fuel” towards renewable energy transition [5].

Another significant event with heavy implications on the global energy markets is the geopolitical conflict between Russia and Ukraine, which started in February 2022. As a result, the US announced a ban on imports of oil, liquefied natural gas and coal from Russia, while the EU reduced their natural gas imports from Russia by two-thirds, with Japan, South Korea, Britain and Canada following suit [6]. Especially for Europe, this meant a significant shift in its energy strategy, since a large percentage of its natural gas needs were covered by Russia. In particular, in the year 2000 56 % of natural gas imported to Europe by pipeline came from Russia. Despite the drop of the percentage to 38 % by 2020, the total amount imported has not dropped since its demand for gas produced elsewhere has been increasing over the years. Natural gas imported by pipeline in 2020, corresponded to roughly 80 % of the total (pipeline and liquefied natural gas – LNG) amount of natural gas imported [6]. Overall, besides natural gas, the imposed sanctions also included petroleum oil products and coal, with the shift caused in the European import strategy being clearly visible in Figure 1.2. Russia was the largest provider of petroleum oils with a share of 26 % in the first quarter of 2022 which dropped to 3.2% in the first quarter of 2023, following the ban on seaborne crude oil imports in December 2022 and the embargo on refined oil products as of February 2023. Additionally, the fifth package of EU sanctions, which included a prohibition to import or transfer coal and other solid fuels in the EU originating from Russia, led to a drop of the Russian share of coal imports dropping from 42 % to zero, with South Africa, Colombia and the United States mainly picking up its share [7]. The invasion of Ukraine by Russia, has led to a new round of energy resources allocation on a global scale, with certain experts suggesting that the crisis was essentially a natural gas crisis, resulting from the complex interactions between energy trade patterns and geopolitics. By 2023, this war has impacted negatively supply chains, economic growth and carbon emissions of numerous countries, by altering the existing energy trade network. Therefore, the significance of a strong strategic energy layout and energy security has once again been highlighted for many affected countries [8]. Overall, trade restrictions, energy security and climate change mitigation are intertwined. Imposed sanctions can cause an increase of the energy prices and welfare costs, while it has also led to an increase of the use of coal, which was beginning to be phased out in countries like Germany, thus increasing the environmental cost. These effects make the need for renewable energy development even more substantial, in order to support deep electrification and energy saving as well as renewable chemicals production at certain stage [9]. According to the Europe and Central Asia economic update published by the World Bank Group in the spring of 2023, the energy and value chain disruptions have led a surging inflation and a slowing

growth in the region, building on the effects of the COVID-19 pandemic. The ongoing energy crisis offers an opportunity for green transition acceleration, which can facilitate the reduction of the region’s energy intensity and environmental degradation [10].

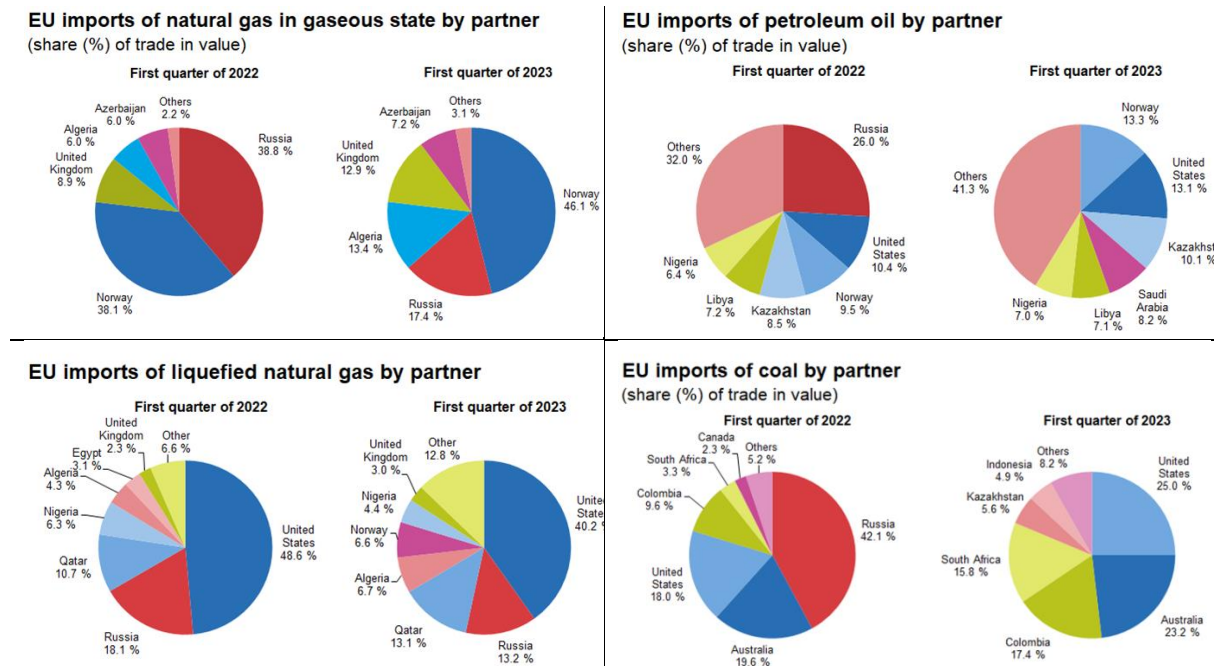


Figure 1.2: Comparison of EU imports of natural gas, petroleum oils, LNG and coal before and after the sanctions imposed to Russia according to the Eurostat database (Comext) and Eurostat Estimates [7].

The umbrella term Renewable Energy Technologies stands for energy conversion using a renewable energy source like solar, wind, water (hydro and tidal), biomass (biofuels), wastes and geothermal heat. A renewable energy system is considered as a power plant that converts renewable energy carriers or sources to electrical, mechanical or thermal energy [11]. Power-to-X technologies also fall under this term, in which renewable electricity is used to produce chemicals and fuels that can be stored and transported more efficiently, as well as renewable chemicals and fuels from agricultural residues, energy crops, forestry and wastes [12, 13]. By the end of 2022, the global capacity for renewable generation amounted to 3372 GW, with hydropower (37%), solar (31%) and wind (27%), being the main contributors (Figure 1.3). Overall, the share of renewables in the net expansion of capacity in 2022 was 83%, with wind and solar contributing 90% of the new renewable capacity and Asia leading in share of new capacity installed (59%) [14]. The renewable capacity additions are expected to further increase in 2023, to more than 440 GW, with solar PV (large scale and small distributed systems) estimated to account for two-thirds of the projected increase. This development is seen as a response to the higher electricity prices caused by the global energy crisis, that has led policy makers to become more active in seeking alternatives to imported fossil fuels to improve energy security. According to some projections, the capacity additions for renewable energy could reach 550 GW in 2024, assuming a faster implementation of recent policies and incentives and depending on the pace of permitting, construction and timely grid connection of projects that are under development. It should also be noted that by 2024, China’s share is set to have expanded to a record 55% of the global annual renewable capacity deployment, delivering 70% of new offshore wind, 60% of onshore wind and 50% of solar PV projects. In Europe, countries eased permitting in 2022 and 2023, by introducing more policy and regulatory changes than over the entire previous decade. Between 2021 and 2023, EU electricity consumers saved approximately EUR 100 billion owing

to the newly installed solar PV and wind capacity, partly mitigating the impact of the energy crisis. Furthermore, the projected growth of renewable energy such as clean electricity, bioenergy boilers, heat pumps, solar thermal and geothermal technologies, could potentially displace roughly 8 and 17 bcm of EU buildings-related gas consumption annually in 2023 and 2024, respectively. This could potentially be a crucial contribution to the struggle to cover the increasing gas demand in the case of extreme weather [15].

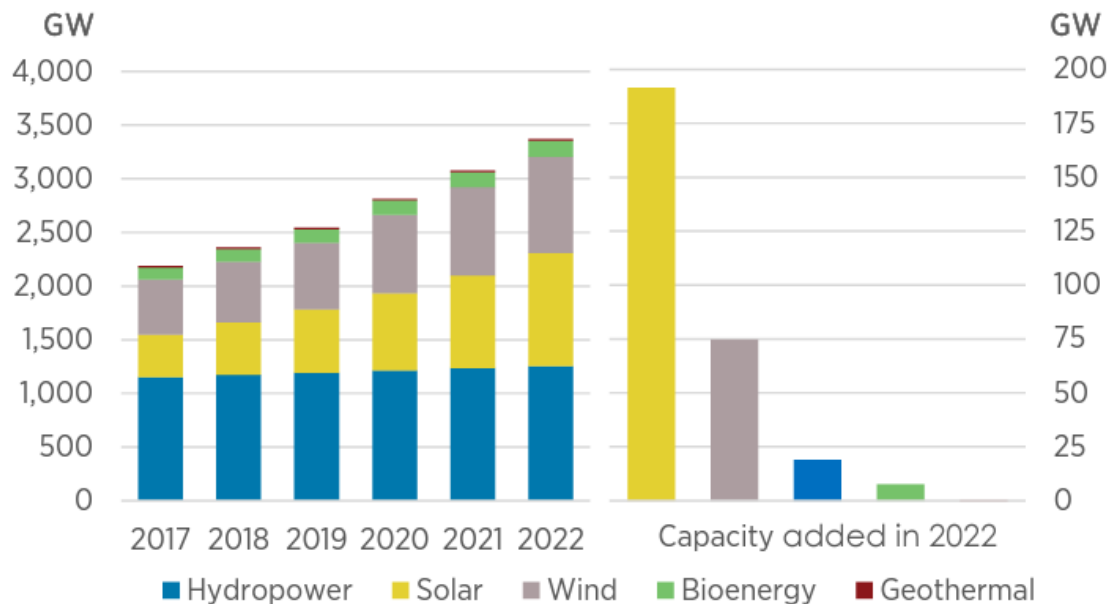


Figure 1.3: Global renewable generation capacity growth from 2016 to 2022 [14].

The above discussion highlights that apart from the necessity of supporting and promoting a green transition to a renewable future to ensure the well-being of mankind in the long term, the energy market in its present form is heavily exposed to shocks that have a significant negative impact on the quality of life of people globally in the very short term. Even though the need for such a transition has been identified and important actions have been taken to that end, further acceleration of this transition is imperative. According to the findings of the IEA World Energy Outlook 2022 report [16], the currently high energy prices are causing a huge transfer of wealth from consumers to producers, mainly for oil and natural gas, while the number of people without access to modern energy supply is rising. Approximately 75 million people with recently gained access to electricity may soon lose the ability to pay for it, while 100 million people may turn back to using traditional biomass for cooking. However, for the first time, a scenario based on the prevailing policy settings, sees a definite peak in the global demand for fossil fuels, with their share expecting to drop from 80 % in 2023 to less than 75 % by 2030 and to barely above 60 % by 2050. Despite promising, this trajectory would still lead to a 2.5 °C rise in global average temperatures by 2100, which while it is lower than implied by the baseline trajectory prior to the Paris Agreement, indicates that further action is required. In general, the world has not been investing enough in energy in the recent years, leaving the energy system vulnerable to shocks. A secure and steady energy transition will require a major increase in clean energy investments, even by tripling the spending by 2030 and shifting investments towards emerging markets and developing economies [16].

1.2 The role of bioenergy

Bioenergy, which is the use of biomass feedstocks for energy supply, is a growing renewable energy source in Europe and globally. This type of energy is produced from organic materials, known as biomass, where the carbon in their composition is absorbed by plants through photosynthesis. According to the United States Energy Information Administration (EIA), biomass is renewable organic material derived from plants and animals, which stores chemical energy produced by plants. Biomass sources for energy include wood and wood processing waste (firewood, wood pellets/chips, lumber, mill sawdust and waste, pulp and paper mill black liquor), agricultural crops and waste materials (e.g. corn, soybeans, sugar cane, switchgrass, woody plants, algae, crop/food processing residues), biogenic materials in municipal solid waste (paper products, cotton, wool, food, food wastes, yard residues) and animal manure and human sewage [17]. During energy production from biomass, the released carbon returns to the atmosphere and as more biomass is produced, an equivalent amount of carbon is absorbed, making modern bioenergy a near zero-emission fuel. In biorefineries, biomass is split into fractions that can be employed for the production of a variety of products such as energy, materials, chemicals, animal feed, pharmaceuticals, etc. Furthermore, intermediate bioenergy carriers, like torrefied pellets, pyrolysis oils or other biocrudes can be used for energy storage, improving the transportability of the energy carriers. Overall, bioenergy installations can be used for heat and electricity provision on demand, by covering baseload and peak demands, or by shifting energy provision between seasons. Bioenergy in its various forms (solid, liquid and gaseous) can be used in hard-to-decarbonise applications, such as high temperature heat production for industrial purposes, long distance aviation, heavy duty transport and international shipping. Combustion, anaerobic digestion, gasification, pyrolysis and hydrothermal liquefaction are some of the most important bioenergy technologies. A wide range of options is available to provide energy to the transport, heat and electricity sectors, along with opportunities for various feedstock and technology combinations for the production of several biorefinery products [18]. Additionally, bioenergy constitutes the most important method for achieving negative GHG emissions, which is required in order to meet the 1.5 °C target, by storing carbon in vegetation (or biochar sequestration), the subsequent biomass conversion to energy and the coupling of the system with a carbon capture and storage (BECCS) concept [19].

To characterize a system as a sustainable bioenergy system, it has to comply with certain criteria in terms of its technological merit (soundness, accessibility), its financial and economic merit (cost effectiveness, sound cost-benefit ratios and coherence with local and national development plan) and ecological soundness. The latter is of the utmost importance, since traditional biomass use, such as its employment in pit fires or inefficient heating devices, is not sustainable. Furthermore, land use change (LUC) considerations must be taken into account for the supply of a bioenergy system with biomass feedstocks. Direct Land Use Change (DLUC) refers to the direct conversion of a specific land area from one use (e.g. forest, agricultural crop, cultivation for food/feed) to another (e.g. crop cultivation for biofuels) [18]. On the other hand, Indirect Land Use Change (ILUC), refers to bioenergy production employing feedstocks grown on arable and pasture land, that can cause ILUC through market mechanisms. According to the EU's Renewable Energy Directive II (RED II) the phasing out of high ILUC risk biofuels, meaning fuels produced from feedstocks that are associated with significant levels of agricultural expansion into land with high carbon stock, is mandated after 2023. This mandate promotes the concept of low ILUC risk biofuels, that are produced from feedstocks that avoid food and feed crop displacement through improved agronomic practises leading to increased yields and through the cultivation of areas not previously used for crop production (including unused, abandoned or severely degraded land) [20].

In global terms, bioenergy can be considered as the most dominant renewable energy source, contributing to roughly 12 % of the total energy mix in 2019, as can be seen in Figure 1.4. Over 80 % of the bioenergy produced is employed for cooking and heating in buildings and the industry, covering roughly 20 % of the total heat consumption in 2020. However, out of this percentage only 8 % is derived from modern bioenergy concepts, with the rest being produced through traditional biomass use. Approximately 2.4 billion people, mostly in developing regions (sub-Saharan Africa and South Asia), have limited access to affordable and reliable modern energy systems and thus rely on traditional solid biofuels (firewood, charcoal, crop residues and animal dung). These fuels are sourced mostly through informal supply chains or are self-supplied and are used in open cookstoves and fireplaces with low energy conversion efficiencies (less than 15 %). Most importantly though, the use of traditional solid biofuels causes negative health effects, socio-economic and environmental consequences, since it generates health-damaging air pollutants, leading to severe ambient and indoor air pollution. This is considered as the major cause for roughly 3.8 million premature deaths yearly, mostly in low, lower and middle income countries [21]. Overall, ensuring the access of the severely affected global population to cleaner energy solutions is an important part of just transition as is it also addressed in the Affordable and Clean Energy Sustainable Development Goals of the United Nations [22], where the goal of phasing out traditional open fire bioenergy by 2030 is set. The role of modern bioenergy is predominant in that regard, since modern biomass stoves, bioethanol and biogas are some of several options to substitute traditional biomass. When compared to other cleaner cooking solutions such as natural gas, liquefied petroleum gas (LPG) or electricity, the sustainable use of biomass offers, apart from health benefits, the possibility of income generation (e.g. biomass cultivation, ethanol production) and the utilization of waste biomass (e.g. biogas production) [18].

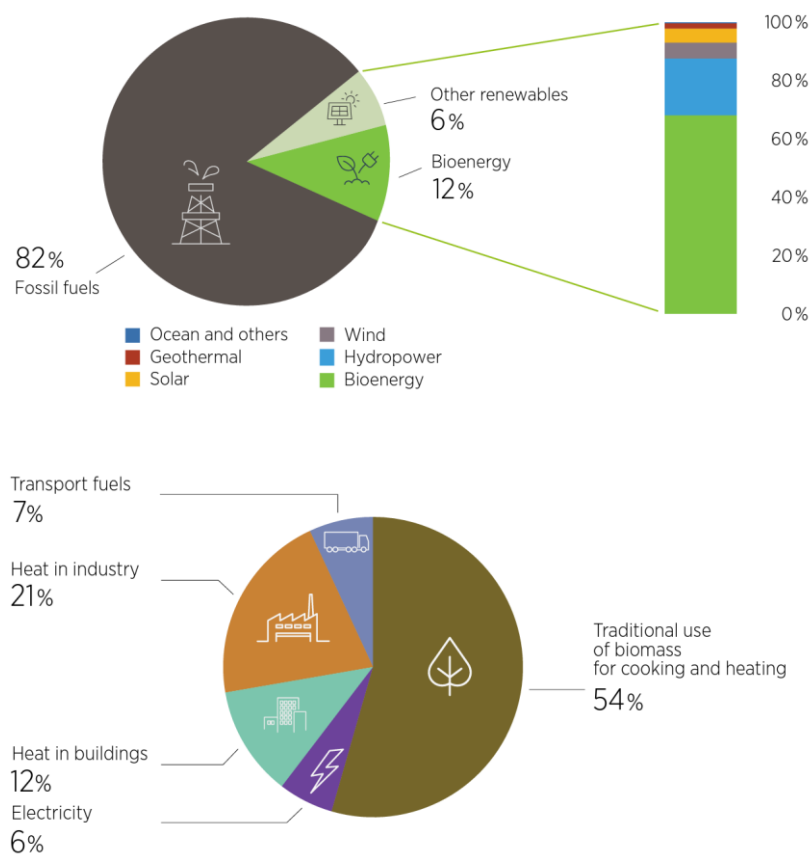


Figure 1.4: Share of renewables in global total final energy consumption in 2019 (top) and share of global bioenergy consumption by end use in 2020 (bottom) [21].

Modern bioenergy is considered to be one of the largest sources of renewable energy in the world, contributing to 55 % of renewable energy and over 6 % of the global energy supply in 2022. Overall, the use of bioenergy has experienced an average yearly increase of 3 % between 2010 and 2022 and is following an upward trend. In 2022, biofuels represented 3.5 % of the global transport energy demand, intended mostly for road transport. The growth of biofuels utilization has been following a 6% increase from 2017 to 2022, with the exception of 2020 due to the impact of the COVID-19 pandemic [23]. According to the Net Zero Emissions by 2050 (NZE) Scenario of the IEA [24], a rapid increase in the use of bioenergy by 8 % per year is required between 2022 and 2030, while making sure that this production is free of negative social and environmental consequences. The same scenario requires the increase of the contribution of biofuels to transport to 9 % by 2030, which would keep the share of fuel demand for road vehicles at the same level. Additionally, the usage of advanced feedstocks should also expand, since only 9 % of the total biofuel demand was covered from waste, residues and non-food energy crops in 2021, with the target for 2030 being over 40 %. More effort is required for aviation biofuels, where the less than 0.1 % coverage of demand in 2022, would need to scale-up to roughly 10 % in 2030. The success of this endeavour depends on several key factors, including the reduction of the cost gap between bio-jet and fossil jet fuel, the implementation of clear regulatory framework and the diversification of sustainable feedstock supply beyond waste and edible oils.

As mentioned in the previous paragraphs, there is a wide range of bioenergy technologies, offering a significant breadth of feedstock – product possibilities to contribute in the global energy mix. In general, bioenergy technologies can be broadly divided into two main categories, namely biochemical and thermochemical. Biochemical technologies (or biological) include anaerobic digestion and fermentation, where biomass is converted to gas (i.e. biogas) or liquid (i.e. bioethanol) product using bacteria, microorganisms and enzymes. On the other hand, thermochemical conversion technologies include hydrothermal liquefaction/carbonization, combustion, gasification and pyrolysis. In these technologies, fuels, chemicals or electricity are obtained through biomass using heat and in some cases catalysts. A separate type of bioenergy technology is mechanical extraction, a physio-chemical conversion process, consisting principally of extraction combined with esterification [25, 26]. As can be understood, there are several conversion pathways for biomass feedstocks that can lead to the production of a variety and combination of end-products. An overview of these technologies is presented in Figure 1.5.

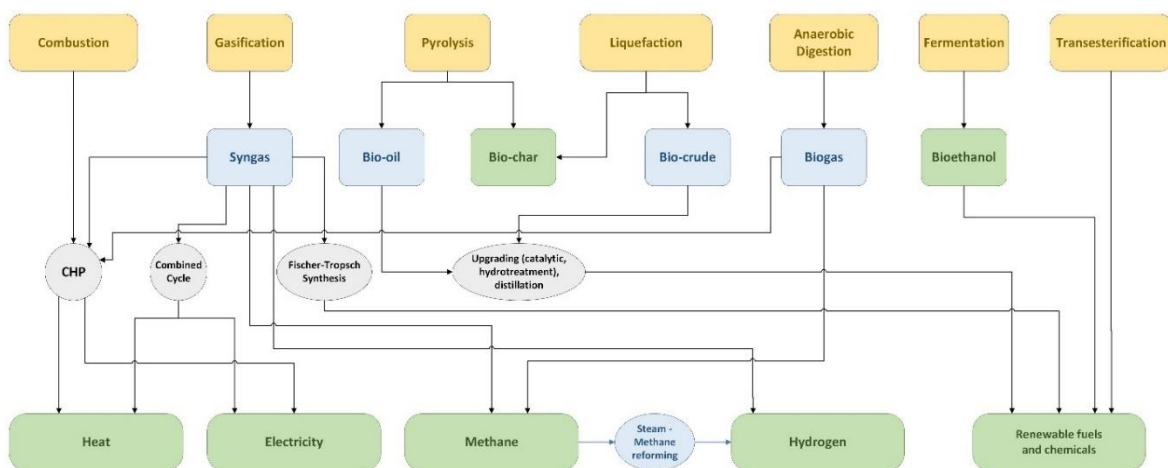


Figure 1.5: Overview of some biomass conversion technologies and derived products [27-29].

1.3 Biomass gasification and pyrolysis

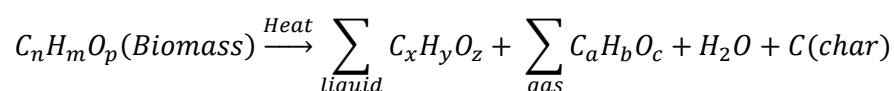
1.3.1 Pyrolysis

Pyrolysis can be defined as the thermochemical decomposition of (biomass) feedstocks into various products, without the presence of oxidizing agents (air, oxygen, steam, etc.), or with a limited one, which does not allow the occurrence of gasification to an appreciable extent. It should also be mentioned that pyrolysis constitutes one of the first reaction steps that take place during gasification. Through pyrolysis the large and complex hydrocarbon molecules decompose to smaller and simple gas, liquid and solid (char) molecules. As a process, it has an extended overlap with other processes such as devolatilization, carbonization, dry and destructive distillation, as well as thermolysis. However, the absence of chemical reactions with an external agent set it apart from gasification. Another major difference between the two processes is the temperature range in which they take place. Pyrolysis is typically conducted between 300 °C and 650 °C, while gasification occurs between 800 °C and 1000 °C [30].

In general terms, during a pyrolysis process, the biomass is heated to the final (pyrolysis) temperature at a certain heating rate and it is stabilized there for a certain time interval. The final products mainly depend on the biomass type, the pyrolysis temperature, heating rate and residence time. However the main phenomena that take place during the process can be generalized as follows [31]:

- Heat is provided by a source, the fuel/biomass temperature increases and moisture is released;
- Primary pyrolysis reactions are initiated at the final pyrolysis temperature and volatiles are released along with the formation of solid (char) residue;
- The now hot volatiles flow towards the lower temperature solids and heat transfer occurs;
- Certain parts of the volatiles are condensed in these lower temperature zones and subsequent secondary reactions can lead to tar formation;
- Autocatalytic secondary pyrolysis reactions take place simultaneously and in competition with the aforementioned primary pyrolysis reactions;
- Depending on the process characteristics (e.g. residence time and temperature/pressure profile) further thermal decomposition, reforming, water gas shift reactions, radicals recombination and dehydration reactions take place.

In summary, the primary pyrolysis products are char and gases, from where condensable gases further decompose into non-condensable gases (CO, CO₂, H₂ and CH₄), liquids and more char. This decomposition takes place mostly through homogeneous gas-phase reactions and at a lesser degree through heterogeneous thermal gas-solid phase reaction. During the latter, condensable vapours break down to smaller permanent gases molecules (CO, CO₂, etc.). The pyrolysis process can be generally described through the following reaction scheme [30]:



According to the employed process conditions, different types of pyrolysis exist. The main parameters that dictate the pyrolysis type however are temperature, heating rate and the residence time of the primary products in the reaction zone. In flash pyrolysis, the feedstock is heated at heating

rates above 1000 °C/s at temperatures between 450 °C and 600 °C, while the condensable and non-condensable gases produced are removed from the reactor after 30 to 1500 ms. The main difference between this type of pyrolysis and the much more commonly employed fast pyrolysis lies in the residence time of the gases, which is significantly lower for flash pyrolysis [32]. In fast pyrolysis, the feedstock decomposes to produce vapours, aerosols and charcoal at very high heating rates (1000 – 10000 °C/s) at 500 °C, with the residence time of the product gases being less than 2 s. In both fast and flash pyrolysis, a finely ground feedstock is required to achieve the desired heat and mass transfer rates, while the rapid quenching/condensation of the condensable products is of the essence for the maximization of the liquid yield, which is the main target of these types of pyrolysis [33]. On the contrary, in slow pyrolysis or carbonization, the production of charcoal or char is the main goal, constituting the oldest pyrolysis method, being employed for thousands of years. In slow pyrolysis, the feedstock is heated at heating rates below 100 °C/min at temperatures between 400 °C and 600 °C for extended residence time of the products (on hours scale), which allows their conversion into char and mostly non-condensable gases [34].

Regardless of the employed process parameters, a pyrolysis process yields gaseous (non-condensable vapours), liquid (condensable vapours) and solid products (char). The selection of the process parameters regulates the amounts, relative yields and composition of the final products, as was also described above. The liquid product of pyrolysis, bio-oil, is a combination of roughly 80 % polar organic compounds and 20 % water (mass). It consists of several compounds with different functional groups, such as phenolics, carboxylic acids, alcohols, hydroxyketones, esters, hydroxyaldehydes, sugars/anhydrosugars, lignin-derived oligomeric compounds and furan/pyran ring derivatives. Balancing the composition of bio-oil to fit the desired application purposes is a complex process consisting of trade-offs between composition and yields depending on the temperature and residence time effects. For example, when very short residence times are employed, depolymerization of the biomass feedstock's lignin content is not completed, leading to the presence of higher molecular weight oligomeric fractions in the bio-oil. This negatively affects bio-oil properties for certain application (e.g. increased viscosity). On the other hand, longer residence times can lead to secondary cracking of the pyrolysis condensable products, leading to significantly lower yields [35]. In terms of physicochemical properties, which are a direct translation of the above stated impact of its composition, the most critical ones are oxygen and moisture content, viscosity, acidity and ash content. In general, bio-oil has many special features and properties, that differ significantly from fossil fuel derived oils, as for example the fact that the stability of bio-oil is usually rather limited. Therefore, special considerations are required in regards to its storage, transport and application, making its upgrading a necessity in the vast majority of cases. The bio-oil properties that are the cause of this need are, among others, high viscosity and water content, low pH, inhomogeneity, temperature sensitivity and the presence of suspended char particles and alkali metals in its composition [31]. Applications of bio-oil include (co-)firing in boilers and combustion engines for heat and power generation, the production of liquid fuels such as diesel and ethanol (or blends) after refining, the production of chemicals such as olefins and aromatics upgrading after hydrotreatment, as well as the recovery of commodity chemicals (e.g. phenolics). An overview of potential bio-oil applications is presented in Figure 1.6. The solid product of pyrolysis, called char or bio-char, consists mainly of carbon (up to 85 %) and at a lesser degree also contains oxygen and hydrogen. Furthermore, it also contains inorganic materials and depending on the process characteristics (e.g. temperature), unconverted organics and carbonaceous residues from the degradation of organic biomass components. The inorganic content of char is lower compared to char derived from the pyrolysis of fossil fuels, which leads to overall lower yields. A typical lower heating value of biomass char is 32 MJ/kg, which is higher than that of the parent biomass and the one of the pyrolysis liquid product. This lower heating value is comparable to lignite and coke [30, 36]. Applications of pyrolysis char

include soil amendment and carbon sequestration, soil fertility improvement, pollution remediation and agricultural by-product/waste recycling. Furthermore, char can also be employed in several high-value applications such as catalysts, energy storage, environmental protection (sorber for pollutants removal in water and flue gases) and as a sustainable platform carbon material. Finally, the main gases produced during pyrolysis are carbon dioxide, carbon monoxide, hydrogen, methane, ethane, ethylene, propane, sulfur and nitrogen oxides and ammonia. Carbon dioxide and monoxide mainly originate from the decomposition and reforming of carboxyl and carbonyl groups, light hydrocarbons from weak methoxy and methylene bonds decomposition and hydrogen from the reforming and decomposition of C-H groups and aromatics. The gaseous product of pyrolysis is most commonly employed for internal process heat requirements [37].

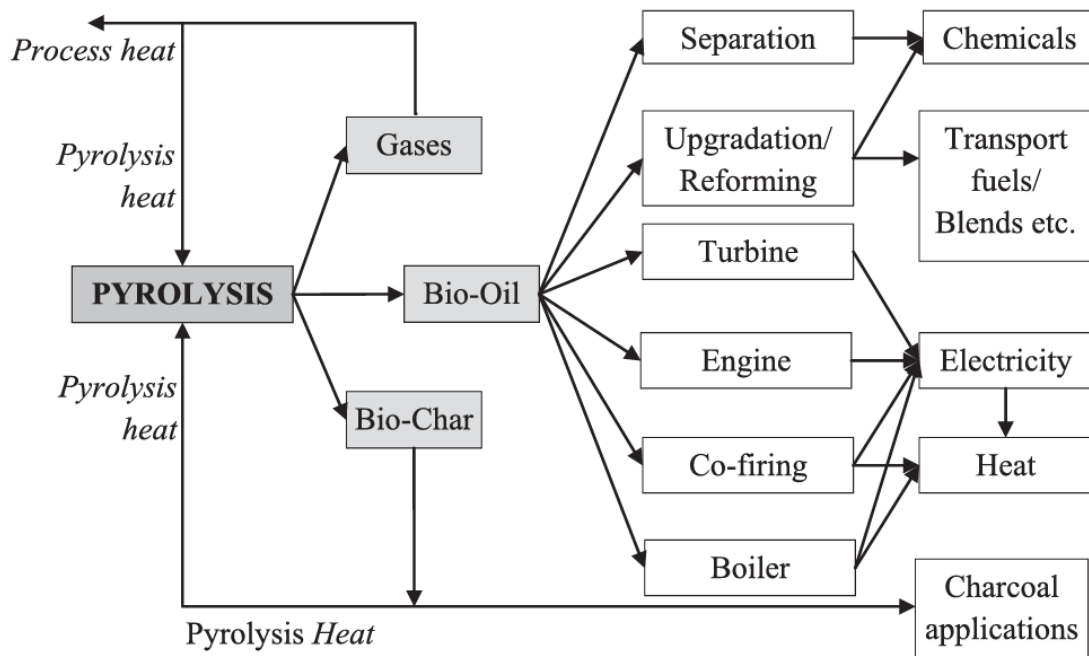


Figure 1.6: Applications of pyrolysis products [38].

1.3.2 Gasification

Gasification is the process by which a carbonaceous solid material is transformed mainly to a gaseous product called syngas, mostly comprised out of CO, CO₂, H₂ and CH₄, char, ash and tars. This process is taking place in the presence of a gasification agent at high temperatures. Drying, pyrolysis, combustion and reduction are the main stages of a gasification process as depicted in Figure 1.7. In general terms, gasification is a process by which chemical energy is stored into chemical bonds in the gas, in contrast to combustion where these bonds are broken for the release of heat. During gasification, hydrogen is added and carbon is stripped away from the feedstock, in order to produce gases with a higher hydrogen to carbon ratio. A variety of gasification media can be employed for this purpose, typically oxygen, air, CO₂ and steam. These agents assist with breaking down solid carbon and heavy hydrocarbons to low molecular weight gases, such as CO and H₂. The choice of gasification medium heavily influences the composition and heating value of the product gases, with steam favouring the production of a gas with high H/C ratio, while the employment of pure O₂ leads to a higher heating value of the gas. It should be noted that while the employment of air, despite having

certain process benefits (no need for an elaborate and costly N_2 removal process), leads to the dilution of the product gas with N_2 which significantly hinders its quality [39].

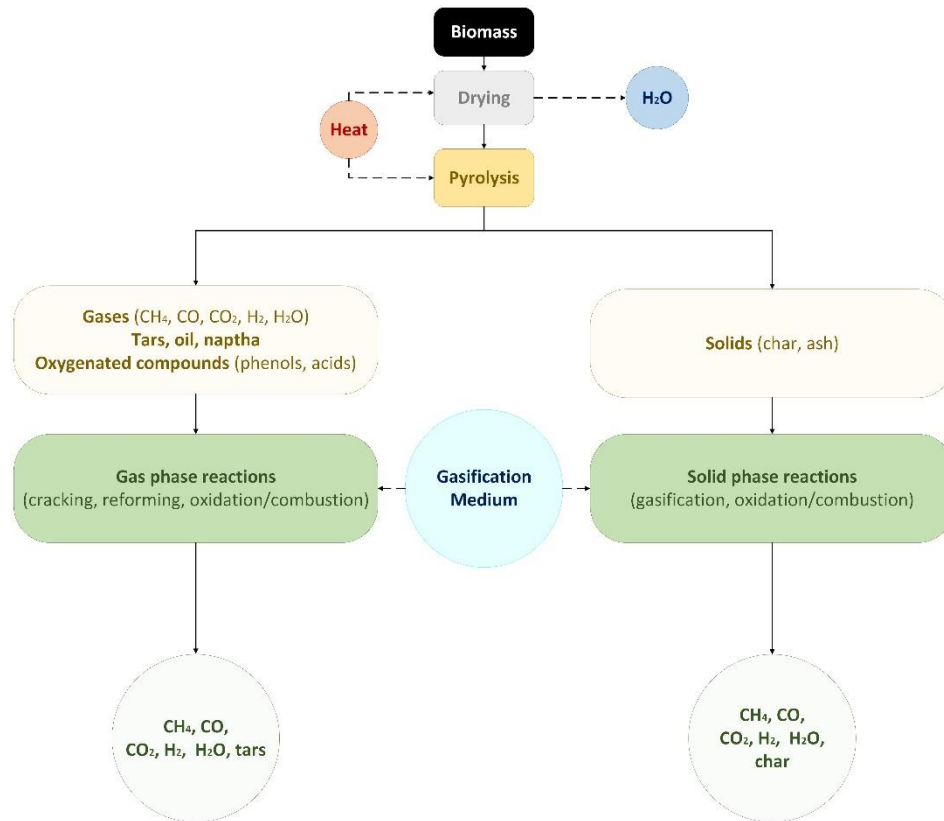
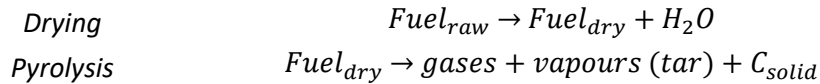


Figure 1.7: Biomass gasification pathway (adapted from [40]).

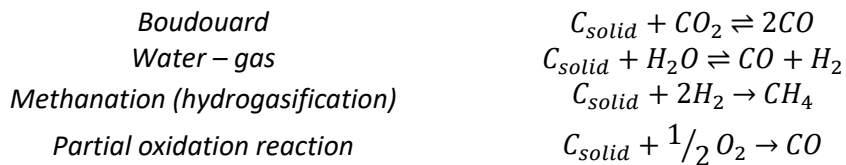
The conversion steps that an organic feedstock such as biomass undergoes during gasification, are depicted in Figure 1.7 and the governing reactions are presented in Table 1.1. During drying the moisture of the fuel is evaporated, while during pyrolysis the dried feedstock is decomposed in a solid fraction (char) and a volatile fraction comprised out of non-condensable (permanent) gases and condensable vapours (tar). The products of the pyrolysis step further react with the externally supplied gasification agent, as well as with O_2 , CO_2 and H_2O (steam) produced during the process. When there is a local depletion of oxygen in the gasification reactor, gasification or reforming reactions will proceed. These reactions, with the exception of the water-gas-shift reaction are endothermic, thus requiring external provision of heat to maintain the desired gasification temperature. Depending on the employed concept, this is either achieved by the supply of oxygen so that the heat of combustion can balance the heat required by the reduction reactions (“Direct Gasification”), or by heating the reactor from an external source, like a circulating heat carrier (“Indirect Gasification”) [41].

Table 1.1: Typical gasification reactions (adapted from [39, 41])

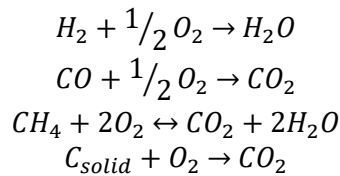
Carbon reactions



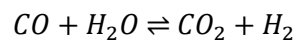
Carbon reactions



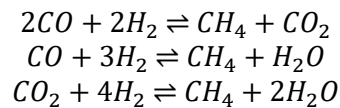
Oxidation reactions



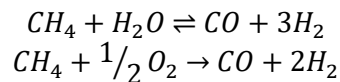
Water – gas shift reaction



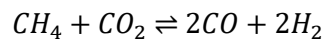
Methanation reactions



Steam reforming



Dry reforming



One of the aspects of gasification that requires specific attention is the production of tar which, as elaborated above, is one of the products of the pyrolysis process embedded in a gasification system. Tar is a complex mixture of condensable hydrocarbons, which include single to 5-ring aromatic compounds along with other oxygen containing hydrocarbons and complex polyaromatic hydrocarbons (PAH). According to the EU/IEA/US-DOE definition from 1998 though, tar is defined as all organic contaminants with a molecular weight larger than benzene [42]. During gasification, a large variety of tar products are generated depending on the operating conditions. The most important process parameters in that regard are temperature, pressure, residence time of the produced gas,

equivalence ratio and feedstock composition. In general, tar is an undesirable by-product of gasification, that can cause severe problems in downstream applications, such as [43, 44]:

- Blocking and fouling of pipelines, heat exchangers, engines and turbines
- Corrosion of downstream equipment
- Degradation of fuel cells
- Cracking in filter pores
- Lower cold gas efficiency and heating value of syngas
- Coking that can lead to catalyst deactivation, especially regarding downstream processes such as methanol synthesis, Fischer Tropsch synthesis and methanation.
- Production of phenolic wastewater
- Human and environmental risks due to the carcinogenic nature of tar compounds

The formation and transformation of tar compounds is a challenging process, since very fast and complicated mechanisms are involved, mostly due to the complex nature of biomass, which includes different polymeric units and cross-linkages in its main constituents (lignin, cellulose, hemicellulose). Furthermore, the large number of competing tar reactions that involve highly reactive radicals with complex chemistry add to this effect. In general, tar formation follows sequential steps. At temperatures below 500 °C, the produced tar is mainly comprised of oxygenated organic compounds, referred to as primary tar. Such tar species are vanillin, catechol, guaiacol and anisol. At temperatures above 500 °C primary tar is converted into secondary tar through dihydroxylation, demethoxylation and demethylation reactions that occur simultaneously. Secondary tar is mainly comprised of branched and heteroatom compounds such as phenol, cresols and xylenes. As the temperature increases to higher levels and especially in the 800 – 1000 °C region, secondary tar evolves to more stable compounds (tertiary tar), through ring condensation and polymerization reactions. Tertiary tars are divided to alkyl tertiary compounds (compounds with methyl branches) such as toluene, indene, methyl acenaphthylene and methyl naphthalene and polycyclic aromatic hydrocarbons (e.g. benzene, naphthalene, phenanthrene, anthracene, pyrene, etc.). Especially, the presence of PAH is highly problematic for a gasification process and therefore thorough understanding of their underlying formation mechanisms and their precursors is of essence. Briefly, there are two main pathways for tar formation, one considering phenol as the main precursor, while the other considers benzene. In both cases, the lignin content of biomass can be regarded as the most crucial aspect of its composition in that regard, since it includes an aromatic ring structure [43]. Finally, it should be mentioned that the aforementioned classification of tar compounds follows the structure suggested by Milne et al. in [45], based on their reactivity and order of appearance. Alternative classification methods exist however, in particular the one developed by the Energy research Centre of The Netherlands (ECN), Toegepast Natuurwetenschappelijk Onderzoek (TNO) and University of Twente (UT) within the framework of the project 'Primary measures for the inhibition /reduction of tars in biomass fuelled fluidised-bed gasifiers', funded by the Dutch Agency for Research in Sustainable Energy (SDE) [46]. This approach is based on the solubility and condensability of the tar compounds instead of their reactivity, but does not change the above stated conclusions.

During gasification, several tar decomposition reactions are taking place (steam reforming and dealkylation, thermal cracking, cracking and dry reforming), depending on the process conditions (e.g. temperature and residence time) and potentially the presence of catalysts in the system (catalytic bed material, downstream syngas cleaning, etc.). An overview of the most important tar reactions during gasification is given in Table 1.2. As can be seen, tar decomposition leads to the formation of gas species such as H₂, CO, CO₂ and CH₄, directly affecting the syngas yield and the equilibrium of the main gasification reactions [44]. Overall, the above stated "tar problem" requires the development of

efficient methods for tar removal, that promote tar decomposition reactions while not affecting negatively the formation of useful products. The methods that are currently in use can be divided into two main categories: (1) in-situ or primary tar reduction which takes place inside the gasifier and prevents tar formation and (2) post-gasification or secondary reduction that takes place outside the gasifier [42, 47]. In-situ or primary methods are the measures taken in the gasification process to prevent the formation of tar in the gasifier, or to convert it. Ideally, the concept of in-situ methods completely eliminates the need for post-gasification treatments. Consequently, to obtain high quality exit gas, the gasifier's performance needs to be optimized. The most decisive factors in this direction are the proper selection of operating conditions, the use of suitable bed material or catalyst and the gasifier's design [42]. Post-gasification or secondary methods, treat the hot product gas of the gasifier and they are chemical or physical in their nature. The chemical methods include thermal or catalytic tar cracking downstream of the gasifier. On the other hand, physical methods include the use of cyclones, baffle, ceramic, electrostatic and fabric filters, rotating particle separators and scrubbers. Secondary methods can be further divided into dry and wet gas cleaning. Dry gas cleaning is employed before the cool-down of the gas where the temperature is higher than 500°C and partly below 200°C after the gas has been cooled. On the other hand, wet gas cleaning is used after the gas has been cooled down to temperatures around 20 - 60°C. For example, cyclones, rotating and electrostatic precipitators and filters are examples of equipment of dry gas cleaning applications, while spray and wash towers, scrubbers, etc. are used in wet gas cleaning [48].

Table 1.2: Main tar decomposition reactions during tar reforming (adapted from [44])

Reaction Name	Equation
Steam reforming (1)	$C_nH_m + nH_2O \rightleftharpoons H_2 + CO$
Steam reforming (2)	$C_nH_m + H_2O \rightleftharpoons H_2 + CO_2$
Steam dealkylation (1)	$C_nH_m + nH_2O \rightleftharpoons C_xH_y + H_2 + CO$
Steam dealkylation (2)	$C_nH_m + H_2O \rightleftharpoons C_xH_y + H_2 + CO_2$
Thermal cracking	$C_nH_m \rightleftharpoons C_{solid} + C_xH_y + gas$
Cracking	$C_nH_m (Heavy\ tar) \rightleftharpoons C_nH_y (Light\ tar) + H_2$
Hydro cracking	$C_nH_m + H_2 \rightleftharpoons CH_4$
Hydro dealkylation	$C_nH_m + H_2 \rightleftharpoons C_xH_y + CH_4$
Dry reforming	$C_nH_m + CO_2 \rightleftharpoons H_2 + CO$
Carbon formation	$C_nH_m \rightleftharpoons C_{solid} + H_2$

* C_nH_m represents tar and C_xH_y represents lighter hydrocarbons

Gasifiers can be classified according to certain operation characteristics. One type of classification is based on the gas-solid interaction within the unit and it includes fixed or moving bed (downdraft, updraft, crossdraft) gasifiers, fluidized bed gasifiers (bubbling, circulating and dual) and entrained flow gasifiers (top-fed and side-fed). Additionally, gasifiers can also be classified according to the gasifying medium employed (air, CO₂, steam, etc.). Other relevant gasification technologies that can be identified, include plasma gasification and supercritical water gasification. An important distinction between gasifier types, can also be made according to the way that the heat required for the gasification of a feedstock is provided to the system. The later classification, which splits gasification technologies in direct and indirect systems, will be further discussed in Chapter 5. In this section the types of reactor technologies, depending on the interaction of gas and fuel within the system, are going to be briefly discussed.

The category of fixed and moving bed gasifiers constitutes perhaps the most popular commercial option due to the simplicity of their design and operation. In these systems the fuel moves down the gasifier in the form of a plug and depending on the contact between gasifying agent and fuel, fixed

bed gasifiers can be further divided in updraft, down-draft and cross-draft systems. In updraft gasifiers, the fuel flows from the top of the reactor, while the gasifying agent enters from the bottom in a counter-current configuration. In this case, the bottom portion of the reactor acts as the combustion zone for the drying and pyrolysis products, aiding to the increase of the temperature of the combustion zone and the up-flowing gases. These gases are then reduced in the reduction zone and can also serve as a medium for the drying of the biomass. These characteristics showcase the high thermal efficiency of this process, due to the low exit temperature of the gases from the system. Furthermore, updraft gasifiers have a low sensitivity in the amount of ash present in the feed, since the highest temperature point where the risk of ash fusion is most significant is located at the bottom of the reactor, close to the ash discharge point. In downdraft gasifiers, the gasifying agent is fed in the combustion zone, with the fuel being fed from the top to firstly the drying and then to the pyrolysis zone. After the combustion that takes place in the middle of the system, the gases flow into the reduction zone. Overall, downdraft or co-current gasifiers, have lower tar production rates compared to updraft gasifiers, however also possess lower thermal efficiencies, due to the higher gas outlet temperatures. Additionally, ash content in the feed should be fairly limited since high temperatures in the oxidation zone can lead to ash melting that could obstruct the flow of solids and ash discharge. Finally, cross-draft gasifiers employ a configuration where the gasifying agent is fed from the side and the fuel is fed from the top. However, in contrast to the updraft and downdraft concepts, the product gas is released from the opposite side to where the gasifying agent enters. In these type of systems high temperatures can be achieved in the combustion zone (around 1500 °C) and this is perhaps the most important reason that the lowest amount of tar is produced compared to the other configurations [49].

The operation of fluidized bed gasifiers is based on the concept of fluidization, where the fuel and the bed material employed behave as a fluid, when a fluidization medium (air, steam, oxygen or mixtures) is allowed to force through this solid inventory of the reactor. This concept offers enhanced mixing and heat transfer between the fuel particles, the bed material and the produced gases, with the fluidized bed operating at near isothermal conditions. Inert materials such as silica, as well as materials with catalytic activity such as sand, olivine, dolomite and glass beads (mostly for research purposes) are employed as bed materials, with the latter assisting greatly in the effort of tar minimization. The temperature of such systems is limited by the melting point of the bed material (typically between 700 °C and 900 °C) and in conjunction with the short residence time, leads to a high hydrocarbon content in the product gas compared to downdraft fixed bed systems, since chemical equilibrium is not achieved. However, these gasifiers have a high carbon conversion efficiency (reportedly up to 95 %) due to the back-mixing of solids and are suitable for scaling up due to their excellent mixing properties and feed – flexibility with regards to particle size and type of feed. Furthermore, in contrast to other reactor types, fluidized beds offer the possibility of employing additives for the in-situ removal of pollutants and to enhance tar conversion [50]. Depending on the velocity of the fluidizing medium, fluidized bed gasifiers can be divided in bubbling and circulating bed gasifiers. Bubbling fluidized bed gasifiers are designed to operate at lower gas velocities (around 1 m/s), while in circulating fluidized beds the velocities are typically between 3 and 10 m/s, leading to solid particles moving upwards along with the gas flow. These particles are then separated in a cyclone and recycled to the bottom of the bed. In both cases, the majority of the reactions take place in the dense bed region and substantial tar conversion takes place in the freeboard. Probably the weakest point in the fluidized bed technology comes from the employment of fuels with high ash content and in particular alkali metals, which can form eutectics with silica present in the bed material or the fuel itself, while the presence of chlorine also adds to this effect. The melting point of those eutectics is lower than the one of the bed material, leading to their melting at process temperature and the formation of bigger lumps called agglomerates. These agglomerates dramatically affect the

hydrodynamics of the reactor, leading to defluidization and correspondingly to a shut-down. However, options that reduce these phenomena and allow the use of high ash content fuels do exist and have been thoroughly discussed in the relevant literature [41]. The schematic representation of the two fluidized bed concepts is presented in Figure 1.8.

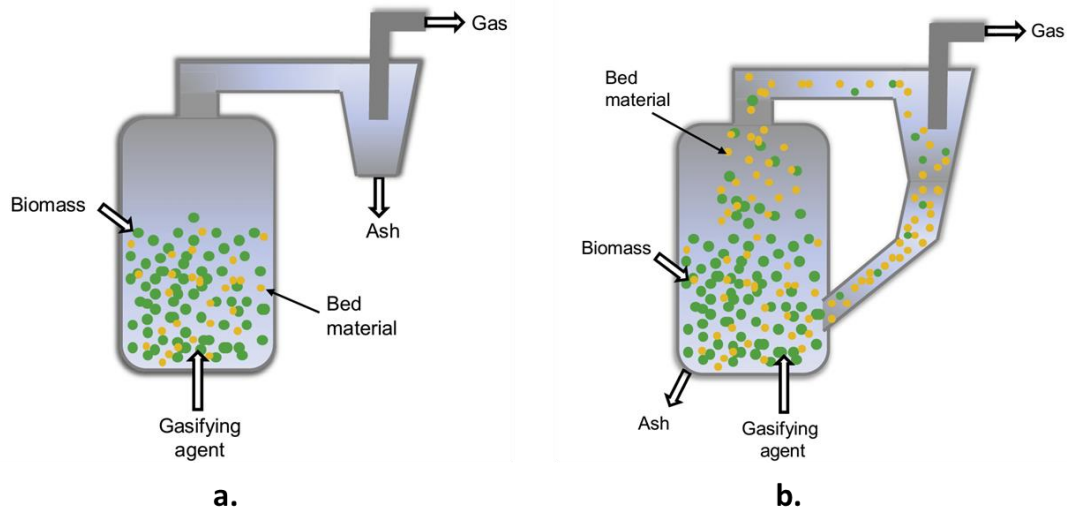


Figure 1.8: Schematic representation of bubbling (a) and circulating (b) fluidized bed gasification concepts (adapted from [51]).

Entrained flow gasification systems are perhaps the most widely used type of gasifiers, since they are commonly employed for large scale gasification of coal, petroleum coke and refinery residues. Unlike fluidized bed reactors, in this case no solid material is required. Instead, the feedstock is fed co-currently with the oxidizing agent by the means of a burner and a pneumatic transport regime is achieved due to the high flow velocity. Compared to both fixed and fluidized bed systems, entrained flow gasifiers operate at much higher temperatures, typically between 1200 °C and 1500 °C, allowing the thermal conversion of both tar and high hydrocarbons. This practically means that the product gas composition is near the chemical equilibrium composition and thus close to syngas quality [41]. A simplified schematic of the working principle of an entrained flow reactor is shown in Figure 1.9. At this point it should be mentioned that entrained flow reactors require the grinding of the feedstock to a very fine particle size. In the reactor the high velocity jet flow of pulverized fuel and oxidizing agent forms a recirculation zone near the entry point, allowing the fine particles to be rapidly heated by radiative heat from the reactor chamber walls and the hot gases downstream. This process takes place in excess of oxygen, which is depleted in its duration, with the remaining char undergoing much slower gasification reactions in a CO₂ and H₂O environment. The extended time interval required for these reactions, leads to the need of the employment of a large reactor for such systems. Entrained flow reactors can be classified in top-fed and side-fed systems. In top-fed entrained flow gasifiers, a vertically cylindrical vessel is used, where pulverized fuel and gasifying agents are conveyed by oxygen and injected from the top. On the contrary, in side-fed systems, the fuel is injected through horizontal nozzles placed opposite of each other in the lower section of the reactor. This way, a stirred-tank reactor effect is formed and the product gas moves upwards exiting from the top. Due to the high temperatures and the high oxygen availability in the mixing zone, the gas temperature is raised above the ash melting point (> 1400 °C), leading to the formation of slag which is then drained from the reactor. In general, entrained flow gasification of biomass feedstocks is rather limited mainly due to the very low particle size requirements (< 50 μm) calling for the employment of extensive pre-treatment measures (e.g. torrefaction), as well as the high alkali content of biomass ash. Regarding

the later, the molten ash from biomass can lead to corrosion of the gasifier's refractory and metal lining [30].

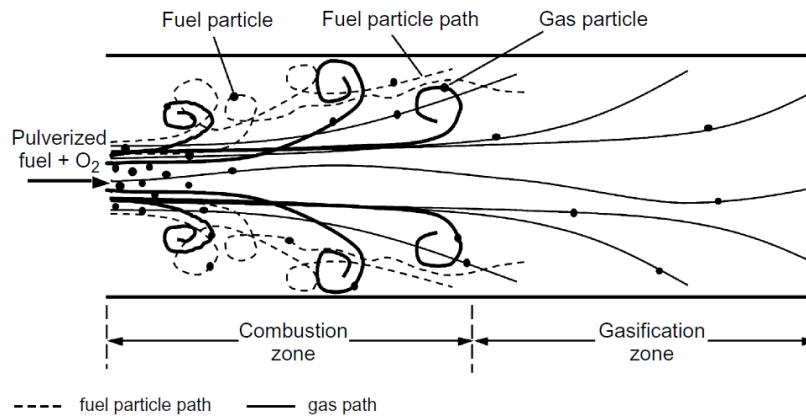


Figure 1.9: Simplified schematic of the working principle of an entrained flow reactor [30].

The last type of gasification unit to be discussed within this chapter is the supercritical water gasifier. In supercritical water gasification, wet biomass feedstocks can also be utilized, elevating the energy savings due to absence of drying needs. During this process, supercritical water is used as a solvent, offering a low dielectric constant and enhanced solubility. In particular, the solubility of organic material and gases significantly improves, materials insoluble in water or vapour can be dissolved, while inorganic materials solubility is decreased, in supercritical conditions. Water is in its supercritical state above the critical point of 22.12 MPa pressure and 374.12 °C temperature. The main products of the process are H₂, CH₄ and CO₂, with CO content being typically lower compared to other gasification processes due to the enhanced water gas shift and methanation reactions. Furthermore, fast solution of the formed gas in the supercritical water leads to the suppression of tar and coke formation. The temperature of the water influences greatly the composition of the product gas, since until 450 °C CH₄ is the main component and above 600 °C, H₂ becomes the main product. Overall, the ability of supercritical water gasification systems to treat wet feedstocks is one of its main advantages, along with the production of hydrogen-rich gas, the high process efficiency and the low tar formation. However, the use of special anti-corrosion and pressure/temperature resistant equipment increases the investment costs of the process. The operational costs are also significant due to the high energy requirements of the process. For this purpose, the use of catalysts is often suggested (e.g. Pt, alkali metals) to reduce the reaction temperature [49, 52].

As presented in the previous paragraphs, there is a wide range of gasification technologies that can be utilized for the production of a variety of feedstock – product combinations. An overview of the potential products from a biomass gasification process is presented in Figure 1.10. According to data from IEA Bioenergy, there were already over 1700 operational gasification based CHP plants in Europe, mostly using woody biomass as a feedstock, rendering this particular application a well-established technology. These types of facilities are able to facilitate the energy demands of hospitals, schools and hotels, they are employed in district heating concepts, as well as in sawmills, food production facilities and farms where the feedstock is readily available. Syngas from gasification can also be combusted in gas turbines, gas engines or boiler/steam turbine configurations for electricity production, internal combustion or Stirling engines for the generation of mechanical work and in high temperature fuel cells also for electricity generation. Co-combustion of the syngas with conventional fuels (coal, heavy oil or biomass) in power plants is also an option [53-56].

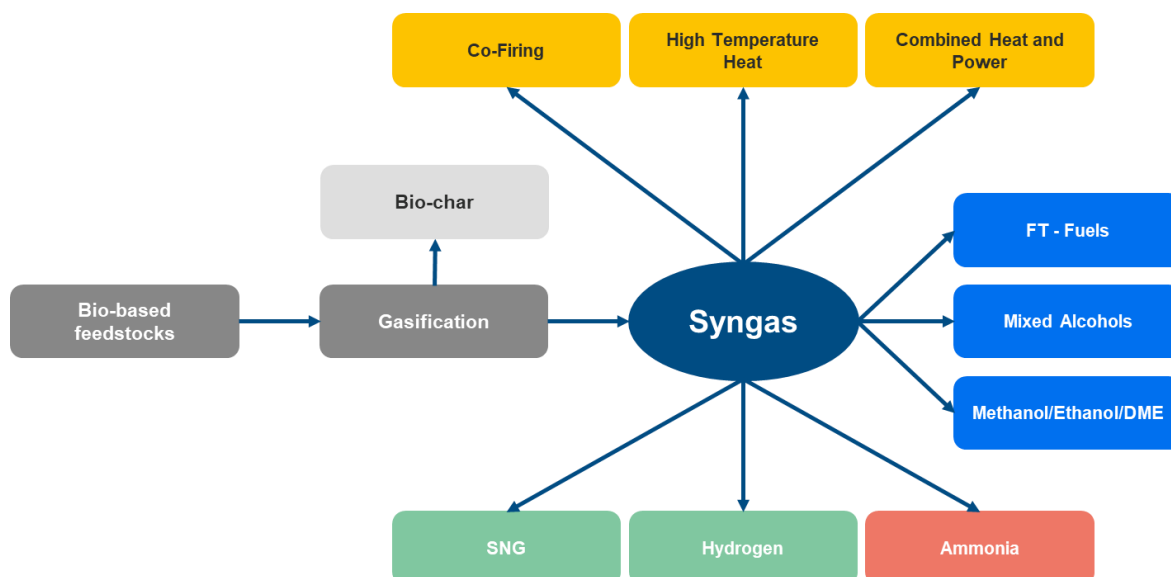


Figure 1.10: Syngas from biomass gasification utilization pathways (adapted from [53]).

Apart from the primary ways to utilize the syngas produced from gasification, several methods exist for its utilization after downstream processing. An overview of potential pathways for the valorisation of syngas is provided in Figure 1.11. The hydrogen content of syngas can be enhanced through steam reforming and water-gas shift reactions while methanol can be produced through the hydrogenation of carbon oxides over a suitable catalyst. Methanol can be further converted to diesel, gasoline, dimethyl ether (DME) and olefins, among else. Additionally, the Fischer-Tropsch synthesis process, which includes CO hydrogenation over a Fe, Co or Ru catalyst for the production of mainly higher hydrocarbons and oxygenates, is an important route of biomass gasification syngas utilization [57]. Furthermore, synthetic natural gas (SNG) can be produced using gasification syngas through methanation reactions over a catalyst (typically Nickel-based) [58]. Another method for syngas utilization is syngas fermentation, which is often referred to as a hybrid thermochemical and biochemical process. During syngas fermentation, acetogenic bacteria are used as biocatalysts for the microbial conversion of syngas into short-chain organic acids and alcohols (e.g. ethanol, acetate) [59]. Finally, the char byproduct of biomass gasification can be employed in several applications, such as tar removal, gasification feedstock, activated carbon, contaminants adsorbent, direct carbon fuel cell (DCFC) production, additive for anaerobic digestion and catalysts production [60].

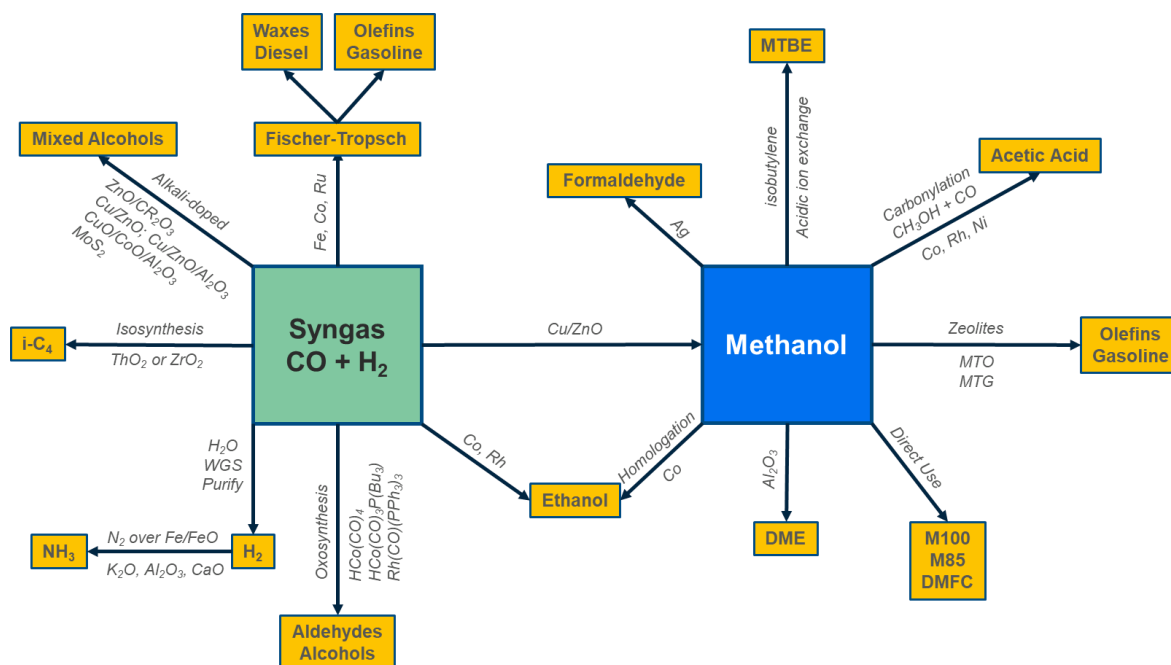


Figure 1.11: Overview of main syngas conversion pathways and final products (adapted from [61]).

1.4 Scope and research questions

One of the goals of this work is to explore and finally develop experimental and analytical methods, as well as relevant models, for the investigation of biomass pyrolysis. As extensively outlined in the Introduction, pyrolysis, apart from a stand-alone process aimed at the valorisation of biomass feedstocks, constitutes also a crucial step in a biomass gasification process and a method for fuels characterization in general. Therefore, the work performed within this PhD project, has a two-fold purpose, since the methods and models developed for biomass pyrolysis also constitute a significant input for the field of biomass gasification. For this reason, it was carefully considered that the employed methodology would be appropriately adjusted to be applicable in both these lines of biomass-related research. The second goal of this study was to investigate a new type of indirect gasifier, the Indirectly Heated Bubbling Fluidized Bed Steam Reformer. Within the context of this work, a 50 kW_{th} pilot reactor was developed and built through a collaboration between TU Delft and the company Petrogas. The scientific effort also included its commissioning and the conduction of experimental as well as modelling work to explore its operational characteristics and behaviour, while evaluating the industrial relevance of the proposed system in the field of biomass gasification. The corresponding investigation was focused on presenting a first, well-rounded overview of the properties and potential of such a novel biomass gasification unit. To achieve the aforementioned goals, the following research questions were formulated and addressed:

- How can the Polyaromatic Hydrocarbons (PAHs) formed during biomass pyrolysis, be sampled and quantified in a fast and accurate way?
- Which is the proper experimental and modelling methodology that needs to be employed in order to derive reproducible and accurate biomass pyrolysis mass loss kinetics?
- Can Artificial Neural Networks (ANN) be employed for the accurate prediction of biomass pyrolysis product class yields?
- What are the operational characteristics, occurring phenomena, performance metrics and product attributes of the novel Indirectly Heated Bubbling Fluidized Bed Steam Reformer?

- Can the hydrodynamic performance of the Indirectly Heated Bubbling Fluidized Bed Steam Reformer be accurately predicted and subsequently investigated, using numerical modelling via Computational Fluid Dynamics?

1.5 Thesis outline

In Chapter 1, a general introduction to the motivation and the concepts explored within this PhD thesis were presented. In Chapter 2, an experimental and analytical method developed for PAH sampling and quantification from woody biomass fast pyrolysis in a Pyroprobe reactor with a modified tar sampling system, is presented. Subsequently, Chapter 3 includes an assessment of biomass pyrolysis Thermogravimetric Analysis (TGA) through an international round robin. Chapter 4, discusses the topic of the estimation of lignocellulosic biomass pyrolysis product yields using Artificial Neural Networks. Furthermore, in Chapter 5, the experimental results from the gasification of woody biomass in the novel Indirectly Heated Bubbling Fluidized Bed Steam Reformer are examined, while in Chapter 6, its hydrodynamic performance is investigated using two-phase numerical modelling of Geldart B particles. Finally, in Chapter 7 the major conclusions and recommendations of the present work are summarized. It should be noted that, with the exception of the first and final one, each chapter has been published separately in peer-reviewed journals. Overall, the work conducted within this thesis, was performed within the context and with the support of the European project Biofuels Research Infrastructure (BRISK) 2 funded by EU Horizon 2020 (Grant Agreement Number: 731101).

Bibliography

1. Intergovernmental Panel on Climate Change (IPCC), *AR6 Synthesis Report: Climate Change 2023*. 2023.
2. Murdock, H.E., et al., *Renewables 2020 - Global status report*. 2020: France. p. 501.
3. Tian, J., et al., *Global low-carbon energy transition in the post-COVID-19 era*. Applied Energy, 2022. **307**: p. 118205.
4. Commission., E. *Tackling rising energy prices: a toolbox for action and support*. 2021 13/07/2023]; Available from: <https://eur-lex.europa.eu/legal-content/EN/TXT/?uri=COM%3A2021%3A660%3AFIN&qid=1634215984101>.
5. Zakeri, B., et al. *Pandemic, War, and Global Energy Transitions*. Energies, 2022. **15**, DOI: 10.3390/en15176114.
6. Cui, L., et al., *Exploring the risk and economic vulnerability of global energy supply chain interruption in the context of Russo-Ukrainian war*. Resources Policy, 2023. **81**: p. 103373.
7. Eurostat. *EU imports of energy products - latest developments*. 2023 14/07/2023]; Available from: [https://ec.europa.eu/eurostat/statistics-explained/index.php?title=EU imports of energy products recent developments&oldid=554503](https://ec.europa.eu/eurostat/statistics-explained/index.php?title=EU_imports_of_energy_products_recent_developments&oldid=554503).
8. Thompson, H., *The geopolitics of fossil fuels and renewables reshape the world*. Nature, 2022. **603**(7901): p. 364-364.
9. Perdana, S., M. Vielle, and M. Schenckery, *European Economic impacts of cutting energy imports from Russia: A computable general equilibrium analysis*. Energy Strategy Reviews, 2022. **44**: p. 101006.
10. Izvorski, I.L., Michael M.; Roseman Norfleet, Julia Renee; Singer, Dorothe; Torre, Iván, *Europe and Central Asia Economic Update, Spring 2023: Weak Growth, High Inflation, and a Cost-of-Living Crisis*. 2023: Washington, DC : World Bank.
11. Zepf, V., *Chapter 4 - The dependency of renewable energy technologies on critical resources*, in *The Material Basis of Energy Transitions*, A. Bleicher and A. Pehlken, Editors. 2020, Academic Press. p. 49-70.
12. Rego de Vasconcelos, B. and J.-M. Lavoie, *Recent Advances in Power-to-X Technology for the Production of Fuels and Chemicals*. Frontiers in Chemistry, 2019. **7**.
13. Chandel, A.K., et al., *The role of renewable chemicals and biofuels in building a bioeconomy*. Biofuels, Bioproducts and Biorefining, 2020. **14**(4): p. 830-844.
14. IRENA - International Renewable Energy Agency, *Renewable capacity highlights*. 2023: Abu Dhabi, United Arab Emirates.
15. IEA, *Renewable Energy Market Update - June 2023*, IEA, Editor. 2023: Paris.
16. IEA, *World Energy Outlook 2022*. 2023: Paris.
17. U.S. Energy Information Administration (EIA). *Biomass explained*. 18/07/2023]; Available from: <https://www.eia.gov/energyexplained/biomass/#:~:text=Biomass%E2%80%94renewable%20energy%20from%20plants%20and%20animals&text=Biomass%20was%20the%20largest%20source,and%20as%20a%20transportation%20fuel>.
18. IEA Bioenergy, *IEA Bioenergy Report 2023: How bioenergy contributes to a sustainable future*. 2023.
19. Faaij, A.P.C., *Repairing What Policy Is Missing Out on: A Constructive View on Prospects and Preconditions for Sustainable Biobased Economy Options to Mitigate and Adapt to Climate Change*. Energies, 2022. **15**(16): p. 5955.
20. Panoutsou, C., et al., *Opportunities for Low Indirect Land Use Biomass for Biofuels in Europe*. Applied Sciences, 2022. **12**(9): p. 4623.

21. IRENA, *Bioenergy for the Transition: Ensuring Sustainability and Overcoming Barriers*. 2022: Abu Dhabi.
22. United Nations, *The Sustainable Development Goals Report*. 2022: United States of America.
23. IEA, *Tracking Clean Energy Progress 2023*, IEA, Editor. 2023: Paris.
24. IEA, *Global Energy and Climate Model*, IEA, Editor. 2022: Paris.
25. Adams, P., et al., *Chapter 8 - Biomass Conversion Technologies*, in *Greenhouse Gas Balances of Bioenergy Systems*, P. Thornley and P. Adams, Editors. 2018, Academic Press. p. 107-139.
26. Alper, K., et al., *Sustainable energy and fuels from biomass: a review focusing on hydrothermal biomass processing*. *Sustainable Energy & Fuels*, 2020. **4**(9): p. 4390-4414.
27. McKendry, P., *Energy production from biomass (part 2): conversion technologies*. *Bioresource Technology*, 2002. **83**(1): p. 47-54.
28. Faaij, A., *Modern Biomass Conversion Technologies*. *Mitigation and Adaptation Strategies for Global Change*, 2006. **11**(2): p. 343-375.
29. Liu, B. and D. Rajagopal, *Life-cycle energy and climate benefits of energy recovery from wastes and biomass residues in the United States*. *Nature Energy*, 2019. **4**(8): p. 700-708.
30. Basu, P., *Biomass Gasification and Pyrolysis Practical Design and Theory*. 2010: Elsevier Inc.
31. Mohan, D., C.U. Pittman, and P.H. Steele, *Pyrolysis of Wood/Biomass for Bio-oil: A Critical Review*. *Energy & Fuels*, 2006. **20**(3): p. 848-889.
32. Jahirul, M., et al., *Biofuels Production through Biomass Pyrolysis —A Technological Review*. *Energies*, 2012. **5**(12): p. 4952.
33. Bridgewater Anthony V., *Biomass fast pyrolysis*. *Thermal Science*, 2004. **8**(2).
34. Czernik, S. and A.V. Bridgewater, *Overview of Applications of Biomass Fast Pyrolysis Oil*. *Energy & Fuels*, 2004. **18**(2): p. 590-598.
35. Amenaghawon, A.N., et al., *Biomass pyrolysis technologies for value-added products: a state-of-the-art review*. *Environment, Development and Sustainability*, 2021. **23**(10): p. 14324-14378.
36. Yaman, S., *Pyrolysis of biomass to produce fuels and chemical feedstocks*. *Energy Conversion and Management*, 2004. **45**(5): p. 651-671.
37. Hu, X. and M. Gholizadeh, *Biomass pyrolysis: A review of the process development and challenges from initial researches up to the commercialisation stage*. *Journal of Energy Chemistry*, 2019. **39**: p. 109-143.
38. Dhyani, V. and T. Bhaskar, *A comprehensive review on the pyrolysis of lignocellulosic biomass*. *Renewable Energy*, 2018. **129**: p. 695-716.
39. Basu, P., *Chapter 7 - Gasification Theory*, in *Biomass Gasification, Pyrolysis and Torrefaction (Second Edition)*, P. Basu, Editor. 2013, Academic Press: Boston. p. 199-248.
40. Tezer, Ö., et al., *Biomass gasification for sustainable energy production: A review*. *International Journal of Hydrogen Energy*, 2022. **47**(34): p. 15419-15433.
41. Siedlecki, M., *PhD Thesis: On the gasification of biomass in a steam-oxygen blown CFB gasifier with the focus on gas quality upgrading: technology background, experiments and mathematical modeling*. 2011, Delft University of Technology.
42. Devi, L., K.J. Ptasinski, and F.J.J.G. Janssen, *A review of the primary measures for tar elimination in biomass gasification processes*. *Biomass and Bioenergy*, 2003. **24**(2): p. 125-140.
43. Cortazar, M., et al., *A comprehensive review of primary strategies for tar removal in biomass gasification*. *Energy Conversion and Management*, 2023. **276**: p. 116496.
44. Islam, M.W., *A review of dolomite catalyst for biomass gasification tar removal*. *Fuel*, 2020. **267**: p. 117095.
45. Milne, T.A., R.J. Evans, and N. Abatzoglou, *Biomass Gasifier "Tars": Their Nature, Formation, and Conversion*. 1998, National Renewable Energy Laboratory (NREL) (NREL/TP-570-25357).
46. Devi, L., et al., *Catalytic decomposition of biomass tars: use of dolomite and untreated olivine*. *Renewable Energy*, 2005. **30**(4): p. 565-587.

47. Kumar, A., D.D. Jones, and M.A. Hanna, *Thermochemical Biomass Gasification: A Review of the Current Status of the Technology*. *Energies*, 2009. **2**(556-581).
48. Anis, S. and Z.A. Zainal, *Tar reduction in biomass producer gas via mechanical, catalytic and thermal methods: A review*. *Renewable and Sustainable Energy Reviews*, 2011. **15**(5): p. 2355-2377.
49. Mishra, S. and R.K. Upadhyay, *Review on biomass gasification: Gasifiers, gasifying mediums, and operational parameters*. *Materials Science for Energy Technologies*, 2021. **4**: p. 329-340.
50. Sansaniwal, S.K., et al., *Recent advances in the development of biomass gasification technology: A comprehensive review*. *Renewable and Sustainable Energy Reviews*, 2017. **72**: p. 363-384.
51. Bermudez, J.M. and B. Fidalgo, *15 - Production of bio-syngas and bio-hydrogen via gasification*, in *Handbook of Biofuels Production (Second Edition)*, R. Luque, et al., Editors. 2016, Woodhead Publishing. p. 431-494.
52. Heidenreich, S. and P.U. Foscolo, *New concepts in biomass gasification*. *Progress in Energy and Combustion Science*, 2015. **46**: p. 72-95.
53. IEA Bioenergy, *IEA Bioenergy Task 33 report: Gasification applications in existing infrastructures for production of sustainable value-added products*. 2021.
54. Pereira, E.G., et al., *Sustainable energy: A review of gasification technologies*. *Renewable and Sustainable Energy Reviews*, 2012. **16**(7): p. 4753-4762.
55. Molino, A., S. Chianese, and D. Musmarra, *Biomass gasification technology: The state of the art overview*. *Journal of Energy Chemistry*, 2016. **25**(1): p. 10-25.
56. Sikarwar, V.S., et al., *An overview of advances in biomass gasification*. *Energy & Environmental Science*, 2016. **9**(10): p. 2939-2977.
57. Santos, R.G.d. and A.C. Alencar, *Biomass-derived syngas production via gasification process and its catalytic conversion into fuels by Fischer Tropsch synthesis: A review*. *International Journal of Hydrogen Energy*, 2020. **45**(36): p. 18114-18132.
58. Rauch, R., J. Hrbek, and H. Hofbauer, *Biomass gasification for synthesis gas production and applications of the syngas*. *WIREs Energy and Environment*, 2014. **3**(4): p. 343-362.
59. Liakakou, E.T., et al., *Connecting gasification with syngas fermentation: Comparison of the performance of lignin and beech wood*. *Fuel*, 2021. **290**: p. 120054.
60. You, S., et al., *A critical review on sustainable biochar system through gasification: Energy and environmental applications*. *Bioresource Technology*, 2017. **246**: p. 242-253.
61. Spath, P.L. and D.C. Dayton, *Preliminary Screening -- Technical and Economic Assessment of Synthesis Gas to Fuels and Chemicals with Emphasis on the Potential for Biomass-Derived Syngas*. 2003, National Renewable Energy Lab (NREL), Golden, CO (United States): NREL/TP-510-34929.

2. PAH sampling and quantification from woody biomass fast pyrolysis in a Pyroprobe reactor with a modified tar sampling system

Chapter published in:
Journal of Analytical and Applied Pyrolysis, Volume 147, May 2020, 104802

2.1 Introduction

Concern around environmental changes, the future depletion of conventional fossil fuel reserves as well as the ever-increasing need for energy self-reliance and the global concern around environmental change caused by their use, have made heat and power generation from alternative and sustainable resources a primary research focus worldwide. Biomass is such a resource, constituting a potentially clean and renewable fuel, while being the third fuel resource worldwide, after coal and oil, in terms of abundance. Thermochemical conversion of biomass can be employed for heat, power, chemicals and fuels production. Pyrolysis, torrefaction, gasification, combustion and hydrothermal carbonization or liquefaction are considered as the major employed thermochemical conversion methods [1]. Pyrolysis is the thermochemical process of biomass decomposition, either in the absence of an oxidation medium, or with a minor amount which does not enable gasification to an appreciable extent [2]. Pyrolysis generates char, bio-oil and gases, depending on the reactor's operational regime. Pyrolysis is also a sub-process of solid fuel gasification and tar formation therein. During gasification, primary and secondary pyrolysis reactions occur among other reactions such as the water-gas shift reaction and char oxidation [3]. Biomass gasification is receiving a lot of attention as a route for (large-scale) energy conversion. However, the presence of tar in the product is linked to several issues such as condensation, formation of tar aerosols and polymerization for the formation of more complex structures. Such structures can damage process equipment including engines and turbines [4]. The amount and nature of the produced tars depend both on the operational parameters and on the type of the biomass feedstock. Therefore, the study of a biomass feedstock's tar production potential is essential for its successful application in gasification applications.

Tar is a complex mixture of oxygenated organic compounds, 1 to 5 – ring aromatic hydrocarbons and complex polycyclic aromatic hydrocarbons. According to the EU/IEA/US-DOE meeting on tar measurement protocol (Brussels, 1998), the components of thermochemical conversion products with a molecular weight higher than benzene are defined as tars [5]. In the present work however, the first definition is going to be used. Tars are produced primarily through depolymerisation during pyrolysis and their formation depends greatly on the reaction conditions. At intermediately high temperatures, secondary reactions take place in the gas phase converting the oxygen-containing tar compounds produced primarily to light hydrocarbons, aromatics, oxygenates and olefins. Subsequently, higher hydrocarbons and larger polycyclic aromatic hydrocarbons are formed [6]. Polycyclic aromatic hydrocarbons (PAH) are ubiquitous environmental pollutants that are formed from natural and anthropogenic sources [7]. Low molecular weight PAHs (less than four benzene rings) are acutely toxic, while high molecular weight PAHs are mutagenic and carcinogenic [8]. They are considered as by – products of high temperature pyrolysis and incomplete combustion reactions [9]. Tars can be broadly classified into four main categories: primary, secondary, alkyl tertiary and condensed tertiary tars. Primary tars are produced during primary pyrolysis (200 °C – 500 °C) and include cellulose – derived products such as levoglucosan, hydroxyacetaldehyde and furfurals, along with analogous hemicellulose-derived products and lignin derived methoxyphenols. Secondary tars mainly include phenolics and olefins and are produced from the thermal cracking of the primary tars at temperatures higher than 500 °C. The class of alkyl tertiary tars includes methyl derivatives of aromatics, such as methylacenaphthylene, methylnaphthalene, toluene and indene, while the condensed tertiary tars class includes PAHs (naphthalene, acenaphthylene, anthracene/phenanthrene, pyrene, etc.). Tar products belonging to those classes appear at pyrolysis temperatures higher than 650 °C and 750 °C, respectively [10]. Another tar classification scheme is proposed in [11] based on the solubility and condensability of the tar compounds instead of their reactivity. According to this scheme, tars can be divided into the following groups: GC – undetectable tars, heterocyclic tars which contain hetero atoms along with highly water soluble compounds (pyridine, phenol, cresols, etc.), light

aromatic tars including light hydrocarbons with a single ring (toluene, ethylbenzene, xylenes and styrene), light polyaromatic tars, which are two- or three-ring compounds (indene, naphthalene, methylnaphthalene, biphenyl, acenaphthalene, fluorene, phenanthrene and anthracene) and heavy polyaromatic tars such as fluoranthene, pyrene and chrysene which have more than three rings. Among these classes light polycyclic tars condense at low temperatures while heavy polycyclics condense at high temperatures, both at low concentrations [11]. Consequently, the use of an appropriate configuration of the tar sampling method is essential for the accurate determination of the tar production spectrum.

In processes such as gasification to produce producer gas or upgraded syngas and fast pyrolysis, which is mainly focused on bio-oil production, rapid heating rates are employed (higher than 100 °C/s). As a result, the investigation of tar formation under such conditions requires the use of reactors that can ensure such heating rates and the use of appropriate tar sampling techniques. Typical analytical pyrolysers that are used in such experimental studies include furnace type of pyrolysers, heated foil reactors, Curie – Point/Pyroprobe reactors, entrained flow/drop tube reactors, as well as small scale fluidized bed reactors [12, 13]. In furnace type of pyrolysers, the (small particle size) sample is introduced into a preheated zone rapidly. In Curie – point pyrolysers, the samples are placed on ferromagnetic wires or small sheets and they undergo pyrolysis at the Curie temperature of the ferromagnetic alloys [13]. Heated foil reactors, pyrolyse a thin disk of particles in an electrically heated wire mesh, while the heating rate and holding time are controlled by the proper adjustment of the current to the screen [12]. Pyroprobe reactors perform platinum filament heated pyrolysis, where the temperature of the filament surrounding the sample is controlled by variation of the voltage drop [14]. Drop tube furnaces are mostly vertical and down – fired and the samples are introduced in pulverized form. Entrained flow reactors are a variation of the drop tube furnace where the fuel particles are entrained in a carrier gas along the axis of the furnace into a flowing preheated gas stream. All these types of pyrolysers can achieve maximum temperatures above 1400 °C and appropriate heating rates for the conduction of fast or flash pyrolysis experiments [15]. Tar sampling from such instruments is based on cold trapping techniques followed by solvent absorption. The obtained volatiles can be analysed by the means of high – performance liquid chromatography (HPLC), size – exclusion chromatography – UV, gas chromatography (GC) – flame ionisation detection (FID) or GC – mass spectrometry (MS) [16]. In Table 2.1, the reader can find a brief overview on some tar sampling methods for PAH detection from fast pyrolysis reactors.

Pyroprobe reactors have been widely employed in the investigation of the pyrolysis characteristics of biomass species. Analysis of the produced volatiles is usually performed by means of GC - MS [17-25]. This choice however, creates an obstacle regarding the quantification of PAH species produced during pyrolysis. The main reason is that during devolatilization/pyrolysis most condensable gases are absorbed in the pyroprobe trap. By increasing the local temperature, desorption of the tars takes place at a maximum temperature of 350 °C. This temperature is not sufficient for the desorption of all the PAHs and especially the heavier ones. For example, the boiling point of pyrene and fluoranthene are 393 °C and 383°C, respectively [26]. Furthermore, limitations are imposed by the maximum GC inlet temperature and the maximum temperature of the GC line interface (typically below 300 °C and 200 °C, respectively [27]). Heavy PAHs can also recondense on the GC column under the aforementioned conditions. In general, quantitative results on the production of PAH cannot be obtained through PY – GC/MS pyrolysis [28]. Only qualitative results can be obtained, through the determination of the total calibrated chromatographic peak areas for several experiments performed at different temperatures with the same sample mass [29].

Table 2.1: PAH capturing and analysis methods from pyrolysis reactors reported in literature.

Feed	Pyrolysis reactor	Temperature (°C)	Heating rate	Tar sampling method	Post sampling	Tar analysis instrument	PAH species detected	Ref.
Xylan, cellulose, lignin	Fixed bed reactor	800	350 °C/min	Air and dry ice condensers	Washing by ethyl acetate	GC/MS	2, 3 and 4 ring PAHs	[30]
Municipal solid waste	Fixed bed reactor	800	350 °C/min	Air and dry ice condensers	Removal of aliphatic compounds and part of the aromatic tar fraction by washing with hexane. Remaining aromatics were obtained through ethyl acetate washing. Aliphatic and aromatic compounds were separated with a silica – alumina sorbent packed column.	GC/MS	2, 3 and 4 ring PAHs	[31]
Sawdust	Continuously fed drop-tube furnace	600 – 1400	n.a.	One sampling probe with a quartz filter and three 2-propanol filled impinger bottles; two at room temperature and one placed in a methanol – CO ₂ ice bath	Evaporation at room temperature for 20 – 30 h to constant weight. Heavy tars condensed in the sampling line were added to this residue after washing with tetrahydrofuran.	Identification by GC/MS and quantification by GC-FID	2, 3 and 4 ring PAHs	[32, 33]
Cellulose, pectin, chlorogenic acid	Quartz tube reactor	700 - 850	n.a.	Cambridge pad	Extraction with methanol from the pad. The reactor was rinsed with methanol.	GC/MS	2, 3 and 4 ring PAHs	[9]
Wood chips	Quartz tubular reactor	700	n.a.	1) Two frit – less ice cooled impingers, immerse in ice and liquid N ₂ and 2-propanol. Another two impingers with glass frit immerse in ice. 2) SPA tubes (Carbotrap 300 packed within stainless steel tubes) heated at 350 °C	Injection of internal standards	1)GC/MS 2)Thermal desorption with capillary GC/MS	2 and 3 ring PAHs	[16]
Acetylene	Quartz reactor	800 - 1000	n.a.	Light PAHs were retained as they passed through a fine tube filled with XAD-2 resin. Heavy PAHs were adsorbed on the produced soot or on the reactor walls or they were collected using quartz fibre filters.	Soxhlet extraction followed by PAH concentration by rotary evaporation and micro-concentration under nitrogen stream.	GC/MS	2, 3 and 4 ring PAHs	[34]
Poplar wood	Pyroprobe reactor	500	20 °C/ms	1) Solid phase extraction (Py-SPE). Silica gel was introduced to a glass tube packed with glass wool and conditioned with n-hexane. 2) Solid phase micro-extraction (Py-SPME) through a carboxen/polydimethylsiloxane fibre placed at the exit of the pyrolysis chamber.	1) The trapping apparatus was spiked with a surrogate PAH mix, rinsed with n-hexane and the solvent was collected in a vial after passing through the silica gel. The solution was subsequently blown down under N ₂ . 2) The fibre was introduced into an ammonia aqueous solution under magnetic stirring for 15 min and then dried under N ₂ flow.	GC/MS	Up to 6 ring PAHs	[35]

In this work, PAH formation during the fast pyrolysis of woody biomass within a high temperature range (500 °C to 1000 °C) is investigated. An additional purpose of this study is to present a fast and accurate method for PAHs sampling and quantification from pyrolysis experiments in a Pyroprobe reactor. More specifically, condensation of the produced PAHs was achieved by the coupling of the built – in trapping system of the Pyroprobe with an isopropanol filled condenser at room temperature. The obtained tars, dissolved in isopropanol, were analysed using an HPLC for the quantification of each PAH content, without the need for a solvent evaporation step. Besides the time and accuracy benefits of this method, the simultaneous sampling of the non – condensable pyrolysis products is possible. Thus, at least satisfactory mass balance values can be obtained and links between tar and permanent gases evolution can be investigated. Moreover, the decoupling of the Pyroprobe reactor from a GC/MS system allows the conduction of experiments with oxidizing agents such as air, oxygen and CO₂, although such attempts were not part of this study. Overall, this method offers a more complete determination of a biomass feedstock’s fast devolatilization characteristics and the effects of operational parameters on the products’ nature and distribution. The results were compared to those obtained from a heated foil reactor at the same process conditions. Significant differences, however, exist between the two reactor systems related to heat and mass transfer characteristics,

sample size, tar sampling procedure, etc. Considering the limitations in both cases (e.g. sample size), both reactor systems were used in such a way as to ensure yields relevant to the relatively high heating rate industrial application cases for all product fractions (gas, char, tar), which would also positively affect the identification of its individual gaseous and tar (in this case PAH) compounds afterwards. Therefore, the purpose of any comparison of the two performed, is to highlight the differences in PAH quantification from biomass fast pyrolysis by following two different procedures.

2.2 Materials & methods

2.2.1 Proximate and ultimate analysis of the fuels

Raw biomass supplied by the Dutch company Synvalor was employed. In particular, a waste softwood mixture, a by-product of furniture manufacturing was used as a feedstock. Prior to the experiments the biomass was ground and sieved to powder with particle size <90 μm . Proximate and ultimate analysis of the wood is provided in Table 2.2. Analytical description of the procedures followed for the analysis, as well as the sugar and biochemical composition of the feedstocks can be found in [36].

Table 2.2: Proximate and ultimate analysis of waste softwood

	a.r.	d.b.	daf
Moisture^a (wt%)	7.9	-	-
Ash^a (wt%)	0.7	0.8	-
VM^a (wt%)	72.1	78.3	78.9
FC^a (wt%)	19.3	21.0	21.1
C (wt%)	45.6	49.5	49.8
H (wt%)	4.7	5.0	5.1
N (wt%)	0.5	0.5	0.5
S (wt%)	0.04	0.04	0.04
O^b (wt%)	36.5	39.6	39.9
HHV (MJ/kg)	18.1	20.6	20.7

^a calculated by TGA

^b calculated by difference

2.2.2 Apparatus and experimental procedure

Fast pyrolysis experiments within this work, were conducted on a CDS Pyroprobe Model 5200. The Pyroprobe is a pyrolysis instrument which can perform multistep platinum filament heated pyrolysis, in order to provide gas samples for gas chromatography, mass spectrometry or FTIR. By calculating the resistance of the filament at a particular temperature, the very temperature of the filament can also be controlled by voltage variation. The temperatures for the pyrolysis filament can reach up to 1400 °C at heating rates from 0.01 °C/min to 20 000 °C/s, while the interface temperatures can be set to 350 °C. In Pyroprobe, a great variety of biomass feedstocks can be investigated, ranging from woody biomass to sludge. The typical sample size is 30 mg. For solid materials, preferably small particles sizes (<75 μm) are used to avoid heat transfer limitations. Furthermore, nitrogen, air or CO₂ can be used as mediums.



Figure 2.1: CDS Pyroprobe 5200 setup during a fast pyrolysis experiment

Pyroprobe is equipped with a ½" coil probe, able to house a 2.1 mm quartz tube with maximum capacity of approximately 300 mg of sample. Figure 2.2 presents a schematic overview of the equipment and the experimental procedure. This configuration allows higher biomass loading, compared to traditional Py-GC/MS applications where the typical biomass loading is 2-3 mg. In this way the inaccuracies and uncertainties during product collection and determination can be significantly reduced. For each experiment, a sample of approximately 30 mg weight was placed in the middle of the quartz tube, with the support of some quartz wool in both ends. The sample holder and the quartz wool are cleaned with pressurized air and seared respectively, to avoid contaminants. This sample size was selected to avoid the introduction of heat and mass transfer limitations imposed by larger sample sizes. At the same time, this sample size is considered large enough to lead to the production of considerable yields of the products investigated.

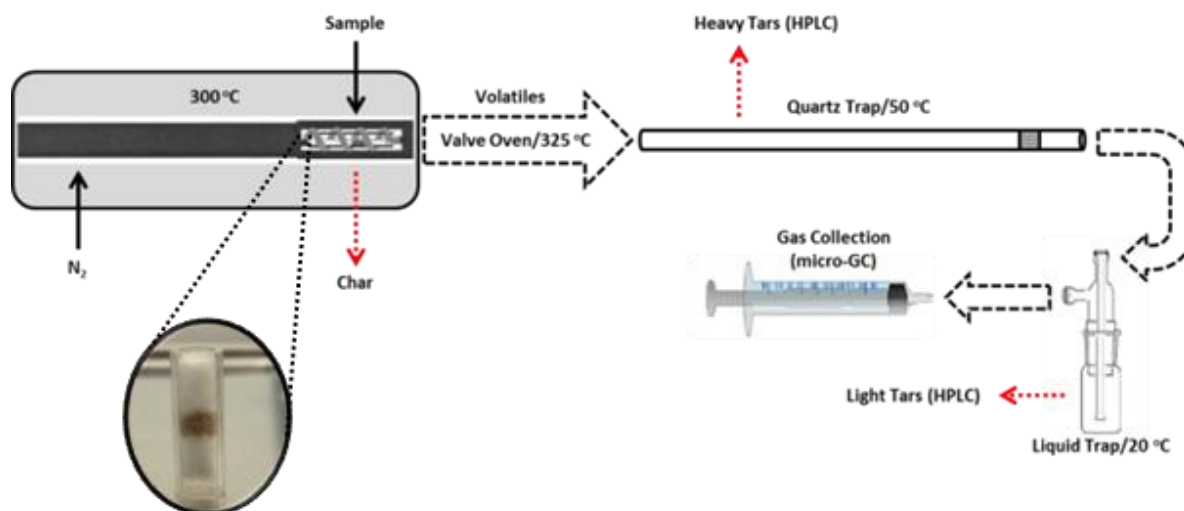


Figure 2.2: A schematic overview of the experimental procedure and product sampling methods that were followed in the conduction of the pyrolysis experiments.

The coil probe, loaded with the quartz tube containing the sample was introduced in the Pyroprobe interface. The interface was heated from an initial temperature of 50 °C to 300 °C at a heating rate of 100 °C/min. Afterwards, the coil was heated with a heating rate of 600 °C/s to the desired pyrolysis temperature, which was maintained for 10 s. It must be noted that the actual temperature inside the quartz tube differs from the one that is set for the probe coil. According to the manufacturer, the difference is approximately 100 °C. Nitrogen (purity 99.999 %) was used as a purge gas at a constant flow of 10 mL_n/min using a flowmeter. The pyrolysis vapours flowed from the quartz sample tube to the trap through the valve oven which was kept at 325 °C (Figure 2.3). The trap consisted of a quartz tube (114 mm L, 4 mm I.D.) equipped with a glass frit to facilitate aerosol condensation. The trap was heated with a heating jacket at 50 °C because of the high temperature in the oven upstream the trap (325 °C). The majority of condensable products (tars and moisture) condensed in the trap. However, an additional liquid trap was connected downstream this quartz tube trap to ensure the condensation of lighter tar species. The liquid trap consisted of an impinger bottle filled with 2 mL of 2-propanol (IPA) (99.9 % purity). At the exit of the liquid trap gases were collected in a syringe with a freely moving piston for subsequent analysis by micro-GC. After the end of the sample heating, with the interface temperature still at 300 °C the operation continues for 5 min to achieve complete collection of the gaseous and liquid product.

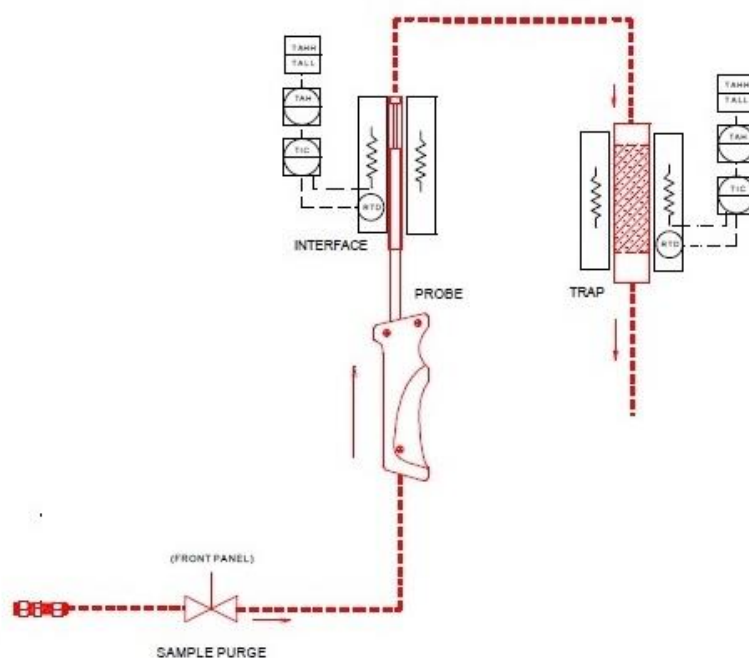


Figure 2.3: Diagram of the pyroprobe reactor and purge flow pathway

At the end of the experiment, the char product and the liquid product (tars and with pyrolytic water) that condensed in the quartz trap were determined gravimetrically by weighing the sample quartz tube and the quartz trap, respectively. Initially, the weight of the holder with one piece of quartz wool on one end is measured. Afterwards, the weight including the biomass sample and subsequently the other piece of quartz wool is measured. It should be noted that the weight measured during this procedure also includes the moisture of the sample. Furthermore, before the initiation of the experiment the weight of the empty trap is also noted. After the completion of the experiment both the weight of the holder and the trap are measured again. This way, the amount of volatiles released and the gravimetric tar content of the biomass are measured. After the end of the experiment

and the weighing, the quartz trap is inserted in a testing tube along with the 2 mL of isopropanol plus an additional 3 mL. The trap remains there for approximately 40 min, so that the tars can dissolve. Afterwards, the solvent is filtered and is collected in a vial which is subsequently refrigerated. It should be mentioned here, that after a certain point, due to damage on the impinger bottle, a two – traps configuration was employed. That practically means that a second trap was used instead of a glass tube in the condenser. This particular adaptation did not influence the overall process or the results in any way. However, during the sampling procedure, the second trap was immersed in the 2 ml of IPA in the condenser, while the 3 ml were used only for the first trap. Additionally, the total amount of gas that is collected in the syringe is measured as it is used in the gas yield determination. All experiments were performed at least in triplicate.

The heated foil reactor employed was coupled with an FTIR for the simultaneous analysis of the product gases. A detailed schematic of the reactor and the overall procedure can be found in [36]. Briefly, the biomass sample was ground and sieved to particle sizes below 90 μm and subsequently, 10 mg were compressed into a tablet (2.5 mm diameter, 0.7 mm thickness) by using a pellet press (force of 2 t). The sample size employed is limited to 10 mg, since for larger sample sizes, the increased thickness of the tablet would impose significant temperature gradients in the sample, as it was found by the authors in [37]. The tablet was then placed on the stainless steel foil and the reactor was purged with N_2 (purity 99.999 %) in order to create an inert atmosphere. No temperature correction was employed in the case of the heated foil experiments, since the thermocouple of the instrument is located on the plate where the sample is placed. Subsequently, the sample was heated to the final pyrolysis temperature (500 – 1000 $^\circ\text{C}$) for 10 s at a heating rate of 600 $^\circ\text{C}/\text{s}$. A circulation pump was used for carrying the product gases to the FTIR for analysis. After the gas analysis, the reactor was cooled down by a N_2 stream and the remaining char was retrieved from the foil and measured gravimetrically. Glass wool was placed at the outlet of the main chamber (before the circulation pump) to serve as a tar trap. The tar trapped in the glass wool filters was washed with DCM (dichloromethane) and mixed with the tar obtained from the reactor's walls and lid (also washed with DCM). After filtering, the total solution was subjected to DCM evaporation at room temperature in a fume hood and the final total tar yield was determined gravimetrically. All experiments were performed in triplicate.

2.2.3 Analysis of the products

Tars from pyrolysis experiments were analysed by means of a high performance liquid chromatograph (HPLC) supplied by KNAUER System. Separation was achieved on an UltraSep ES PAH QC, 60 \times 2.0 mm column, with a mobile phase of water/acetonitrile at a flow rate of 0.5 ml/min. The analysis temperature and analysis time were 25 $^\circ\text{C}$ and 17 min, respectively. Determination of tar composition was accomplished with a combination of ultraviolet-visible light (UV) and fluorescence detectors. According to the US Environmental Protection Agency (EPA) [38], the UV detector is recommended for the determination of naphthalene, acenaphthylene, acenaphthene, and fluorene while the fluorescence detector is recommended for the remaining PAHs. The UV detector wavelength was set at 254 nm. In the fluorescence detector, unlike in the UV detector, the wavelength varies with time during each experiment. The fluorescence excitation (EX) and emissivity (EM) wavelengths were set for the individual groups of PAHs as: EX-275 nm, EM-325 nm for naphthalene, acenaphthene and fluorene; EX-255 nm, EM-375 nm for phenanthrene and anthracene; EX-270 nm, EM-420 nm for fluoranthene and pyrene; EX-275 nm, EM-383 nm for benzo(a)anthracene and chrysene; EX-295 nm, EM-410 nm for benzo(b)fluoranthene, benzo(k)fluoranthene and benzo(a)pyrene; EX-301 nm, EM-420 nm for dibenzo(a,h)anthracene and benzo(g,h,i)perylene and finally EX-304 nm, EM-501 nm for

indeno(1,2,3-cd)pyrene. Due to the limited amount of strongly fluorescent compounds, the fluorescence detection is highly selective.

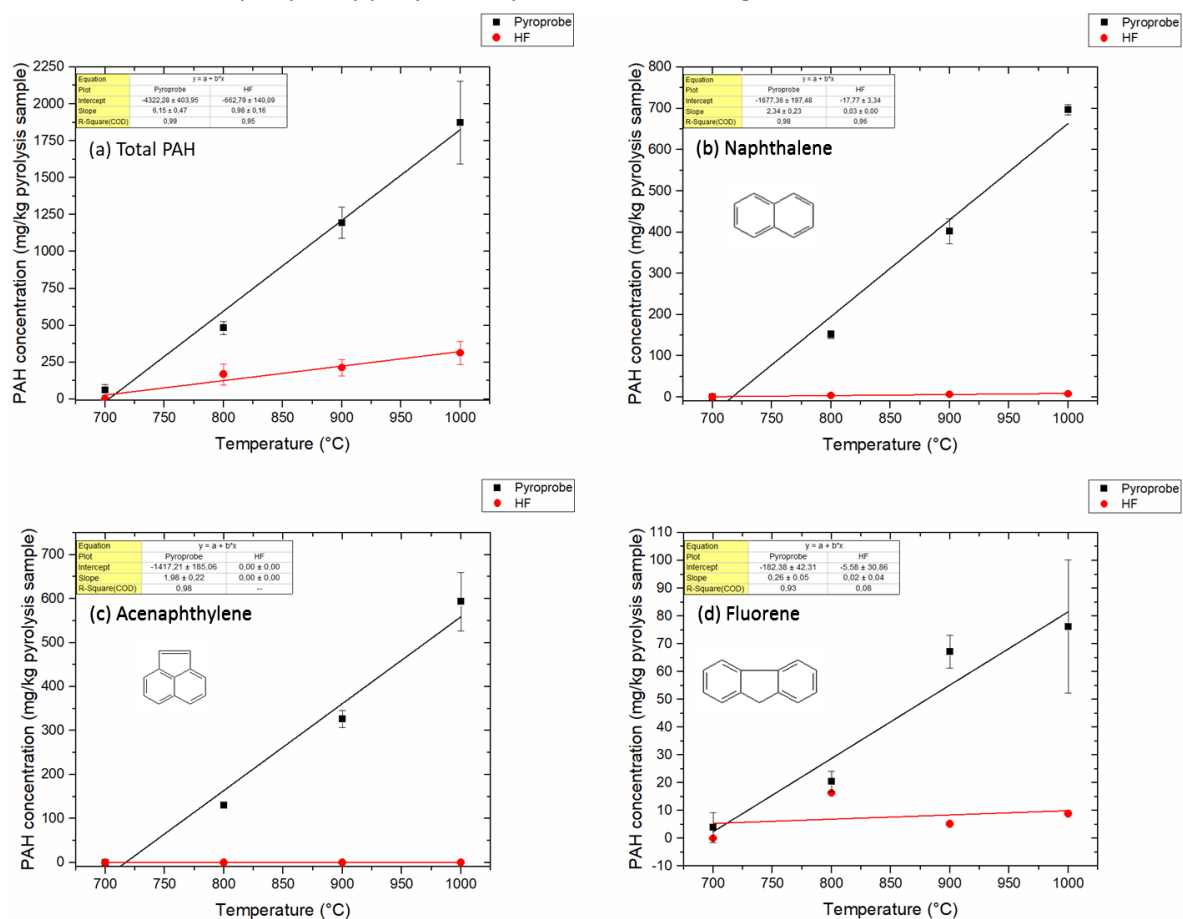
A certified PAH standard mixture (SS EPA 610 PAH Mix 100-2000 $\mu\text{g}/\text{ml}$ methanol : methylene chloride 1:1) was supplied by Sigma Aldrich for calibration of the HPLC system. The calibration was carried out using the standards at 7 different concentrations. Each calibration standard was injected three times to check the analysis repeatability and the calibration curve was prepared by considering the whole set of injections. The correlation factor obtained after the calibration procedure was $R^2 > 0.99$ for all the PAH compounds under investigation. The fluorescence detector, being very sensitive concerning PAH analysis, can detect very low concentrations. The system was calibrated with a lowest concentration limit of 0.2 $\mu\text{g}/\text{ml}$.

Gas analysis for the pyroprobe experiments was performed on a Varian $\mu\text{-GC}$ CP4900. Separation of H_2 , CO , CO_2 and CH_4 was achieved on a 1 m CP-COX column and detection and quantification by a TCD detector with Argon used as carrier gas. For the heated foil experiments, a Thermo Nicolet NEXUS 6700 FTIR was used. The FTIR was calibrated for CO_2 , CO , CH_4 and H_2O detection and quantification. The resolution was 0.25 cm^{-1} and 3 scans were averaged every 9 s for a total time of 3 min.

2.3 Results & discussion

2.3.1 Influence of pyrolysis temperature on PAH evolution

The total PAH along with the main individual PAH compounds found in the product tar/oil from wood pyrolysis (600 °C/s, 10 s holding time) at different temperatures from both analytical pyrolysers (pyroprobe – PP and heated foil reactor – HF) are depicted in Figure 2.4. Appreciable quantities of PAHs were found only at peak pyrolysis temperatures exceeding 700 °C.



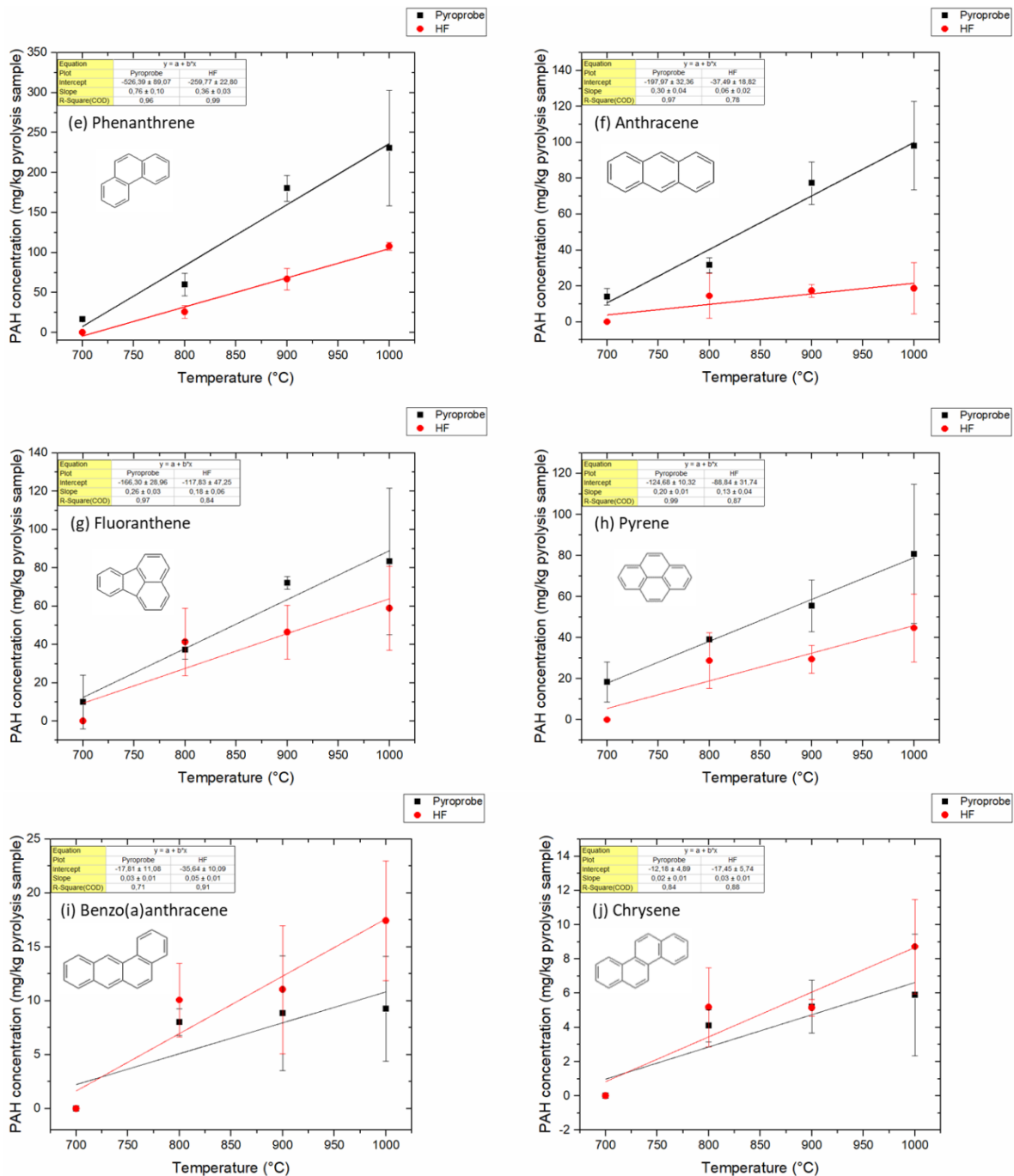


Figure 2.4: PAH evolution during pyrolysis (600 °C/s, 10 s holding time) of wood at different temperatures, comparison between pyroprobe and heated foil (HF).

In the case of the PP experiments, the total PAH yield increased from 60 mg/kg at 700 °C to approximately 1900 mg/kg at 1000 °C. The total PAH yield, as can be seen in Figure 2.4 (a), was significantly higher for the pyroprobe experiments in all temperatures examined and this difference increased for increasing temperature. In particular, no PAHs were detected for the HF experiments at 700 °C while the corresponding yield for the PP was 60 mg/kg of sample. For 800 °C, the PP experiments resulted in almost twice the PAH yield compared to the HF tests, while for 900 °C and 1000 °C PP PAHs were approximately 4.5 and 5 times higher, respectively. The differentiation between the two experimental procedures arises mainly from the effectiveness of light PAH capture. Light polyaromatic tars include two and three ring compounds and have the tendency to condense at

intermediate to low temperatures even at very low concentrations. On the other hand heavy polyaromatic compounds (larger than three rings) condense mostly at high temperatures [11].

Naphthalene was the most abundant PAH detected in the PP experiments. The difference between the two methods was significant and it increased with increasing temperature, since the naphthalene yield increased as well. Specifically, the naphthalene yield was roughly 40, 60 and 90 times higher for the PP experiments in comparison to the HF tests at 800, 900 and 1000 °C, respectively (Figure 2.4 (b)). In the case of the HF experiments, fluoranthene at 800 °C and phenanthrene at 900 °C and 1000 °C were the PAH produced at the highest concentrations. It is interesting to note, that despite this fact, the fluoranthene yields of the two reactors were comparable at 800 °C (41 mg/kg – HF versus 37.4 mg/kg – PP) while PP pyrolysis produced more than two times higher phenanthrene yields at 900 °C and 1000°C.

Another major difference between the two reactor systems, was the absence of acenaphthylene from the HF pyrolysis products, while in the case of PP it constituted the second higher PAH specie yield detected. In general, the HF reactor underperformed in comparison to the PP in terms of light polyaromatic compounds production (naphthalene, acenaphthylene, fluorene, phenanthrene and anthracene). As it can also be seen in Figure 2.4 (d), (e) and (f) the yields of fluorene were on average 7.6 times higher for PP experiments, the ones of phenanthrene 2.4 times higher and anthracene's approximately 4 times higher. These differences correspond to 800 °C, 900 °C and 1000 °C, since at 700 °C, no PAH were detected at all for the HF. One potential explanation for the less successful light PAH sampling from the HF, lies in the employment of the evaporation step in those experiments. It is very likely, that lighter PAH species evaporated as well during the DCM evaporation, causing these differences with the PP experiments. The situation however was different for heavier PAH compounds. In particular, some species that were captured in the HF experiments were not present in the PP ones. Namely, benzo(b)fluoranthene, benzo(k)fluoranthene, benzo(a)pyrene and indeno (1,2,3-cd)pyrene were detected only in the HF tar samples. However, their concentration was particularly low, ranging from 14.6 mg/kg of wood for benzo(a)pyrene at 1000 °C to as low as 2.6 mg/kg of wood for benzo(b)fluoranthene at 800 °C. Regarding the rest of the species, as can also be observed in Figure 2.4 (g), (h), (i) and (j) the differences were minimal between the two reactors, with the HF test results having a slight edge over the PP results for benzo(a)anthracene and chrysene. Heavy polyaromatic tars can condense at high temperatures and at low concentrations as it was mentioned earlier. This can potentially explain the differences between the two reactors, since tar sampling for the HF was performed closer to the sample in comparison to the PP. It is possible that part of the heavier PAH condenses on the tube in the PP oven or escapes the tar sampling system due to its low concentration [39, 40].

Limited information is available in literature concerning PAH formation at high pyrolysis temperatures, since pyrolysis is not usually employed at temperatures higher than 800 °C. Morf et al. [41] conducted homogeneous tar conversion experiments by initially pyrolysing fir/spruce wood chips at 380 °C and subsequently guiding the evolved gases to the tar conversion zone where they remained for less than 0.2 s. The naphthalene yield obtained from those experiments ranged between 200 mg/kg at 830 °C and 1167 mg/kg at 990 °C. These values are comparable to the results presented in this study since they also regard the secondary conversion of primarily formed tars in a continuously fed reactor. Zhou et al. performed fast pyrolysis of xylan, cellulose and dealkaline lignin in a fixed bed reactor at 800 °C [30, 31]. Tar sampling was performed with two air and dry ice cooled condensers and analysed by GC/MS. The authors reported total PAH yields of 156.2 mg/kg, 59.1 mg/kg and 541 mg/kg for xylan, cellulose and lignin, respectively, which were also close to the results presented here. The results also compare well to the work previously published by the same group [42], where using the same type of PP reactor wood residues and ash wood was pyrolysed, producing a PAH yield ranging

from 291 mg/kg to 1189 mg/kg and 143 mg/kg to 1549 mg/kg between 800 °C and 1000 °C, respectively. The yields of acenaphthalene, fluorene, phenanthrene, anthracene and pyrene in the present work are also consistent with the findings of Brage et. al at [43] although somewhat lower (i.e. fluorene yield of 276 mg/kg at 900 °C versus 67,18 mg/kg for PP). On the contrary, the naphthalene yields reported were three and four times higher at 800 °C and 900 °C, respectively, compared to the PP results. Brage et al. conducted hardwood pyrolysis at 700 °C and steam cracking of the produced gases between 700 °C and 900 °C. Tar sampling was performed through a series of Liebig condensers and cryogenic traps, the latter immersed in ice-acetone and dry-ice-acetone. The tars were extracted by washing with dichloromethane and acetone and the samples were introduced in a GC-MS, following solid-phase extraction. It is apparent, that steam cracking facilitated the decomposition of primary and secondary tars to produce PAH. Furthermore, experiments of Dufour et al. presented in [16] also yielded significantly higher amounts of naphthalene, acenaphthylene and phenanthrene compared to the present study. These experiments were performed with wood chips as feedstock in a quartz tubular reactor and the sampling procedure was described earlier in the introduction. A possible reason for the observed differences is the presence of a gas cracking/conversion zone in the Dufour et al. reactor which lies right after the biomass sample location and before the SPA sampling point. According to Cypres [44], the primary mechanism of phenol cracking is the simultaneous formation of CO and cyclopentadiene, with dibenzofurane formation being the second primary reaction. Further cracking of cyclopentadiene leads to benzene, toluene, indene and naphthalene formation along with H₂. Yu et al. [45], proposed a second pathway to PAH formation. According to the authors, benzene generates bicyclic or polycyclic PAHs through the abstraction of hydrogen atoms, the addition reaction of ethylene molecules or by the benzene ring condensation reaction of PAHs. Therefore, there is the possibility that phenol or benzene cracking can lead to higher PAH yields in the reactor of Dufour et al. Finally, it is interesting to note that in both Brage's and Dufour's work, pyrene and phenanthrene, were the heavier PAHs reported, respectively, in contrast with the present work which reports PAH until indeno (1,2,3-cd)pyrene. Heavy PAH are generally found in low concentrations in biomass tars, as it also apparent here, but their detection and quantification is crucial for the scale – up of any pyrolysis or gasification process.

The present study reports a wider range of PAH compared to other studies. In particular, only naphthalenes are reported in [46] for *Jatropha fast* pyrolysis at 500 °C for 30 s in a pyroprobe – GC/MS system. In [47], again for Pyroprobe – GC/MS pyrolysis of sawdust between 500 °C and 800 °C, only naphthalene, phenanthrene and anthracene are reported. Trubetskaya et al. in [48], report 14 PAH in total (up to C₁₇H₁₂) from lignocellulosic compounds pyrolysis at a drop tube reactor between 800 °C and 1250 °C. However, to achieve this, before the quantitative analyses in a GC – FID the tar compounds were annotated using a dual detector system (GC/MS – GC-FID). Numerical comparison with the previously mentioned studies was unfortunately not possible since either area or mol percentages were reported.

Some interesting observations can also be made by studying the distribution of the PAH species between the quartz and the impinger trap for the PP reactor. In Figure 2.5 (a), it becomes apparent that at 800 °C, a temperature associated with lower PAH concentrations (compared to higher temperatures), the vast majority of PAHs tend to condense in the first trap (quartz) of the system. Less than 15 wt% of each of two or three ring compounds (light polyaromatics) was found in the impinger trap. However, a major shift is observed at 1000 °C, especially for the two major PAH species formed (naphthalene and acenaphthylene) (Figure 2.5 (b)). At this temperature, roughly 95 wt% and 80 wt% of the naphthalene and acenaphthylene yields were found present in the impinger trap, while the presence of the other PAHs in the liquid (impinger) trap also increased (except for chrysene). These data suggest that a cold zone is sufficient in order to trap the major fraction of PAHs formed at lower temperatures (e.g. 800 °C) where total PAH yield is relatively low (approximately 500

mg/kg at 800 °C). However, at higher temperatures (e.g. 1000 °C) and higher PAH concentrations (approximately 1900 mg/kg at 1000 °C) the cold trap is not sufficient for effective condensation of PAHs, especially light PAHs (2 and 3 rings). This can be also attributed to a local increase of the temperature of the cold trap, due to the increase of the temperature of the product gas flow.

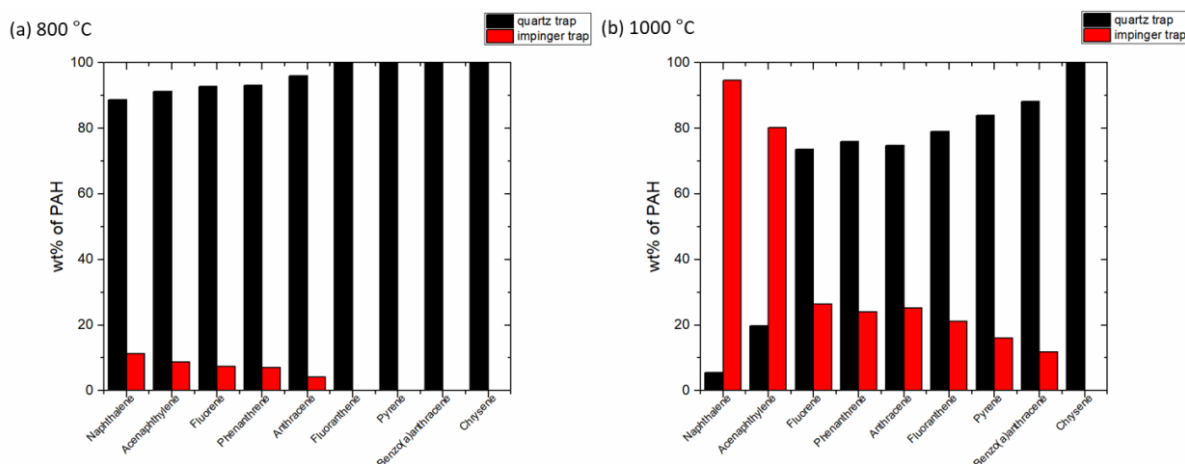


Figure 2.5: PAH condensation on quartz and liquid traps from wood pyrolysis on PP (600 °C/s, 10 s holding time) at (a) 800 °C and (b) 1000 °C.

2.3.2 Gravimetric liquid and char from PP and HF reactors

The char and liquid yields of the PP and HF reactors are presented as percentages of the initial biomass feed in Figure 2.6. Regarding the char product, very similar trends can be observed in both cases. Char production decreases with increasing temperature until 700 °C for the PP, before attaining a near-constant profile for higher temperatures. The corresponding temperature for the HF was 800 °C. Liquid production peaks for both cases at 600 °C and subsequently decreases until 800 °C, maintaining a fairly constant yield above this temperature. The char yield reduction with the increase of the temperature, is attributed to the increased primary decomposition of the biomass (hemicellulose, cellulose and lignin decomposition) as well as to the secondary char decomposition which mainly leads to non – condensable gases production [49]. The decrease of the liquid yield between 600 °C and 800 °C, for both the HF and PP reactor can originate from secondary cracking of liquid products to lighter volatiles (H₂, CO, CH₄, C₂H₄, etc.) despite the short residence time in the apparatus employed [50, 51] or from rigorous reactions in the decomposing biomass [52]. In general, the observed char yields and their trend for increasing temperature are in good agreement with several earlier similar studies of biomass fast pyrolysis [53-56]. The same holds for the liquid yields [54-56].

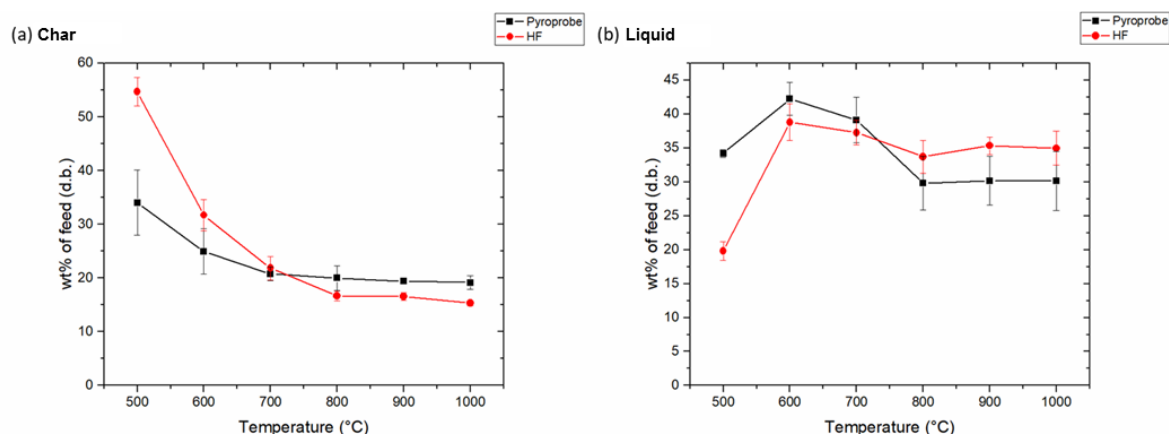


Figure 2.6: Effect of pyrolysis (600 °C/s, 10 s holding time) temperature on (a) char and (b) gravimetric liquid (condensables on quartz trap) yields.

The differences between the char and liquid yields from the two reactors are more pronounced in the lower temperature range. In particular, the char yields were higher for the HF reactor at 500 °C and 600 °C by ~20.6 wt% and 6.8 wt%, respectively. This can be attributed to the thermal lag in the biomass sample in heating foil reactors. The poor thermal conductivity of woody biomass and the non-distributed source of heating (foil) in heating foil reactors creates temperature gradients inside the pyrolysing sample [37]. This thermal lag is more pronounced at lower temperatures and low residence times. At temperatures higher than 600 °C the average difference was 2.2 wt% in favour of the PP. This difference can be attributed to minor inaccuracies occurring during the gravimetric determination of char yields. Higher sample mass was used in PP experiments (30 mg) compared to HF experiments (10mg) which would reduce any inaccuracies during char yield determination. Furthermore, inaccuracies during gravimetric char yield determination should be contained at minimum in case of PP experiments, since the resultant char was weighed in the sample quartz tube originally containing the starting feedstock. On the contrary, in case of HF experiments the resultant char had to be manually removed from the foil and subsequently weighed, a procedure during which minor losses of char particles can occur.

The lower extent of devolatilization of wood sample in the HF reactor at 500 °C and 600 °C resulted in less liquid yield as expected. Nonetheless, liquid yields as determined gravimetrically were comparable at 600 °C and 700 °C for both analytical pyrolysers (42wt% for PP compared to 39wt% for HF at 600 °C, 39wt% for PP compared to 37wt% for HF at 700 °C). At higher pyrolysis temperature (>800 °C) the liquid yield determined gravimetrically from the HF was higher than that of PP. Considering the values of the standard deviation, the difference in this temperature range becomes less significant. However, as it was also shown in Figure 2.5, at high temperatures, naphthalene and acenaphthylene, which constitute the larger fraction of the detected tars tend to condense in the impinger trap for the PP. This liquid yield is not measured gravimetrically, as it was mentioned earlier. Therefore, it is fair to assume that along with light PAHs, lighter condensables also tend to condense in the impinger, thus explaining this difference between the two methods. Overall, it can be observed that PAH compounds constitute only a very small part of the total liquid yield from the fast pyrolysis experiments (maximum 0.2 wt% at 1000 °C). Lower molecular weight compounds (i.e. levoglucosan, phenolics, olefins, etc.) as well as pyrolytic water represent the by far larger part of fast pyrolysis liquid yield. As it was also evident in the previous work published by the authors, for woody biomass fast pyrolysis in the same pyroprobe reactor, only the phenol yield at 800 °C can be 8 times higher than the total PAH yield [42].

2.3.3 Analysis of the product gas

The total amount of gases produced from the two reactors were similar, ranging from 12 wt% to 34 wt% for the PP and from 6.5 wt% to 33 wt% for the HF. From Figure 2.7, it can be derived that the main reason for this difference is the lower amount of CO₂ produced during the HF experiments at 500 °C and 600 °C, due to the lower extent of devolatilization of biomass sample as explained earlier. Furthermore, the CH₄ yield became stable for the HF above 800 °C in contrast with the PP where the increase continued until 1000 °C. The values for CO were similar, while H₂ was not measured in the case of the HF.

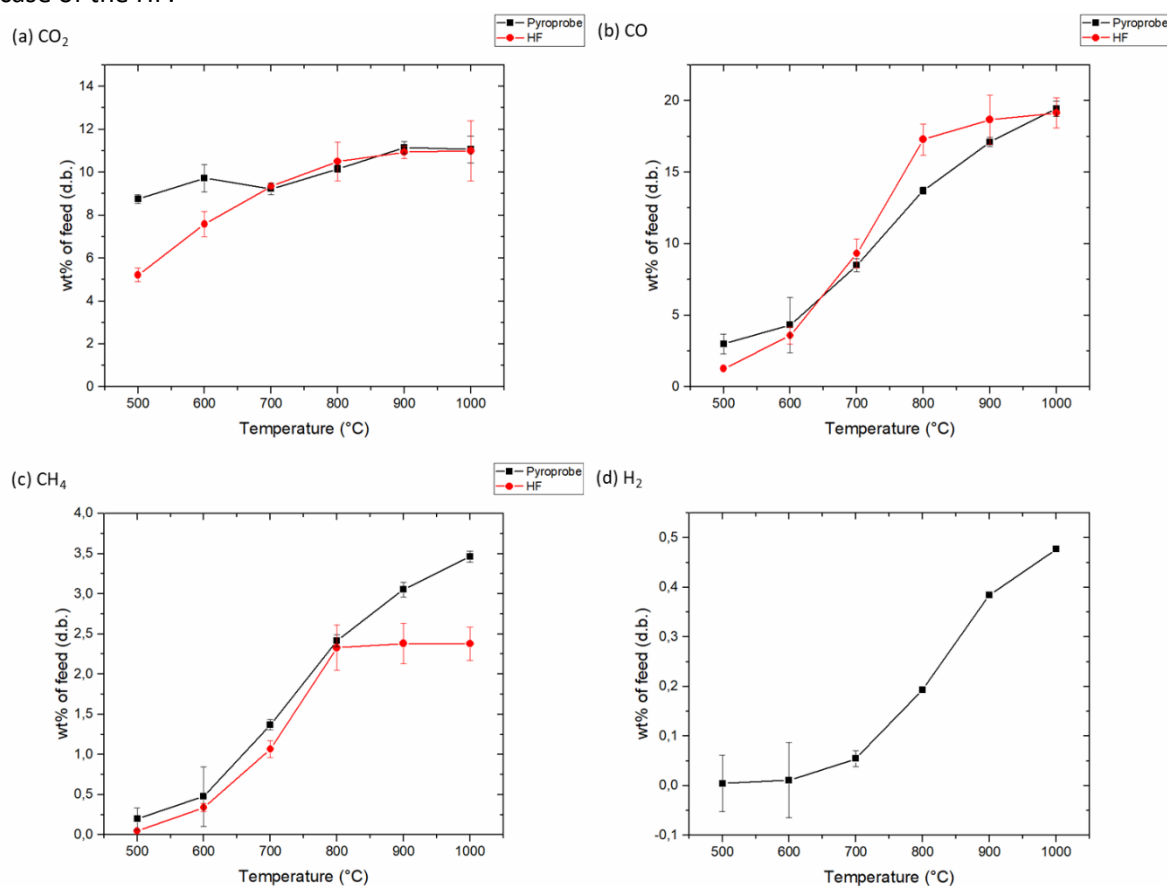


Figure 2.7: Gas evolution over temperature during pyrolysis (600 °C/s, 10 s holding time) of wood: (a) CO₂, (b) CO, (c) CH₄ and (d) H₂. Comparison between pyroprobe and heated foil.

It is important to notice that CO₂ is the highest yielding gas until a temperature of 700 °C for both reactors studied. Above this temperature, CO becomes the most prominent gas and as can be seen in Figure 2.7 (d) and the yield of H₂ monotonously increases despite remaining at low levels overall. Keeping in mind the stable char yield and the decreasing liquid yield at temperatures above 700 °C, it can be concluded that secondary decomposition (cracking) of tar compounds is responsible for the increasing gas yield above this temperature. Primary devolatilization of the softwood sample leads to the production of mainly tar and CO₂ until 700 °C. However, the further increase of the pyrolysis temperature leads to subsequent tar decomposition, producing more CO and H₂ [50, 51]. Furthermore, as it was also mentioned before, phenol and BTEX (primarily benzene) compounds can both serve as PAH precursors. The rapid increase of the H₂ yield observed here can be therefore linked to PAH formation, either through phenol cracking [45] or through the HACA sequence [41]. Finally,

regarding CH₄, the steep increase of its yield from 0.2 wt% to 3.5 wt% from 500 °C to 1000 °C can also be attributed to the reforming and cracking of tar compounds [57].

2.3.4 Overall mass balance of the experiments

The overall mass balance of the experiments was calculated as the summation of the individual product classes' yields (gas, liquid and char) for both the HF and PP reactors. For the PP reactor, the average mass balance closure value was 80 wt% while the corresponding value for the HF was slightly higher (81.7 wt%), but similar overall. In both cases, the mass balance closure values increased for increasing temperature. In the HF reactor mass losses can occur from the char collection especially at high temperatures since the sample is not contained in the heating system, unlike in the case of pyroprobe where the sample is contained in a removable quartz tube. In both cases, there is a fraction of the product gases that is not measured, namely higher hydrocarbon gases, such as C₂H₄, C₂H₆, C₃H₆ and C₃H₈ as well as H₂ in the case of the HF reactor and H₂O in the case of pyroprobe. The total yield of higher hydrocarbon gases can sum up to 2 – 5 wt% depending always on the experimental conditions and the biomass type [51, 56, 58], while the H₂ production is usually close to, or less than 1 wt%, as it was also shown in the present study [50, 59]. For both cases however, the largest amount of losses can be attributed to the liquid product gravimetric measurements. As it was shown in Section 3.1, the HF reactor fails in terms of PAH determination by underestimating their total yield even by 5 times compared to the PP. However, the main drawback of the PP system is the inability to measure gravimetrically the products condensing in the impinger trap. As it was shown in Figure 2.5, as temperature increases the bigger part of the PAH condenses there. Lighter tar compounds are also expected to be found present in significant quantities in the impinger trap rather than in the quartz trap. Furthermore, as it was also mentioned earlier, there is a possibility of heavy PAH condensation in the transfer tube situated in the oven area of the PP reactor. Finally, pyrolytic water production was not measured for the PP experiments, in contrast with the HF tests. Pyrolytic water can account for 10 – 12 wt% of the dry feed [60-62] and part of it condenses in the impinger trap for the PP experiments.

2.4 Conclusions

Fast pyrolysis of woody (softwood mixtures) biomass was conducted in a Pyroprobe (PP) reactor, with the purpose of studying PAH formation at high pyrolysis temperatures with an efficient, accurate and user – friendly method. Comparison of the results with the ones obtained from experiments conducted with a heated foil (HF) reactor showed a definite improvement in terms of PAH capture, except for some heavier PAH, which however contribute very little to the overall PAH yield. The PP reactor was also more efficient with respect to the total yields determination, due to the absence of thermal lag at lower temperatures, that leads to higher char yields for reactors such as the HF. Overall, it was also concluded that the HF reactor is not applicable for PAH quantification related studies, without making significant changes in the reactor's configuration (sample size, pyrolysis chamber size, etc.) and tar sampling methods.

PAH yields were found to increase with increasing pyrolysis temperature approaching a maximum of 1900 mg/kg (roughly 0.2 wt% of the overall yield) at 1000 °C for the PP experiments. Naphthalene and acenaphthylene were the main compounds detected, while also significant amounts of phenanthrene were detected. PAH evolution was linked with the simultaneous increase of the CO, H₂ and CH₄ yields, the stabilization of the char yield and the decrease of the liquid yield, suggesting that it is mainly a product of secondary decomposition.

The PP system produced reasonably good mass balance closure values (80 wt% on average). Char and gas yields were determined with high accuracy, however gravimetric liquid analysis lacked in this sense mainly due to the inability to measure the yield condensing in the impinger bottle. There is a trade – off between the gravimetric determination of the total liquid yield and the quantification of its constituents. By adding a solvent evaporation step for example, one might improve the mass balance closure values, but at the same time it would hamper the efficiency of determination of the liquid compounds. It was shown, that while a single cold trap is sufficient for PAH condensation at low concentrations (and therefore low pyrolysis temperatures), the same does not hold for higher concentrations. Therefore, an expanded condensation/trapping system, such as the one presented here, is required.

Overall, the proposed system was successful in the reproducible quantification of PAH produced from biomass fast pyrolysis experiments. The flexibility of the system allows the fast conduction of multiple experiments, which minimizes the time required for sampling and its complexity. Furthermore, specific compounds of interest can be targeted for the analysis (PAH, sugars, acids, phenolics, etc.), depending on the experimental conditions and the purpose of the study.

Bibliography

1. Wang, S., et al., *Lignocellulosic biomass pyrolysis mechanism: A state-of-the-art review*. Progress in Energy and Combustion Science, 2017. **62**: p. 33-86.
2. Basu, P., *Biomass Gasification and Pyrolysis Practical Design and Theory*. 2010: Elsevier Inc.
3. Dufour, A., et al., *Evolution of Aromatic Tar Composition in Relation to Methane and Ethylene from Biomass Pyrolysis-Gasification*. Energy Fuels, 2011. **25**: p. 4182-4189.
4. Devi, L., K.J. Ptasiński, and F.J.J.G. Janssen, *A review of the primary measures for tar elimination in biomass gasification processes*. Biomass and Bioenergy, 2003. **24**(2): p. 125-140.
5. Basu, P., *Combustion and Gasification in Fluidized Beds*. 2006: Taylor and Francis.
6. Li, C. and K. Suzuki, *Tar property, analysis, reforming mechanism and model for biomass gasification—An overview*. Renewable and Sustainable Energy Reviews, 2009. **13**(3): p. 594-604.
7. Pakdel, H. and C. Roy, *Hydrocarbon content of liquid products and tar from pyrolysis and gasification of wood*. Energy & Fuels, 1991. **5**(3): p. 427-436.
8. Boonchan, S., M.L. Britz, and G.A. Stanley, *Degradation and Mineralization of High-Molecular-Weight Polycyclic Aromatic Hydrocarbons by Defined Fungal-Bacterial Cocultures*. Applied and Environmental Microbiology, 2000. **66**(3): p. 1007.
9. McGrath, T., R. Sharma, and M. Hajaligol, *An experimental investigation into the formation of polycyclic-aromatic hydrocarbons (PAH) from pyrolysis of biomass materials*. Fuel, 2001. **80**(12): p. 1787-1797.
10. Milne, T.A., R.J. Evans, and N. Abatzoglou, *Biomass Gasifier “Tars”: Their Nature, Formation, and Conversion*. 1998, National Renewable Energy Laboratory (NREL).
11. Devi, L., et al., *Catalytic decomposition of biomass tars: use of dolomite and untreated olivine*. Renewable Energy, 2005. **30**(4): p. 565-587.
12. Solomon, P.R., M.A. Serio, and E.M. Suuberg, *Coal pyrolysis: Experiments, kinetic rates and mechanisms*. Progress in Energy and Combustion Science, 1992. **18**(2): p. 133-220.
13. Jakab, E., *Chapter 3 - Analytical Techniques as a Tool to Understand the Reaction Mechanism*, in *Recent Advances in Thermo-Chemical Conversion of Biomass*, A. Pandey, et al., Editors. 2015, Elsevier: Boston. p. 75-108.
14. Tsekos, C., *Fast Pyrolysis of Woody Biomass in a Pyroprobe Reactor: Effect of Torrefaction on the Pyrolysis Products*. 2016, Delft University of Technology: Delft.
15. Di Nola, G., *Biomass fuel characterization for NO_x emissions in cofiring applications, in Mechanical, Maritime and Materials Engineering*. 2007, Delft University of Technology: Delft.
16. Dufour, A., et al., *Comparison of two methods of measuring wood pyrolysis tar*. Journal of Chromatography A, 2007. **1164**(1): p. 240-247.
17. Caballero, J.A., et al., *Flash pyrolysis of Klason lignin in a Pyroprobe 1000*. Journal of Analytical and Applied Pyrolysis, 1993. **27**(2): p. 221-244.
18. García, A.N., R. Font, and A. Marcilla, *Kinetic studies of the primary pyrolysis of municipal solid waste in a Pyroprobe 1000*. Journal of Analytical and Applied Pyrolysis, 1992. **23**(1): p. 99-119.
19. Fahmi, R., et al., *The effect of alkali metals on combustion and pyrolysis of Lolium and Festuca grasses, switchgrass and willow*. Fuel, 2007. **86**(10): p. 1560-1569.
20. Kelkar, S., et al., *Aromatics from biomass pyrolysis vapour using a bifunctional mesoporous catalyst*. Green Chemistry, 2014. **16**(2): p. 803-812.
21. Wang, S., et al., *Mechanism research on cellulose pyrolysis by Py-GC/MS and subsequent density functional theory studies*. Bioresource Technology, 2012. **104**: p. 722-728.
22. Ross, A.B., et al., *Investigation of the pyrolysis behaviour of brown algae before and after pre-treatment using PY-GC/MS and TGA*. Journal of Analytical and Applied Pyrolysis, 2009. **85**(1): p. 3-10.

23. Lu, Q., et al., *Influence of pyrolysis temperature and time on the cellulose fast pyrolysis products: Analytical Py-GC/MS study*. Journal of Analytical and Applied Pyrolysis, 2011. **92**(2): p. 430-438.
24. Zhang, S., et al., *Effects of water washing and torrefaction on the pyrolysis behavior and kinetics of rice husk through TGA and Py-GC/MS*. Bioresource Technology, 2016. **199**: p. 352-361.
25. Zhao, J., et al., *Thermal degradation of softwood lignin and hardwood lignin by TG-FTIR and Py-GC/MS*. Polymer Degradation and Stability, 2014. **108**: p. 133-138.
26. White, C.M., *Prediction of the boiling point, heat of vaporization, and vapor pressure at various temperatures for polycyclic aromatic hydrocarbons*. Journal of Chemical and Engineering Data, 1986. **31**: p. 198-203.
27. Zhang, M., F.L.P. Resende, and A. Moutsoglou, *Catalytic fast pyrolysis of aspen lignin via Py-GC/MS*. Fuel, 2014. **116**: p. 358-369.
28. González-Pérez, J.A., et al., *Appraisal of polycyclic aromatic hydrocarbons (PAHs) in environmental matrices by analytical pyrolysis (Py-GC/MS)*. Journal of Analytical and Applied Pyrolysis, 2014. **109**: p. 1-8.
29. Zhang, B., et al., *Production of aromatic hydrocarbons from catalytic co-pyrolysis of biomass and high density polyethylene: Analytical Py-GC/MS study*. Fuel, 2015. **139**: p. 622-628.
30. Zhou, H., et al., *Effect of interactions of biomass constituents on polycyclic aromatic hydrocarbons (PAH) formation during fast pyrolysis*. Journal of Analytical and Applied Pyrolysis, 2014. **110**: p. 264-269.
31. Zhou, H., et al., *Polycyclic Aromatic Hydrocarbon Formation from the Pyrolysis/Gasification of Lignin at Different Reaction Conditions*. Energy & Fuels, 2014. **28**(10): p. 6371-6379.
32. Zhang, Y., et al., *Tar destruction and coke formation during rapid pyrolysis and gasification of biomass in a drop-tube furnace*. Fuel, 2010. **89**(2): p. 302-309.
33. Zhang, Y., et al., *Peculiarities of Rapid Pyrolysis of Biomass Covering Medium- and High-Temperature Ranges*. Energy & Fuels, 2006. **20**(6): p. 2705-2712.
34. Sánchez, N.E., et al., *Formation of PAH and soot during acetylene pyrolysis at different gas residence times and reaction temperatures*. Energy, 2012. **43**(1): p. 30-36.
35. Fabbri, D., A. Adamiano, and C. Torri, *GC-MS determination of polycyclic aromatic hydrocarbons evolved from pyrolysis of biomass*. Analytical and Bioanalytical Chemistry, 2010. **397**(1): p. 309-317.
36. Anastasakis, K., I. Kitsiou, and W. de Jong, *Fast devolatilization characteristics of 'low cost' biomass fuels, wood and reed. Potential feedstock for gasification*. Fuel Processing Technology, 2016. **142**: p. 157-166.
37. Anastasakis, K., C. Saenz, and W. de Jong. *Modeling physical phenomena during fast pyrolysis of biomass in a heated foil reactor*. in *21st International Symposium on Analytical and Applied Pyrolysis*. 2016. Nancy.
38. United States Environmental Protection Agency (EPA). *Method 610: Polynuclear Aromatic Hydrocarbons*. 1984 [cited 2019 25/11/2019]; Available from: https://www.epa.gov/sites/production/files/2015-10/documents/method_610_1984.pdf.
39. Oesch, P., E. Leppämäki, and P. Ståhlberg, *Sampling and characterization of high-molecular-weight polyaromatic tar compounds formed in the pressurized fluidized-bed gasification of biomass*. Fuel, 1996. **75**(12): p. 1406-1412.
40. Jordan, C.A. and G. Akay, *Effect of CaO on tar production and dew point depression during gasification of fuel cane bagasse in a novel downdraft gasifier*. Fuel Processing Technology, 2013. **106**: p. 654-660.
41. Morf, P., P. Hasler, and T. Nussbaumer, *Mechanisms and kinetics of homogeneous secondary reactions of tar from continuous pyrolysis of wood chips*. Fuel, 2002. **81**(7): p. 843-853.

42. Tsalidis, G.A., et al., *The impact of dry torrefaction on the fast pyrolysis behavior of ash wood and commercial Dutch mixed wood in a pyroprobe*. Fuel Processing Technology, 2018. **177**: p. 255-265.
43. Brage, C., Q. Yu, and K. Sjöström, *Characteristics of evolution of tar from wood pyrolysis in a fixed-bed reactor*. Fuel, 1996. **75**(2): p. 213-219.
44. Cypres, R., *Aromatic hydrocarbons formation during coal pyrolysis*. Fuel Processing Technology, 1987. **15**: p. 1-15.
45. Yu, H., et al., *Characteristics of tar formation during cellulose, hemicellulose and lignin gasification*. Fuel, 2014. **118**: p. 250-256.
46. Vichaphund, S., et al., *Production of aromatic compounds from catalytic fast pyrolysis of Jatropha residues using metal/HZSM-5 prepared by ion-exchange and impregnation methods*. Renewable Energy, 2015. **79**: p. 28-37.
47. Sun, L., et al., *Comparison of catalytic fast pyrolysis of biomass to aromatic hydrocarbons over ZSM-5 and Fe/ZSM-5 catalysts*. Journal of Analytical and Applied Pyrolysis, 2016. **121**: p. 342-346.
48. Trubetskaya, A., N. Souihi, and K. Umeki, *Categorization of tars from fast pyrolysis of pure lignocellulosic compounds at high temperature*. Renewable Energy, 2019. **141**: p. 751-759.
49. Horne, P.A. and P.T. Williams, *Influence of temperature on the products from the flash pyrolysis of biomass*. Fuel, 1996. **75**(9): p. 1051-1059.
50. Hajaligol Mohammed, R.M., *Product compositions and kinetics for rapid pyrolysis of cellulose*. Industrial and Engineering Chemistry Process Design and Development, 1982. **21**(3): p. 457.
51. Nunn Theodore, R.T., *Product compositions and kinetics in the rapid pyrolysis of sweet gum hardwood*. Industrial and Engineering Chemistry Process Design and Development, 1985. **24**(3): p. 836.
52. Hoekstra, E., et al., *Fast pyrolysis in a novel wire-mesh reactor: Decomposition of pine wood and model compounds*. Chemical Engineering Journal, 2012. **187**: p. 172-184.
53. Dufour, A., et al., *Synthesis gas production by biomass pyrolysis: Effect of reactor temperature on product distribution*. International Journal of Hydrogen Energy, 2009. **34**(4): p. 1726-1734.
54. Figueiredo, J.L., et al., *Pyrolysis of holm-oak wood: influence of temperature and particle size*. Fuel, 1989. **68**(8): p. 1012-1016.
55. Caballero, J.A., R. Font, and A. Marcilla, *Kinetic study of the secondary thermal decomposition of Kraft lignin*. Journal of Analytical and Applied Pyrolysis, 1996. **38**(1): p. 131-152.
56. Becidan, M., Ø. Skreiberg, and J.E. Hustad, *Products distribution and gas release in pyrolysis of thermally thick biomass residues samples*. Journal of Analytical and Applied Pyrolysis, 2007. **78**(1): p. 207-213.
57. Jahirul, M., et al., *Biofuels Production through Biomass Pyrolysis —A Technological Review*. Energies, 2012. **5**(12): p. 4952.
58. Bridgwater, A.V. and G.V.C. Peacocke, *Fast pyrolysis processes for biomass*. Renewable and Sustainable Energy Reviews, 2000. **4**(1): p. 1-73.
59. Di Blasi, C., et al., *Product Distribution from Pyrolysis of Wood and Agricultural Residues*. Industrial & Engineering Chemistry Research, 1999. **38**(6): p. 2216-2224.
60. Liden, A.G., F. Berruti, and D.S. Scott, *A KINETIC MODEL FOR THE PRODUCTION OF LIQUIDS FROM THE FLASH PYROLYSIS OF BIOMASS*. Chemical Engineering Communications, 1988. **65**(1): p. 207-221.
61. Mohan, D., C.U. Pittman, and P.H. Steele, *Pyrolysis of Wood/Biomass for Bio-oil: A Critical Review*. Energy & Fuels, 2006. **20**(3): p. 848-889.
62. Bridgwater, A.V., D. Meier, and D. Radlein, *An overview of fast pyrolysis of biomass*. Organic Geochemistry, 1999. **30**(12): p. 1479-1493.

3. Biomass pyrolysis TGA assessment with an international round robin

Chapter published in:
Fuel, Volume 276, 15 September 2020, 118002

3.1 Introduction

Biomass is currently the main renewable energy source and it is expected to play a key role to reach the target formulated in the special IPCC report to limit global warming to 1.5 °C [1, 2]. Biomass combustion for bio-heat production is a consolidated technology and it is currently the main bioenergy use. Besides, biomass has the potential to play a more relevant role in the production of power, liquid fuels or chemicals. Thermochemical processes applied to lignocellulosic biomass are very promising for this purpose. Pyrolysis itself is a promising conversion process that can be used to produce liquid bio-oil [3, 4] and biochar [5], and is a main intrinsic sub-process in other thermochemical conversion processes such as gasification or combustion. Biomass mass loss behaviour is commonly determined by thermo-gravimetric analysis (TGA). TGA experiments with small samples and low heating rates can be conducted in a pure kinetic regime, i.e. without heat and mass transport limitations. For cellulose pyrolysis, it was concluded by Antal et al. [6] that mass loss at low heating rates can be described with a single first order reaction with a high activation energy (191–253 kJ/mol). Gronli et al. [7] conducted a round robin at 8 European labs with commercial cellulose Avicel PH-105, showing some although limited scattering in the results, with a temperature of peak conversion at 327 ± 5 °C and activation energy of 244 ± 10 kJ/mol at 5 °C/min.

For lignocellulosic biomass pyrolysis, the derivation of kinetics is more challenging. Mass loss description with a single reaction is inaccurate, and the most common approach is to employ three reactions with a parallel reaction scheme, where each component represents cellulose, hemicellulose and lignin, respectively [8]. The main peak in conversion rate corresponds to cellulose, the shoulder at lower temperatures to hemicellulose and the tail at high temperatures to lignin. The kinetic parameters for each component are determined with model-based (model-fitting) methods, where the reaction model (commonly first and nth order) is selected before the fitting. Very different activation energies are however reported for each component, and especially for lignin [9]. This leads to a concern about the reliability of TGA data [10]. It has been pointed out that experiments should be conducted at different heating rates to minimize the influence of compensation effects [11, 12]. Besides, it has been reported that the selection of higher order reaction models for lignin leads to better predictions [9, 13], as it was also the case for the use of a distributed activation energy model (DAEM) [14].

Isoconversional (model-free) methods are also applied for deriving kinetics removing the need for a reaction model assumption. Integral isoconversional methods as Kissinger-Akahira-Sunose (KAS), Flynn-Wall-Ozawa (FWO) or Vyazovkin can provide the activation energies along conversion when experiments at different heating rates are conducted. The obtained kinetic data with these methods cannot be straightforwardly employed in a particle and reactor model, as the kinetic parameters change along conversion, but their complementary application with fitting (model-based) methods can increase the consistency of the obtained kinetic data through fitting, especially the selected reaction models, as suggested by Khawam and Flanagan [15] and applied by Anca-Couce et al. [9] for bio-mass pyrolysis. Anca-Couce et al. [16] recommended that for a reliable determination of biomass pyrolysis kinetics the reference experiments with pure commercial cellulose from Gronli et al. [7] should be first reproduced. Subsequently, experiments with biomass should be conducted at different heating rates and assessed with isoconversional methods, to verify the reliability of the experiments as well as the employed reaction model and obtained activation energies in a fitting routine.

In a thorough review conducted by Anca-Couce [16] in 2016, where concern about the variation of kinetics values in literature was raised, activation energy values for hemicellulose, cellulose and lignin pseudo-components in the parallel reaction scheme were reported from biomass pyrolysis experiments conducted at several heating rates. Cellulose values ranged from 190 kJ/mol to 250 kJ/mol, while the respective ranges for hemicellulose and lignin were of 70 – 215 kJ/mol and 20 – 190

kJ/mol, respectively. This review was updated in the present work to include investigations conducted after 2016. In Figure 3.1, the activation energies are reported from the kinetic analyses conducted for pure biomass components (cellulose, hemicellulose and lignin) using various methods [17-29]. A very wide range of activation energies has been reported for each component, namely 114 – 288 kJ/mol for cellulose, 34 – 179 kJ/mol for hemicellulose and 7 – 226 kJ/mol for lignin. Figure 3.2 includes the results from kinetic analyses conducted for various biomass species employing three (or four in some cases) pseudo-components [30-47]. Very large variations are also present for each pseudo-component. The ranges for the activation energies of each pseudo-component were 72 – 244 kJ/mol for cellulose, 58 – 200 kJ/mol for hemicellulose and 16 – 205 kJ/mol for lignin. The initial sample mass employed in these works was on average of 9.2 ± 5.0 mg, which is a relatively high value that can cause thermal lag in certain cases [6, 7]. The initial sample mass was however not directly correlated with the obtained activation energies. These large variations observed for the activation energy values of pure and pseudo components in very recent works raise concerns regarding the reliability of both the experimental and the modelling side of the analyses performed in the literature.

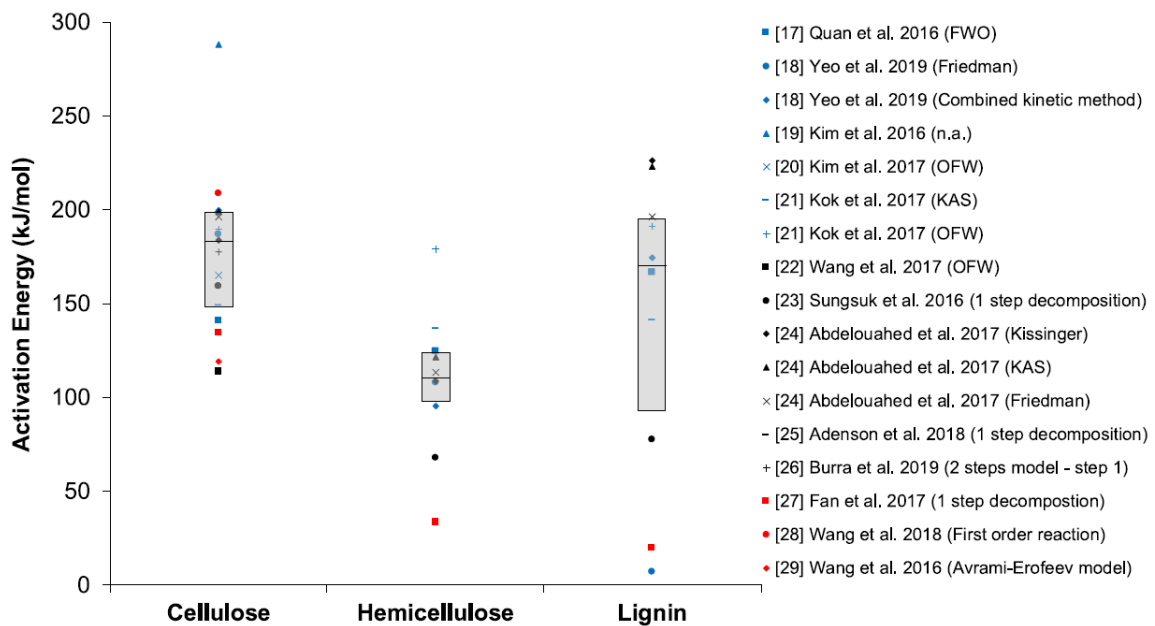


Figure 3.1: Activation energies reported in literature for pure biomass components pyrolysis using several kinetic analysis methods [17-29]. Box plots indicate the median and interquartile ranges.

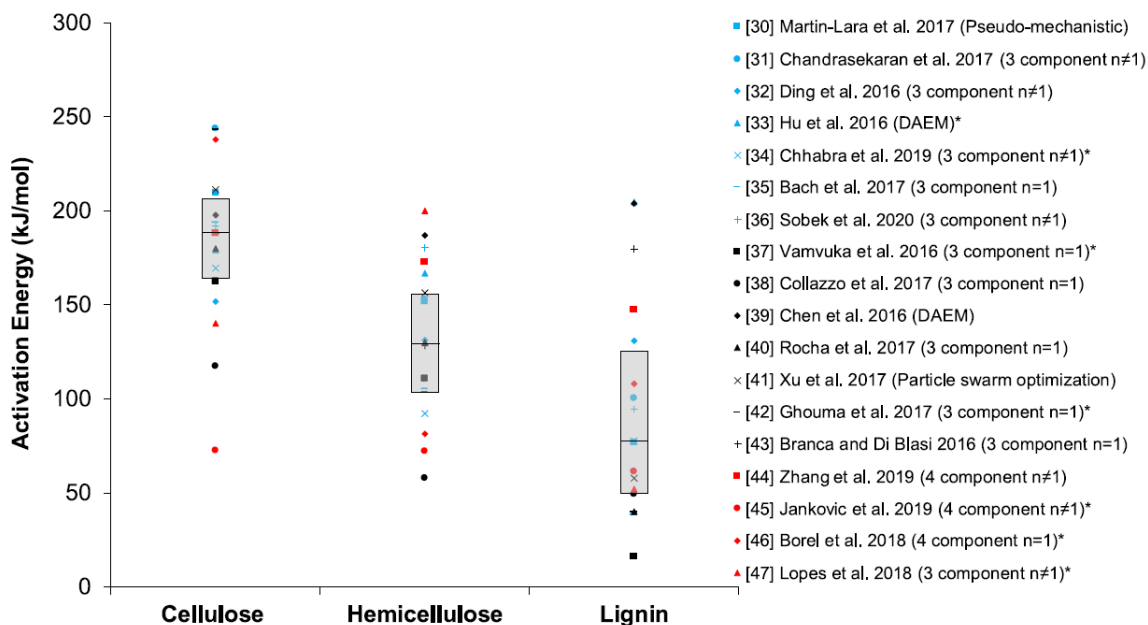


Figure 3.2: Activation energies reported in literature for pseudo-components in biomass pyrolysis using several kinetic analysis methods [30-47]. The values denoted with a * are mean values obtained from experiments performed under various heating rates or with different biomass species. For cases with 4 components, the 4th is either extractives [45, 46] or a second hemicellulose component [44]. Boxplots indicate the median and interquartile ranges.

The objective of this work is to investigate the reproducibility of TGA biomass pyrolysis experiments and the deviations that can be expected when mass loss kinetics are derived from the same sample with different TGA devices. An international round robin has been conducted for this purpose with 7 European partners. Experiments have been first conducted with commercial cellulose to reproduce the results from a previous round robin conducted by Gronli et al. [7]. Subsequently, experiments were conducted at different heating rates with homogenized beech wood and the results were analysed with fitting and isoconversional methods for kinetics derivation. The reported activation energies for woody biomass pyrolysis in literature vary in a broad range and this variability is attributed to a certain extent to the inherent variability in biomass composition. This uncertainty in composition is removed in this study, which is focused on investigating the deviations that can be expected when TGA pyrolysis experiments are conducted with different devices by experienced users and the kinetics are derived using reliable methods. The results of this work will lead to relevant conclusions regarding the accuracy that can be expected in determining biomass pyrolysis mass loss kinetics.

3.2 Materials and methods

3.2.1 TGA experiments

The instruments used in the round robin in this study are listed in Table 3.1. The partners were requested to conduct pyrolysis experiments with cellulose at a constant heating rate of 5 K/min and with beech wood at 4 constant heating rates in the range from 1 to 20 K/min (1, 5, 10 and 20 K/min for all partners, except #5 which conducted experiments at 2 K/min instead of 1 K/min). The samples were centrally distributed to all the partners involved in the round robin. Commercial Avicel® PH-101 cellulose (CAS Number: 9004-34-6) was purchased from Sigma-Aldrich. Beech wood chips were homogenized according to ISO 14,780 and milled to particle sizes < 200 µm. The same homogenized

sample was used by every participant in the round robin. The proximate, ultimate and elemental analysis of beech is presented in Table 3.2.

Table 3.1: TGA instruments list and characteristics as well as employed initial mass and nitrogen purge flow for partners #1 to #7.

Partner	Model	Sensitivity (µg)	Temperature accuracy (°C)	Type	Initial mass (mg)	N ₂ Purge flow (ml/min)	Sample holder	Calibration
#1	TA SDT Q600	0.1	0.001	Horizontal	3	50	Ceramic	Curie point
#2	Perkin Elmer TGA 7	0.1	0.5	Vertical	3	20	Platinum	Curie point
#3	Netzsch STA 409	1	1	Vertical	100	70	Alumina	Melting point
#4	Mettler Toledo TGA/DSC 2 Star System	0.1	0.001	Horizontal	3	30	Ceramic	Melting point
#5	Netzsch STA 449 F3 Jupiter	1	0.001	Vertical	3	100	Alumina	Melting point
#6	Perkin Elmer PYRIS 6 TGA	5	2	Vertical	10	100	Alumina	Curie point
#7	TG-DTA/DSC Setsys-1750 (Setaram)	1	0.001	Vertical	12	105	Alumina	Melting point

Table 3.2: Proximate, ultimate and elemental analysis of Beech wood. ^{a)} Calculated by difference.

Proximate analysis	
Moisture (wt%, a.r.)	9.9
Volatiles (wt%, a.r.)	73.2
Fixed carbon (wt%, a.r.) ^a	16
Ash (wt%, a.r.)	0.9
Ultimate analysis	
C (wt%, d.b.)	49.5
H (wt%, d.b.)	6.5
N (wt%, d.b.)	0.25
S (wt%, d.b.)	0.05
Cl (wt%, d.b.)	-
O (wt%, d.b.) ^a	42.9
Elemental Analysis	
Al (ppm, d.b.)	65
Ca (ppm, d.b.)	3668
Fe (ppm, d.b.)	60
K (ppm, d.b.)	1490
Mg (ppm, d.b.)	654
Na (ppm, d.b.)	65
Si (ppm, d.b.)	106
Zn (ppm, d.b.)	2

The partners were requested to conduct experiments with their usual procedure, employing an initial mass sample as low as possible, ideally of 3 mg (following the ASTM E1641 – 16 standard [48]). Some partners employed a higher initial mass, as shown in Table 3.1, following their commonly employed methods. In case #3 an open weighing system was employed, which inherently limits the precision of the system, and a compromise must be found between background noise and measurement signal. In cases #6 and #7 it was employed the minimum quantity that is required to cover the whole surface of the crucible, to maximize the exposed surface with an even distribution of the sample. The ASTM E1641 – 16 standard is similar to ISO 11,358 – 2 but differs mainly in its mathematical treatment and it was employed as a general guideline in the present study. The TGA experiments were conducted from room temperature up to 500 °C, however the results were analysed and presented only for the interval between 150 °C and 500 °C. To ensure complete moisture evaporation until the aforementioned lower limit, a holding time of 10 – 15 min was employed from the partners at temperatures around 110 °C. The char yield is reported at 500 °C, considering the initial mass as the one at a temperature of 150 °C.

3.2.2 Kinetic analysis

The kinetic analysis is done in the range from 150 to 500 °C. Conversion (α) is defined in Equation (1) and it is calculated as a function of the current mass (m) as well as the initial and final masses at 150 and 500 °C, respectively. The raw data is treated to provide 200 points for conversion in this range for further kinetic analysis. Conversion is employed instead of mass loss to do not account for the differences in char yield, as the current study focuses on mass loss kinetics without considering differences in product composition. These conversion values for all data sets are provided in the supplementary information. Besides, standard deviations in this manuscript are calculated with the “n – 1” method to estimate them in a conservative way.

$$\alpha = 1 - \frac{m - m_{500\text{ °C}}}{m_{150\text{ °C}} - m_{500\text{ °C}}} \quad (1)$$

Kinetics are calculated with the model fitting method considering nth order reactions to determine the reaction rate ($d\alpha/dt$), as shown in Equation (2), where A is the pre-exponential factor, E is the activation energy, R the gas constant, T the temperature and n the reaction order. Cellulose pyrolysis is described with one first order reaction ($n = 1$). Beech wood pyrolysis is described with 3 reactions, including one first order reaction representing cellulose and two nth order reactions representing hemicellulose and lignin. The model fitting routine derives the kinetic parameters from the derivative thermogravimetry (DTG) curves, where $d\alpha/dt$ is plotted as a function of temperature, and employs a least minimum squares method (nlinfit routine from Matlab [49]). The error in the fit for each experiment is normalized by the maximum of the DTG curve, as described elsewhere [9, 50].

$$\frac{d\alpha}{dt} = A \exp\left(\frac{-E}{RT}\right) (1 - \alpha)^n \quad (2)$$

Besides, the isoconversional KAS method has been applied at defined conversion intervals. The temperatures $T_{\alpha,i}$ at which a certain conversion α is achieved at each heating rate $(\Delta T/\Delta t)_i$ are first calculated. The activation energy at that conversion E_α is then calculated based on Equation (3). For that, an Arrhenius plot of the left side of Equation (3) versus $1/T_{\alpha,i}$ is derived, and the activation energy is calculated from its slope which is equal to $-E_\alpha/R$. It was previously shown that other integral isoconversional methods as FWO or Vyazovkin lead to very similar results for biomass pyrolysis [9].

$$\ln\left(\frac{\Delta T/\Delta t}{T_{\alpha,i}^2}\right) = \ln\left(\frac{A_\alpha R}{E_\alpha g(\alpha)}\right) - \frac{E_\alpha}{RT_{\alpha,i}} \quad (3)$$

3.3 Results and discussion

3.3.1 Cellulose pyrolysis

The thermogravimetry (TG) and derivative thermogravimetry (DTG) results of cellulose pyrolysis experiments at 5 K/min are shown in

Figure 3.3. For TG the conversion α is shown in the range 150 – 500 °C and for DTG the reaction rate $d\alpha/dt$ (calculated from the percentage of conversion) is shown for the same temperature interval. The averaged heating rate, char yield and temperature of the peak in reaction rate (DTG) are shown in Table 3.3. The shape of the curves is similar for all cases, but some deviations are present. The

maximum reaction rate was achieved on average at a temperature of 328.3 ± 9.2 °C, while it was of 327 ± 5 °C in a previous round robin with the same commercial cellulose, conducted by Gronli et al. [7]. The obtained averaged heating rates (5.12 ± 0.26 K/min) are close to the target of 5 K/min.

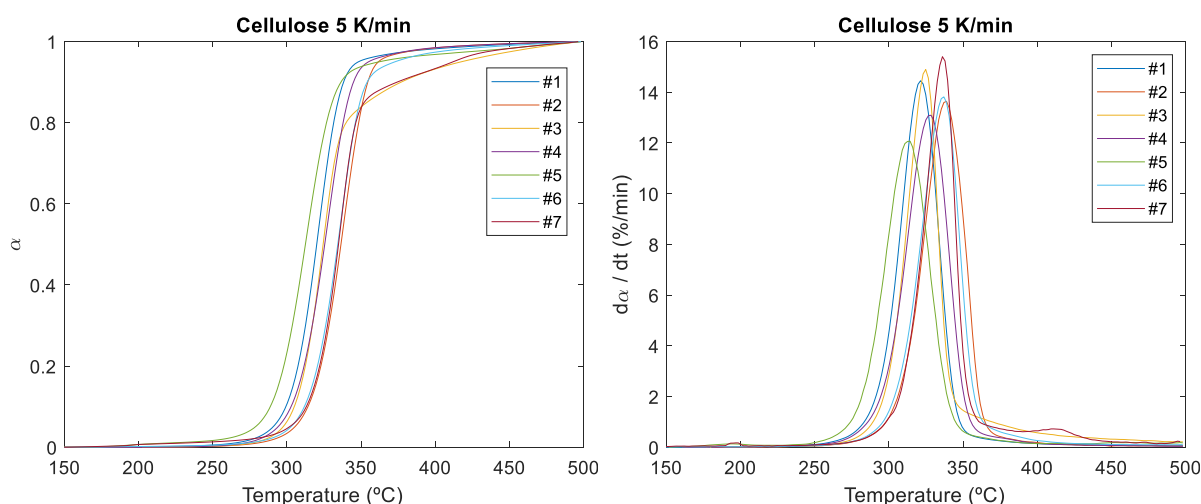


Figure 3.3: TG (left) and DTG (right) curves for cellulose pyrolysis at 5 K/min.

Table 3.3: Temperature of the peak in reaction rate (DTG), char yield, averaged heating rate, kinetic parameters and error in the fitting for the cellulose pyrolysis experiments at 5 K/min.

Partner	T peak DTG (°C)	Char yield (%)	$\Delta T/\Delta t$ (K/min)	E (kJ/mol)	$\log_{10}(A)$ (s^{-1})	Error fit (%)
#1	321.5	2.3	5.01	224.5	17.48	2.1
#2	338.1	5.2	5.11	224.3	16.89	1.7
#3	324.5	21.4	5.10	236.5	18.50	5.0
#4	327.6	4.4	5.14	208.4	15.85	2.0
#5	313.5	8.5	5.06	182.3	13.91	3.1
#6	336.5	9.5	4.77	225.4	17.09	2.4
#7	336.6	12.2	5.64	252.7	19.50	4.1
Mean	328.3	9.1	5.12	222.0	17.03	2.9
	± 9.2	± 6.4	± 0.26	± 22.1	± 1.81	± 1.2
Gronli et al.	327	7.2	5.0	244	19	0.6
	± 5	± 2.4	± 0.1	± 10	± 1.1	± 0.2

Regarding the char yields, significantly higher deviations were obtained among the partners. The obtained values from cases #1, #2, #4 and #5 ($5.1 \pm 2.5\%$), employing initial mass samples of 3 mg, are similar to the ones of the round robin by Gronli et al. [7] ($7.2 \pm 2.4\%$ with an initial mass sample of 4.1 ± 1.3 mg). However, the obtained char yields are higher for cases #6, #7 and especially for the case #3 (9.5%, 12.2%, 21.4%, respectively), which leads to higher values of the mean char yield and standard deviation. These 3 cases were also the ones employing a higher initial mass for the experiments (10, 12 and 100 mg for cases #6, #7 and #3, respectively). The correlation shown in Figure 3.4 between initial mass sample and char yield may be due to for bigger samples, where the retention time of the volatiles in contact with the sample is increased, secondary charring reactions are promoted leading to higher char yields [16, 51]. The char yield should also depend on the configuration of sample holder and inert flow.

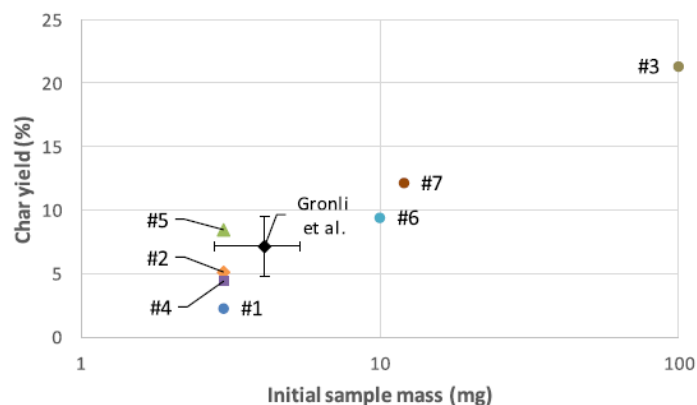


Figure 3.4: Char yield as a function of initial sample mass for commercial Avicel® PH-101 cellulose pyrolysis at a heating rate of 5 K/min for partners #1 to #7.

The DTG experiments were modelled with a first order reaction. The obtained kinetic parameters and error in the fit for all cases are shown in Table 3.3. Moreover, the DTG curves for experiments and model are shown in Figure 3.5 for the cases #1 (left) and #3 (right), considered as representative cases. The obtained activation energies and (log10) pre-exponential factors were on average of 222.0 ± 22.1 kJ/mol and 17.03 ± 1.81 s⁻¹, respectively. In the previous round robin values of 244 ± 10 kJ/mol and 19 ± 1.1 s⁻¹ were respectively achieved [7]. The averaged error in the fitting was of $2.9 \pm 1.2\%$. For most of the cases the error was very low, around 2%, as shown in Figure 3.5 - left for the case #1. This error took mainly place at temperatures around 350 °C due to the tail of the DTG curve, which cannot be modelled with a single reaction. This tail was more pronounced for the cases #3 and #7, which leads to a higher error (see the DTG curve in Figure 3.5 – right for case #3) and can be attributed to a more relevant char devolatilization in these cases with a higher char yield. The obtained char yields for cases #7 and specially #3 were higher than the range reported in the round robin by Gronli et al. [7], as seen in Figure 3.4. In this previous round robin, the error in the fit was generally lower because it was calculated for the TG curves and in a narrower temperature range [7].

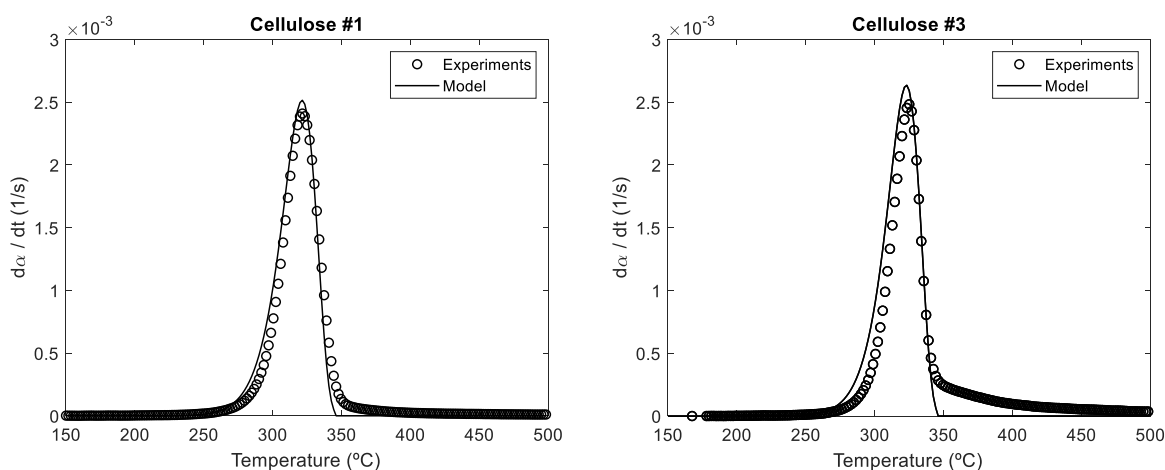


Figure 3.5: Comparison of DTG experiment (circles) and model fitting (line) profiles for Avicel® PH-101 cellulose pyrolysis at a heating rate of 5 K/min with one first order reaction for the #1 (left) and #3 (right) cases.

The obtained results show a good reproducibility of the previously conducted round robin by Gronli et al. [7]. The peak of reaction rate is at the same temperature, although with a higher variability. The case number #5 is the only one clearly outside the general trend, with the peak being observed at 15 °C less than the average. The obtained activation energies are in a similar range, except

for case #5 and to a lower extent case #4, where lower values are obtained. It is also remarkable that for cases #3 and #7 a significant conversion takes place at temperatures higher than 370 °C, which leads to a higher error in the fitting as previously commented. This may be related to the higher values of char yield observed for these two partners (see Table 3.3), probably caused by the higher initial cellulose mass (100 and 12 mg for the case #3 and #7, respectively) leading to char devolatilization in this region.

It can be concluded from the cellulose results that previous results from literature could be well reproduced for most of the cases, although with a slightly higher variability. The main discrepancies were present in the char yield, which is significantly affected by the initial mass sample. Mass loss in cellulose pyrolysis is already well understood and the current results show that deviations are to be expected among experiments conducted from different partners, but they are limited, especially if small initial sample masses are employed. The next section will analyse the results of the round robin with beech wood at different heating rates, which is the main novelty of this work.

3.3.2 Beech wood pyrolysis

The TG and DTG curves for beech wood pyrolysis at 1, 5, 10 and 20 K/min are shown in Figure 3.6 and Figure 3.7, respectively. The averaged heating rate, temperature of the peak and temperature of the shoulder in DTG curves and char yields are shown in Table 3.4. The temperature of the shoulder is calculated from the local minimum of the derivative of the DTG curve. For the experiments at 1 K/min, the data of #4 is analysed only in the range from 150 to 450 °C, as the heating rate of the experiment significantly increases after 450 °C, and data of #5 is not present as the experiment was conducted at 2 K/min.

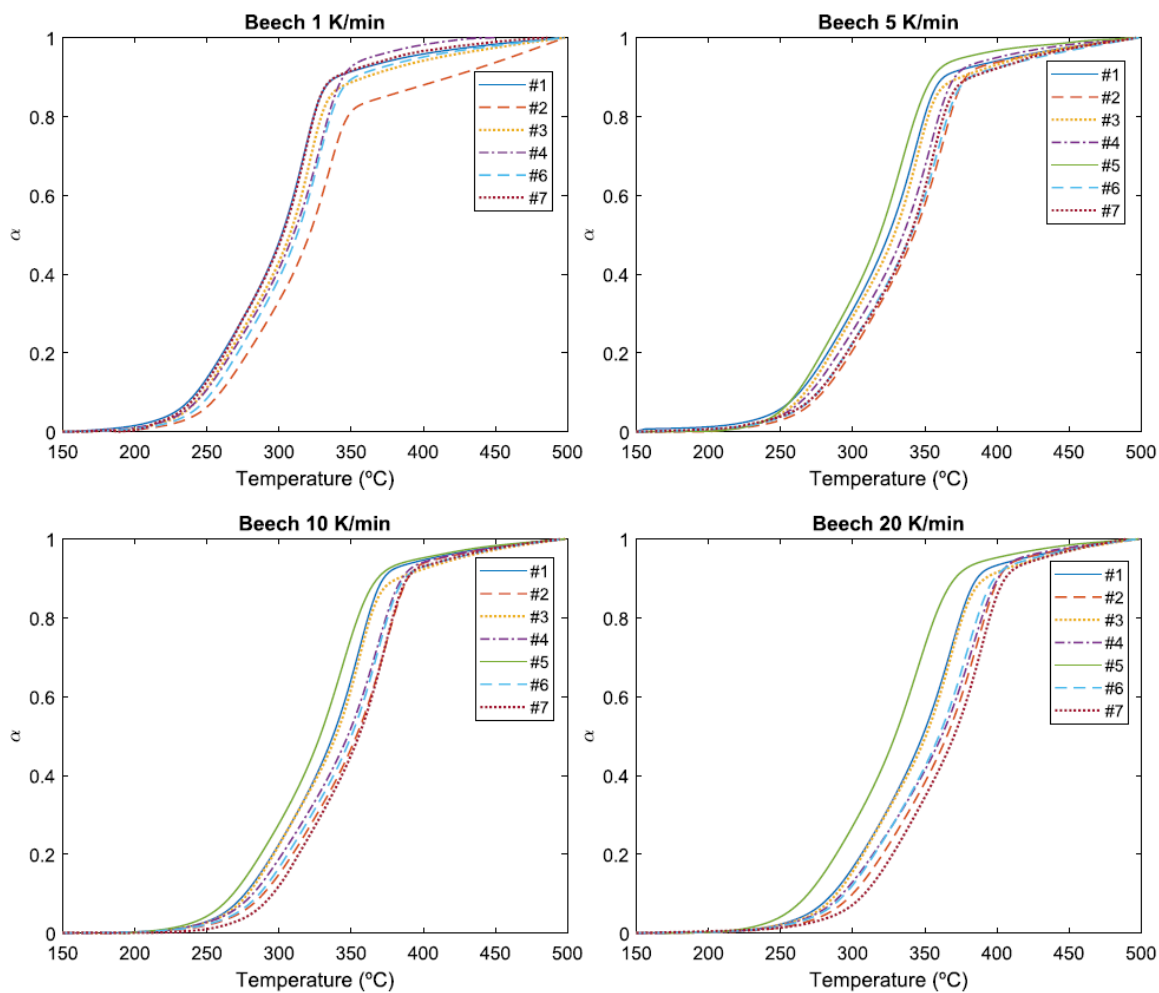


Figure 3.6: TG curves for beech wood pyrolysis at heating rates of 1, 5, 10 and 20 K/min for partners #1 to #7.

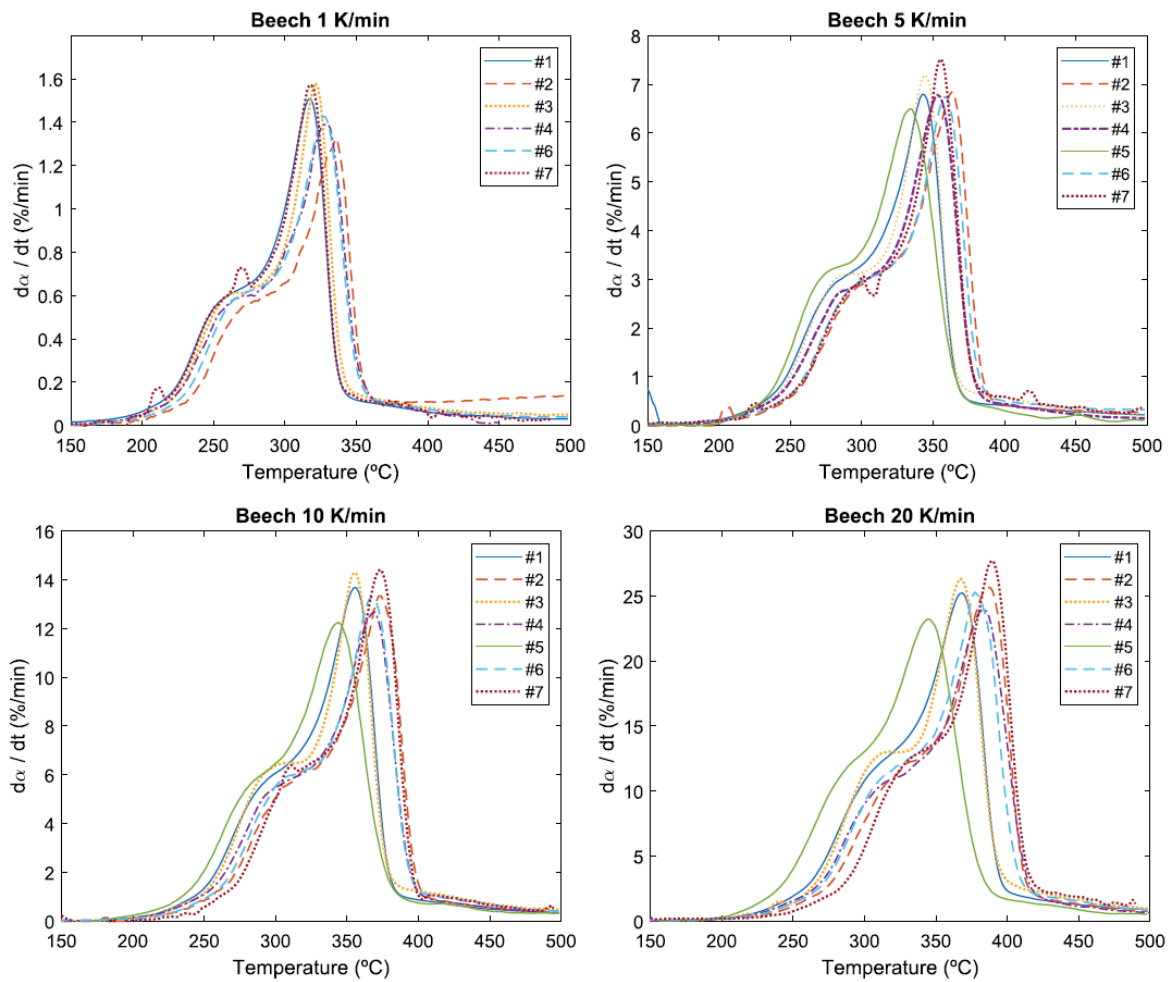


Figure 3.7: DTG curves for beech wood pyrolysis at heating rates of 1, 5, 10 and 20 K/min for partners #1 to #7.

Table 3.4: Average heating rate (K/min or °C/min – equivalent units), temperature of the peak and shoulder in DTG curve (°C) and char yield (%) for beech wood pyrolysis experiments at heating rates of 1, 5, 10 and 20 K/min (* result at 2 K/min, not considered for the mean).

	Partner	1 K/min	5 K/min	10 K/min	20 K/min
Heating rate (K/min)	#1	1.00	5.00	10.0	20.1
	#2	1.00	5.11	10.2	20.4
	#3	0.99	5.01	10.7	22.9
	#4	1.38	5.32	11.6	25.0
	#5	-- *	5.40	10.4	19.8
	#6	1.00	4.77	10.1	20.8
	#7	1.00	5.65	10.1	20.6
	Mean		1.06 ± 0.16	5.18 ± 0.30	10.5 ± 0.6
Peak temperature DTG curve (°C)	#1	317.2	343.1	355.5	367.9
	#2	335.7	363.0	373.0	387.0
	#3	321.5	344.2	355.3	367.5
	#4	328.4	353.4	368.5	383.0
	#5	314.7 *	334.2	343.7	344.8
	#6	327.3	358.7	367.5	377.6
	#7	317.9	355.3	372.9	389.2
	Mean		324.7 ± 7.1	350.3 ± 10.1	362.3 ± 11.1
Shoulder temperature DTG curve (°C)	#1	268.1	292.8	301.2	316.1
	#2	288.8	313.7	323.3	333.4
	#3	267.6	293.5	309.8	321.0
	#4	274.8	289.7	312.0	320.6
	#5	272.1 *	285.3	291.0	296.0
	#6	278.2	308.0	312.7	321.5
	#7	272.9	304.3	314.6	340.1
	Mean		275.1 ± 7.8	298.2 ± 10.5	309.2 ± 10.4
Char yield (%)	#1	13.9	18.9	20.4	21.5
	#2	13.7	20.3	20.3	20.2
	#3	27.0	26.5	26.6	26.6
	#4	21.7	19.5	20.4	21.6
	#5	22.8	28.9	27.2	26.8
	#6	20.9	21.0	21.9	22.4
	#7	20.9	19.7	24.3	22.0
	Mean		19.7 ± 5.1	22.1 ± 3.9	23.0 ± 3.0

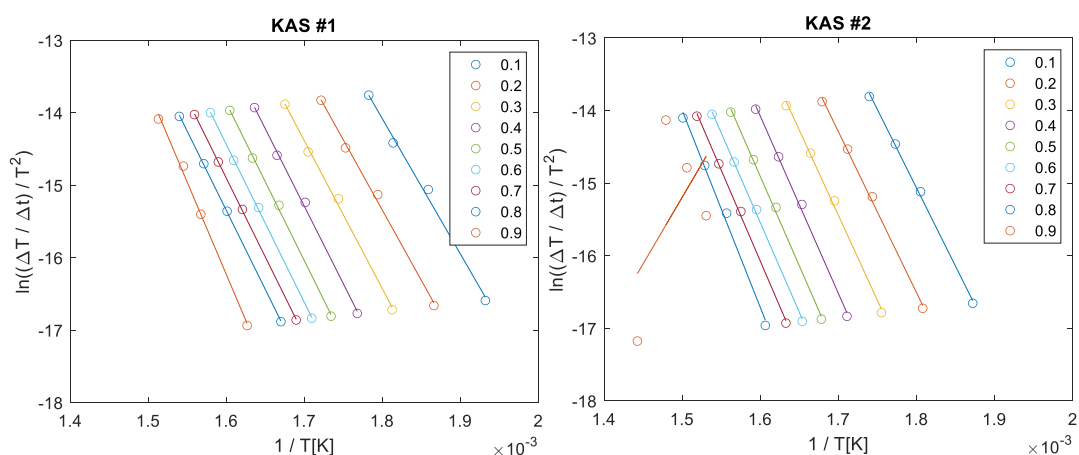
As for cellulose, the shape of the curves is similar for all cases, but some deviations are present. The obtained peak and shoulder temperatures in DTG curves at 5 K/min (350.3 ± 10.1 and 298.2 ± 10.5 , respectively) are similar to literature experiments conducted as well with beech wood at 5 K/min (349 and 295 °C, respectively [8]). The obtained deviations among experiments with different devices are of a similar order as in the previously presented cellulose pyrolysis round robin. Besides, the deviations from average presented the same tendency for most cases, e.g. peak of DTG at lower temperatures than average for #1, #3 and #5 and higher temperatures than average for #2 and #6.

The obtained averaged heating rates were very close to the targets for most of the cases, although some deviations were present. In case #4, the heating rate increased at the end of the experiment. The experiment at 1 K/min was analysed only until 450 °C, as previously stated, because at higher temperatures the heating rate became too high. However, the most critical experiment of #4 is the one at 20 K/min, as the increase in heating rate takes place already when the conversion is not high (i.e. a significant fraction of biomass has not yet pyrolysed, as opposite to other experiments when the increase in heating rate takes place when conversion is already very high). In the experiments of #3 the heating rate is higher at the begin of the experiment for the cases at 10 and 20 K/min. In all other cases the deviations were minor.

Regarding the char yields, the obtained deviations are lower than for cellulose. The highest char yields were obtained for cases #3, with the highest initial sample mass, and #5. The results are surprising for case #5 as the initial sample mass was of 3 mg. Cases #6 and #7, with an initial sample mass of 10 – 12 mg had generally higher char yields than the other cases with an initial sample mass of 3 mg (#1, #2 and #4). Besides, the char yield was slightly lower at the lowest heating rate in some cases, which points out a higher uncertainty in the determination at these very low heating rates.

3.3.2.1 Isoconversional KAS method results

The isoconversional KAS method has been applied to determine the activation energies along conversion for all cases. The Arrhenius plots are shown in Figure 3.8. For a certain conversion, one point is obtained from each experiment at a different heating rate. Therefore, 4 points are presented for each conversion since experiments were conducted at 4 heating rates. The slope of the Arrhenius plots at a certain conversion determines the activation energy. The quality of the linear fit is good for most of the cases. There are however two exceptions: the experiment from #2 at 1 K/min for high conversions (see at $\alpha = 0.9$ in Figure 3.8) and the experiment from #5 at 20 K/min.



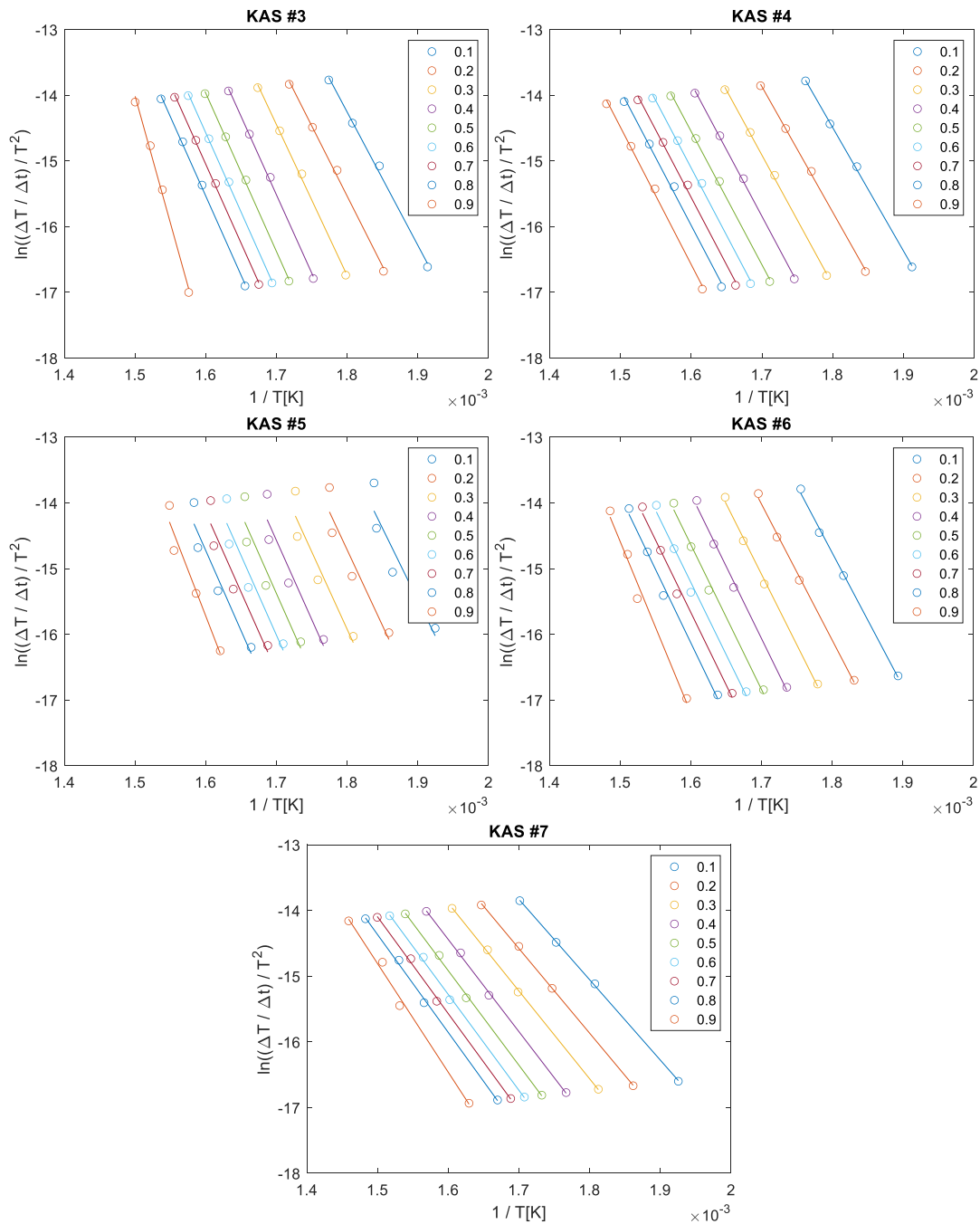


Figure 3.8: Arrhenius plots from the KAS method for conversions from 0.1 to 0.9 for beech wood pyrolysis at heating rates of 1, 5, 10 and 20 K/min for partners #1 to #7.

The obtained activation energies from the KAS method and R-squared values are presented in Table 3.5 and Table 3.6, respectively. For #2 and #5 the values are reported for all heating rates and also without the experiments considered as outliers (at 1 K/min for #2 and at 20 K/min for #5). Including all experiments, the obtained R-squared values were low at all conversions for #5 (values around 0.9) and very low at conversions higher than 0.8 for #2. These 2 outliers were therefore easily detected with the isoconversional KAS method, looking at the R-squared values as well as the Arrhenius plots in Figure 3.8. Without the outliers, the obtained R-squared values are very high for all cases (see Table 3.6), obtaining values above 0.99 for the seven data sets for conversions between 0.1 and 0.85 (except for #5 without outliers at conversions of 0.1 and 0.15, with R-squared values of 0.97

and 0.98). The R-squared values are a bit worse for some cases at low conversions ($\alpha = 0.05$) and they are much worse at high conversions (especially at $\alpha = 0.95$).

Table 3.5: Activation energies (kJ/mol) along conversion from KAS method for beech wood pyrolysis – data of #2 and #5 presented as well without outliers (#2 at 1K/min and #5 at 20 K/min).

α	#1	#2	#3	#4	#5	#6	#7	Mean	#2 No out.	#5 No out.	Mean (#2, #5 no out.)		
0.05	148.9	185.7	169.7	157.4	172.3	173.3	104.5	158.8	±26.7	166.5	134.8	150.7	±24.4
0.1	155.1	179.4	168.6	156.1	182.4	169.2	106.5	159.6	± 25.6	166.0	145.2	152.4	± 22.0
0.15	157.7	180.3	172.0	157.1	188.5	169.6	109.1	162.0	± 25.9	166.8	151.5	154.8	± 21.5
0.2	161.1	184.4	177.3	158.8	191.7	172.0	112.6	165.4	± 26.1	169.4	154.7	158.0	± 21.5
0.25	165.2	189.4	184.3	161.2	193.6	175.2	114.4	169.1	± 26.9	172.8	156.3	161.3	± 22.7
0.3	169.8	195.0	190.9	164.1	195.6	178.4	116.8	172.9	± 27.7	176.1	157.7	164.8	± 23.7
0.35	174.2	199.7	195.6	166.7	197.9	181.2	120.0	176.5	± 27.9	180.5	159.3	168.2	± 24.2
0.4	177.7	203.2	198.3	168.1	200.2	182.7	122.5	178.9	± 28.1	184.4	161.1	170.7	± 24.4
0.45	179.8	204.3	199.5	168.3	201.5	183.2	124.3	180.1	± 28.0	187.4	162.0	172.1	± 24.4
0.5	180.8	204.9	200.3	168.6	201.9	183.3	125.5	180.8	± 27.7	188.5	162.4	172.8	± 24.3
0.55	181.2	204.9	200.7	169.6	201.8	183.0	126.4	181.1	± 27.4	189.8	162.5	173.3	± 24.2
0.6	181.2	205.5	200.6	170.3	201.4	182.9	127.1	181.3	± 27.2	191.3	162.5	173.7	± 24.1
0.65	181.0	206.7	200.3	170.4	201.1	183.0	127.6	181.4	± 27.1	193.0	162.6	174.0	± 24.1
0.7	180.8	208.3	199.8	170.5	201.1	183.5	128.2	181.8	± 27.1	194.0	163.0	174.3	± 23.9
0.75	180.8	212.4	199.6	170.8	201.4	184.3	128.8	182.6	± 27.6	194.3	163.8	174.6	± 23.7
0.8	181.3	225.6	200.5	171.0	203.0	186.0	129.7	185.3	± 30.2	195.0	165.7	175.6	± 23.7
0.85	184.0	329.2	207.3	171.5	207.2	190.8	131.6	203.1	± 61.3	197.9	170.3	179.1	± 24.8
0.9	211.4	- 152.4	321.5	173.8	231.7	216.9	142.9	163.7	± 150.0	212.7	194.0	210.5	± 55.6
0.95	332.3	- 218.8	667.6	184.0	125.0	300.6	192.7	226.2	± 265.4	131.8	16.6	260.8	± 207.7

Table 3.6: R-squared values from KAS method for beech wood pyrolysis – data of #2 and #5 presented as well without outliers (#2 at 1K/min and #5 at 20 K/min).

α	#1	#2	#3	#4	#5	#6	#7	Mean	#2 No out.	#5 No out.	Mean (#2, #5 no out.)		
0.05	0.9849	0.9966	0.9947	0.9995	0.8061	0.9966	0.9773	0.9651	0.0706	1	0.9184	0.9816	± 0.0291
0.1	0.9949	0.9984	0.9965	0.9993	0.8672	0.9978	0.9947	0.9784	0.0491	0.9999	0.9662	0.9928	± 0.0119
0.15	0.9965	0.9983	0.9971	0.9995	0.8925	0.9975	0.997	0.9826	0.0398	0.9998	0.9835	0.9958	± 0.0056
0.2	0.9968	0.9980	0.9972	0.9993	0.9023	0.9976	0.9985	0.9842	0.0361	0.9999	0.9907	0.9971	± 0.0031
0.25	0.997	0.9977	0.9974	0.9993	0.9034	0.9976	0.9984	0.9844	0.0357	0.9999	0.9936	0.9976	± 0.0021
0.3	0.9972	0.9971	0.9979	0.9989	0.9011	0.9973	0.9973	0.9838	0.0365	1	0.9941	0.9975	± 0.0018
0.35	0.9975	0.9971	0.9984	0.9989	0.8980	0.9966	0.9969	0.9833	0.0376	1	0.9938	0.9974	± 0.0020
0.4	0.998	0.9974	0.9987	0.9989	0.8965	0.9956	0.9969	0.9831	0.0382	1	0.993	0.9973	± 0.0024
0.45	0.9985	0.9979	0.9989	0.9988	0.8955	0.9943	0.997	0.9830	0.0386	1	0.9923	0.9971	± 0.0028
0.5	0.999	0.9981	0.9991	0.9985	0.8965	0.993	0.9972	0.9831	0.0382	1	0.9919	0.9970	± 0.0032
0.55	0.9994	0.9984	0.9992	0.9981	0.8990	0.9919	0.9975	0.9834	0.0373	1	0.9916	0.9968	± 0.0036
0.6	0.9997	0.9986	0.9991	0.9976	0.9026	0.9916	0.9976	0.9838	0.0359	1	0.9918	0.9968	± 0.0036
0.65	0.9998	0.9987	0.9991	0.9972	0.9069	0.9917	0.9979	0.9845	0.0343	1	0.9924	0.9969	± 0.0034
0.7	0.9999	0.9986	0.999	0.9968	0.9118	0.9918	0.9981	0.9851	0.0325	1	0.9932	0.9970	± 0.0033
0.75	0.9999	0.9978	0.9989	0.9964	0.9170	0.9922	0.9982	0.9858	0.0304	1	0.9943	0.9971	± 0.0030
0.8	0.9998	0.9937	0.9986	0.9961	0.9235	0.9926	0.9979	0.9860	0.0277	1	0.9959	0.9973	± 0.0026
0.85	0.9997	0.6652	0.9979	0.9960	0.9328	0.9924	0.9967	0.9401	0.1235	1	0.9983	0.9973	± 0.0026
0.9	0.9968	0.2786	0.9954	0.9973	0.9504	0.9832	0.971	0.8818	0.2665	0.9994	0.9965	0.9914	± 0.0104
0.95	0.7913	0.7932	0.9721	0.9459	0.1091	0.6413	0.8536	0.7295	0.2949	0.0266	0.0036	0.6049	± 0.4173

The obtained activation energies with the KAS method along conversion are presented in Figure 3.9. The values are shown on the top for all experiments and on the bottom for the experiments without outliers in cases #2 and #5. The cases with outliers had (together with case #3) higher activation energies than the other 4 cases. Including them would lead to an erroneous higher determination of activation energies with this method. Excluding the experiments considered as outliers led to lower activation energies in these cases, following the general trend for case #2 and with lower values for case #5. The predicted activation energies on average (without outliers) are a bit above 150 kJ/mol at low conversions and they increase along conversion for all cases, achieving values above 170 kJ/mol at a conversion of 0.4 and up to around 180 kJ/mol at a conversion of 0.85 (see Table 5). The obtained standard deviations until this conversion are in the range 20 – 25 kJ/ mol (25 – 30 for all experiments including outliers). At yet higher conversions, the activation energies increase significantly, but the obtained deviations among all cases are much higher. The obtained results from the KAS method will be critically discussed in the next subsection.

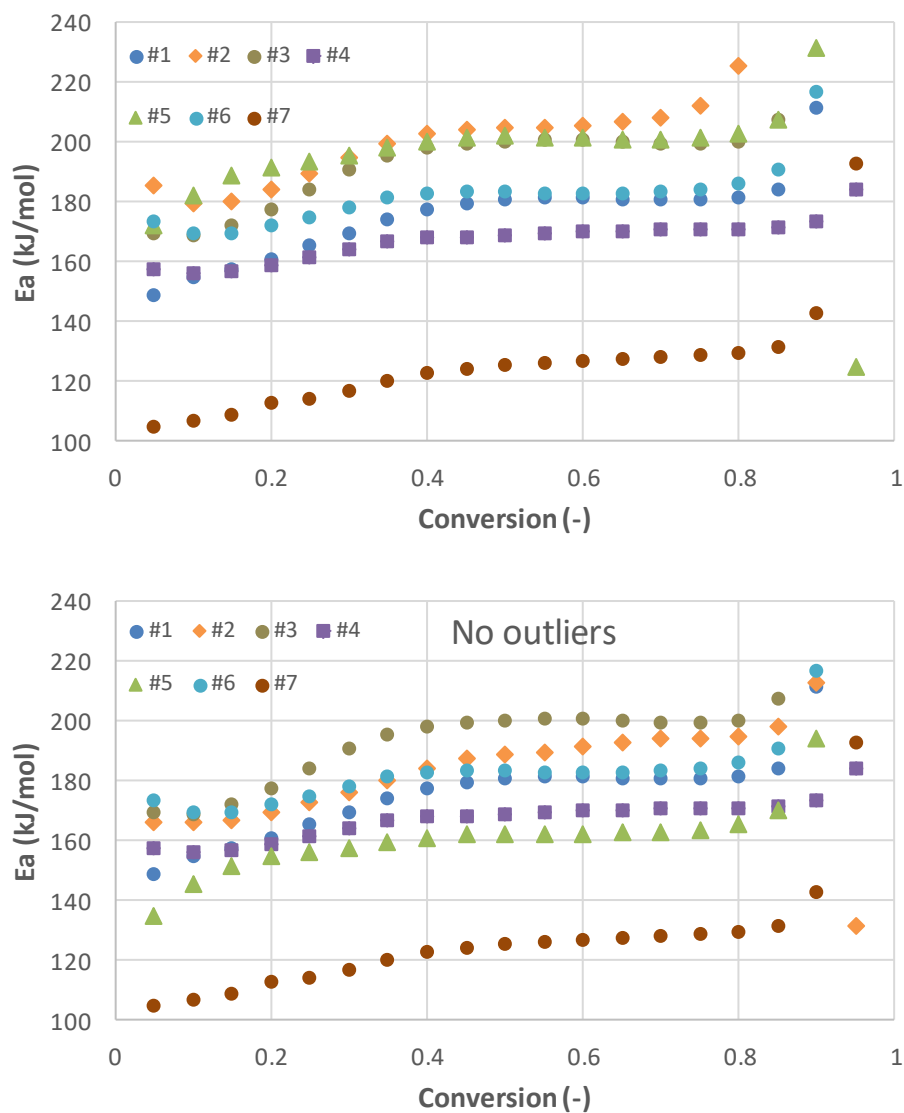


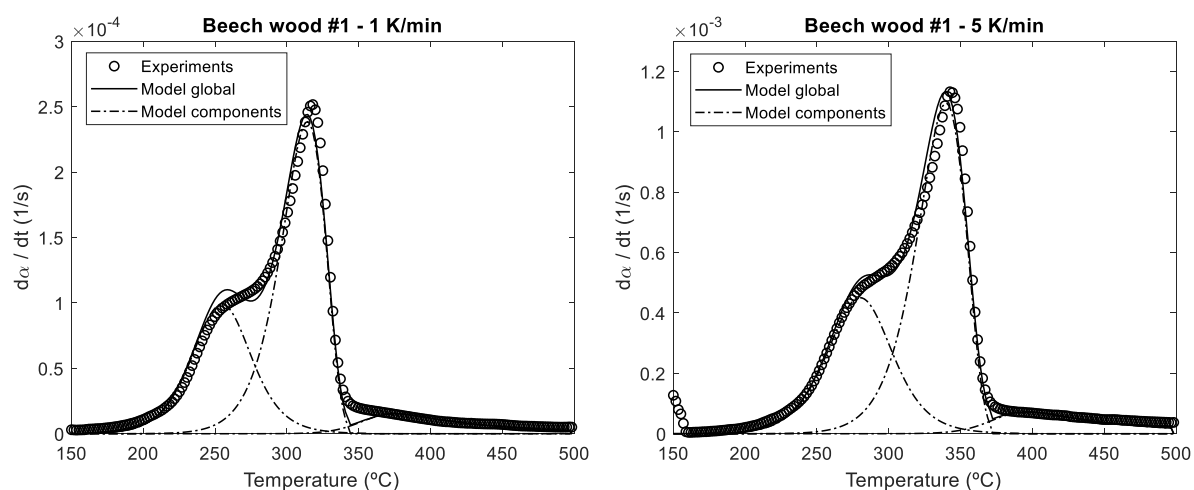
Figure 3.9: Activation energies along conversion (KAS method) for all experiments (top) and for experiments without outliers (#2 at 1 K/min and #5 at 20 K/min – bottom) for beech wood pyrolysis.

3.3.2.2 Model fitting results

The results of the model fitting method are shown in Table 3.7. Three components are considered for the fit: cellulose, hemicellulose and lignin. In Figure 3.10, the DTG curves for experiments and model fitting are shown for case #1 and for all heating rates. In Figure 3.11, the DTG curves for other cases at 5 K/min are shown. The main component is cellulose ($c \approx 0.57$), which has been modelled with a first order reaction and describes the main peak of the DTG curve. Hemicellulose ($c \approx 0.33$) and lignin ($c \approx 0.1$) describe respectively the shoulder at lower temperatures and the tail at high temperatures with an nth order reaction. The error in the fitting is generally low, with values around 2% for all cases. Similar results are obtained for all cases and the only exception is case #7, where the best fit was obtained when the first order reaction describes lignin and cellulose is described with a reaction with an order lower than one. The error in the fitting was also a bit higher in this case (3.1%). It should be mentioned that the same initial values were employed in the fitting routine for the fitted parameters in all cases, and it was checked that with different values a better fit was not obtained.

Table 3.7: Kinetic parameters from model fitting method for beech wood pyrolysis for hemicellulose (HC), cellulose (CEL) and lignin (LIG).

		#1	#2 No out	#3	#4	#5 No out	#6	#7	Mean	Mean No #7
HC	$\log_{10}(A)$ (s^{-1})	11.50	10.46	12.86	11.66	11.38	11.97	7.48	11.04 \pm 1.73	11.64 \pm 0.78
	E (kJ/mol)	147.1	140.5	161.7	150.6	143.6	154.8	107.8	143.7 \pm 17.3	149.7 \pm 7.7
	n (-)	1.78	1.81	1.79	2.33	1.99	1.84	0.82	1.76 \pm 0.46	1.92 \pm 0.22
	c (-)	0.324	0.378	0.331	0.370	0.328	0.326	0.225	0.326 \pm 0.050	0.343 \pm 0.024
CEL	$\log_{10}(A)$ (s^{-1})	12.90	14.06	14.63	12.29	11.52	12.80	8.01	12.32 \pm 2.17	13.04 \pm 1.14
	E (kJ/mol)	179.2	198.9	199.6	175.8	160.8	181.8	126.0	174.6 \pm 25.3	182.7 \pm 14.8
	n (-)	1	1	1	1	1	1	0.56	0.94 \pm 0.17	1 \pm 0
	c (-)	0.579	0.552	0.542	0.563	0.567	0.571	0.662	0.576 \pm 0.040	0.562 \pm 0.013
LIG	$\log_{10}(A)$ (s^{-1})	18.55	31.10	25.17	21.24	36.04	15.88	4.70	21.81 \pm 10.32	24.66 \pm 7.71
	E (kJ/mol)	268.2	440.7	347.6	305.7	461.1	238.9	97.2	308.5 \pm 124.8	343.7 \pm 90.9
	n (-)	5.88	7.62	7.26	5.20	11.47	4.82	1	6.18 \pm 3.19	7.04 \pm 2.44
	c (-)	0.097	0.070	0.128	0.067	0.105	0.104	0.113	0.098 \pm 0.022	0.095 \pm 0.023
Error fit	(%)	2.32	2.04	2.34	2.61	1.74	2.61	3.14	2.40 \pm 0.45	2.28 \pm 0.34



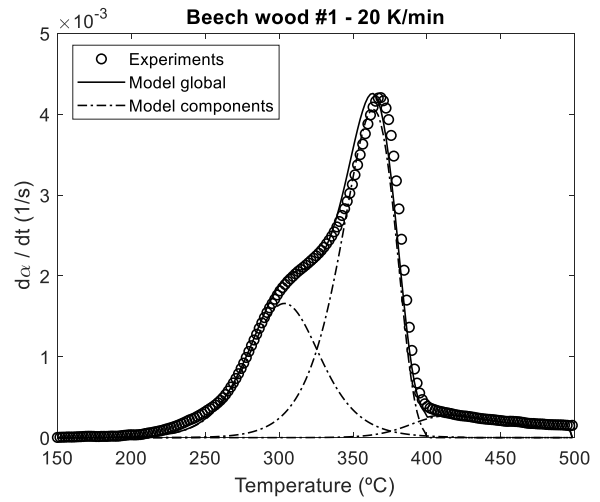
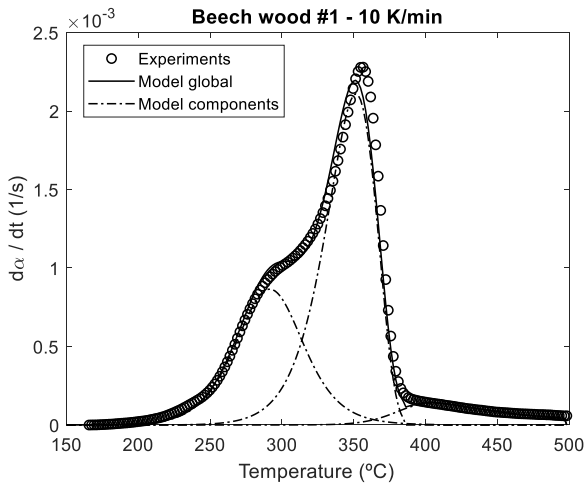
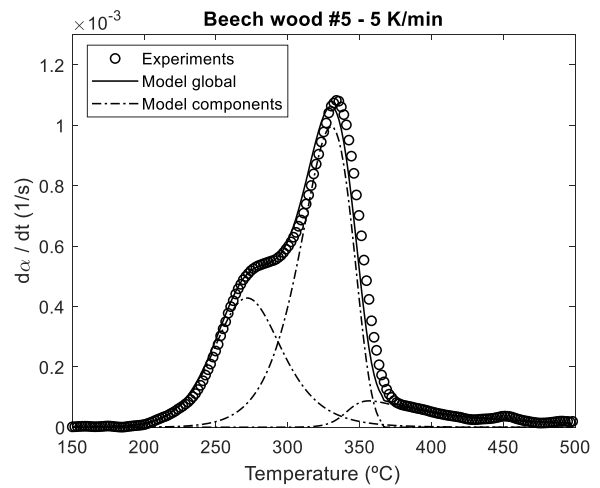
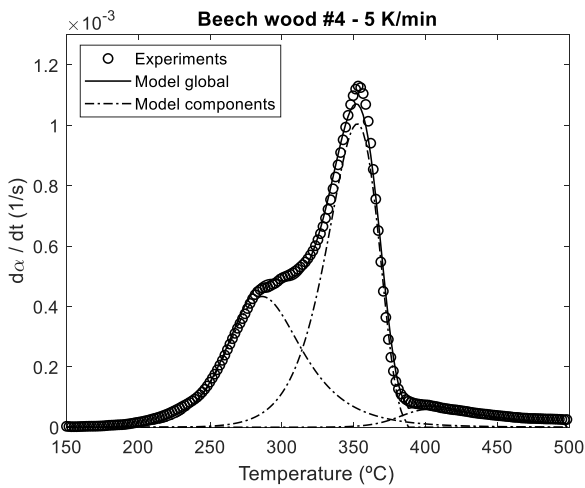
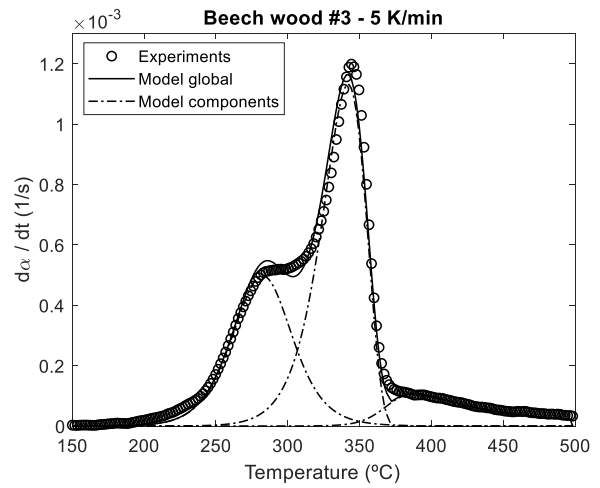
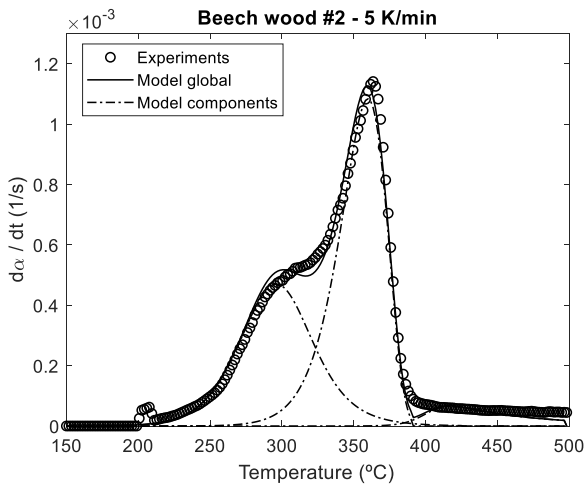


Figure 3.10: DTG experiments (circles) and model fitting (line) for beech wood at heating rates of 1, 5, 10 and 20 K/min for case #1.



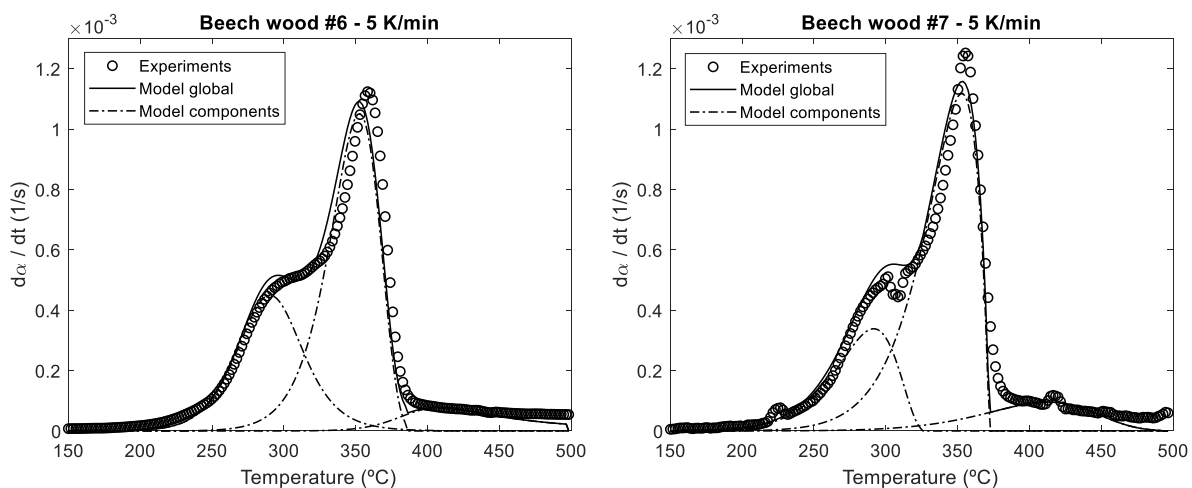


Figure 3.11: DTG experiments (circles) and model fitting (line) for beech wood at a heating rate of 5 K/min for cases #2 to #7.

The obtained activation energies for cellulose with the fitting routine are around 180 kJ/mol. For hemicellulose lower activation energies are obtained, around 150 kJ/mol, with an order of reaction close to two. The obtained standard deviations from all cases are moderate, especially when not including case #7 (15 and 8 kJ/mol for cellulose and hemicellulose, respectively). For lignin the obtained activation energies (over 300 kJ/mol) and reaction orders (around 7) are high, and the variability is much higher than for the other compounds.

3.3.2.3 Comparison of isoconversional KAS and model fitting results

In Table 3.8 the activation energy values obtained from the fitting and the isoconversional KAS method are compared. For cellulose, the derived activation energy with the fitting method is compared to the value from the KAS method obtained at the conversion level with the maximum reaction rate in the DTG curve, which is around 0.7. A very good agreement is obtained between both activation energies and the highest difference is 5 kJ/mol for case #4. For hemicellulose, the shoulder of the DTG curve is selected as a representative point for the comparison. The shoulder is observed at conversions around 0.25 and at this point, where the curvature of the DTG curves changes, the cellulose and hemicellulose compounds have a similar relevance (see Figure 3.10 and Figure 3.11). Therefore, the activation energy from the KAS method at the conversion where the shoulder takes place is compared to the averaged activation energy of cellulose and hemicellulose from the fitting method. In this case a very good agreement is as well achieved, and the highest deviation is 7 kJ/mol for case #6. Therefore, the isoconversional KAS method validates the obtained activation energies from the fitting method obtained for cellulose and hemicellulose. For lignin, the comparison is more challenging. The lignin compound in the fitting method describes the tail at high temperatures in the DTG curve. This tail starts at conversions around 0.9. The activation energies from the KAS method at this stage increase for all cases, but also the R-squared values are lower. At a conversion of 0.95 the R-squared values are already quite low for most of the cases (see Table 3.6). For the comparison with the fitting method, the activation energies of the KAS method at a conversion of 0.92 are selected. At this stage the R-squared values are generally acceptable (see Table 3.8). From the comparison the results from the isoconversional method suggest that there is an increase in activation energy during the last stage of conversion, which was also obtained from the fitting method for lignin, although discrepancies in the obtained values are present.

Table 3.8: Comparison of activation energies in kJ/mol with fitting method for cellulose (CEL), hemicellulose (HC) and lignin (LIG) and KAS isoconversional method at selected points.

	#1	#2 No out	#3	#4	#5 No out	#6	#7	Mean	
Fit CEL	179.2	198.9	199.6	175.8	160.8	181.8	126.0	174.6	± 25.3
α maximum (-)	0.713	0.735	0.693	0.723	0.674	0.698	0.711	0.707	± 0.020
KAS α maximum	180.8	194.2	199.9	170.6	162.8	183.5	128.3	174.3	± 23.9
Difference CEL [Fit CEL – KAS max.]	-1.7	4.7	-0.3	5.1	-2.0	-1.7	-2.3	0.3	± 3.2
Fit HC	147.1	140.5	161.7	150.6	143.6	154.8	107.8	143.7	± 17.3
Fit (HC+CEL)/2	163.1	169.7	180.7	169.6	152.2	168.3	116.9	159.1	± 20.5
α shoulder (-)	0.250	0.283	0.261	0.247	0.242	0.249	0.252	0.255	± 0.014
KAS α shoulder	165.3	175.0	185.7	160.5	156.0	175.1	114.5	161.7	± 23.1
Difference HC [Fit (HC+CEL)/2 – KAS sh.]	-2.2	-5.3	-5.0	2.7	-3.8	-6.8	2.4	-2.6	± 3.8
Fit LIG	268.2	440.7	347.6	305.7	461.1	238.9	97.2	308.5	± 124.8
KAS α = 0.92	283.6	249.5	412.6	177.2	257.1	263.2	160.7	257.7	± 82.3
R-squared α = 0.92 (-)	0.956	0.990	0.999	0.999	0.851	0.888	0.873	0.937	± 0.065
Difference LIG [Fit LIG - KAS α = 0.92]	-15.4	191.1	-65.0	128.5	204.0	-24.3	-63.5	50.8	± 42.5

3.3.2.4 Discussion

The conduction of TGA for biomass pyrolysis and its evaluation is inherently difficult. Cellulose mass loss at 5 K/min can be well described with a single first order reaction with a high activation energy (above 200 kJ/mol). The results of this round robin show however that standard deviations of 9 °C in the position of the maximum in the DTG curve at 5 K/min and 22 kJ/mol in activation energy were obtained. Such deviations are therefore to be expected when conducting experiments with different devices.

For beech wood pyrolysis, the obtained standard deviations in the positions of the peak and shoulder of the DTG curves (around 10 °C at 5 K/min) are of a similar order as for pure cellulose. These deviations arise therefore only from the use of different devices with different operation modes. The variability in TGA data for biomass pyrolysis in literature is commonly attributed to the inherent heterogeneity in biomass composition. This work shows that the use of different devices and methods with the same samples further adds variability in the results.

The determination of mass loss kinetics from wood pyrolysis is more challenging than for pure cellulose. As already discussed in the introduction, experiments at different heating rates are required. Isoconversional methods are a suitable tool to assess the reliability of wood pyrolysis TGA experiments. The integral isoconversional KAS method has been applied in this work and it was shown that outliers can be detected when low R-squared values are present. Two outliers (at 1 K/min for case #2 and at 20 K/min for case #5) were detected from the 7 data sets with different TGA devices evaluated and therefore removed from further analysis. High R-squared values, over 0.99 during most of the conversions (except at the very begin and specially at the end of the conversions) are to be expected from reliable experiments at different heating rates, as it is the case for the experiments without outliers in this work.

The kinetics were determined using a fitting method which employs three parallel reactions (cellulose, hemicellulose and lignin), and validated with the isoconversional KAS method. A variable reaction order was assumed for hemicellulose and lignin, and a first order for cellulose. The obtained activation energy for cellulose is high (around 180 kJ/mol), but lower than for pure cellulose. The

activation energy for hemicellulose (around 150 kJ/mol) is lower than for cellulose. In both cases, the values obtained from the fitting are supported by the isoconversional KAS method with a good accuracy. For lignin, very high activation energies are obtained with both fitting and isoconversional methods (above 200 kJ/mol), but the deviations for different cases are large.

The obtained deviations in activation energies for cellulose and hemicellulose with the fitting method and for the KAS method for conversions up to 0.9 are around 20 kJ/mol (without outliers). These deviations are of similar order as the results with pure cellulose. A closer inspection of the results shows that the deviations are especially higher for case #7, obtaining much lower activation energies than the average and significant differences in reaction orders. For the other cases, the differences are smaller, but it can yet be detected that lower activation energies are obtained for case #5 and higher for case #3. These 3 cases (#3, #5 and #7) were also the ones for which higher discrepancies were found for the cellulose experiments. The conversion took place at significantly lower temperatures for case #5, with the peak in the DTG curve at 15 °C less than the average. This behaviour was also seen in the beech wood experiments for this case (see Figure 3.6 and Figure 3.7). For cases #3 and #7, a remarkably higher char yield was obtained for cellulose, as well as a higher error in the fitting due to char devolatilization at temperatures higher than 370 °C. It is not clear if this influences also significantly the beech wood experiments, but anyhow in both cases the deviations were higher for cellulose and also the highest initial mass samples were employed. If these cases for which deviations were already present for cellulose are not considered for the beech wood analysis, the obtained standard deviations are much lower.

The averaged kinetic parameters for cases #1, #2 (without 1 K/ min), #4 and #6 are shown in Table 3.9 and the obtained activation energies with the KAS method in Figure 3.12. These selected cases are the ones which could reproduce with a good accuracy the experimental results with pure cellulose and for case #2 the experiment at 1 K/min was not considered after an analysis of the results applying the isoconversional KAS method. The previously described trends remain the same, but the obtained deviations are quite lower, with 10 or less kJ/ mol for the conversions up to 0.9 with beech wood, as well as for the cellulose and hemicellulose compounds in beech wood and for pure cellulose. Besides, the averaged activation energy of the cellulose component in the selected cases (183.9 ± 10.3 kJ/mol) is higher than when considering all cases (174.6 ± 25.3 kJ/mol) and very close to the values commonly reported in literature from detailed analysis (in the vicinity of 47 kcal/ mol–197 kJ/mol - according to Burnham et al. [52]).

Table 3.9: Averaged kinetic parameters from model fitting method and comparison of activation energies to from fitting and isoconversional KAS method for selected cases #1, #2 (without 1K/min), #4 and #6.

		Beech wood				Pure cellulose			
		Hemicellulose		Cellulose		Lignin			
Fit	$\log_{10}(A)$ (s^{-1})	11.40	± 0.65	13.02	± 0.75	21.69	± 6.64	16.83	± 0.69
	E (kJ/mol)	148.2	± 6.0	183.9	± 10.3	313.4	± 89.2	220.7	± 8.2
	n (-)	1.94	± 0.27	1	-	5.88	± 1.24	1	-
	c (-)	0.350	± 0.028	0.566	± 0.012	0.084	± 0.019	-	-
E_a KAS (kJ/mol) [α shoulder, max., 0.92]		169.0	± 7.3	182.3	± 9.7	243.4	± 46.3	-	-
Difference (kJ/mol) [Fit (HC+CEL)/2 – KAS shoulder, Fit CEL – KAS max., Fit LIG – KAS $\alpha = 0.92$]		-2.9	± 4.2	1.6	± 3.8	70.0	± 106.9	-	-

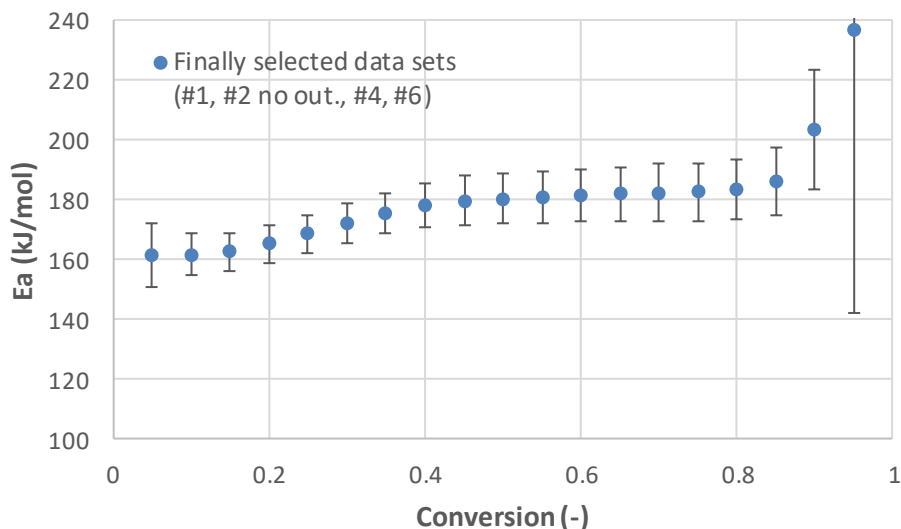


Figure 3.12: Activation energies along conversion (KAS method) for selected cases #1, #2 (without 1K/min), #4 and #6.

It also interesting to discuss possible causes leading to results outside the general trends for cases #3, #5 and #7, which are the finally not selected cases because they could not reproduce the results with pure cellulose. For cases #3 and #7 higher initial masses were employed than other cases (see Table 3.1). It is therefore advised to employ initial masses lower than 10 mg (the exact value probably depends on the device), as higher values led to deviations in this work. This is consistent with previous literature works with cellulose, which showed that thermal lag can only be completely avoided with samples of a few mg at low heating rates (up to 10 K/min) and even smaller samples at higher heating rates [52, 53]. Despite it, initial sample masses of 10 mg and higher are still commonly employed in literature for determining biomass pyrolysis kinetics, as shown in the review of recent works presented in the introduction, where the initial sample mass was on average of 9.2 ± 5.0 mg. For case #5, with an initial sample mass of 3 mg, it was found after the experiments of the round robin that differences in the peak temperature (15 °C lower than the average for pure cellulose) was due to: 1) the temperature calibration, as a recalibration considering the nonlinear behaviour of the furnace lead to a difference of 3.8 °C in the peak temperature for cellulose (the furnace was originally calibrated with melting points of 5 pure metals including Ag and Au - melting points of 962 and 1064 °C -, which led to deviations at lower temperatures), and 2) over geometry and purge gas flow direction, as the purge gas flows downwards in the employed device (as opposite to the most common devices) promoting the decomposition; and this effect can be diminished by using pan lids, leading to a difference of 7.2 °C in the peak temperature for cellulose.

Furthermore, deviations in the target heating rate were present for case #3 at 10 and 20 K/min. Additionally, for case #4 the heating rates were higher than the target. A detailed analysis shows that the experiment at 20 K/min of case #4 is slightly outside the general trend, which is probably due to the higher heating rates obtained in that experiment when a significant conversion was still taking place. Slightly higher activation energies would be obtained for case #4 without the experiment at 20 K/min, but the current deviations are considered acceptable.

Other characteristics of the employed TGA instruments and methods besides the initial sample mass have shown to not be critical for deriving reliable kinetics. The finally selected cases as the most reliable (#1, #2 without outlier, #4 and #6) span the whole range of tested possibilities regarding TGA configuration type (horizontal and vertical), N₂ purge flow, sensitivity and temperature accuracy (from the lowest to highest values), sample holder (ceramic, platinum and alumina) and calibration method (Curie point or melting point), as shown in Table 3.1.

The results of this work show that a certain variability is present in the experimental results employing several TGA devices with beech wood and pure cellulose pyrolysis, and it is of a similar order regarding temperature differences than in the round robin conducted by Gronli et al. [7] with pure cellulose. However, these deviations can lead to larger discrepancies in the calculated activation energies for beech wood pyrolysis, where several components decompose in parallel. This result should not discourage the use of TGA to determine kinetics, but this needs to be conducted with care, reproducing first TGA results of pure cellulose and employing isoconversional methods as suggested in this work to validate the reliability of the experiments. Besides, kinetics should be derived with reliable methods, as in this work combining fitting and isoconversional methods, which is not always the case in literature and adds further variability to the reported values.

Finally, it is not the target of this work to claim that the conducted kinetic analysis for beech wood pyrolysis is the optimal one. A parallel scheme was selected as it is the most common option in literature and it provides reasonable results for mass loss, although it cannot predict the yield of different products as char or bio-oil. An n th order reaction for hemicellulose and first order reaction for cellulose provided good results. The determination of the lignin parameters is more complicated, and the employed n^{th} order reaction is one possible alternative. With the current approach the lignin component is modelling only the tail at high temperatures. Lignin pyrolysis actually covers a wider temperature range and it starts reacting at low temperatures [54]. In fact, the proportion of lignin in hardwood is around 22% [55], which is higher than the $\approx 10\%$ proportion of the lignin component in the fittings in this work. It is already known that the proportions of each component in a parallel reaction scheme derived from the fitting method with TGA data does not completely resemble the biomass composition, due to interaction of compounds or different char yields. The high deviation in this case for lignin is also due to lignin reactions taking place at lower temperatures which are not covered by this component in the current fitting. Additionally, a very high reaction order is obtained in this work for lignin. This high reaction order, and probably also the very high activation energy for lignin in some cases, is mainly an artefact so that it is possible to model a compound with a relatively flat DTG curve, which in principle can be obtained for one single reaction with a low activation energy (which is not meaningful according to the KAS method) or a high reaction order (which was the case of this work). This high reaction order does not represent a real chemical phenomenon and it rather masks the complexity of several consecutive chemical reactions being modelled with one single reaction. These issues (proportion and reaction order of lignin) are however not a main limitation of this work, as it was an advantage that the lignin compound was covering only the conversion at higher temperatures, to have an easier comparison with isoconversional methods at high conversions. Anyhow, the obtained high values for the activation energy of lignin should be taken with caution, especially when there are big differences with the values from isoconversional methods. Furthermore, this work supports that for lignin a first order reaction or low activation energies [9, 54] (which are employed/derived in many works, and are commonly cause and consequence respectively), are not supported by isoconversional methods, at least for the high conversion region. However, other models may be more suited to describe lignin than the one employed here (e.g. DAEM [14]). Other reaction models can also be employed for cellulose and hemicellulose, but the obtained activation energies should be supported by isoconversional methods, as in this work.

3.4 Conclusions

The determination of mass loss kinetics for biomass pyrolysis is still an unresolved topic, due to the broad range of values reported in literature. An international round robin of TGA pyrolysis experiments with pure cellulose and beech wood has been conducted by 7 partners. Cellulose pyrolysis has been modelled with one first order reaction and beech wood pyrolysis with 3 parallel reactions employing a fitting routine. The isoconversional KAS method has been employed to support the kinetic analysis for beech wood. It was shown that certain deviations are obtained in DTG curves for all cases, of around 10 °C in the position of the peak at 5 K/min and 20 – 30 kJ/mol in the predicted activation energies for cellulose, hemicellulose and conversions up to 0.9 for beech wood. Higher deviations are obtained for yet higher conversions and for lignin.

The following method [9, 16] for determining biomass pyrolysis kinetics has been employed and is hereby recommended to increase the reliability of kinetics derived from biomass pyrolysis:

- Pure cellulose pyrolysis experiments conducted at 5 K/min from Gronli et al. [7] should first be reproduced, in order to assess the employed TGA device and methods. This study shows that a good reproducibility can be generally obtained and the cases with higher deviations were the ones who led to higher discrepancies in the determination of kinetics for beech wood. Relevant examples were two cases for which an initial mass higher than 10 mg was employed, leading to a significantly higher char yield. As often stated in literature, lower initial mass samples are recommended to avoid thermal lag.
- Pyrolysis experiments with biomass should be conducted at different heating rates and isoconversional methods should be employed to validate the reliability of the experiments, as well as of the derived kinetic parameters from a fitting method. This study shows that high R-squared values (over 0.99), except at very low and high conversions, are to be expected from isoconversional methods. Outliers who clearly did not fulfil this criterion were detected for two separate cases and not considered for further analysis. Finally, isoconversional methods should support the activation energies for cellulose and hemicellulose derived with a fitting method, while higher quantitative deviations are expected for lignin.

Following strictly this method, the data of three out of seven cases in this work was not selected for the final evaluation, and for a fourth one the data at one heating rate was disregarded. The deviations in the values of activation energy for these selected cases following the previous method were of 10 kJ/mol or lower (less than half than when considering all experiments), except for lignin. An activation energy of around 180 kJ/mol was obtained for the cellulose component in beech wood, which was a bit lower than for pure cellulose. A value of 150 kJ/mol was derived for hemicellulose while the in the case of lignin the value was higher than 200 kJ/mol. This method does not completely guarantee that optimal kinetics are derived, but at least ensures that the obtained kinetics are chemically meaningful and can help in the effort to reduce the variability in biomass kinetics in literature, which can be attributed to a significant extent to the lack of consistency in data acquisition and kinetic analysis of TGA experiments.

Bibliography

1. International Energy Agency (IEA). *Energy Technology Perspectives 2017*. [03.02.2020]; Available from: <https://www.iea.org/etp>.
2. Intergovernmental panel on climate change (IPCC). *Special Report: Global Warming of 1.5C*. 2018 [03.02.2020]; Available from: <https://www.ipcc.ch/sr15/>.
3. Bridgwater, A.V., *Review of fast pyrolysis of biomass and product upgrading*. Biomass and Bioenergy, 2012. **38**: p. 68-94.
4. Oasmaa, A., et al., *Norms, Standards, and Legislation for Fast Pyrolysis Bio-oils from Lignocellulosic Biomass*. Energy & Fuels, 2015. **29**(4): p. 2471-2484.
5. Schmidt, H.-P., et al., *Pyrogenic carbon capture and storage*. GCB Bioenergy, 2019. **11**(4): p. 573-591.
6. Antal, M.J., G. Várhegyi, and E. Jakab, *Cellulose Pyrolysis Kinetics: Revisited*. Industrial & Engineering Chemistry Research, 1998. **37**(4): p. 1267-1275.
7. Grønli, M., M.J. Antal, and G. Várhegyi, *A Round-Robin Study of Cellulose Pyrolysis Kinetics by Thermogravimetry*. Industrial & Engineering Chemistry Research, 1999. **38**(6): p. 2238-2244.
8. Grønli, M.G., G. Várhegyi, and C. Di Blasi, *Thermogravimetric Analysis and Devolatilization Kinetics of Wood*. Industrial & Engineering Chemistry Research, 2002. **41**(17): p. 4201-4208.
9. Anca-Couce, A., A. Berger, and N. Zobel, *How to determine consistent biomass pyrolysis kinetics in a parallel reaction scheme*. Fuel, 2014. **123**: p. 230-240.
10. White, J.E., W.J. Catallo, and B.L. Legendre, *Biomass pyrolysis kinetics: A comparative critical review with relevant agricultural residue case studies*. Journal of Analytical and Applied Pyrolysis, 2011. **91**(1): p. 1-33.
11. Branca, C., A. Albano, and C. Di Blasi, *Critical evaluation of global mechanisms of wood devolatilization*. Thermochimica Acta, 2005. **429**(2): p. 133-141.
12. Sánchez-Jiménez, P.E., et al., *Comments on "Pyrolysis kinetics of biomass from product information" (Applied Energy 110 (2013) 1–8) regarding the inability to obtain meaningful kinetic parameters from a single non-isothermal curve*. Applied Energy, 2014. **125**: p. 132-135.
13. Manyà, J.J., E. Velo, and L. Puigjaner, *Kinetics of Biomass Pyrolysis: a Reformulated Three-Parallel-Reactions Model*. Industrial & Engineering Chemistry Research, 2003. **42**(3): p. 434-441.
14. Cai, J., W. Wu, and R. Liu, *An overview of distributed activation energy model and its application in the pyrolysis of lignocellulosic biomass*. Renewable and Sustainable Energy Reviews, 2014. **36**: p. 236-246.
15. Khawam, A. and D.R. Flanagan, *Complementary Use of Model-Free and Modelistic Methods in the Analysis of Solid-State Kinetics*. The Journal of Physical Chemistry B, 2005. **109**(20): p. 10073-10080.
16. Anca-Couce, A., *Reaction mechanisms and multi-scale modelling of lignocellulosic biomass pyrolysis*. Progress in Energy and Combustion Science, 2016. **53**: p. 41-79.
17. Quan, C., N. Gao, and Q. Song, *Pyrolysis of biomass components in a TGA and a fixed-bed reactor: Thermochemical behaviors, kinetics, and product characterization*. Journal of Analytical and Applied Pyrolysis, 2016. **121**: p. 84-92.
18. Yeo, J.Y., et al., *Comparative studies on the pyrolysis of cellulose, hemicellulose, and lignin based on combined kinetics*. Journal of the Energy Institute, 2019. **92**(1): p. 27-37.
19. Kim, S.-S., et al., *Thermogravimetric characteristics of α -cellulose and decomposition kinetics in a micro-tubing reactor*. Korean Journal of Chemical Engineering, 2016. **33**(11): p. 3128-3133.
20. Kim, Y.-M., et al., *New approach for the kinetic analysis of cellulose using EGA-MS*. Polymer Testing, 2017. **60**: p. 12-17.

21. Kok, M.V. and E. Ozgur, *Characterization of lignocellulose biomass and model compounds by thermogravimetry*. Energy Sources, Part A: Recovery, Utilization, and Environmental Effects, 2017. **39**(2): p. 134-139.
22. Wang, S., et al., *Influence of torrefaction on the characteristics and pyrolysis behavior of cellulose*. Energy, 2017. **120**: p. 864-871.
23. Sung Suk, P., et al., *Prediction of pyrolysis kinetic parameters from biomass constituents based on simplex-lattice mixture design*. Chinese Journal of Chemical Engineering, 2016. **24**(4): p. 535-542.
24. Abdelouahed, L., et al., *Comparative investigation for the determination of kinetic parameters for biomass pyrolysis by thermogravimetric analysis*. Journal of Thermal Analysis and Calorimetry, 2017. **129**(2): p. 1201-1213.
25. Adenson, M.O., et al., *Kinetics of cellulose pyrolysis: Ensuring optimal outcomes*. The Canadian Journal of Chemical Engineering, 2018. **96**(4): p. 926-935.
26. Burra, K.R.G. and A.K. Gupta, *Modeling of biomass pyrolysis kinetics using sequential multi-step reaction model*. Fuel, 2019. **237**: p. 1057-1067.
27. Fan, Y., et al., *Effects of the cellulose, xylan and lignin constituents on biomass pyrolysis characteristics and bio-oil composition using the Simplex Lattice Mixture Design method*. Energy Conversion and Management, 2017. **138**: p. 106-118.
28. Wang, Z., et al., *Thermal behavior and kinetics of co-pyrolysis of cellulose and polyethylene with the addition of transition metals*. Energy Conversion and Management, 2018. **172**: p. 32-38.
29. Wang, S., et al., *Kinetic modeling of biomass components pyrolysis using a sequential and coupling method*. Fuel, 2016. **185**: p. 763-771.
30. Martín-Lara, M.A., et al., *Kinetic modelling of torrefaction of olive tree pruning*. Applied Thermal Engineering, 2017. **113**: p. 1410-1418.
31. Chandrasekaran, A., S. Ramachandran, and S. Subbiah, *Determination of kinetic parameters in the pyrolysis operation and thermal behavior of Prosopis juliflora using thermogravimetric analysis*. Bioresource Technology, 2017. **233**: p. 413-422.
32. Ding, Y., et al., *Estimation of beech pyrolysis kinetic parameters by Shuffled Complex Evolution*. Bioresource Technology, 2016. **200**: p. 658-665.
33. Hu, M., et al., *Thermogravimetric kinetics of lignocellulosic biomass slow pyrolysis using distributed activation energy model, Fraser–Suzuki deconvolution, and iso-conversional method*. Energy Conversion and Management, 2016. **118**: p. 1-11.
34. Chhabra, V., S. Bhattacharya, and Y. Shastri, *Pyrolysis of mixed municipal solid waste: Characterisation, interaction effect and kinetic modelling using the thermogravimetric approach*. Waste Management, 2019. **90**: p. 152-167.
35. Bach, Q.-V., et al., *Pyrolysis characteristics and kinetics of biomass torrefied in various atmospheres*. Energy Conversion and Management, 2017. **141**: p. 72-78.
36. Sobek, S. and S. Werle, *Kinetic modelling of waste wood devolatilization during pyrolysis based on thermogravimetric data and solar pyrolysis reactor performance*. Fuel, 2020. **261**: p. 116459.
37. Vamvuka, D., et al., *Kinetic modeling of five sustainable energy crops as potential sources of bioenergy*. Energy Sources, Part A: Recovery, Utilization, and Environmental Effects, 2016. **38**(12): p. 1812-1818.
38. Collazzo, G.C., et al., *A detailed non-isothermal kinetic study of elephant grass pyrolysis from different models*. Applied Thermal Engineering, 2017. **110**: p. 1200-1211.
39. Chen, T., J. Zhang, and J. Wu, *Kinetic and energy production analysis of pyrolysis of lignocellulosic biomass using a three-parallel Gaussian reaction model*. Bioresource Technology, 2016. **211**: p. 502-508.
40. Rocha, E.P.A., et al., *Kinetics of pyrolysis of some biomasses widely available in Brazil*. Journal of Thermal Analysis and Calorimetry, 2017. **130**(3): p. 1445-1454.

41. Xu, L., Y. Jiang, and L. Wang, *Thermal decomposition of rape straw: Pyrolysis modeling and kinetic study via particle swarm optimization*. Energy Conversion and Management, 2017. **146**: p. 124-133.
42. Ghouma, I., et al., *Pyrolysis of Olive Pomace: Degradation Kinetics, Gaseous Analysis and Char Characterization*. Waste and Biomass Valorization, 2017. **8**(5): p. 1689-1697.
43. Branca, C. and C. Di Blasi, *A summative model for the pyrolysis reaction heats of beech wood*. Thermochemica Acta, 2016. **638**: p. 10-16.
44. Zhang, X., et al., *Pyrolytic behavior and kinetic of wood sawdust at isothermal and non-isothermal conditions*. Renewable Energy, 2019. **142**: p. 284-294.
45. Janković, B., et al., *Characterization analysis of Poplar fluff pyrolysis products. Multi-component kinetic study*. Fuel, 2019. **238**: p. 111-128.
46. Borel, L.D.M.S., et al., *Pyrolysis of brewer's spent grain: Kinetic study and products identification*. Industrial Crops and Products, 2018. **121**: p. 388-395.
47. Lopes, F.C.R., J.C. Pereira, and K. Tannous, *Thermal decomposition kinetics of guarana seed residue through thermogravimetric analysis under inert and oxidizing atmospheres*. Bioresource Technology, 2018. **270**: p. 294-302.
48. *ASTM E1641-18, Standard Test Method for Decomposition Kinetics by Thermogravimetry Using the Ozawa/Flynn/Wall Method*. 2018: ASTM International, West Conshohocken, PA.
49. *Matlab Release R2019b. The MathWorks, Inc.*
50. Anca-Couce, A., et al., *Smouldering of pine wood: Kinetics and reaction heats*. Combustion and Flame, 2012. **159**(4): p. 1708-1719.
51. Anca-Couce, A., et al., *Kinetic scheme of biomass pyrolysis considering secondary charring reactions*. Energy Conversion and Management, 2014. **87**: p. 687-696.
52. Burnham, A.K., X. Zhou, and L.J. Broadbelt, *Critical Review of the Global Chemical Kinetics of Cellulose Thermal Decomposition*. Energy & Fuels, 2015. **29**(5): p. 2906-2918.
53. Richter, F. and G. Rein, *The Role of Heat Transfer Limitations in Polymer Pyrolysis at the Microscale*. Frontiers in Mechanical Engineering, 2018. **4**(18).
54. Jiang, G., D.J. Nowakowski, and A.V. Bridgwater, *A systematic study of the kinetics of lignin pyrolysis*. Thermochemica Acta, 2010. **498**(1): p. 61-66.
55. Anca-Couce, A. and I. Obernberger, *Application of a detailed biomass pyrolysis kinetic scheme to hardwood and softwood torrefaction*. Fuel, 2016. **167**: p. 158-167.

4. Estimation of lignocellulosic biomass pyrolysis product yields using artificial neural networks

Chapter published in:
Journal of Analytical and Applied Pyrolysis, Volume 157, August 2021, 105180

4.1 Introduction

The increasing concern regarding environmental change, the looming depletion of conventional fossil fuel reserves together with the also increasing need for energy self-reliance and the global concern surrounding their use, lead to the employment of alternative and sustainable resources for heat and power generation, fuels and chemicals production. Biomass constitutes a potentially clean and renewable fuel, which is also readily available worldwide, being the third most abundant fuel source after coal and oil. Biomass thermochemical conversion is a candidate for the production of heat, power, chemicals and fuels production, with pyrolysis, torrefaction, gasification, combustion and hydrothermal liquefaction constituting the majorly employed thermochemical conversion methods [1].

Pyrolysis can be defined as the thermochemical process of biomass decomposition, either in the absence of an oxidation medium, or with a minor amount that does not enable gasification to an appreciable extent [2]. The main products of pyrolysis are char, bio-oil and gases and their quality and quantity are dependent on the reactor's operational conditions. Furthermore, pyrolysis is a sub-process of gasification and tar formation therein. Primary and secondary pyrolysis reactions occur during gasification among other reactions such as the water – gas shift and char oxidation [3]. Pyrolysis and gasification processes can be modelled or simulated using a variety of different models such as thermodynamic equilibrium models, kinetic models, computational fluid dynamics (CFD) models or machine learning techniques [4]. The important developments in the computer science and data analysis fields have led to an increase in the implementation of machine learning techniques for biomass thermochemical conversion processes and especially gasification. Artificial neural networks (ANNs) are widely used for this purpose (Table 4.1), as well as other machine learning models like the support vector machine (SVM) [5] or the random forest (RF) method [6]. However, the present work focuses exclusively on ANNs.

Artificial Neural Networks (ANNs) can be defined as structures comprised of densely interconnected adaptive simple processing elements (artificial neurons or nodes), capable of performing massively parallel computations for data processing and knowledge representation. Constituting drastic abstractions of their biological counterparts, ANNs employ the functionality of the biological networks in the effort to solve complex problems, rather than replicating their operation [7]. Since the 1940s, when the modern view of neural networks started and their resurgence in the 1980s, neural networks have been applied in hundreds of fields including medicine, robotics, telecommunications, oil and gas, banking etc. [8]. ANNs employing supervised learning are able to “learn” mathematical relationships between inputs and corresponding outputs through “training”, by using a data set of input variables and known or associated outcomes. According to the perceived relationship between inputs and outputs, the internal weights of the ANN are adjusted and after the training, the network can be used for pattern recognition or classification tasks in a separate data set [9]. ANNs have several features that make them an attractive option for predictive tasks. To begin with, in contrast with traditional model-based methods, ANNs are data-driven self-adaptive methods, which do not include, at least to an appreciable extent, a priori assumptions regarding the problem under study. Additionally, the generalization capabilities of ANNs allow them to infer the unseen part of the sample data correctly, even if significant noise exists, given the obtained right training parameters and data. Furthermore, the ANNs are universal function approximators, a characteristic that allows them to approximate any continuous function to a desired accuracy, no matter how complex or non-linear [10]. However, the use of ANNs comes with some inherent disadvantages, such as the limitation to identify possible causal relationships between inputs and outputs explicitly. ANNs are actually a “black box”. Furthermore, ANNs are often computationally expensive and sometimes

prone to overfitting, while model development is somehow empirical and methodological issues remain to be resolved [9].

Several studies employing ANN models for the prediction of biomass thermochemical conversion processes product yields or behaviour in general can be found in the literature. As can be seen in Table 4.1, the majority of the cases concerns biomass gasification, however substantial work has been also performed regarding pyrolysis. Despite that fact, important lessons can be learned from the implementation of ANNs in biomass gasification processes modelling also concerning their use in pyrolysis models. Additionally, it is interesting to note that a substantial amount of work has been dedicated to the prediction of biomass higher heating value using ANN models [11-17]. Regarding pyrolysis ANN models, researchers appear to focus mostly on the use of thermogravimetric analysis (TGA) results aiming either to the prediction of the weight loss [18-21] or to the determination of the kinetic parameters (activation energy, pre-exponential factor, reaction order) [6, 22]. Fewer studies deal with the pyrolysis products composition [23, 24] or pyrolysis gas composition in particular [25], while char yield and its characteristics have also been investigated [5, 26]. The overview of the gasification ANN models is much more one sided, since most of the studies focuses on the prediction of the product gases yield and composition (Table 4.1). Interestingly, in some of these studies the gasification temperature [27, 28] is introduced as a prediction of the model, while Serrano et al. [29] aimed exclusively to the prediction of the total tar yield. In general, the inherent ability of ANN models to process large amounts of data has led to the development of quite a few models that employ data available from multiple literature sources for pyrolysis [6, 22, 23, 26], combustion [30] and gasification [29, 31, 32]. Nevertheless, the most common approach in ANN development remains the employment of one reactor setup for the generation of the data. In the studies where literature data were employed, biomass composition in terms of major constituents (cellulose, hemicellulose, lignin) [6, 22] or proximate and ultimate analysis [23, 26, 29-32] were the main model inputs. Depending on the process and the desired outputs, operational parameters were also introduced as inputs but they were limited in the temperature [23] and heating rate [6] for pyrolysis and in temperature, equivalence ratio [29, 31, 32], gasification agent and steam/biomass ratio [32] for gasification. On a final note, it is interesting to mention that the increasing interest on ANNs within the biomass thermochemical conversion field is manifested by the fact that most of the relevant studies were published after 2015.

The artificial neuron is the base unit of ANNs, in which an array of inputs is fed along with a scalar weight and a bias resulting in a scalar. This scalar is subsequently passed on using an output function. The most common classes of output functions are step, linear (purelin) and sigmoidal (logistic – logsig or hyperbolic tangent – tansig). Multiple neurons can be arranged to generate complex and different architectures. Often, neurons are arranged in layers, where they are placed in parallel, receiving the same inputs but producing different outputs based on the individual weights, biases and transfer functions. The multilayer feedforward (FF) network (MFNN) is a series of neuron layers of which the outputs are used sequentially as inputs to the next layer. Depending on the definition, the inputs of the model can be considered as a layer, while the model outputs constitute the output layer. Any number of layers in the middle are the hidden layers and in general, a network with more than one layer is defined as an MFNN [8]. MFNNs are almost exclusively used in biomass thermochemical conversion ANNs as can be observed in Table 4.1. Alternative architectures are used in some cases [23, 33, 34] with the cascade forward (CF) operation being the most prominent one. In a CFNN, each neuron layer is connected to all the neurons of the previous layers [33]. In terms of network training, supervised training by the means of the Levenberg – Marquardt (LM) backpropagation (BP) method is mostly applied in the context of biomass thermochemical conversion ANNs. The BP algorithm firstly propagates the input forward through the network, secondly propagates also the sensitivities backward through the network (last up to the first layer) and finally updates the weights and the biases using the approximate steepest descent rule [35]. The differences between BP algorithms in general,

lies in the way that the resulting derivatives are used to update the weights [8]. The LM algorithm is an intermediate optimization algorithm between the Gauss – Newton (GN) method and the gradient descent algorithm. On the one hand, the GN algorithm is very fast but very dependent on the initial weights selection. The gradient descent algorithm is less dependent on the initial weights selection, but the speed of convergence is much lower. LM is a hybrid of the two, using gradient descent to improve on the initial guesses for its parameters, before transforming to the GN algorithm once it approaches the minimum of the cost function. At this point it re-transforms to the gradient descent algorithm to improve accuracy [36]. In the context of the present review regarding ANNs for biomass thermochemical conversion, the alternative training algorithms proposed by researchers include two similar methods, namely the Gaussian curve membership function [27] and the chemotaxis algorithm [37]. The latter algorithm, postulates that weight adjustment occurs randomly and follows a multivariate Gaussian distribution with a zero mean and therefore adjusts the weights by adding Gaussian distributed values to old weights [37].

In this work, ANNs were employed for the prediction of the solid, liquid and gas yields from pyrolysis processes. A database was constructed using literature data from pyrolysis experiments, focused solely on batch type reactors. In this context, a wide range of input parameters was selected (lignocellulosic, ash and moisture content, pyrolysis temperature, heating rate, gas residence time, holding time, particle and sample size) and their effect on each product type prediction capabilities as well as the ability of the ANNs to successfully learn the expected trends were evaluated. As it can be also extracted from Table 4.1, ANN models for the prediction of pyrolysis products based on multiple studies from different researchers are scarce in the literature. According to the authors knowledge, the only attempt similar to the one presented in this study was by Merdun et al. [23], since other literature based pyrolysis ANN models focus either on the estimation of kinetic parameters through TGA data or on the char product specifically. However the study of Merdun et al., used a smaller amount of samples and the literature data were limited only on studies conducted in Turkey. Therefore, the applicability of ANNs for a condensed and simplified description of a pyrolysis process is going to be investigated, in terms of both accuracy and scientific meaningfulness using a large amount of input data and parameters.

Table 4.1: Implementation of ANNs for the description of biomass thermochemical conversion processes in literature

#	Thermochemical process	Biomass Type	Architecture	Number of hidden layers	Transfer function	Training algorithm	Output type*	Data sets – Data sources**	Model inputs	Model outputs	Accuracy	Ref.
1	Pyrolysis	Cattle manure	FF	2	n.d.	n.d.	MISO	33	Pyrolysis temperature, heating rate, holding time, moisture content, sample mass	Biochar yield	R ² = 0.804	[5]
2	Pyrolysis	Pine sawdust	FF	1	logsig, purelin	BP/LM	MIMO	14***	Space velocity, pyrolysis temperature, particle size	H ₂ , CO, CH ₄ and CO ₂ selectivity	R ² = 0.999	[25]
3	Pyrolysis	Lignocellulosic biomass (from literature)	FF	1	tansig, purelin	BP/LM	MISO	150 - 28	Cellulose, hemicellulose and lignin content	Pre-exponential factor, activation energy and reaction order	n.a.	[22]
4	Pyrolysis	Durian rinds, Banana peels	FF	2,1	tansig, purelin	BP/LM	MISO	176	Pyrolysis temperature, time	Weight loss	R ² = 0.999	[18, 19]
5	Pyrolysis	Olive oil residue, lignocellulosic forest residue	FF	1,2	tansig, logsig	BP/LM	MISO, MIMO	8000	Heating rate, temperature	Weight loss	n.a.	[20]
6	Pyrolysis	Algal mat	FF	1	tansig	BP/LM	MISO	n.d.	Instantaneous temperature, target temperature, heating rate	Weight loss	R ² > 0.97	[21]
7	Pyrolysis	Various (from literature)	FF	1	tansig	n.d.	MIMO	163	Cellulose, hemicellulose and lignin content, heating rate	Pre-exponential factor, activation energy and reaction order	R ² > 0.81	[6]
8	Pyrolysis	Various (from literature)	FF, CF	2	logsig	BP/LM	MIMO	72 – 44	Moisture, volatile, fixed carbon, ash, C, H, O, N contents, HHV,	Char, liquid and gas products	RMSE = 5.71 – 9.16	[23]

9	Pyrolysis	Cotton, tea, olive and hazelnut	FF	1	logsig, tansig	BP/ Gradient descent with adaptive learning	MIMO	18	heating rate, temperature Lignin, cellulose, hemicellulose, fixed carbon, volatile, moisture and ash contents, temperature	Char, liquid and gas products	R ² = 0.99	[24]
10	Pyrolysis (carbonization)	Various (from literature)	FF	1	tansig, purelin	BP/LM	MISO	168 - 20	C, H, O content, fixed carbon, volatile matter and ash content, carbonization temperature and time, activation temperature, time and steam to biochar ratio	Activated carbon yield and BET surface area	R ² > 0.92	[26]
11	Combustion	MSW – coal mixture	FF	1	tansig, purelin	BP/LM	MISO	2200	Feeding rate, temperature, change rate of temperature, outlet gas temperature, steam flow, temperature and pressure, primary and secondary air flow	Heating value	n.a.	[38]
12	Combustion	Various (from literature)	FF	1	tansig, purelin	BP/LM	MISO	100 - 34	Fixed carbon, volatile and ash contents, O ₂ concentration and equivalence ratio	Pre-exponential factor, activation energy and reaction order	R ² > 0.94	[30]
13	Gasification	Woody biomass (from literature)	FF	1	tansig, purelin	BP/LM	MISO	18, 36 – 2, 4	Moisture, ash, C, H and O content, gasification temperature and equivalence ratio	Product gas composition (CO, CO ₂ , CH ₄ and H ₂) and total gas yield	R ² > 0.98	[31]
14	Gasification	n.d.	n.d.	n.d.	n.d.	Gaussian curve membership function	MISO, MIMO	600****	Fuel flow, air flow, time from last fuel supply and syngas temperature	Temperature and product gas composition (CO, CO ₂ , CH ₄ and H ₂)	n.a.	[27]
15	Gasification	Poplar sawdust, pine saw-dust, comminuted sugar cane bagasse and cotton stem	FF	1	logsig, n.d.	Chemotaxis algorithm	MISO	7 or 6****	Bed temperature and gasification time	Product gas composition (CO, CO ₂ , CH ₄ and H ₂) and total gas yield	n.a.	[37]
16	Gasification	n.d.	FF, CF	1, 2	tansig, logsig, purelin	BP/LM	MISO	213	C, H, O, moisture and ash content, equivalence ratio, reaction temperature, steam/biomass ratio and bed material	Product gas composition (CO, CO ₂ , CH ₄ and H ₂) and total gas yield	R ² = 0.9394 – 0.9734	[33]
17	Gasification	Sawdust, coconut shell, coffee husk, sugarcane bagasse and ground nutshell	FF	1	tansig, purelin	BP/LM	MIMO	70	C, H, O, moisture and ash content, equivalence ratio and reaction temperature	Product gas composition (CO, CO ₂ , CH ₄ and H ₂)	R ² = 0.987	[39]
18	Gasification	Wood sawdust	FF	1	tansig, tansig	BP/LM	MISO, MIMO	n.d.	Equivalence ratio, steam to biomass ratio and axial position in the reactor (only for the temperature model)	Gasification temperature and product gas composition (N ₂ , CO, CO ₂ , CH ₄ and H ₂)	R ² = 0.968	[28]
19	Gasification	n.d.	FF	1	tansig, purelin	BP/LM	MISO	63 – 18	C, H, O, moisture and ash content and reduction zone temperature	Product gas composition (N ₂ , CO, CO ₂ , CH ₄ and H ₂)	R ² > 0.98	[40]
20	Gasification	MSW	FF	2	tansig, logsig, purelin	BP/LM	MISO, MIMO	67	C, H, O, N, S, moisture and ash content, equivalence ratio and gasification temperature	LHV and LHV _g of product gas and product gas yield	R ² > 0.98	[41]
21	Gasification	MSW	FF	1	tansig, logsig, purelin	n.d.	MIMO	91	Percentages of wood, paper, kitchen garbage, plastic and textile in the samples, equivalence ratio, temperature	LHV of gas, LHV of gasification products, gas yield	Relative error: 8.7 – 22.3 %*****	[42]
22	Gasification	Various (from literature)	FF	1	tansig	n.d.	MISO, MIMO	181 – 21	Moisture, ash, volatile, C, H and O content, equivalence ratio, steam/biomass ratio, temperature and gasification agent	H ₂ , CO, CH ₄ , CO ₂ and C ₂ H ₆ yields	Pearson R – correlation: 0.98 – 0.99	[32]
23	Gasification	Pinecone, wood	FF, CF, Time-delay, Elman, NARX	1	tansig	BP/LM	MIMO	3831	Temperature distribution, Equivalence ratio, air flow rate, C, H, O, N, Moisture, Volatile, Fixed Carbon, Ash contents	CO, CO ₂ , CH ₄ , H ₂ yields and LHV _{gas}	R ² > 0.98	[34]
24	Gasification	Various (from literature)	FF	1, 2	tansig, logsig, purelin	BP/LM	MISO	120 – 16	C, H, O, moisture and ash contents, equivalence ratio, temperature	Total tar concentration (including benzene)	R ² > 0.96	[29]

*The output type refers to multiple input – multiple output (MIMO) or multiple input – single output (MISO) models

**In case the data were obtained from literature, the data sources number corresponds to the number of studies used. The data sets include the training, validation and testing sets.

***The number of data sets was not explicitly mentioned in the study. It was calculated by the authors by adding the data points of each input variable (5, 6 and 3 respectively).

****Experimental data from five gasification experiments were used for a total time of 60 min with a sampling interval of 30 s.

*****Separate models were built for each biomass specie and each gaseous compound studied.

*****The relative error was calculated as the predicted value minus the experimental value, all divided by the experimental value

4.2 Methods

4.2.1 Database development

The experimental data required for the development of the ANN model within this work, were extracted from literature studies focused on biomass pyrolysis according to the following two criteria. Firstly, most of the selected parameters (Table 4.2) need to be reported in the study. Secondly, parameters necessary for the database, but not reported in the study can be reasonably estimated through data from the study itself or external sources. An example of the latter was the derivation of the cellulose, hemicellulose and lignin content from the Phyllis2 database [43] when they were not reported in the selected study. Gas residence time is another parameter, that although it plays a significant role in a pyrolysis process, it is seldom reported in the relevant studies. For this purpose, when necessary, its value was calculated based on the reported reactor volume and the gas flow rate of the purging gas. Of course, in this case the impact of the release of volatiles during pyrolysis was neglected.

The parameters reported and therefore extracted from the literature sources, are summarized in Table 4.2, along with their respective range. The complete database is provided in the supplementary information.

Table 4.2: Biomass pyrolysis experimental parameters obtained from literature sources, which were included in the database, serving as inputs and outputs of the developed ANN model respectively.

Inputs		Outputs	
Parameter	Range	Parameter	Range
Cellulose content (wt % a.r.)	0 – 90.5	Char yield (wt % a.r.)	0 – 98.9
Hemicellulose content (wt % a.r.)	0 – 95.3	Liquid yield (wt % a.r.)	0 – 81.5
Lignin content (wt % a.r.)	0 – 93	Gas yield (wt % a.r.)	1 – 69.5
Ash content (wt % a.r.)	3 – 21		
Moisture content (wt % a.r.)	0.1 – 23.5		
Pyrolysis temperature (°C)	227 – 1129		
Heating rate (Ks ⁻¹)	0.12 – 10000		
Gas residence time (s)	0 – 4803		
Holding time (s)	0 – 3600		
Average particle size (mm)	0.035 – 17.5		
Sample size (mg)	0.2 – 250000		

From Table 4.2, it is apparent that a wide range of biomass feedstocks as well as experimental conditions was studied. This choice was made to evaluate the (inherent) applicability of ANN models for a wide range of biomass feedstocks and operating conditions. With respect to the latter, as it is evident from the ranges of the heating rates, gas residence and holding times, both slow and fast pyrolysis processes were taken into consideration. When it comes to the reactor type, the only type that was explicitly excluded from the investigation were continuous feeding reactors, thus such reactor-based studies were removed from the database. The significant differences in the definition of the aforementioned parameters (e.g. heating rate, holding time, etc.), would render the introduction of such setups problematic for the development of the ANN model. Some operational

parameters are either not applicable in a continuous process or their estimation would require delving into uncertain assumptions regarding transport phenomena and devolatilization behaviour in a system. For example, the heating rate, in most cases is irrelevant for continuous processes operating in a steady state temperature and it concerns mostly the heating rate of each particle. The holding time can also not be easily defined in a continuous pyrolysis process, since it required extensive knowledge of a feedstocks devolatilization behaviour. To correctly define or assume values of such operational parameters, the knowledge of additional parameters such as the particle size and the residence time distributions would also be required. Furthermore, the amount of data available for batch – type setups was significantly larger compared to continuous systems. The inclusion of continuous setups would be possible if certain operational parameters were removed. However, the choice was made to rather differentiate between the two reactor categories, although this way high throughput systems are excluded from the study (large scale reactors are typically continuous). Regarding the average particle size, this value was calculated (when not reported explicitly) according to the upper and lower values of the sieves used. The selected studies along with the respective biomass types are presented in Appendix B. Each study was assigned an ID number with which they will be referred with in this work. The database includes in total 482 data points.

The char, liquid and gas yield of the pyrolysis process, were selected as the outputs of the ANN model. The char yield refers to the solid residue of the pyrolysis process, therefore including ash if present. The liquid yield, in the context of the present database and model, includes all the condensable pyrolysis products including water. For this purpose, when the water produced from the pyrolysis was mentioned separately in a study it was added to the total liquid product. Otherwise, it was considered part of it unless explicitly mentioned. Finally, the gas yield refers to the total amount of non-condensable gases produced from the pyrolysis process. All the respective yields were converted to a wt% ar basis, according to the data provided in each study.

At this point, it should be mentioned that significant discrepancies might arise from the incorrect employment of different bases (ar, db and daf) and conversion between them, in the expression of experimental pyrolysis product yields. This issue was encountered in the construction of the present database, but it can also have important implications for the comparability of different literature studies that focus on the determination of pyrolysis product yields both in terms of classes (gas, liquid, solid) and specific compounds (tars, gases, etc.). Such discrepancies reduce the scientific accuracy and therefore the value of several studies and hinder significantly the development of a comparative review or of a predictive model for biomass pyrolysis.

The use of different bases of analysis, is typically meant for the expression of the composition of a fuel in an as – received (ar), air – dry, total – dry (db) or dry and ash – free (daf) basis. This allows the easier comparison of different fuels with respect to their volatile matter and fixed carbon content. The problem arises when such bases are used for the expression of the product yields of in this case pyrolysis. When the gravimetrically or volumetrically measured products are expressed on a db or daf basis without the simultaneous subtraction of the moisture and regarding daf also ash content from the respective products, the mass balance closure values must add up to more than 100 %. This issue does not often manifest for two reasons. Firstly, incomplete experimental mass balance closures, which are often the case, can compensate for the overestimation of these products. Secondly, another common practice in the literature, the calculation of a product class by difference when the other two classes' yields are measured also masks such discrepancies. In the context of the present work, only two studies in which the mass of ash and moisture of the initial sample were explicitly subtracted from the solid and the liquid product respectively, were found [44, 45]. This method assumes that all of the ash of the initial sample ends up in the solid product, as does the moisture in the liquid and in general can be viewed as a fair assumption. However, one should keep in mind that depending on the

temperature, volatile ash can also end up in the liquid product [46], while moisture could remain in the vapour phase and be collected along with the gases.

The ambiguities arising from the abovementioned different approaches regarding the expression of pyrolysis product yields can easily be bypassed by the authors stating firstly the calculation procedure followed for the conversion to db or daf basis as done for example by Park et al. [44] and Lee et al. [45]. Furthermore, it is essential for the authors to always provide the moisture and ash values necessary for the conversion to the basis used. Surprisingly, these values are frequently not provided [46-51]. Finally, closing the mass balances by difference often masks intrinsic mass losses of the apparatus used, but this can also lead to incorrect conclusions and misplaced amounts of mass in certain product yields. This practice was noted in literature more widely, especially for the gas yield [49, 52-56], and can have a negative influence on model development but also scientific accuracy.

4.2.2 ANN development

Keras, a high-level Python based neural network application programming interface (API), was chosen as the main tool for the design of the ANN model. *Keras*' high degree of flexibility and ease of use were the main reasons behind this choice. *TensorFlow* was used as backend, handling low level operations such as tensor products, convolutions, etc. For the training of the models *Adam* was used, which is a backpropagation algorithm for first-order gradient-based optimization of stochastic objective functions [57]. *Adam* performed better than other algorithms tested (*RMSprop* and the stochastic gradient descent) and, in general, it is well suited for large data and parameter applications. Furthermore, hyperparameters (the model parameters controlling the learning process) have intuitive interpretations leading to fewer tuning requirements. With respect to the testing set, it consisted of studies that were excluded from the training of the network, representing a wide range of input space. In particular, the references with IDs 6, 17, 28, 30, 36, 37 and 38 were used, which in total contribute to 11 % of the entire dataset. In general, in the samples selected for the sensitivity analysis there is a lower contribution of fast pyrolysis samples. Sample 17 is indeed corresponding to fast pyrolysis, as well as 28 and 30, however the latter two are rather on the limit with slow pyrolysis. Unfortunately, this is representative of the amount of fast pyrolysis studies present in the total database itself, which is indeed somewhat lower compared to slow pyrolysis. It should also be mentioned that it is not possible to take specific samples out of a study and use them as part of the testing set as this would skew the analysis by making us obtain artificially good performance.

In total, three different ANN models were developed, each corresponding to each pyrolysis product class studied (char, liquid and gas yield), following a MISO approach. Each of the ANN models developed was a feedforward network consisting of three layers: the input layer, one hidden layer and the output layer. The number of neurons in the hidden layer of each model was determined through a trial-and-error optimization process. The transfer functions employed were hyperbolic tangent. To prevent overfitting, Gaussian noise was added to the connection weights of the inputs during training. As long as the amount of added noise is contained, it can lead to better generalization, since the network becomes less prone to memorization of the data points [58, 59]. For the same purpose, dropout was also employed. The key idea of this technique is to randomly drop neurons (along with their connections) from the network during training. During testing, the full network is used, albeit with the connection weights scaled down by the retention probability for the related unit, in order to compensate for the higher number of neurons [60]. Both the noise standard deviation (σ) and the dropout probability (p) were determined during the optimization of the network's hyperparameters.

Features of the database, namely the inputs: heating rate, gas residence time, holding time, average particle size and sample size, have values that span over multiple orders of magnitude. To

emphasize the order of magnitude of the features and avoid non-meaningful representation, the features were passed through a base 10 logarithmic function (Eq. 1), modified to account for the possibility of 0 values. In (Eq. 1), x is the original value of the feature and x_{low} is the lowest value in the dataset for this specific feature, excluding zero.

$$f(x) = \begin{cases} \log_{10}(x), & \text{for } x \geq x_{low} \\ \log_{10}(x_{low}) - 1, & \text{for } x = 0 \end{cases} \quad (\text{Eq. 1})$$

The first step was the scaling of the database input and output values to zero mean and unit variance using (Eq. 2), where x stands for each value of the feature, μ is the average of the feature being scaled and σ is its standard deviation. This equation is also used for the inverse transformation of the outputs, by solving for x .

$$z = \frac{x - \mu}{\sigma} \quad (\text{Eq. 2})$$

The scaling operation, although not necessary, prevents the network from having to learn how to adjust the weights of the connections to cope with the different magnitudes of the features described [61]. The weights of the connections are randomly initialized by selecting them from a normal distribution with zero mean and 0.05 standard deviation. Scaling provides a tangible performance boost, by reducing the amount of epochs required by the model.

Concerning the input layer of the ANN model, the high degree of correlation between heating rate and sample size, led to the decision for the removal of the latter from the list. This choice was made using mostly qualitative criteria, since the meaningfulness of the correlations was not evaluated using hypothesis-testing methods. This correlation is presented and analysed in section 3.1 more extensively. This choice limits the flexibility of the model in possible future iterations with additional data; however, it is appropriate in the context of the present database. In general, there is a trade-off when the inputs of an ANN model are selected. A high number of inputs and therefore a high number of free parameters, makes overfitting more likely to occur. On the other hand, reducing the number of inputs may lead to loss of information and consequently impaired prediction capability. In this work, two different approaches regarding the input features of the model were followed. The first one was to include all the possible (10, excluding the sample size) pyrolysis parameters as inputs of the model. The second one was to build a “reduced” inputs model, including only the parameters that showed the highest influence on the network. This selection was carried out by performing two kinds of tests (hereby called *powerset* and *sequential*), as described in [61]. From this procedure, only temperature was excluded since it was considered a fundamental predictor both in a conceptual way (related to the pyrolysis process) but also due to its high degree of correlation with the products as it was evident by the analysis of the database (Section 3.1).

A *powerset*, which is the set of all the possible subsets of the database features, was used to test every possible input combination for each the three networks (char, liquid and gas). To perform this test, five ANN models were trained for each combination of inputs and then tested on different portions of the database according to a five-fold cross validation procedure. The mean squared error of the validation set, which was selected as the performance metric, was averaged and recorded for each input combination. From this analysis, the heating rate emerged as a strong predictor for the models, scoring consistently low MSE values, followed by the particle size. This result was highly expected, given the heating rate’s primary role in a pyrolysis process. In the sequential test, temperature and heating rate were considered as fundamental predictors, meaning that they were always included in the network’s inputs. For this testing, the remaining candidate inputs were

introduced one by one, cyclically to the list of inputs. Five ANN models were trained in the same way as it was described for the *powerset* test. For each cycle, the MSE for the inclusion of each input was recorded and the one that scored the lowest was added to the list of inputs. The cycle was repeated until the depletion of the input candidates. The results of the sequential test were evaluated using a simple order-to-score assignment. The three top scoring parameters for each one of the three networks were selected for the reduced versions of the ANNs along with the temperature and the heating rate and they are presented in Table 4.3. The values of the hyperparameters used in both the *powerset* and sequential tests are mentioned in Appendix B.

Table 4.3: Results of the sequential test. The parameters are reported in descendent order of strength as predictors.

Char		Liquid		Gas	
<i>Parameter</i>	<i>Score</i>	<i>Parameter</i>	<i>Score</i>	<i>Parameter</i>	<i>Score</i>
Lignin	152	Lignin	170	Gas residence time	170
Ash	112	Particle size	124	Moisture	130
Particle size	100	Cellulose	79	Particle size	110

Lignin (content) was found to be the strongest predictor for both the char and the liquid ANN models. Lignin can be considered as the main source of char formation for biomass materials pyrolysis as it has also been reported in the literature [62, 63]. However, the effect of lignin in the prediction of the liquid yield can be viewed as an indirect effect of its influence on the char yield. Ash content, which is the second stronger predictor for the char model, is also positively correlated with char formation due to its presence in the solid residue in general. Particle size was a strong predictor for all three models. A small value of particle sizes favouring volatile production, has the opposite effect on char production and is in general a crucial factor in a pyrolysis process due to its effects on heat and mass transport phenomena [64, 65]. The cellulose content of biomass mainly contributes to volatiles formation [66], so its presence in the list of strong predictors for the liquid model can be explained. Gas residence time scored higher than all parameters for the gas model. Long gas residence times, favour secondary tar cracking thus yielding higher gas yields [2]. However, the qualification of moisture as a strong predictor for the gas model can be viewed as a surprise. Moisture, on the one hand, can contribute to the formation of smaller molecules via hydrolysis and reforming reactions, however other parameters such as the lignocellulosic content for example, were expected to have a bigger impact on the gas yield. A possible explanation could be that the model sees an indirect correlation between the liquid yield and moisture and this is passed on to the gas model. Nevertheless, as it was also mentioned in the previous chapter, the calculation of the gaseous yield by difference, adds a certain degree of unreliability to parts of the database that correspond to these particular measurements.

4.3 Results and discussion

4.3.1 Analysis of literature data

To identify trends in the available data regarding both input and output parameters, 2D scatter plots of all the possible combinations were generated. Additionally, the Pearson's correlation coefficient (R) values of the distributions were calculated. The purpose of this process was to validate the database by identifying trends known from the literature, as well as provide some feedback for the development of the ANN model. It should be noted, that while high R values do identify correlations, low R values do not exclude them in the particular case studied. During biomass pyrolysis a wide variety of parameters influence the process and its yields, therefore the correlation between just two of them may not always be direct. Finally, as it was also mentioned in Section 2, hypothesis – testing methods need to be employed to fully evaluate the quality of the correlations.

Regarding correlations between inputs and outputs, the one between char yield and gas yield with temperature was the most obvious. Figure 4.1 shows that with increasing temperatures the char yields decrease, in contrast to the gas yield. Both trends have been well established in literature [67-69]. As for the relationship between temperature and the liquid yield, the correlation becomes more evident with the removal of part of the dataset and in particular of the values corresponding to ID 34 [70]. In this work, a wide set of conditions is studied, with temperatures ranging between 300 and 1100 °C and heating rates between 100 and 10000 Ks⁻¹. Along with the large amount of data points from this study (97), this wide range of conditions on the one hand helps to expand the input domain of the database and the corresponding ANN model. On the other hand, it does not allow this particular 2D visualization by skewing it significantly. By removing reference 34 from the data set and using a locally weighed linear regression fit, a trend showing the liquid yield increasing until a temperature of 550 °C before decreasing emerges. This behaviour is consistent with secondary tar cracking as it has been described in literature [67, 71, 72].

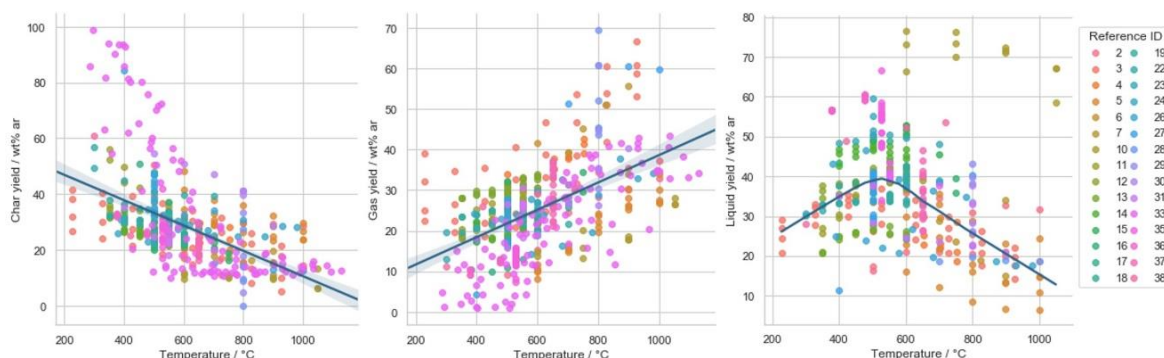


Figure 4.1: Char yield (left), gas yield (middle) and liquid yield (right) over temperature for the pyrolysis experiments database, excluding reference with ID 34 for the liquid product. Linear regression along with 95 % confidence interval is shown for char and gas ($R = 0.5226$ and $R = 0.5376$ respectively) and a locally weighed linear regression for the liquid.

From this analysis of the database interesting correlations can also arise between inputs. An example is presented in Figure 4.2, where the sample size is plotted against the heating rate with a high value of R (0.9293). The trend shown does not represent a causal relationship between the two parameters, but it rather shows that usually fast pyrolysis experiments are conducted with small samples sizes, while the contrary holds for slow pyrolysis experiments. This observation has a two-fold effect on the ANN model development. Firstly, it assists in defining the boundaries of the input space since by showing that the network has little or no information on how to behave in the case of slow pyrolysis with small sample sizes or fast pyrolysis with big sample sizes. Furthermore, the strong

correlation between the two parameters indicates that they contain the same redundant information in the context of the database. Similar correlations were found between heating rate and particle size and gas residence time, although to a lesser extent (R values of 0.6615 and 0.4587, respectively).

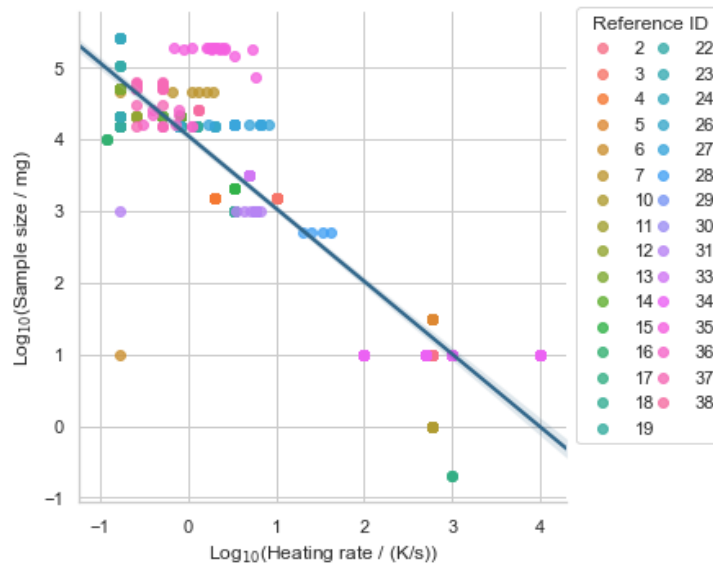


Figure 4.2; Logarithmic plot of sample size over heating rate. Linear regression along with 95 % confidence interval is shown (R = 0.9293).

4.3.2 ANN results

4.3.2.1 Full and reduced models performance

The optimal values of the hyperparameters obtained through the optimization process are presented in Appendix B, while the values of weights and biases for the hidden and output layers are included in the supplementary information. Furthermore, the analysis and presentation of the results was performed with root mean square error (RMSE) as a metric. However, to facilitate comparison with other models, the corresponding R^2 values are also presented in Appendix B.

The reduced char model (Figure 4.3), using temperature, heating rate, lignin content, ash content and particle size as input parameters, performed better compared to the full model in the prediction of the char yield (root mean square value of 5.1 wt% ar versus 5.9 wt% ar). In general, char constituted the product for which the best estimations were achieved for both types of models used. The fact that the reduced model performed better, supports the argument that a reduced representation of data can lead to better results due to improved generalization capabilities. Among the data points used in this ANN's testing, 38a1 appears to be the main outlier. The high magnitude of the error for this point can be attributed to the combination of an especially large particle size (10 mm), a very low pyrolysis temperature (300 °C) along with a value of heating rate which lies in the margin between slow and fast pyrolysis (80 Kmin⁻¹). This combination makes this point stand out among the rest, making it difficult for the ANN to successfully predict the value. Similar high error values were obtained for this data point also in the full char ANN.

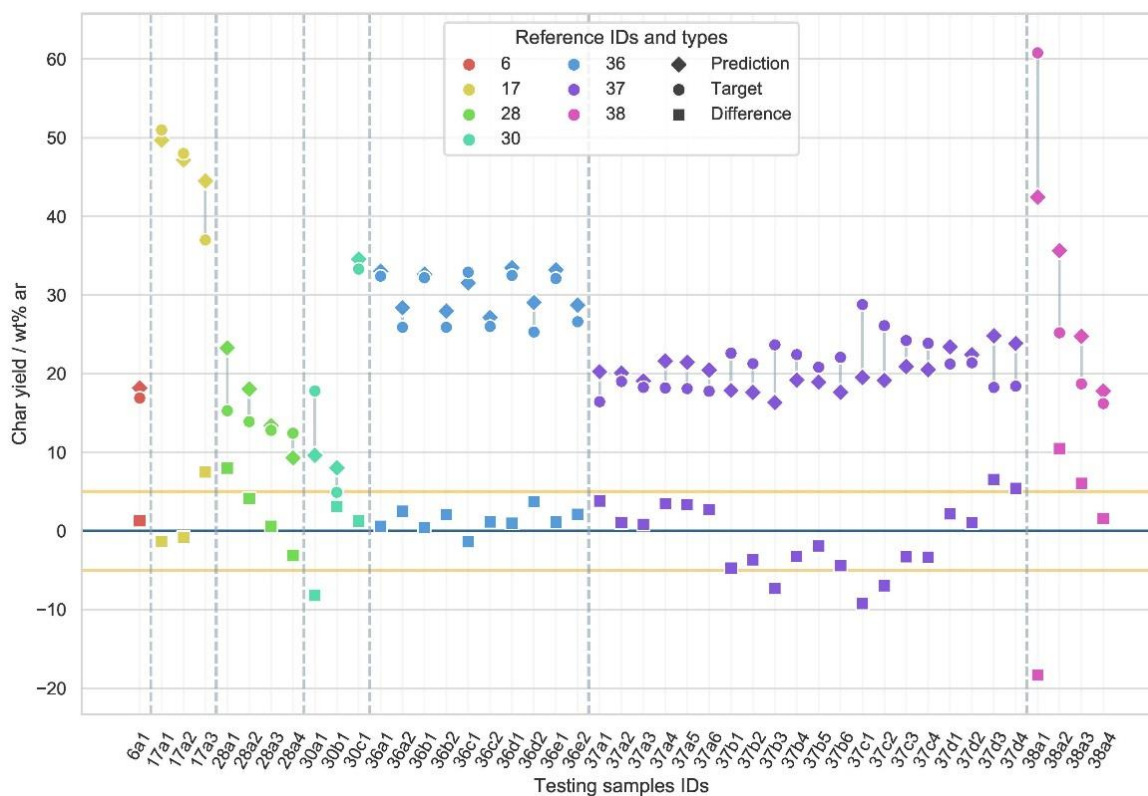


Figure 4.3: Performance of the reduced char ANN over the test set. Predictions of the networks are shown alongside the targets for each single sample in the test set. Indicative boundary lines are shown ± 5 wt% ar around the zero line.

To evaluate the influence of each parameter on the best performing networks behaviour, a sensitivity analysis was performed by varying each one while keeping the rest unaltered. The purpose of this sensitivity analysis is mostly to signify the importance of analysing the performance of an ANN not only in terms of the RMSE values obtained but also on whether it is able to indeed “learn” the required scientific correlations from the inputs. For this analysis, eight specific samples from the testing set were used, each representing different conditions and combinations. In particular, 17a1 corresponds to a sample with a high ash content that underwent fast pyrolysis at a very high heating rate ($1000 \text{ }^\circ\text{C s}^{-1}$), while 28a1 and 28a4 differ in terms of pyrolysis temperature ($700 \text{ }^\circ\text{C}$ and $1000 \text{ }^\circ\text{C}$, respectively). Samples 36a1 and 36c1 correspond to low pyrolysis temperature ($377 \text{ }^\circ\text{C}$) with different particle sizes (0.3 mm versus 5 mm). Finally, 37b3 has a lower lignin and higher cellulose content than 37c1 and 37c3, while the latter two differ in terms of heating rate (0.25 K s^{-1} versus 0.5 K s^{-1}). The results of this analysis are presented in Figure 4.4 and as can be observed, char yield values decrease with increasing temperature. An increase of the lignin and ash content also appears to lead to an increase of the char yield, as it is the case for increasing particle sizes, although to a lesser extent. The latter can be seen as a surprise, since a more intense correlation was expected between char yield and particle size. A positive correlation between the heating rate and the char yield was also established. Although it is difficult to examine the effect of heating rate irrespectively of the rest of the pyrolysis conditions, generally slower heating rates favour char production [73]. However, faster heating rates can also be linked to lower conversion levels, thus leading to an increase of the solid residue yield, which apart from char can also contain some unreacted volatiles, which rather contradicts the previous statement. Of course, it is difficult to say whether the ANN shows this behaviour due to the aforementioned reason. In general, it appears that the reduced char ANN reproduces the trends established by literature successfully. Similar trends were observed also in the corresponding analysis of the full char ANN, however some overfitting behaviour was presented for the cases of ash content and particle size.

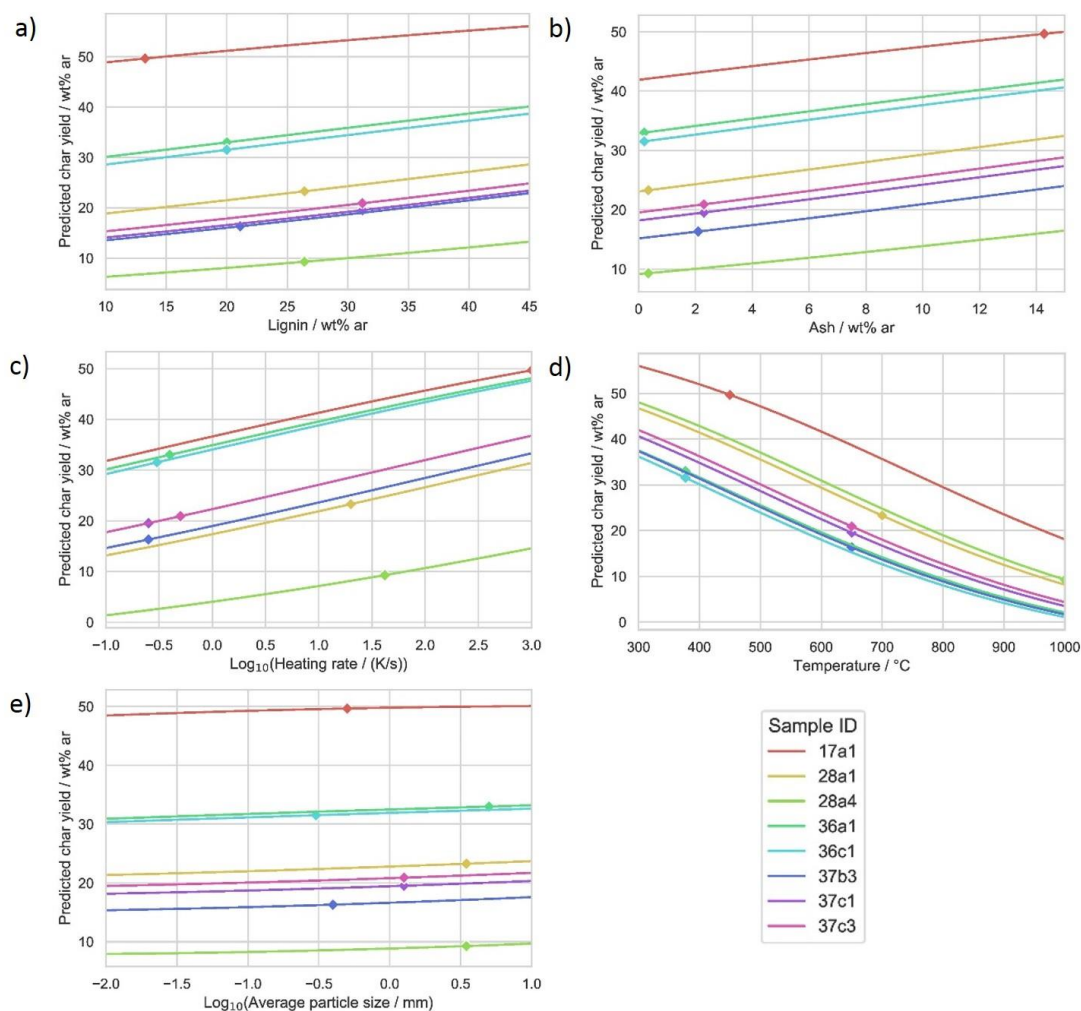


Figure 4.4: Predictions of the reduced char ANN for varying values of lignin (a), ash (b), heating rate (c), temperature (d) and average particle size (e) for specific test samples.

In the case of the liquid model, the full version (Figure 4.5) performed significantly better (RMSE of 6.9 wt% ar) compared to the reduced one (RMSE of 9.3 wt% ar) with temperature, heating rate, lignin and cellulose content and particle size as inputs. For the liquid models, being the worst performing ones among the three, the loss in generalization performance by the addition of the extra inputs in the full model was compensated by the amount of information added. The same kind of analysis as in the case of the reduced char model presented above, was also conducted for the full liquid model, using the same samples from the database. As can be seen in Figure 4.6, the full liquid ANN was able to correctly learn the correlation between temperature and liquid product yield. For each of the samples tested, the liquid product maximum yield was obtained in the temperature range 400 - 600 °C. The behaviour of the heating rate was diverse on the other hand. Figure 4.6 b shows that all the samples apart from 36a1 and 36c1 point to a positive correlation between heating rate and liquid yield. Similar results were obtained also for the rest of the parameters used as inputs for the liquid model, with possible overfitting being encountered for some of them.

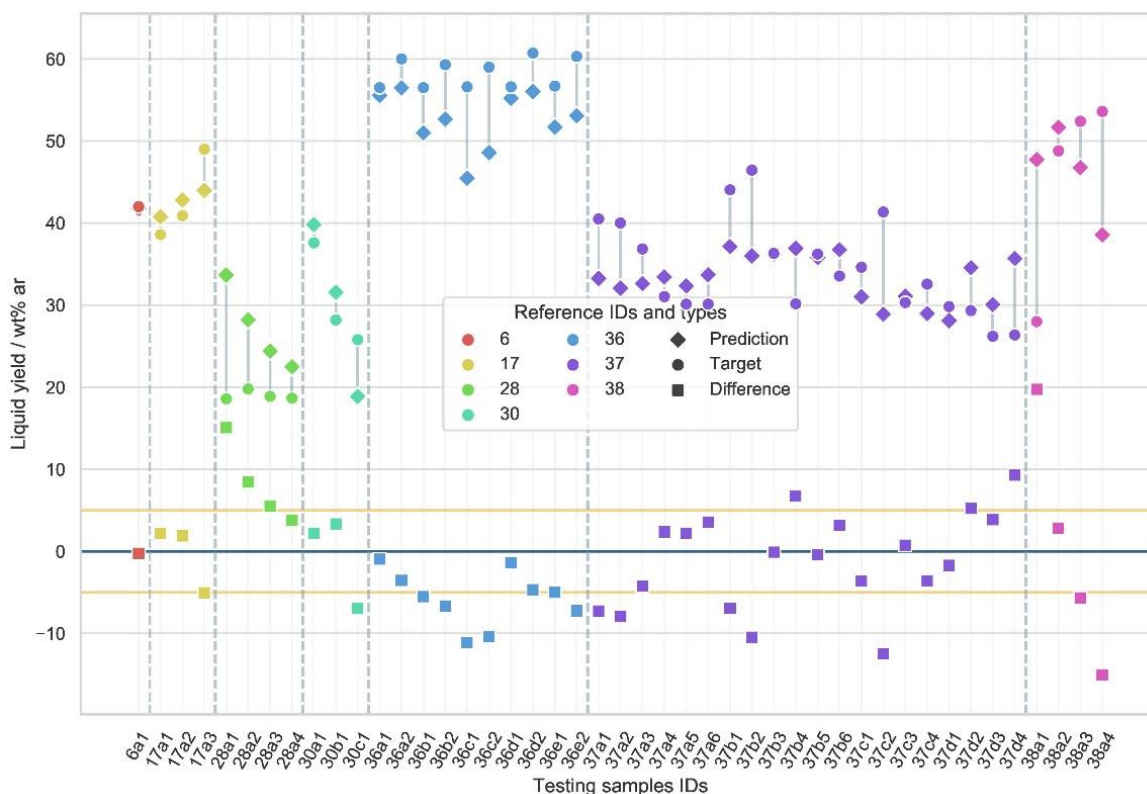


Figure 4.5: Performance of the full liquid ANN over the test set. Predictions of the networks are shown alongside the targets for each single sample in the test set. Indicative boundary lines are shown ± 5 wt% ar around the zero line.

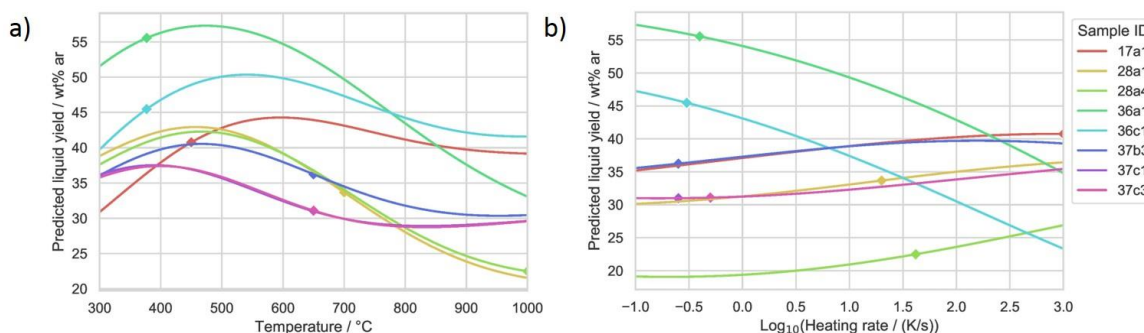


Figure 4.6: Predictions of the full liquid ANN for varying values temperature (a) and heating rate (b) for specific test samples.

Regarding the gas prediction models, the reduced version (temperature, heating rate, moisture content, gas residence time and particle size) produced a RMSE of 5.6 wt% ar (Figure 4.7), which was slightly better compared to the full version (RMSE of 6 wt% ar). In Figure 4.7, for the reference with ID 36, the variation of the gas yield values due to the heating rate alternating between 0.4 Ks^{-1} and 0.8 Ks^{-1} was correctly predicted. However, this behaviour was not successfully generalized as apparent from reference ID 37. For this reference, data points a1, a2, a3, b1, b2, b3, c1, c2, d1 and d2 correspond to a heating rate of 0.25 Ks^{-1} while the rest relate to 0.5 Ks^{-1} . From the results, it can be concluded that the heating rate variation does not affect the prediction significantly. Furthermore, by observing Figure 4.8 b, it is apparent that while for slow heating rates the positive correlation with gas yields is properly established, the trend stops and reverses for faster heating rates. This probably indicates the need for the inclusion of more fast pyrolysis experiments in the database. Another interesting

observation can be made for the poor performance of samples 30b1 and 30c1, which correspond to pure cellulose and lignin pyrolysis experiments, respectively. This poor prediction stems from the fact that lignocellulosic content is not an input for the reduced gas network. For sample 30a1 (pure xylan), the good prediction can be attributed partly to chance and also to the fact that hemicellulose in general is not predominantly linked to the formation of particular product classes, contrary to cellulose and lignin [74]. It is interesting to note, that even though the full network performed slightly worse overall, it was more successful at the prediction of the ID 30 samples. This observation shows that despite the reduced accuracy of the full gas model, the inclusion of certain parameters leads to correct learning behaviour. Finally, through Figure 4.8 a, it is possible to affirm that the expected behaviour of the gas yield rising for increasing temperatures was correctly predicted, at least qualitatively.

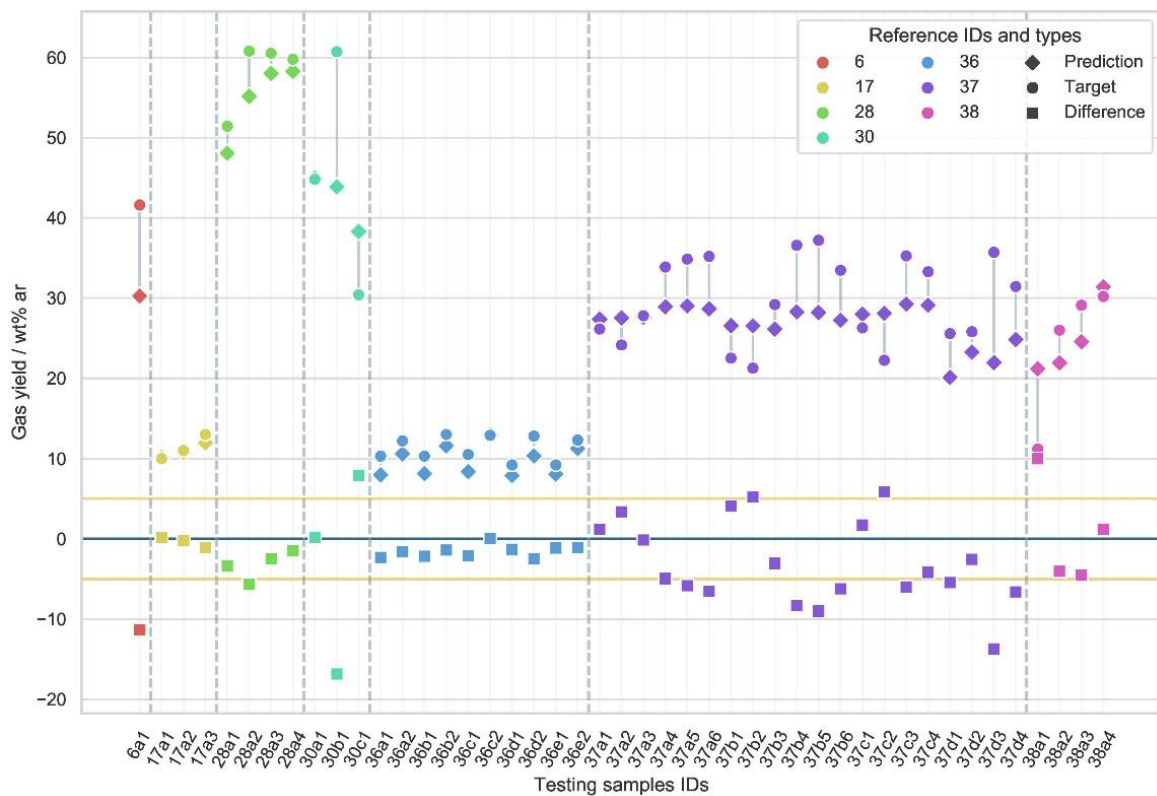


Figure 4.7: Performance of the reduced gas ANN over the test set. Predictions of the networks are shown alongside the targets for each single sample in the test set. Indicative boundary lines are shown ± 5 wt% ar around the zero line.

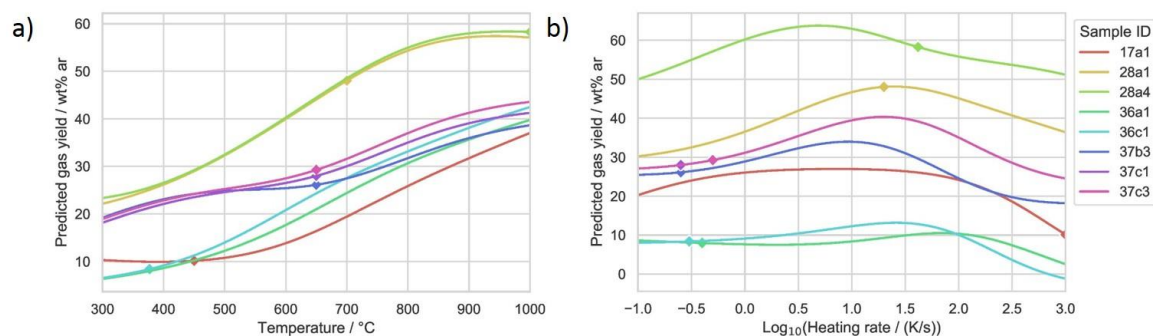


Figure 4.8: Predictions of the reduced gas ANN for varying values temperature (a) and heating rate (b) for specific test samples.

On a general note, the superior performance of the char models can be attributed to the higher reliability of the char yield measurement from a slow or fast pyrolysis lab scale experiment. The char yield typically consists of the residual mass in the reactor after the completion of the experiment, along with what is captured in a particle separator, cyclone or filter if one of these methods is employed [75]. It can therefore be argued that there is a higher consistency and intrinsic accuracy in the measurement of the char yield compared to the gaseous and liquid yields, for which several different methods are employed in the literature. Especially in the measurement of the liquid products, several methods exist in the literature for its quantification. The various methods employed include different sampling train configurations, solvents (and solvent evaporation methods) used, temperatures under which the sampling takes place, as well as different types of detectors used for the detection and quantification of certain compounds [75, 76]. The lack of robust guidelines for the measurement in the liquid product from small scale pyrolysis experiments, as is the tar protocol for larger setups [77], can lead to significant discrepancies between studies. Additionally, the previously mentioned approach of calculating one of the product classes' yield by difference can lead to similar results. Lastly, it should be mentioned, that the networks that have been obtained in this work, are mutually independent and possess no information regarding the mass balance over the three products. Therefore, the sum of the predictions of the three models do not add up to 100 %. However, it is possible to add the average mass closure of the training set in the model, by normalizing the results of each product with it. This can lead to marginal improvement of the predictions for the liquid and gas products, but not for the char. The description of these ANNs was omitted for brevity.

4.3.2.2 *Char as an input feature*

From the previously presented results, it became obvious that the char models were the best performing ones among the ANNs developed. This fact, along with the higher inherent accuracy of char measurements from pyrolysis experiments, led to the decision of the inclusion of char as an input to the liquid and gas ANN models. For this purpose, the full liquid and the reduced gas ANN were trained with char (experimentally derived) as an additional input. It should be mentioned, that for the generalization and refinement of the conclusions derived from this particular approach the powerset and sequential tests would have to be repeated. Furthermore, correlations between the char yield and inputs such as the temperature and the heating rate might exist that make the use of them redundant in the context of the information fed into the ANN models. However, such an investigation was outside the context of the present work.

This move led to significantly improved predictions for both models. More specifically the RMSE of the full liquid ANN improved from 6.9 wt% ar to 5.5 wt% ar and the reduced gas ANN from 5.6 wt% ar to 4.9 wt% ar. As can be seen in Figure 4.9, the variation of both yields over the char yield, shows a negative correlation between them. This was certainly expected, since increasing char yields are usually accompanied by decreasing volatile production in thermochemical processes in general. The results obtained from those models fall very consistently within ± 25 % accuracy boundaries and the difference between the measured and predicted yields is also consistently less than 10 wt% ar, making them comparable to the results of Neves et al. [75]. In the aforementioned work, a model for the prediction of pyrolytic volatiles was developed employing a system of equations where elemental and energy balances are combined with empirical parameters. For this work char was also used as an input parameter, however only the results of one study were used for the testing of the model.

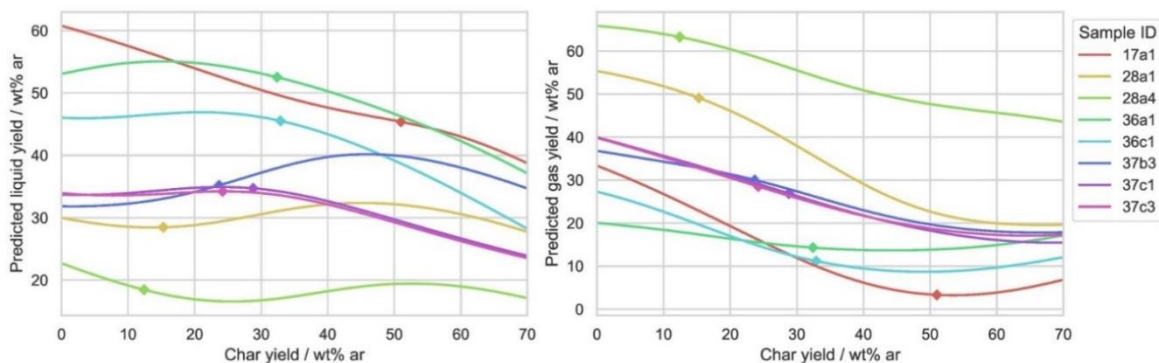


Figure 4.9: Predictions of the full liquid (left) reduced gas (right) ANN for varying char values for specific test samples

4.3.2.3 Single study ANNs

In general, pyrolysis regression ANN models for single sets of experimental results are described in the literature (e.g. [5, 19, 25, 39]). To investigate the behaviour of the ANN models for single studies, references with ID 34 and ID 12 were examined. The first one, which is a study by Nik-Azar et al. [70] with beech wood, has a significant amount of data points (97) and only particle size, heating rate and temperature were varied experimentally. The second study by Aysu and Küçük [53] had a smaller amount of data points (27) and the temperature, the heating rate and the gas residence time were varied. Therefore, two ANN models for each reference were developed, with only the corresponding data points constituting the training and testing sets in each case. The figures containing the results of these models are presented in the Appendix B. The char ANN for ID 34 resulted in an RMSE of 1.9 wt% ar and the liquid ANN an RMSE of 1.5 wt% ar. The results for ID 12 were even better (RMSEs of 0.43 wt% ar for char and 0.63 wt% ar for gas), showing that not many data points are required from the model, especially for narrower ranges of experimental conditions. It should be mentioned that optimization of the hyperparameters was not performed for either case. From this brief analysis, it can be shown that ANN models can deliver very good predictions when it comes to a limited range of inputs in terms of experimental parameters. However, these models are not generalizable; they are reactor and biomass type specific. Furthermore, any variation of the input parameters beyond the limits of each study would constitute an extrapolation on behalf of the model.

4.4 Conclusions

The ANN models proposed within this work for the estimation of solid, liquid and gaseous pyrolysis product yields focus on generalizability and aim to achieve the best possible results over different reactor systems, conditions and biomass types. This was made possible through the creation of a unique, large database, consisting of a variety of small-scale experimental pyrolysis studies. It can be argued that the implementation of the ANN models was successful, given the quite reasonable values of RMSE of the predictions. However, the ANN models cannot be compared to ones obtained from single or in general more limited studies. The models developed in this work appeared to be able to consistently reproduce the expected behaviours for the respective yields, especially in relation to temperature variation. However, a difficulty in extracting useful information from inputs such as gas residence time and holding time was also noted. Furthermore, a reduction of the input parameters was attempted, based on an evaluation of the most effective parameters. The increased generalization capabilities achieved through this method were observed in terms of prediction quality improvement for the char and gas ANNs, while in the case of the liquid ANN the loss of information

led to worse performance. Finally, it was shown that the inclusion of the experimentally derived char yield as an input parameter in the ANN models, can lead to improved predictive capabilities.

For the cases of the char and gas ANNs, the reduced input networks performance was only slightly better compared to the full ones. The liquid product ANN was the worst performing one, with the reduced version being also considerably less accurate (RMSE of 9.3 wt% ar) than the full one (6.9 wt% ar). Among the three product classes, the char models were the best performing ones, largely due to the higher accuracy of char yield experimental measurements compared to the ones for the liquid and gaseous products. The wide variety of methods employed for pyrolysis liquid product determination as well as the calculation of either the liquid or the gaseous product by difference add to that effect. Considering the lower reliability of the gas and liquid yields measurement from pyrolysis experiment, the reason for the significantly better performance of the gas models in the present work can be sought in the actual numerical values of the yields. In the present database, the standard deviation of the gas yield values (10.9 wt% ar), is significantly lower compared to the ones of the char (15 wt% ar) and liquid (14.7 wt% ar). This means that there is a lower variability in the reported gaseous yields and therefore their prediction, which falls within a smaller interval, entails a smaller error.

In general, the maximum achievable accuracy for the models obtained in this work is limited due to a number of factors. That of course does not exclude the possibility of improvements for example by further optimization of the ANNs, the inclusion of continuous reactors in the database by making the necessary adaptations in the models, the reduction of the models' scope (e.g. focus on specific pyrolysis regime) or the introduction of stricter criteria for the induction of data in the database. Furthermore, the feature reduction method, could be further refined, by utilizing hypothesis – testing methods for the derivation of correlations within the dataset. Additionally, the reported lack of fast pyrolysis samples could be addressed by the removal of some input parameters and/or by focusing on specific regimes, that would allow the expansion of the database to include studies previously left out due to incomplete information. In any case however, the limitations induced through discrepancies in the literature are still significant. Firstly, the composition of biomass samples can be measured using different methodologies of which the results might differ significantly. The standards that are used are often not mentioned in the literature. Furthermore, fundamental parameters are also sometimes omitted, such as the lignocellulosic composition, the gas residence time, even in some cases the heating rate. Finally, the implications of the employment of different methods for products measurement, the calculation of product yields by difference and the ambiguity in definition of units of measurement have already been discussed thoroughly in the present work. In a world that is rapidly shifting its focus towards the realm of big data, it is essential to provide high amounts of quality data that can be easily used and compared by these types of models. Therefore, the pyrolysis scientific community needs to be aware of using higher standards in terms of reported data quality.

Bibliography

1. Wang, S., et al., *Lignocellulosic biomass pyrolysis mechanism: A state-of-the-art review*. Progress in Energy and Combustion Science, 2017. **62**: p. 33-86.
2. Basu, P., *Biomass Gasification and Pyrolysis Practical Design and Theory*. 2010: Elsevier Inc.
3. Dufour, A., et al., *Evolution of Aromatic Tar Composition in Relation to Methane and Ethylene from Biomass Pyrolysis-Gasification*. Energy & Fuels, 2011. **25**(9): p. 4182-4189.
4. Basu, P., *Chapter 7 - Gasification Theory*, in *Biomass Gasification, Pyrolysis and Torrefaction (Second Edition)*, P. Basu, Editor. 2013, Academic Press: Boston. p. 199-248.
5. Cao, H., Y. Xin, and Q. Yuan, *Prediction of biochar yield from cattle manure pyrolysis via least squares support vector machine intelligent approach*. Bioresource Technology, 2016. **202**: p. 158-164.
6. Xing, J., et al., *Predictive single-step kinetic model of biomass devolatilization for CFD applications: A comparison study of empirical correlations (EC), artificial neural networks (ANN) and random forest (RF)*. Renewable Energy, 2019. **136**: p. 104-114.
7. Basheer, I.A. and M. Hajmeer, *Artificial neural networks: fundamentals, computing, design, and application*. Journal of Microbiological Methods, 2000. **43**(1): p. 3-31.
8. Hagan, M.T., et al., *Neural Network Design*. 2014.
9. Tu, J.V., *Advantages and disadvantages of using artificial neural networks versus logistic regression for predicting medical outcomes*. Journal of Clinical Epidemiology, 1996. **49**(11): p. 1225-1231.
10. Khashei, M. and M. Bijari, *An artificial neural network (p,d,q) model for timeseries forecasting*. Expert Systems with Applications, 2010. **37**(1): p. 479-489.
11. Keybondorian, E., et al., *Application of MLP-ANN strategy to predict higher heating value of biomass in terms of proximate analysis*. Energy Sources, Part A: Recovery, Utilization, and Environmental Effects, 2017. **39**(22): p. 2105-2111.
12. Darvishan, A., et al., *Application of MLP-ANN as a novel predictive method for prediction of the higher heating value of biomass in terms of ultimate analysis*. Energy Sources, Part A: Recovery, Utilization, and Environmental Effects, 2018. **40**(24): p. 2960-2966.
13. Dashti, A., et al., *Estimation of biomass higher heating value (HHV) based on the proximate analysis: Smart modeling and correlation*. Fuel, 2019. **257**: p. 115931.
14. Özyuğuran, A. and S. Yaman, *Prediction of Calorific Value of Biomass from Proximate Analysis*. Energy Procedia, 2017. **107**: p. 130-136.
15. Uzun, H., et al., *Improved prediction of higher heating value of biomass using an artificial neural network model based on proximate analysis*. Bioresource Technology, 2017. **234**: p. 122-130.
16. Estiati, I., et al., *Fitting performance of artificial neural networks and empirical correlations to estimate higher heating values of biomass*. Fuel, 2016. **180**: p. 377-383.
17. Li, H., et al., *Prediction of the physicochemical properties of woody biomass using linear prediction and artificial neural networks*. Energy Sources, Part A: Recovery, Utilization, and Environmental Effects, 2016. **38**(11): p. 1569-1573.
18. Arumugasamy, S. and A. Selvarajoo, *Feedforward Neural Network Modeling of Biomass Pyrolysis Process for Biochar Production*. Chemical Engineering Transactions, 2015. **45**: p. 1681-1686.
19. Selvarajoo, A., D. Muhammad, and S.K. Arumugasamy, *An experimental and modelling approach to produce biochar from banana peels through pyrolysis as potential renewable energy resources*. Modeling Earth Systems and Environment, 2020. **6**(1): p. 115-128.
20. Çepelioğullar, Ö., et al., *Activation energy prediction of biomass wastes based on different neural network topologies*. Fuel, 2018. **220**: p. 535-545.

21. Mayol, A.P., et al. *Application of Artificial Neural Networks in prediction of pyrolysis behavior for algal mat (LABLAB) biomass*. in *2018 IEEE 10th International Conference on Humanoid, Nanotechnology, Information Technology, Communication and Control, Environment and Management (HNICEM)*. 2018.
22. Sunphorka, S., B. Chalermsoinsuwan, and P. Piumsomboon, *Artificial neural network model for the prediction of kinetic parameters of biomass pyrolysis from its constituents*. *Fuel*, 2017. **193**: p. 142-158.
23. Merdun, H. and I.V. Sezgin, *Modeling of pyrolysis product yields by artificial neural networks*. *International Journal of Renewable Energy Research* 2018. **8**(2).
24. Aydinli, B., et al., *The prediction of potential energy and matter production from biomass pyrolysis with artificial neural network*. *Energy Exploration & Exploitation*, 2017. **35**(6): p. 698-712.
25. Sun, Y., et al., *Pyrolysis products from industrial waste biomass based on a neural network model*. *Journal of Analytical and Applied Pyrolysis*, 2016. **120**: p. 94-102.
26. Liao, M., S.S. Kelley, and Y. Yao, *Artificial neural network based modeling for the prediction of yield and surface area of activated carbon from biomass*. *Biofuels, Bioproducts and Biorefining*, 2019. **13**(4): p. 1015-1027.
27. Mikulandrić, R., et al., *Artificial neural network modelling approach for a biomass gasification process in fixed bed gasifiers*. *Energy Conversion and Management*, 2014. **87**: p. 1210-1223.
28. Sreejith, C.C., C. Muraleedharan, and P. Arun, *Performance prediction of fluidised bed gasification of biomass using experimental data-based simulation models*. *Biomass Conv. Bioref*, 2013(3): p. 283-304.
29. Serrano, D. and D. Castelló, *Tar prediction in bubbling fluidized bed gasification through artificial neural networks*. *Chemical Engineering Journal*, 2020. **402**: p. 126229.
30. Sunphorka, S., B. Chalermsoinsuwan, and P. Piumsomboon, *Application of artificial neural network for kinetic parameters prediction of biomass oxidation from biomass properties*. *Journal of the Energy Institute*, 2017. **90**(1): p. 51-61.
31. Puig-Arnabat, M., et al., *Artificial neural network models for biomass gasification in fluidized bed gasifiers*. *Biomass and Bioenergy*, 2013. **49**: p. 279-289.
32. de Souza Jr, M., et al., *Neural network based modeling and operational optimization of biomass gasification processes*. *Gasification for Practical Applications, InTech*, 2012: p. 297-312.
33. Serrano, D., I. Golpour, and S. Sánchez-Delgado, *Predicting the effect of bed materials in bubbling fluidized bed gasification using artificial neural networks (ANNs) modeling approach*. *Fuel*, 2020. **266**: p. 117021.
34. Yucel, O., E.S. Aydin, and H. Sadikoglu, *Comparison of the different artificial neural networks in prediction of biomass gasification products*. *International Journal of Energy Research*, 2019. **43**(11): p. 5992-6003.
35. Lv, C., et al., *Levenberg–Marquardt Backpropagation Training of Multilayer Neural Networks for State Estimation of a Safety-Critical Cyber-Physical System*. *IEEE Transactions on Industrial Informatics*, 2018. **14**(8): p. 3436-3446.
36. Kermani, B.G., S.S. Schiffman, and H.T. Nagle, *Performance of the Levenberg–Marquardt neural network training method in electronic nose applications*. *Sensors and Actuators B: Chemical*, 2005. **110**(1): p. 13-22.
37. Guo, B., et al., *Simulation of biomass gasification with a hybrid neural network model*. *Bioresource Technology*, 2001. **76**(2): p. 77-83.
38. You, H., et al., *Comparison of ANN (MLP), ANFIS, SVM, and RF models for the online classification of heating value of burning municipal solid waste in circulating fluidized bed incinerators*. *Waste Management*, 2017. **68**: p. 186-197.

39. George, J., P. Arun, and C. Muraleedharan, *Assessment of producer gas composition in air gasification of biomass using artificial neural network model*. International Journal of Hydrogen Energy, 2018. **43**(20): p. 9558-9568.
40. Baruah, D., D.C. Baruah, and M.K. Hazarika, *Artificial neural network based modeling of biomass gasification in fixed bed downdraft gasifiers*. Biomass and Bioenergy, 2017. **98**: p. 264-271.
41. Pandey, D.S., et al., *Artificial neural network based modelling approach for municipal solid waste gasification in a fluidized bed reactor*. Waste Management, 2016. **58**: p. 202-213.
42. Xiao, G., et al., *Gasification characteristics of MSW and an ANN prediction model*. Waste Management, 2009. **29**(1): p. 240-244.
43. ECN.TNO, *Phyllis2, database for (treated) biomass, algae, feedstocks for biogas production and biochar*, <https://phyllis.nl/>.
44. Park, J., et al., *Slow pyrolysis of rice straw: Analysis of products properties, carbon and energy yields*. Bioresource Technology, 2014. **155**: p. 63-70.
45. Lee, Y., et al., *Comparison of biochar properties from biomass residues produced by slow pyrolysis at 500°C*. Bioresource Technology, 2013. **148**: p. 196-201.
46. Waheed, Q.M.K., M.A. Nahil, and P.T. Williams, *Pyrolysis of waste biomass: investigation of fast pyrolysis and slow pyrolysis process conditions on product yield and gas composition*. Journal of the Energy Institute, 2013. **86**(4): p. 233-241.
47. Demirbas, A., *Effect of temperature on pyrolysis products from four nut shells*. Journal of Analytical and Applied Pyrolysis, 2006. **76**(1): p. 285-289.
48. Demirbaş, A., *Yields of hydrogen-rich gaseous products via pyrolysis from selected biomass samples*. Fuel, 2001. **80**(13): p. 1885-1891.
49. Becidan, M., Ø. Skreiberg, and J.E. Hustad, *Products distribution and gas release in pyrolysis of thermally thick biomass residues samples*. Journal of Analytical and Applied Pyrolysis, 2007. **78**(1): p. 207-213.
50. Dufour, A., et al., *Synthesis gas production by biomass pyrolysis: Effect of reactor temperature on product distribution*. International Journal of Hydrogen Energy, 2009. **34**(4): p. 1726-1734.
51. Caballero, J.A., et al., *Flash pyrolysis of Klason lignin in a Pyroprobe 1000*. Journal of Analytical and Applied Pyrolysis, 1993. **27**(2): p. 221-244.
52. Şensöz, S., D. Angın, and S. Yorgun, *Influence of particle size on the pyrolysis of rapeseed (Brassica napus L.): fuel properties of bio-oil*. Biomass and Bioenergy, 2000. **19**(4): p. 271-279.
53. Aysu, T. and M.M. Küçük, *Biomass pyrolysis in a fixed-bed reactor: Effects of pyrolysis parameters on product yields and characterization of products*. Energy, 2014. **64**: p. 1002-1025.
54. Ertaş, M. and M. Hakkı Alma, *Pyrolysis of laurel (Laurus nobilis L.) extraction residues in a fixed-bed reactor: Characterization of bio-oil and bio-char*. Journal of Analytical and Applied Pyrolysis, 2010. **88**(1): p. 22-29.
55. Bahadır, A., et al., *Bio-oil production from fast pyrolysis of maple fruit (acer platanoides samaras): product yields*. World Journal of Engineering, 2017. **14**(1): p. 55-59.
56. Yorgun, S., *Fixed-Bed Pyrolysis of Miscanthus x giganteus: Product Yields and Bio-Oil Characterization*. Energy Sources, 2003. **25**(8): p. 779-790.
57. Kingma, P.D. and J. Ba, *Adam: A method for Stochastic Optimization*, in *3rd International Conference for Learning Representations*. 2015: San Diego.
58. Sietsma, J. and R.J.F. Dow, *Creating artificial neural networks that generalize*. Neural Networks, 1991. **4**(1): p. 67-79.
59. Goodfellow, I., Y. Bengio, and A. Courville, *Deep learning*. 2016: MIT Press.
60. Srivastava, N., et al., *Dropout: a simple way to prevent neural networks from overfitting*. J. Mach. Learn. Res., 2014. **15**(1): p. 1929-1958.
61. Dreyfus, G., *Neural Networks: Methodology and Applications*. 2005: Springer-Verlag Berlin Heidelberg.

62. Zabaniotou, A., et al., *Experimental study of pyrolysis for potential energy, hydrogen and carbon material production from lignocellulosic biomass*. International Journal of Hydrogen Energy, 2008. **33**(10): p. 2433-2444.
63. Orfão, J.J.M., F.J.A. Antunes, and J.L. Figueiredo, *Pyrolysis kinetics of lignocellulosic materials—three independent reactions model*. Fuel, 1999. **78**(3): p. 349-358.
64. Bridgwater, A.V., D. Meier, and D. Radlein, *An overview of fast pyrolysis of biomass*. Organic Geochemistry, 1999. **30**(12): p. 1479-1493.
65. Demirbas, A., *Effects of temperature and particle size on bio-char yield from pyrolysis of agricultural residues*. Journal of Analytical and Applied Pyrolysis, 2004. **72**(2): p. 243-248.
66. Diebold, J.P. and A.V. Bridgwater, *Overview of Fast Pyrolysis of Biomass for the Production of Liquid Fuels*, in *Developments in Thermochemical Biomass Conversion: Volume 1 / Volume 2*, A.V. Bridgwater and D.G.B. Boocock, Editors. 1997, Springer Netherlands: Dordrecht. p. 5-23.
67. Kan, T., V. Strezov, and T.J. Evans, *Lignocellulosic biomass pyrolysis: A review of product properties and effects of pyrolysis parameters*. Renewable and Sustainable Energy Reviews, 2016. **57**: p. 1126-1140.
68. Uddin, M.N., W.M.A.W. Daud, and H.F. Abbas, *Effects of pyrolysis parameters on hydrogen formations from biomass: a review*. RSC Advances, 2014. **4**(21): p. 10467-10490.
69. Park, S.-W. and C.-H. Jang, *Effects of pyrolysis temperature on changes in fuel characteristics of biomass char*. Energy, 2012. **39**(1): p. 187-195.
70. Nik-Azar, M., et al., *EFFECTS OF HEATING RATE AND PARTICLE SIZE ON THE PRODUCTS YIELDS FROM RAPID PYROLYSIS OF BEECH-WOOD*. Fuel Science and Technology International, 1996. **14**(4): p. 479-502.
71. Li, J., et al., *Influence of Temperature on the Formation of Oil from Pyrolyzing Palm Oil Wastes in a Fixed Bed Reactor*. Energy & Fuels, 2007. **21**(4): p. 2398-2407.
72. Horne, P.A. and P.T. Williams, *Influence of temperature on the products from the flash pyrolysis of biomass*. Fuel, 1996. **75**(9): p. 1051-1059.
73. Angin, D., *Effect of pyrolysis temperature and heating rate on biochar obtained from pyrolysis of safflower seed press cake*. Bioresource Technology, 2013. **128**: p. 593-597.
74. Zhou, H., et al., *Effect of interactions of biomass constituents on polycyclic aromatic hydrocarbons (PAH) formation during fast pyrolysis*. Journal of Analytical and Applied Pyrolysis, 2014. **110**: p. 264-269.
75. Neves, D., et al., *Characterization and prediction of biomass pyrolysis products*. Progress in Energy and Combustion Science, 2011. **37**(5): p. 611-630.
76. Tsekos, C., et al., *PAH sampling and quantification from woody biomass fast pyrolysis in a pyroprobe reactor with a modified tar sampling system*. Journal of Analytical and Applied Pyrolysis, 2020. **147**: p. 104802.
77. Neeft, J.P.A., et al., *Guideline for Sampling and Analysis of Tars and Particles in Biomass Producer Gases*. Progress in Thermochemical Biomass Conversion, 2001: p. 162-175.

5. Gasification of woody biomass in a novel indirectly heated bubbling fluidized bed steam reformer

Chapter published in:
Fuel Processing Technology, Volume 224, 15 December 2021, 107003

5.1 Introduction

Sustainable resources for heat and power generation as well as for fuels and chemicals production have been attracting a lot of interest amidst concern for environmental change, the depletion of fossil fuel reserves, as well as the increasing need for energy self-reliance. Biomass, the third most abundant fuel resource after coal and oil, constitutes such a potentially clean and renewable fuel, which is also readily available worldwide. Biomass thermochemical conversion processes constitute interesting options for the aforementioned products, with pyrolysis, torrefaction, gasification, combustion and hydrothermal liquefaction comprising the main employed thermochemical conversion methods [1]. Gasification in particular, is the thermochemical conversion process by which carbonaceous materials are converted to a fuel gas or a chemical feedstock in a reducing (oxygen deficient) environment requiring heat [2].

Gasifiers can be classified according to various of their characteristics. One type of classification is based on the gas-solid interaction within the unit and it includes fixed or moving bed (downdraft, updraft, crossdraft) gasifiers, fluidized bed gasifiers (bubbling, circulating and dual) and entrained flow gasifiers (top-fed and side-fed). Another possible way to classify a gasifier is by the gasifying medium employed (air, CO₂, steam, etc.) [2, 3].

An important distinction between gasifier types, can also be made according to the way that the heat required for the gasification of a feedstock is provided to the system. Autothermal or direct gasification occurs when the feedstock is partially oxidized by the gasification agent (usually air or O₂). This way, the heat required for the fuel heating, drying, pyrolysis and gasification reaction is provided by exothermal oxidation reactions within the gasifier. When an oxidising agent is not employed, an external energy source is required and the process is then called allothermal or indirect gasification. Steam is most commonly used as an allothermal gasification agent [4, 5]. In regards to autothermal gasification, the biggest limitation lies within the separation/removal of diluent gases such as N₂, either downstream (from the syngas) or upstream (from air) the gasification unit [6].

According to Karl and Pröll [7], there are three ways of ensuring sufficient provision of heat for the operation of such gasifiers. The first one is by the discontinuous intermittent operation of a single fluidized bed, the second by the circulation of particles between two interconnected fluidized beds and the third through heat transfer surfaces. The first category regards mainly Winkler's fluidized bed gasifier, invented back in 1922, where heating of the fluidized bed was performed through air (or later O₂) blown combustion up to 1100-1200 °C, repeatedly followed by steam blown gasification. The latter two technologies have seen much more application and development in the recent years. The interconnected fluidized beds gasification technology, or as it is most commonly referred to: Dual Fluidized Bed (DFB) gasification, includes the utilization of two separate gasification and combustion reactors [8]. Solid fuel is fed into the gasification reactor, where fuel drying and pyrolysis/devolatilization reactions as well as char gasification are taking place in parallel, under temperatures typically between 750 °C and 850 °C. The bed material along with the char that remains are transported to the combustion reactor which is fluidized with air at temperatures usually between 900 °C and 970 °C. The combustion of the char provides the heat necessary for the gasification reactions. Furthermore, depending on the gasification temperature and therefore the char produced through gasification and available for combustion, additional fuel can be required for the combustion reactor. In general, the temperature in a DFB gasification process is a self-controlling parameter, depending mostly on the fixed carbon content of the fuel employed [9]. Several large-scale applications of the DFB technology have been presented in the recent years. The first DFB steam gasification pilot plant was established in the 1990s at TU Vienna, Austria which led to the construction of an 8 MW_{th} demonstration plant in Güssing, Austria in 2002, a 8.5 MW_{th} plant in Oberwart, Austria in 2008 and a 15 MW_{th} plant in Senden, Germany [10]. The Gothenburg Biomass Gasification (GoBiGas)

32 MW_{th} plant, along with the supporting 2-4 MW research gasifier at the Chalmers University of Technology, Sweden, were established in 2005 and 2007 respectively [11]. According to data from 2019 [12], the demonstration GoBiGas plant had to shut down, since it had to be commercialised. It should also be mentioned that two demonstration plants in Nongbua, Thailand (1 MW_{th}) and Daigo, Japan (1.4 MW_{th}) [13], as well as an upcoming project (2023) Gaya, France [14] are inspired by the Güssing gasifier. In general, all the aforementioned plants employ the “Güssing concept”, which is considered the most successful indirect gasification system worldwide [7]. Another notable DFB gasification system is Battelle’s FERCO gasification process (also referred to as SilvaGas or Taylor gasification process) which consisted of two interconnected circulating fluidized bed and was demonstrated in a commercial scale 40 MW_{th} plant in Burlington (Vermont), USA between 1999 and 2001 [15]. A similar lab scale system was developed by ECN – part of TNO (Netherlands), with the 30 kW MILENA gasifier, which is still in operation [16-18]. More DFB gasification systems along with important technical details are presented by Karl and Pröll in [7] and more recently by Larrson et al. in [19] and Hanchate et al. in [20].

Heat exchanger configurations for the delivery of the heat required for the operation of a gasifier can be designed in different ways. In one concept, the gasification area is completely separated from the “heat provision reactor” and therefore a plethora of different fuels and/or processes for heat supply can be employed. Such a reactor was proposed for the first time by Juengtgen and van Heek in 1975 [21], employing helium produced from nuclear reactors at high temperatures (HTR). According to Karl [22], the large number of heat exchangers required, due to poor heat transfer between the heat carrier gas and the inner tube surface of the heat exchangers, hindered the progress of this process. The concept was revisited in the following decades in an effort to reduce the gasification temperature, in order to minimize the effect of poor heat transfer, through the application of different catalyst types and configurations [23-25], however no commercial demonstrations have been presented so far. In the early 90s the MTCL technology was employed in a pilot scale black liquor gasifier in Erode, India and in several pulp mills in North America in similar configurations [26, 27]. The MTCL gasifier is a steam blown atmospheric fluidized bed reactor, employing in-bed heat exchanger tubes for heat provision. Part of the gas produced from gasification was burned in a pulse combustor that fed the heat exchanger tubes. The highly turbulent flue gas and the low frequent acoustic oscillations produced from pulse combustion can achieve improved heat transfer rates compared to conventional heat exchangers [7, 27]. The most recent concept in indirectly heated fluidized bed gasifiers is the Biomass Heatpipe Reformer, which was presented for the first time in 2001 and has been commercially developed by Agnion Inc. with a 500 kW demonstration plant in Pfaffenhofen, Germany and two commercial 1 MW plants in Grassau, Germany and Auer, Italy. The plant in Grassau was not a success due to very high tar levels, creep behaviour of the heat pipes and reduced cold gas efficiencies due to the combustion chamber design [28]. In 2015, an advanced Heatpipe Reformer pilot plant of 100 kW with optimized combustor design was commissioned in Erlangen-Nuremberg [29]. According to this concept, gasification takes place in a pressurized chamber and the heat is provided by a combustion chamber which is located below it, through several heat pipes. It should be mentioned that both the gasifier and the combustor are fluidized reactors. The two fluidized beds are connected through a series of heat pipes, where the working fluid (usually an alkali metal such as Na, K, etc.) evaporates on one side (combustor) and condenses on the other (gasifier) [29-31]. The use of the Heatpipe concept (evaporation-condensation) is claimed to lead to high heat transfer coefficients and smaller heat transfer areas by a factor of 10 to 20 [22].

In this work, a novel indirectly heated biomass gasification concept is presented along with the respective commissioning experiments. In particular, an atmospheric pressure 50 kW_{th} indirectly heated bubbling fluidized bed steam reformer (IHFBSR) was designed, built and commissioned by the Dutch company Petrogas - Gas Systems in collaboration with the Process and Energy Department

of the Delft University of Technology. The novelty of the reactor lies within the method of heat provision for the gasification reactions. For this purpose, two radiant tube natural gas burners, one in the bottom (bed area) and one in the top (freeboard) of the reactor, are employed (Figure 5.1). Its design aims at the reduction of heat losses, the provision of enough heat for the realization of the biomass steam reforming and cracking reactions and the exploration of scale-up possibilities to an industrial scale process. The commissioning experiments presented in this work are aimed at obtaining understanding of the operation characteristics, fuel conversion and raw product gas composition.

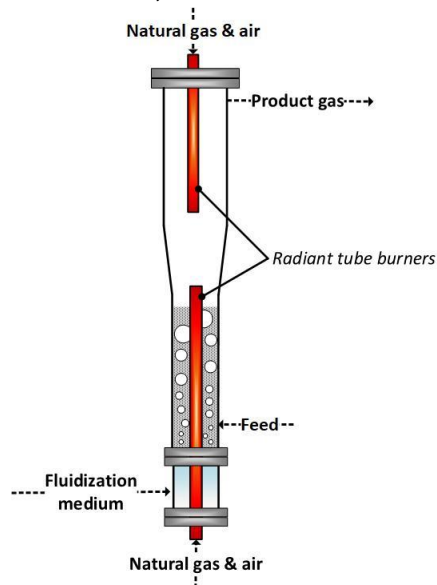


Figure 5.1: Conceptual design of the indirectly heated bubbling fluidized bed steam reformer (IHFBSR)

5.2 The Indirectly Heated Bubbling Fluidized Bed Steam Reformer (IHFBSR)

In this section, the novel 50 kW_{th} Indirectly Heated Bubbling Fluidized Bed Steam Reformer (hereby referred to as IHFBFSR) is presented. A simplified process flow chart of the reactor is presented in Figure 5.2. In this reactor, combustion and gasification reactions are separated to a great extent in a novel way, thus avoiding the dilution of the product gas.

The gases that can be employed as fluidization agents in the IHFBFSR are N₂, air and steam. Steam is produced at a working pressure between 3.5 and 5 bar and then expanded to near atmospheric conditions, depending on the supply. Air and/or nitrogen, which is mainly used during warming up, pass initially through a 4.5 kW preheater (EH01), where they are heated up to 150 °C. The steam, along with the gases that are preheated by EH01, are fed to a second 6 kW preheater (EH02). The gasification media are all fed to the reactor at about 200 mbarg typically. Air can also be directly fed into the freeboard as a measure for tar destruction. The secondary air injection point is located ~90 cm below TC06 (Figure 5.2). The radiant tube burners are supplied with air and natural gas at 80 mbar and 60 mbar, respectively. N₂ is also distributed to the pressure gauges in the reactor (Figure 5.2) (5 ml/min each) and the two cyclones, as well as to the biomass and additive bunkers (4 kg/h).

The reactor is manufactured out of 310S (AISI) steel with a wall thickness of 4.78 mm and a height of roughly 3 m. It is insulated with a 200 mm three-layer mattress. Gases are fed in the windbox and subsequently in the reactor, through a distributor plate consisting of 50 tuyeres each with two 2 mm holes drilled in a 25° angle (downwards). As presented in Figure 5.2, the temperature in the reactor is monitored by thermocouples located in and above the bed zone. The last thermocouple (TC07) is located at almost the same height as the product gas outlet which is on the reactor inner wall. Pressure gauges are located in four spots within the IHFBFSR along with differential pressure transmitters, that

allow the recording of the pressure drop over the distributor plate, the bed zone and the freeboard. In general, data from the various instruments are recorded through a SCADA/PLC coupling employing a LabVIEW interface. The system obtains and records data every 10 s.

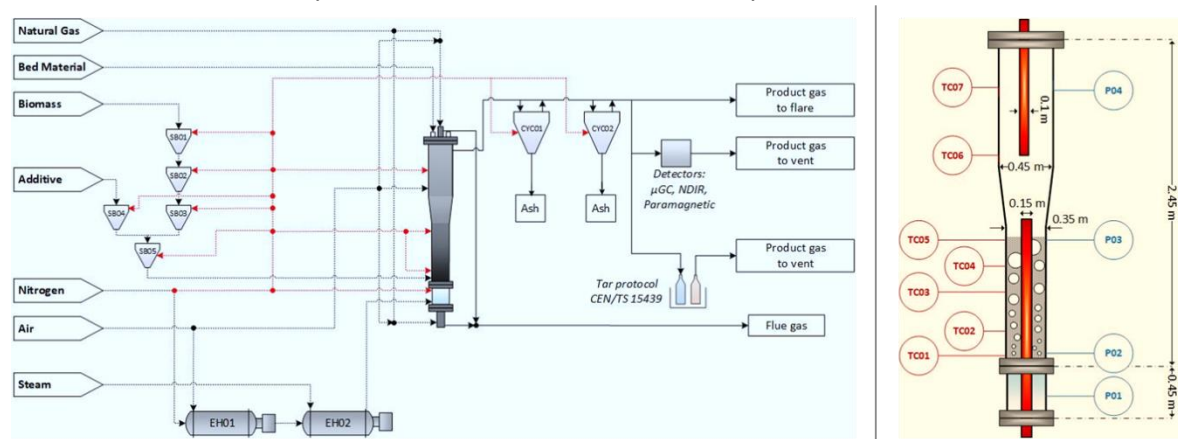


Figure 5.2: IHBFBRS simplified process flow chart (left)/ Basic dimensions and main sensors location in the IHBFBRS reactor chamber. P: pressure gauge, TC: thermocouple (right)

The two self-recuperative ceramic burners utilized for gasification heat provision were supplied by WS – Wärmeprozessestechnik GmbH. Both are placed inside metal radiant tubes in order to protect the ceramic burners from the bed material blasting. Both burners operate in an on/off mode; the bottom burner is controlled by the average values of thermocouples TC01 – TC05 and the top burner by thermocouple TC07. For both burners the maximum allowable set point was at 850 °C according to the safety regulations. The burners operate at a constant capacity of 20 kW_{th} and 12 kW_{th} for the bottom (REKUMAT C100) and top one (REKUMAT C80), respectively. Regarding the bottom radiant tube, its total main body length is ~1.7 m and 1.2 m of this is situated in the bed area. The bottom part of the radiant tube heats up the windbox, as shown in Figure 5.2. The top radiant tube is smaller than the bottom one, both in terms of diameter (0.1 m versus 0.15 m) and of total main body length (1.3 m versus 1.7 m).

Part of the product gas, after the cyclones, is led to the gas analysis section. The gas analysis line is traced at 400 °C and a heated candle filter (350 °C) is used as the main method of char and ash particles removal. After this point, part of the gas is channelled to the tar sampling system, where tars are sampled according to the Tar Protocol CEN/TS 15439 [31]. Downstream the tar protocol is placed, a pump a flowmeter and a gas meter. The rest of the gas passes through a water-cooled condenser and is led to the gas analysis section. There four bottles, three of them filled with isopropanol and one filled with silica gel, are used for tar and moisture removal. Subsequently a Whatman 55 mm paper filter and the pump follow and from there the gas is led to the detectors. A micro-GC, samples from the product gas stream every 4 minutes, measuring CO, CO₂, H₂, CH₄ and N₂. Then the gas flow splits into two streams each passing through the O₂ detector and the Non-Dispersive Infrared Detector (NDIR), for the measurement of CO and CO₂. The use of these analysers is necessary for the online monitoring of the experiment.

5.3 Materials and Methods

5.3.1 Feedstocks, bed material and analytical equipment

The biomass feedstocks employed in this work were two different types of A-quality residual wood (termed Premium Green and Excellent Red), supplied by the company Labeer Group Moerdijk B.V, the Netherlands. Both feedstocks were supplied in the form of pellets with a length of 2 cm and a diameter of 0.6 cm. Premium Green (PG), consists out of woodchips, sawdust and wood shavings of brown leafage wood from Dutch secondary forest biomass. Excellent Red (ExR), is derived from white pine wood woodchips, originating from Scandinavian countries and Russia. Table 5.1 shows the proximate and ultimate analysis of the two feedstocks. The moisture and ash content of the biomass species was determined according to the NREL/TP-510-42621 [32] and NREL/TP-510-42622 [33]. The fixed carbon and volatile content for each feedstock was determined using an SDT Q600 Thermogravimetric Analyser (TGA). In this analysis, ~3 mg of sample was loaded in an alumina TGA crucible and heated in an inert atmosphere (100 ml/min of N₂) up to 600 °C, with a constant 10 °C/min heating rate, where the temperature was held for 10 min. Afterwards, N₂ was substituted with 100 ml/min of air and isothermal operation (600 °C) continued for an extra 10 min. The ultimate analysis was performed using a Vario MICRO CHNS analyser, with the O content being calculated by difference. The lower heating value (LHV) of the two fuels was determined using a Parr 6772 Calorimetric Thermometer (bomb calorimeter).

Table 5.1: Proximate analysis, ultimate analysis and Lower heating Value (LHV) for the two woody biomass feedstocks (PG and ExR) employed in the IHBFSR commissioning experiments.

	PG	ExR
Moisture (wt%)	5.08	5.57
Volatiles (wt%, d.b.)	78.13	84.07
Fixed carbon (wt% d.b.)	21.15	15.44
Ash (wt% d.b.)	0.73	0.49
C (wt%, d.b.)	48.41	47.88
H (wt%, d.b.)	6.02	6.44
N (wt%, d.b.)	0.30	0.06
S (wt%, d.b.)	0.01	0.01
O (wt%, d.b.)	44.53	45.13
LHV (MJ/kg d.b.)	18.98	19.50

Corundum, which is an aluminium oxide (Al₂O₃) containing also traces of iron oxide, titanium oxide and silica, was used as the bed material for the IHBFSR commissioning experiments. This material, supplied by Unicorn ICS B.V., has a density of 3940 kg/m³, a hardness of 9 Mohs and its melting point is 1950 °C. The weighted average particle diameter for the bed material employed in the experiments was 590 µm (F046) and 490 µm (F054), which classifies them in the Geldart B category (sand-like) of solids in bubbling fluidized beds [34]. It has a very high hardness, thus the probability of fines production due to attrition of the particles is reduced. Furthermore, depending on the fluidization conditions, it has very good heat distribution properties [35].

The analysis of the permanent gases (CO, CO₂, CH₄, H₂ and N₂), was performed using a Varian CP4900 micro-Gas Chromatograph. Separation of the individual gases was achieved on a 1 m CP-COX column and detection/quantification by a TCD detector using Argon as carrier gas. For O₂, a Hartmann & Braun Magnox 6G paramagnetic detector was applied, while for CO and CO₂, a Hartmann & Braun Uras 10 NDIR was used. For tar detection and quantification, an Agilent Technologies 7890A GC-FID

system was employed. The acquisition run time was 90 min, including an increase of temperature of the oven from 50 to 300 °C at 5 °C/min rate and a hold time of 38 min. The species measured were: benzene, toluene, ethyl benzene, naphthalene, acenaphthylene, fluorene, anthracene, phenanthrene, pyrene, chrysene, benzo(a)anthracene, benzo(k)fluoranthene, benzo(a)pyrene, dibenz(a,h)anthracene, indeno(1,2,3-cd)pyrene, benzo(b)fluoranthene). Moisture content was determined using a Mettler Toledo V10S volumetric Karl Fischer Titrator with a polarized DM143-SC sensor.

5.3.2 Definition of main process parameters

The experiments conducted within this work, apart from different biomass feedstocks and bed material particle sizes, explored also different operational conditions. In particular, steam gasification experiments were conducted with different steam to biomass ratios (STBR) and different equivalence ratios (ER or λ). These two parameters are described according to the following formulas:

$$STBR = \frac{\dot{m}_{steam} + X_{H_2O} \cdot \dot{m}_{biomass}}{\dot{m}_{biomass (d.a.f.)}} \quad (\text{Eq. 3})$$

$$\lambda = \frac{\dot{m}_{O_2} / \dot{m}_{biomass (d.a.f.)}}{\left(\dot{m}_{O_2} / \dot{m}_{biomass (d.a.f.)} \right)_{stoic}} \quad (\text{Eq. 4})$$

Where, \dot{m}_{steam} is the steam mass flow rate, $\dot{m}_{biomass}$ the biomass feedstock mass flow rate and \dot{m}_{O_2} is the oxygen mass flow rate. Regarding the latter, it should be reminded that in the IHBFSR, oxygen is supplied through air. The STBR, correlates the total amount of steam provided either directly as a feed or as biomass moisture, to the dry-ash-free biomass input. The λ , or stoichiometric oxygen ratio is usually employed for identifying different oxidation regimes, as it compares the amount of oxygen used in an oxidation process to the total amount required for stoichiometric combustion of a fuel's unit. From the formula it can be observed that values of $\lambda \geq 1$ correspond to combustion processes, while $\lambda = 0$ corresponds to pyrolysis (absence of oxidation media). Values in between the two, correspond to gasification. Typically, λ ranges between 0.2 and 0.4, while the STBR between 0.5 and 2 [35]. In regards to the output parameters which were used in order to evaluate the experiments conducted, emphasis was given to the cold gas efficiency (CGE), carbon conversion efficiency (CCE), permanent gas composition and tar and content [36]. The definitions of the calculated process parameters is given below, adapted from [37]. In addition, the overall efficiency of the process was calculated based on a simple energy balance as shown also below.

$$CGE = \frac{\dot{m}_{product\ gas} \cdot LHV_{product\ gas}}{\dot{m}_{biomass} \cdot LHV_{biomass}} \quad (\text{Eq. 5})$$

$$OE = \frac{\dot{m}_{product\ gas} \cdot LHV_{product\ gas}}{\dot{m}_{biomass} \cdot LHV_{biomass} + \dot{Q}_{Burners} + \dot{Q}_{Preheaters}} \quad (\text{Eq. 6})$$

$$CCE = 1 - \frac{\dot{m}_{C,residue}}{\dot{m}_{C,biomass}} \quad (\text{Eq. 7})$$

5.3.3 Experimental procedure and overview

Before each test, 75 kg of bed material (corundum F046 or F054) was loaded in the reactor. This amount of bed material corresponds to a stationary bed height of roughly 0.59 m. Each experiment was initialized by warming up the reactor to an average bed temperature of 850 °C. The average bed temperature was defined as the average values of thermocouples TC01 – TC05. This process included two separate steps. The first step started by introducing the maximum fluidization media flow, which corresponds to 30 kg/h of N₂ and 22 kg/h of air. At the same time, both burners were turned on with a set point of 850 °C, along with the two preheaters. In order to reach the designated temperature, the heat provided by the radiant tube burners does not suffice. Therefore, a biomass combustion step was added to the warming up process. This step of the warming up process, was performed with 22 kg/h of air and the appropriate amount of biomass feedstock to achieve stoichiometric combustion. The biomass flow rate for stoichiometric combustion is approximately 4 kg/h for both PG and ExR, since the two species have similar compositions. It should also be mentioned that preliminary combustion tests were performed with both biomass species, under the exact same conditions as the ones employed for the aforementioned warming up step. These tests showed that close to full conversion was achieved during this process, since no char was found in the bed (particle or fine form) or in the cyclones. Furthermore, after the completion of the combustion warming up step, the cyclones were emptied from the combustion produced ashes, to avoid interference with the subsequent measurements in the gasification phase.

After this point the O₂ and NDIR detectors which are measuring gas composition online, as well as the micro-GC were started. When the set point for the bottom burner was reached gasification could be initiated. Steam and air were supplied to the system according to the STBR and λ required. The goal was to achieve steady state gasification operation, which corresponds to relatively stable temperature and gas composition profiles. When steady state was achieved, tar sampling using the tar protocol was initiated. According to this protocol, tar sampling should be performed for at least 30 min with a gas flow rate between 0.1 and 0.6 Nm³/h. During the steady state, the average value of each gas as measured from the micro-GC, was used for the derivation of the gas composition, which is presented in this work. As it will be thoroughly presented in the results and discussion section, the employment of different lambda values (λ) between the various experiments also influences the operational temperatures throughout the system. This differentiation occurs due to the varying degree of char and/or biomass oxidation reactions that take place when different lambda values are employed. The reduction of the extent of oxidation reactions in the case of low λ (and therefore low temperature) experiments led to increased char accumulation in the bed. That was evident by the increased bed height as observed through the thermocouple values.

During cooling down, to preserve the char in the reactor for weighing and future analysis, only N₂ was fed in the reactor at its maximum flow rate. The tar samples obtained were collected in bottles and refrigerated at ~5 °C. Two samples of each tar protocol were taken in HPLC vials for the subsequent tar analysis (GC-FID) and Karl Fischer titration. After cooling down, the bed material was collected and subsequently sieved to separate the bed material from the larger char particles. This was achieved with the use of a 500 or 600 μm sieve, depending on the bed material used, in combination with a Retsch AS300 sieve shaker. The char was weighed and stored, while the bed material was also weighed and five samples from it were combusted with air at 600 °C for 4 h in a muffle furnace (Nabetherm 30), until constant weight (±0.3 mg). The difference in weight was

assumed to correspond to the amount of fine char particles. The combustion process was also performed for the material removed from the cyclones, which contained both ashes and char particles. Through these three processes, the char yield and therefore also the ash yield, of each experiment was determined.

5.3.4 Experimental matrix

Table 5.2 presents the experiments performed within this work. For the cases with two set points, the first one corresponds to a time before the final steady state was established. The average bed temperature (Average bed T), corresponds to the thermocouples TC01 to TC03 average, since for every experiment the bed area always included only these thermocouples. The experimental results are discussed in the following section.

Table 5.2: Experimental matrix for the PG and ExR steam gasification experiments conducted in the IHBFBRSR

#	Set point	Bed Material	Biomass	Average bed T-°C	Steam-kg/h	Biomass -kg/h	Air-kg/h	Sec. air-kg/h	λ	STBR
1	-	F054	PG	839 (± 1)	9.0	10	11.3	0	0.20	1.0
2	-	F054	PG	840 (± 1)	10.8	10	11.3	0	0.20	1.2
3	-	F054	PG	836 (± 1)	7.3	10	11.2	0	0.20	0.8
4	-	F046	PG	833 (± 1)	10.4	10	11.3	0	0.20	1.2
5	SP1	F046	PG	831 (± 1)	7.3	10	11.3	0	0.20	0.8
	SP2	F046	PG	832 (± 1)	7.3	10	11.3	0	0.20	0.8
6	SP1	F054	ExR	826 (± 6)	10.5	10	13.3	0	0.23	1.2
	SP2	F054	ExR	839 (± 1)	10.7	10	11.3	0	0.20	1.2
7	SP1	F046	ExR	816 (± 6)	10.6	10	13.3	0	0.23	1.2
	SP2	F046	ExR	833 (± 1)	10.5	10	11.3	0	0.20	1.2
8	SP1	F046	ExR	740 (± 14)	8.8	8	1.9	0	0.04	1.2
	SP2	F046	ExR	711 (± 1)	8.7	8	1.9	0	0.04	1.2
9	SP1	F046	ExR	733 (± 12)	8.6	8	1.9	8	0.04	1.2
	SP2	F046	ExR	704 (± 1)	8.7	8	1.9	8	0.04	1.2
10	SP1	F046	ExR	724 (± 8)	8.8	10	1.9	4	0.03	1.0
	SP2	F046	ExR	702 (± 3)	8.8	8	1.9	4	0.04	1.2
	SP3	F046	ExR	710 (± 1)	8.7	8	1.9	4	0.04	1.2
11	SP1	F054	ExR	717 (± 10)	8.7	8	1.9	4	0.04	1.2
	SP2	F054	ExR	715 (± 1)	8.7	8	1.9	4	0.04	1.2
12	SP1	F054	ExR	727 (± 9)	8.9	8	1.9	8	0.04	1.2
	SP2	F054	ExR	722 (± 1)	8.8	8	1.9	8	0.04	1.2

Experiments were conducted with two sizes of bed material (F054 and F046), as well as with two different kinds of wood residue feedstocks. Furthermore, for each bed and biomass specie, STBR values of 0.8, 1 and 1.2 were employed as well as different lambdas (λ) which also led to different bed temperatures. According to the values of λ employed, the overall temperature of the gasifier is influenced. The temperature profiles throughout the system for various operational conditions are presented in Appendix C. Experiments with an average bed temperature above 800 oC will be hereby referred to as high temperature (HT) experiments, while experiments with lower average bed

temperatures will be referred to as low temperature (LT) experiments. Additionally, it should be mentioned, that in the case of HT experiments with ExR, the average bed temperature dropped significantly during the initiation of steam/air gasification when a λ of 0.2 was employed. To maintain a bed temperature comparable to the PG experiments λ was increased to 0.23. To explain this difference noted between the two biomass feedstocks one can look at their compositional characteristics (Table 5.1). Even though the LHV values are slightly higher for PG (19 MJ/kg versus 19.5 MJ/kg), the difference between the values is too small. On the contrary, the much lower fixed carbon content of ExR (15 wt % versus 21 wt %), can presumably lead to less char formation, mainly from the initial pyrolysis stage of the gasification process. The subsequent char oxidation is assumed to be the main reason for maintaining the desired gasification temperature, since the LHV of biomass char is in general much higher compared to the parent biomass [2]. Therefore, the reason for the observed difference in maintaining the required process temperature between the two feedstocks, can be attributed to the lower fixed carbon content of ExR.

Apart from the aforementioned parameters, the effect of the injection of secondary air in the freeboard and the duration of the experiment were also studied. Secondary air injection will be investigated in terms of its efficiency as a tar reduction method, due to the introduction of oxidizer (O_2) and the local increase of temperature. Tar reduction efficiency will be compared to the effect on the product gas composition. This method was employed, due to the presence of the burner in the freeboard. Depending on the effectiveness of the method, the exothermicity of the oxidation reactions can lead to potential energy savings for the top burner. Furthermore, the straightforward and simple implementation of this concept in the IHBFSR, was an advantage for the commissioning phase of the associated project. The duration of the experiment, as briefly mentioned before, can be linked to the accumulation of char in the bed area for LT experiments. Therefore, an early tar sampling (SP1) was performed to be able to compare the two states of the experiment. This is mainly in terms of the effect of char's presence on the product gas' tar content and overall composition.

5.4 Experimental results and discussion

5.4.1 Effect of STBR and bed material particle size

In this section, the effect of STBR and the bed material particle size is examined, using the experiments 1, 2, 3, 4 and 5 (SP2) conducted with PG (Table 5.2). These experiments were performed in the same bed temperature range (833 – 840 °C) and at $\lambda=0.2$. In terms of the temperature profile developed in the reactor, the average values during the steady state for the TC04 – TC05 region were higher by 11 °C, on average, for the experiments conducted with F046 compared to F054. This is, however, compensated by the reverse behaviour for the TC01 – TC03 area of the bed, leading to an average TC01-05 temperature of 850 °C for all the experiments. The difference lies mostly in the fluidization and thus heat transfer characteristics of the two bed material sizes. In general, it is observed that the smaller bed material size (F054) leads to a lower temperature difference between the bed area and the area directly above it, hinting possibly to improved heat transfer compared to the larger bed material size (F046). Regarding the freeboard area (TC06 and TC07), the temperatures were the same for all the experiments conducted (864 °C and 849 ° respectively).

5.4.1.1 CCE

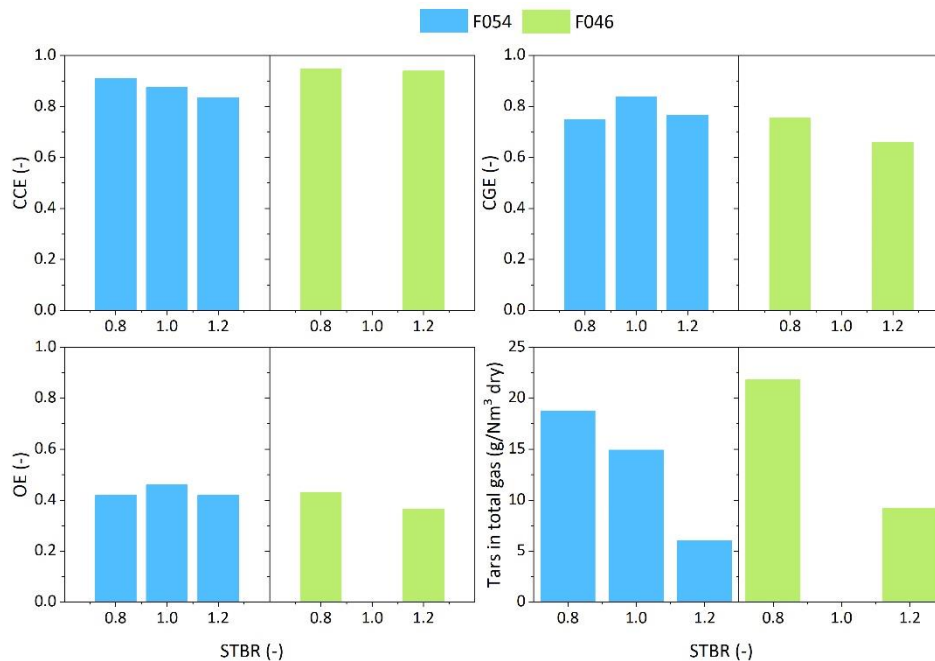


Figure 5.3: Effect of STBR and bed material particle size on the CCE (top left), CGE (top right), OE (bottom left) and tar content (including benzene) in the product gas for PG steam/air gasification with $\lambda = 0.2$ at temperatures between 830 °C and 840 °C in the IHBFBRS. Corresponding experimental indexes: 1,2,3,4 and 5 (SP2).

By examining the CCE and its relationship with the STBR (Figure 5.3), it becomes apparent that it is negative for both bed materials studied. The CCE drops by roughly 4 % when the STBR increased from 0.8 to 1 and from 1 to 1.2 for F054. For F046 the effect of reducing the STBR is less apparent, since the drop was only 1 % between the 0.8 and 1.2 STBR set points. In general, a higher steam supply is expected to promote the water-gas shift (WGS) reaction as well as carbon (heterogeneous WGS), methane and tar reforming, mainly to CO and H₂ [38, 39]. Therefore, higher carbon conversions were expected for increasing STBR at least until a certain point. When very large amounts of steam are introduced in a steam reformer at temperatures lower than the operating temperature, the temperature of the bed also drops. This leads to a subsequent decrease of the carbon conversion efficiency [40]. In the IHBFBRS, temperature is controlled according to a set point, so such a behaviour would not be noted by the temperature readings. An indirect way to evaluate the system's behaviour is through the operation time of the bottom burner, which can provide a correlation between STBR and the power supplied to the system. From Table 5.3, it can be concluded that for both F054 and F046 experiments, a significant decrease in the operating time of the bottom burner for a STBR of 0.8 took place, compared to 1.2 and 1. This indicates that for lower STBR the heat requirement of the process is lower. Since the amount of biomass feed and the λ are the same for all these experiments, that behaviour can be attributed to a lower carbon conversion efficiency. The total amount of char produced from the steam/air experiment corresponds to the amount of carbon residue of the steam reforming process that was not converted through the oxidation reactions with air. For lower STBR, reduced char conversion by steam, leaves more carbon available for the exothermic oxidation reactions. This can lead to reduced heat requirements and increased CCE values for lower STBR, explaining the contradiction of the latter with literature. The lower fluidization velocity/gas residence time imposed with lower STBR, since the biomass and air flow remain constant, add to this effect.

Carbon conversion appears to be promoted by employing a larger particle size (87 % versus 94 % on average, in favour of F046). However, as it has also been reported in [41], smaller bed material particles increase the turbulence in the bed (higher particle-related Reynolds numbers) leading to

improved heat and mass transfer in the area and therefore higher carbon conversion. Additionally, it should be mentioned that for Geldart B particles, such as in this case, the bubble size is independent of the particle size [42], so this aspect of hydrodynamics does not offer any explanations for the observed behaviour. Furthermore, slightly higher bed temperatures (~6 °C on average) and lower initial freeboard temperatures (by 11 °C on average) were reported for the smaller bed material particle size experiments. The latter observation showcases improved heat transfer capabilities although the difference in temperature is not that large. The improved heat transfer is also evident by the reduced operating time of the bottom burner for F046, as shown in Table 5.3. Consequently, the higher carbon conversion noted for the F046 experiments compared to using F054, can be attributed to experimental error in char collection. Alternatively, it can be hypothesized, that the improved heat and mass transfer for the F054 experiments, increases the accessibility of the char particles, thus increasing the tar cracking capabilities of the char bed inventory. This could lead to enhanced secondary coking and therefore higher char yields.

Table 5.3: Percentage of actual operating time for the bottom and top IHBFBRS burner for the various STBR steam/air gasification experiments conducted with PG as feedstock.

	Bed Material				
	F054			F046	
STBR	1.2	1	0.8	1.2	0.8
Bottom burner on (%)	96.3	96.7	81.3	86.5	73.1
Top burner on (%)	84.4	82.3	91.4	91.7	91.1

5.4.1.2 CGE, OE and gas composition

In regard to CGE and OE, where the differentiating factor among the various experiments is the LHV value of the product gas, no clear trends or correlations emerge. Overall, for the F054 steam/air gasification experiments with PG, the average CGE was 78.4 % and average OE was 43.3 %. The higher CGE value noted for the STBR=1 / F054 experiment can be attributed to the lower N₂ content of the product gas of this experiment by roughly 2 vol. % compared to the experiments with STBR of 1.2 and 0.8. The corresponding values for the F046 experiments with PG (which were two instead of three) were 70.6 % and 39.8 %, for CGE and OE, respectively. As it was the case for the STBR=1 / F054 experiment before, also here the low values for the STBR=1.2 / F046 are outliers, due to a much higher N₂ content in the product gas. In Figure 5.4, the dry nitrogen free (dnf) composition of the gas produced, is presented for both F054 and F046 bed material sizes. For both cases, a positive correlation of STBR with H₂ and a negative one with CO is established. For CH₄, a drop is observed, namely 0.4 vol. % dnf on average for F054 and 0.7 vol. % dnf for F046. However, the short range of experimental points (three for F054 and two for F046) along with the low magnitude of the drop, do not allow drawing any concrete conclusions from this observation. Overall, such trends were highly anticipated, since the WGS, CH₄ reforming and tar reforming reactions are promoted by the addition of more steam [43]. Regarding the differences between the two bed materials employed, it can be noted that while CH₄ production was quite similar for both, the increase in bed material size, seemed to lead to lower H₂ and higher CO and CO₂ yields. Overall, the improved heat and mass transfer imposed by the increased turbulence in a system employing lower bed material sizes compared to higher ones, has been reported to lead to increased catalytic activity in the case of olivine bed material in favour of H₂ production [41]. The corundum bed material employed in this work is expected to be inert. However the char that is produced and accumulates in the bed can act as a catalyst for reforming or cracking reactions of hydrocarbons and its presence in general promotes tar destruction and syngas production [44]. Therefore, it can be argued that the increased turbulence of the system when lower bed material particle sizes are employed, enhances interaction with char particles that promotes tar

conversion. It has been shown in literature [45], that aromatic compounds can decompose over the char surface due to coking, forming also H_2 in the process. In general, char's catalytic activity is dependent on its pore size, surface area as well as on its mineral content [46]. By decreasing the bed material particle size employed and thus increasing the turbulence of the system, the char surface area available for tar elimination reactions becomes larger due to the larger accessibility of the char particles.

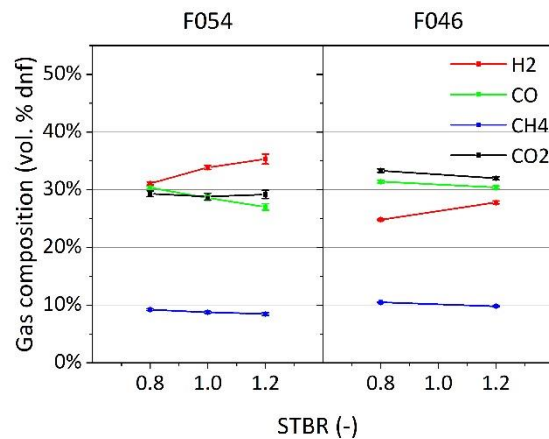


Figure 5.4: Effect of STBR and bed material particle size on the composition of gas produced from PG steam/air gasification with $\lambda = 0.2$ at temperatures between 830 °C and 840 °C in the IHBFSR. Corresponding experimental indexes: 1,2,3,4 and 5 (SP2).

5.4.1.3 Tar and benzene composition

The increasing STBR leads to a significant decrease of the amount of tars produced for both cases of bed material studied (Figure 5.3). For F054, from a 19 g/Nm³ dry concentration for a STBR of 0.8, the tar in total gas content dropped to roughly 6 g/Nm³ dry for a STBR of 1.2. The corresponding drop for the F046 experiments was similar, namely from 22 g/Nm³ dry at 0.8 to 9 g/Nm³ dry at 1.2. In general, the increase of the STBR leads to the enhancement of tar reforming reactions to produce H_2 and CO, an effect very well described in literature [47, 48]. This observation is also consistent with the previous remarks regarding H_2 formation intensification with increasing STBR. The individual tar compounds formed at each case are presented in Figure 5.5. Benzene production is included separately since it is not considered a tar species and is by far the most abundant condensable product compound detected.

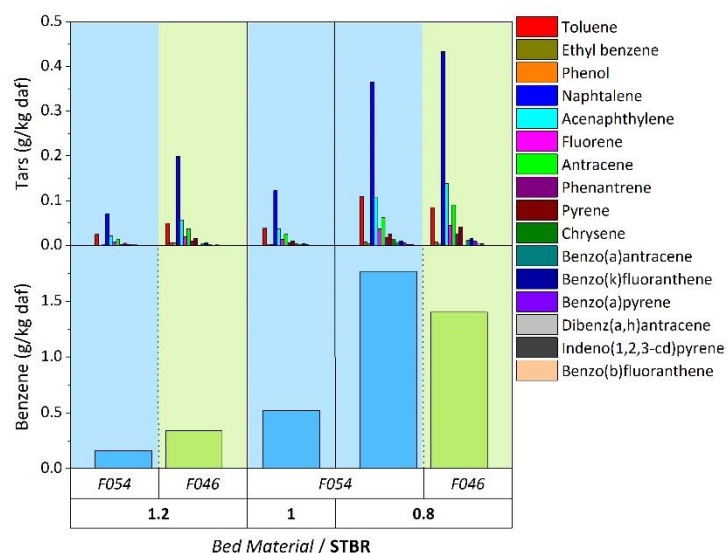


Figure 5.5: Effect of STBR and bed material particle size on the benzene and tar compounds production per kg of d.a.f. PG feed, for steam/air gasification with $\lambda = 0.2$ at temperatures between 830 °C and 840 °C in the IHBFBRSR. Corresponding experimental indexes: 1,2,3,4 and 5 (SP2).

The increase in STBR leads to a decrease of both the amounts of benzene and naphthalene formed. Naphthalene belongs to the light polyaromatic tars category [49], constituting its main representative in terms of abundance in this work and the second most abundant condensable specie formed after benzene. Overall, the increase of STBR led to a decrease in the heterocyclic (phenol), light aromatic (toluene, ethyl benzene) and light polyaromatic tars (naphthalene, acenaphthylene, fluorene, anthracene, phenanthrene). The only exception was noted for the case of heterocyclic (phenol) tars for F046. According to Jess [50], the effect of steam on aromatics conversion can be considered as minimal. Furthermore, it has been suggested that the presence of H_2 inhibits the conversion of benzene and naphthalene in particular [50] or even PAH in general [51]. More specifically, even though the presence of H_2O increases the tar decomposition rate, the presence of H_2 , whose yield is positively correlated to H_2O , depresses the tar decomposition rate. The H_2 reacts with radicals generated to form a stable tar molecule and a hydrogen radical, thus leading to higher concentrations of smaller, more stable PAHs, such as naphthalene and benzene [52]. This effect is not presented in the steam gasification experiments with PG presented here, since both benzene and naphthalene yields decrease with increasing steam supply. In regard to the total tar yield, its negative correlation with STBR has been reported in literature [48, 51]. Correlations between temperature and the efficiency of tar suppression, as well as the selectivity towards lighter compounds and the increase of STBR have also been reported in [53]. It has also been argued, that the presence of steam does not influence aromatic tar yields, as far as no catalyst of temperatures above 1100 °C are employed [54]. For benzene in particular, it has been reported that its decomposition rate is independent of steam concentration [55]. Finally, Qin et al. [56], argue that enhanced production of H radicals at high temperatures during steam gasification can lead to stabilization of tar intermediates and thus prevent their polymerization to aromatic compounds. Therefore, the reason for the observed major reduction in benzene and naphthalene yields for increasing STBR can be attributed to the catalytic activity of the char accumulating in the bed area, promoting benzene and tar steam reforming.

Furthermore, a 3 g/Nm³ difference in tar production (Figure 5.3), was observed between the two bed materials for STBRs of 0.8 and 1.2, with the larger particle size bed material (F046) presenting the higher values. For both STBR values studied, the PAH (light and heavy) yield was significantly higher for the F046 experiments. However, for the STBR = 0.8 experiments, the BTEX content (xylene was not measured) was higher for the F054 experiments (Figure 5.5). The improved heat and mass transfer,

due to the turbulence increase of the system, appears to promote tar destruction. Tar production was probably reduced through the increased catalytic activity of the char particles accumulating in the bed, when the smaller (F054) bed material results are compared to the coarser ones (F046). The higher BTEX yield observed for F054 in the case of STBR of 0.8 can be attributed to the more intense formation of those products through PAH cracking [50] compared to the case of F054.

5.4.2 Effect of λ – high temperature (HT) versus low temperature (LT) experiments

In this section the F046/ExR experiments with experimental indexes 7 (SP2) and 8 (SP2) are compared. The two most pronounced effects of λ reduction concern the temperature of the system as well as the increased char accumulation in the bed area. For the two experiments discussed in this section, with the decrease of λ from 0.2 to 0.04 the average bed temperature (TC01 – TC03) dropped from 833 °C to 711 °C and the maximum freeboard temperature from 878 °C to 825 °C. The average freeboard temperature dropped from 865 °C to 804 °C, while the location of the maximum point moved from TC05 to TC06.

5.4.2.1 CCE, CGE and OE

The reduction of λ , expectedly led to lower carbon conversion levels (89 % versus 82 %) (Figure 5.6). The char mass obtained through the bed sieving process was a factor 8 times higher for the LT experiments (0.04 kg/kg of feed versus 0.005 kg/kg of feed). Overall, the decrease in CCE for lower λ and temperatures, was expected since both factors enhance char oxidation and in general the breakdown of biomass molecular bonds [40]. Regarding CGE, it increased by 4 % for the decrease of λ , due to the increase of the product gas LHV from 4.9 MJ/Nm³ to 6.4 MJ/Nm³, but also due to the lower amount of ExR feed employed (8 kg/h for LT versus 10 kg/h for HT). On the contrary, the OE of the system decreased for lower λ values. This reversal of the behaviours for the OE compared to CGE, is attributed to the fact that the bottom burner was on for 95 % of the time for the HT experiment compared to the LT experiment where it was on constantly. This corresponds to a power input difference of ~3.4 MJ, leading to the slight increase of the overall efficiency for the high λ and temperature experiment, despite the fact the LHV of the product gas is significantly lower in this case and a higher biomass feeding rate was employed. In regard to the LHV, its value increased for lower λ values, apparently due to less effective dilution of the product gas with N₂, considering that the CO concentration was actually lower and the one of CH₄ practically the same for the LT ($\lambda = 0.04$) experiment.

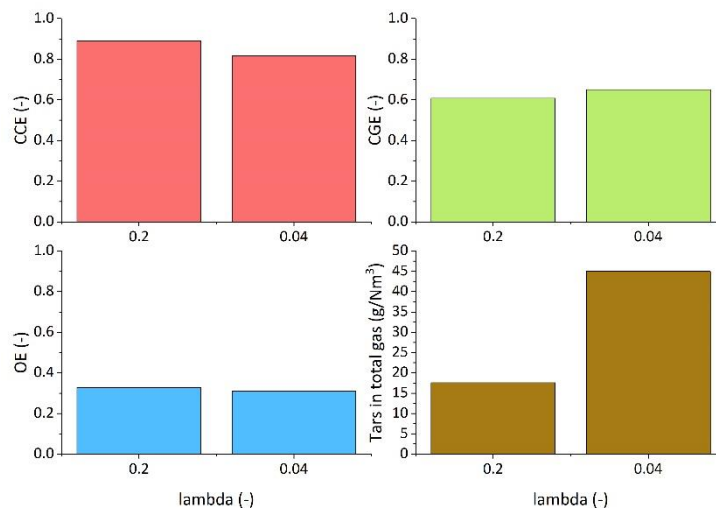


Figure 5.6: Effect of lambda (λ) on the CCE (top left), CGE (top right), OE (bottom left) and tar content (including benzene) in the product gas for ExR steam/air gasification with STBR = 1.2 in the IHBFSR. Corresponding experimental indexes: 7 and 8 (SP2).

5.4.2.2 Gas, tar and benzene composition

In the graphs of Figure 5.7, the volatile products of ExR steam/air gasification LT and HT experiments are presented. The reduction of λ , led to an increase of the H_2 yield by ~12 vol. % dnf. The CO and CO_2 yields decreased by 7.5 and 4 vol. % dnf, respectively, while the CH_4 yield was not affected. The N_2 concentration of the product gas was significantly reduced, namely from 57 vol. % to 46 vol. % dry. It should also be mentioned that the total gas yields of the two experiments were very similar (0.99 and 1.01 Nm^3/kg daf for the HT and LT experiment, respectively). On the other hand, the water content in the produced syngas increased from 28 vol. % for the HT to 47 vol. % for the LT experiment. In regard to total benzene and tar formation (Figure 5.6), the reduction of λ and temperature, led to much higher overall yields. Tar content in the gas product (including benzene) increased from 17.6 g/Nm^3 to 45 g/Nm^3 for the reduction of λ from 0.2 to 0.04. Benzene was the most abundant condensable specie detected by a huge difference, while naphthalene, acenaphthylene, toluene, anthracene and fluorene followed in roughly that order. The yield of each individual compound studied, increased by at least three times for the decrease in λ value, except for ethyl benzene which was not influenced by this change. The most pronounced effect was evident on the yields of phenol and toluene. More specifically, the phenol yield was 14 times and the toluene yield 7 times higher for the LT experiment compared to the HT one.

Since steam reforming reactions are endothermic, the reduction of the reactor temperature as an indirect effect of λ reduction leads to less H_2O and carbon reforming, as it was also evident by the decrease of CCE [57]. Consequently, H_2O and char yields are higher for lower λ , as it was the case in this work. Another effect of the lower system temperature, especially in the bed area, is the steep increase of the phenol yield. Despite phenol not being one of the most abundant tars in these experiments, its presence in the product gas is indicative of the performance of the IHBFSR in terms of tar removal efficiency. In general, lower temperatures favour the formation of tar species such as phenol and toluene, with diversified substituent groups [58]. The present results illustrate, that even though for the LT experiments, the average temperature of the freeboard is around 804 °C, it does not suffice for cracking of such products. Of course, the reduced amount of air in the system compared to the HT experiments enhances this particular behaviour, due to the limitation of tar oxidation reactions. For benzene, its yield for the LT experiment was 2.5 times higher than for the HT experiment. In general, higher temperature and lambda values reduce the total amount of tars

produced but also lead to an increased aromatisation (PAH and BTEX formation) [58, 59]. However, in the LT experiments, the operating temperature and/or oxidative media availability does not suffice for the decomposition of heavier tars to more stable compounds such as benzene and naphthalene. Consequently, benzene formation comes mainly from primary pyrolysis products decomposition in this case. For HT experiments where both pathways for benzene formation are available, the lower yields indicate its decomposition at least to a certain degree. Therefore, it can be argued that in the context of the IHBFBRSR, benzene production is largely dependent on the temperature and/or oxidative media presence. Naphthalene and PAH yields in general are significantly higher for the LT experiment even though their production is expected to be fairly limited at temperatures close to 700 °C [53, 60, 61]. Therefore, one would expect that the amount of PAH produced from the LT experiments would be less than for the HT ones, considering the aforementioned remark. As it mentioned by Milne et al. [61] the addition of oxygen at low temperatures can accelerate the destruction of primary pyrolysis products (levoglucosan, hydroxyacetaldehyde, furfurals, etc.), but it has a minimal effect on benzene and secondary (phenolics, olefins) and tertiary products (BTEX, PAHs) destruction. Therefore, the presence of oxygen is not the deciding factor in this situation since temperature is supposed to be the limiting factor in the formation of PAH. Considering these observations, two different, however non-mutually exclusive hypotheses can be made regarding the higher amount of PAH produced from the LT compared to the HT experiments. The first one is that PAH formation for LT experiments takes place in the freeboard where the temperatures are higher rather than in the bed area. The second hypothesis is based on the catalytic effect of the accumulated char bed, which was already presented for the PG experiments presented in Section 5.4.1. Therefore, it can be hypothesized that the presence of char in the bed could lead to PAH formation at lower temperatures than usual.

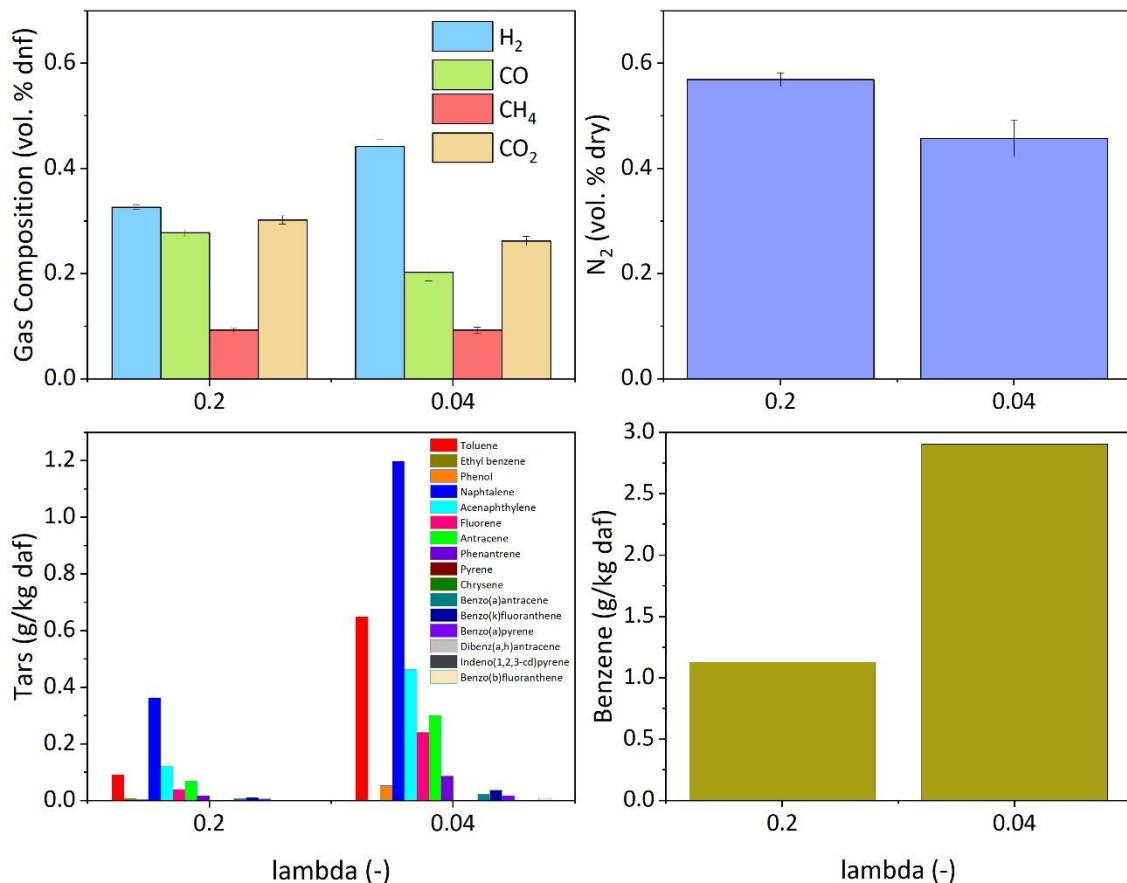


Figure 5.7: Product gas composition (top left), N₂ yield (top right), tar yield (bottom left) and benzene yield (bottom right) for steam/air gasification of ExR with STBR = 1.2 in the IHBFBRSR for different values of lambda (λ). Corresponding experimental indexes: 7 and 8 (SP2).

Regarding H_2 , it was expected that its yield would be negatively influenced by the reduction of the process temperature. H_2 production is generally favoured by high temperatures that promote endothermic char gasification and steam reforming and/or cracking of light hydrocarbons and tars [40, 48]. Furthermore, its production is also linked to tar secondary reactions [60], that for the LT experiments appear to be less active. However, elevated values of λ can also increase H_2 partial combustion rate [40]. Therefore, it can be argued that H_2 production in HT experiments is severely reduced by the combined effect of partial oxidation and the high temperature of the freeboard (865 °C on average). The fact that the H_2 yield is significantly higher for the LT and low λ experiments points to this direction. Regarding the rest of the gases, the increase of CO_2 for higher λ can be attributed to the enhancement of char, CO and CH_4 oxidation reactions [2]. On the other hand, CO values despite being expected to drop for higher λ due to increased partial oxidation [62], showed an increasing trend. This can be potentially attributed to the increased CCE for higher λ / temperature experiments, which hints to the formation of CO through char partial combustion [2]. Additionally, it is also possible that homogeneous tar conversion, can also be responsible for the increased CO formation in this particular case [60].

5.4.3 Effect of secondary air injection

In this section, the effect of the injection of air in the freeboard is going to be examined for both bed materials (F046 and F054) studied in this campaign. The LT/ExR experiments which were studied in that regard, correspond to the index numbers 8 to 12 as described in Table 5.2. Overall, the experiments described in this section were performed with 0, 4 and 8 kg/h of secondary air injected. The addition of 4 kg/h and 8 kg/h of secondary air, corresponds to overall lambda ($\lambda_{overall}$) values of 0.13 and 0.21, respectively. These values were calculated using Eq. 2 and considering both the air injected through the bottom of the IHBFSR and the freeboard. For the F046 experiments the increase of the amount of secondary air led to the increase of the average freeboard temperature (TC04 – TC07) (804, 807 and 814 °C, respectively). The magnitude of the observed differences is low, because TC04 is included in this calculation. For the LT experiments, the increased char accumulation in the bed leads to the expansion of the “bed” area to include also TC04. This explains the overall low average freeboard temperature, since the “char bed” is included in it. If just the last two thermocouples are considered (TC06 – TC07), which correspond to locations above the secondary air injection point, the corresponding temperature values show the actual changed imposed on the system (818 °C for 0 kg/h versus 857 °C for 4 and 8 kg/h). The respective values for F054 are slightly lower in terms of TC04 – TC07 average (796 °C and 805 °C for 4 and 8 kg/h respectively) and 848 °C – 856 °C for the TC06 – TC07 average. Overall, the average bed temperature for the three F046 experiments was 708.6 °C, roughly 10 °C lower from the corresponding value of the two F054 experiments (Table 5.2). In the previous comparison of the effect of bed material particle size on the temperature of the TC01 – TC05 area of the IHBFSR (Section 5.4.1) similar conclusions were derived. Namely, the increased turbulence of the system due to the smaller particle size of the bed material for F054 leads to improved heat and mass transfer, which in its turn leads to smaller differences in temperature between bed area and early (TC04 – TC05) freeboard. This leads to a higher bed and lower initial freeboard temperature for the F054 steam/air gasification experiments with ExR, by 10 °C and 23 °C respectively on average, compared to the F046 experiments.

5.4.3.1 CCE

The CCE values for F046 (coarser) were similar to F054 for 4 kg/h of secondary air, but they were ~3.5 % higher for 8 kg/h (Figure 5.8). This result is fairly consistent with the corresponding results of Section 5.4.1, however the magnitude of the observed differences is significantly smaller. For CCE, a slight increasing trend for increasing amounts of secondary air was noticed in both cases, most notably in the case of F046 where the value rose from 82 %, to 83 % and 88 %, respectively. In both cases of bed material particle size, the amount of char collected through the bed sieving process was not particularly affected by the secondary air injection, as it was expected. However, the total amount of fines in the bed and cyclones decreased significantly for increasing secondary air injection. For F054, a drop of 15 % was noted in the amount of fines produced from 8 kg/h of secondary air compared to the 4 kg/h case. For F046, the corresponding drops were 19 % and 67 % from 0 to 4 kg/h and 4 to 8 kg/h, respectively. Therefore, it can be argued that the introduction of secondary air leads to partial char oxidation reactions in the freeboard, reducing the amount of char collected in the cyclones and thus improving carbon conversion.

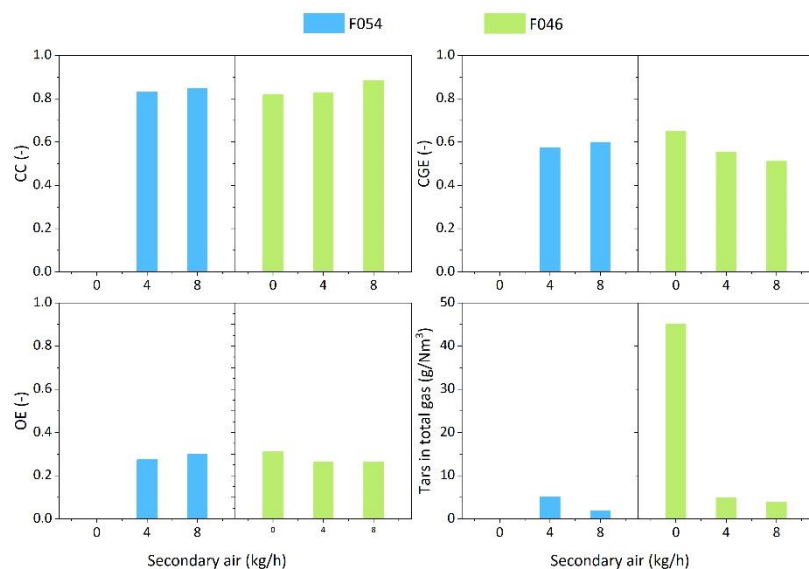


Figure 5.8: Effect of secondary air injection and bed material particle size on the CCE (top left), CGE (top right), OE (bottom left) and tar content (including benzene) in the product gas for ExR steam/air gasification with $\lambda = 0.04$ and STBR = 1.2 in the IHBFSR. Corresponding experimental indexes: 8, 9, 10, 11 and 12 (SP2).

5.4.3.2 CGE and OE

Regarding CGE and OE, contradictory results are obtained from the experiments conducted with the two different bed materials. For the F046 experiments, the increase of the amount of secondary air employed led to lower CGE and OE values, while the opposite behaviour was observed for the F054 experiments. For both cases, LHV values decreased for increasing amounts of secondary air, mostly due to dilution of the product gas with N₂. In particular, for the F046 experiments the LHV fell from 6.4 MJ/Nm³ dry, to 4.9 and 4 MJ/Nm³ dry, when the secondary air injection was changed from 0 to 4 and 8 kg/h, respectively. The corresponding values for F054 were 5 and 4.3 MJ/Nm³ dry for 4 and 8 kg/h, respectively. Considering this trend for the calorific value of the product gas, the observed behaviour of the CGE and OE can be attributed to its actual yield. For the F054 experiments the dry-N₂-free gas yield was favoured by the increase in the amount of secondary air injection, rising from 0.94 to 1.05 Nm³ dnf/kg daf. On the contrary, in the case of F046 the dry-N₂-free gas yield decreased from 1.01 Nm³ dnf/kg daf for no secondary air added, to 0.92 and 0.87 Nm³ dnf/kg daf, for 4 and 8 kg/h, respectively.

5.4.3.3 Gas composition

The aforementioned increase of the gas yield in the case of the F054 steam/air gasification experiments, for increasing amounts of secondary air injection, in contrast to F046, can be attributed to the improved tar conversion achieved with F054, especially when the two respective 8 kg/h secondary air injection experiments are compared. The F054 experiments showed better tar conversion (Figure 5.8 and Figure 5.10), similarly to the previously presented PG experiments in Section 5.4.1. The increased turbulence of the system for lower bed material particle sizes (F054), enhances interaction with char particles that accumulate in the bed promoting tar conversion. When comparing the 8 kg/h secondary air injection experiments in terms of dry product gas, the N₂ in the F054 experiments is roughly 4 vol. % lower than for F046. The opposite behaviour is found for H₂, CO and CO₂. In particular, the corresponding yields were higher for F054 compared to F046 by approximately 3 vol. %, 0.6 vol. % and 1 vol. %, respectively. As previously discussed, H₂ and CO are considered as direct products of tar cracking/reforming reactions, which explains the observed difference. The difference in CO₂ could be due to the occurrence of CO oxidation reactions to a larger extent for the F054 experiments, following its aforementioned increased production. Overall, the improved tar cracking capabilities of smaller corundum bed particle sizes was also proven here. Nevertheless, in terms of the dry-nitrogen-free gas composition, the differences between the bed material sizes were marginal, with the exception of H₂.

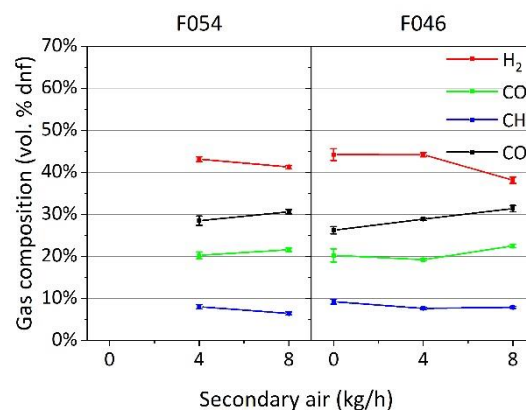


Figure 5.9: Effect of secondary air injection and bed material particle size on the composition of gas produced from ExR steam/air gasification with $\lambda = 0.04$ and STBR = 1.2 in the IHBFBRSR. Corresponding experimental indexes: 8, 9, 10, 11 and 12 (SP2).

When studying the effect of secondary air injection in the dry-N₂-free gas composition, it is clear that it had a negative impact mostly on the H₂ and to a lesser extent on the CH₄ yield. On the contrary, CO and CO₂ yields were positively influenced by the increase of the amount of secondary air introduced. The reduction of the combustible gases yields was expected due to the addition of the secondary air [63, 64], however this was not seen for CO. Therefore, it can be suggested that the enhancement of CO production from tar cracking/reforming as well as from the Boudouard and carbon oxidation reactions, as it is suggested by the higher CCE values, overcomes the increased effect of CO combustion. Furthermore, it is apparent, that the transition from 0 kg/h to 4 kg/h of secondary air had no influence at all in the H₂ yield for the F046 experiments. Apparently, the increased H₂ combustion rate is matched by the increased production through tar cracking and reforming reactions, due to the more reducing environment and the higher temperatures achieved.

5.4.3.4 Tar and benzene composition

The overall positive effect of secondary air addition on tar reduction, due to the oxidative atmosphere and the elevated temperatures achieved in the freeboard (Figure 5.8), has also been reported in the literature [63-66]. Its effect on specific compounds is presented in Figure 5.10. With

the exception of benzene for 4 kg/h of secondary air, the amount of tars and benzene produced from steam/air gasification with corundum F054 were lower than in the F046 experiments, in a behaviour consistent with the HT experiments presented in Section 5.4.1. In regard to the effect of the secondary air injection, for the F046 experiments, the overall tar yield decreased by ~90 %, regardless of the amount. This drop corresponds to a reduction from ~1 vol. % (45 g/Nm³) of the total dry gas to 0.11 vol. % (5 g/Nm³) and 0.09 vol. % (4 g/Nm³) for 4 kg/h and 8 kg/h of secondary air, respectively. For F054, with the increase of the amount of air injected from 4 kg/h to 8 kg/h the total amount of tars and benzene produced, decreased by 63 wt. % to 1.9 g/Nm³.

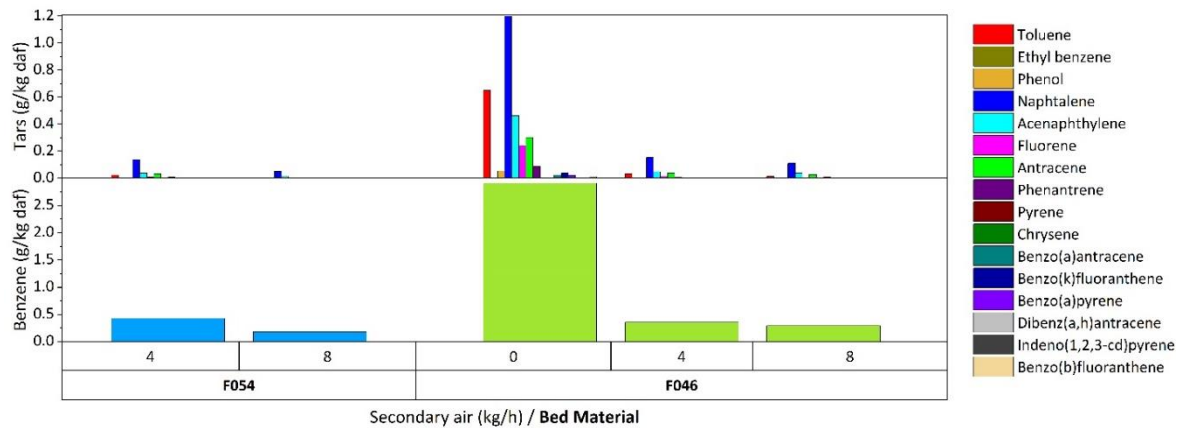


Figure 5.10: Effect of secondary air injection and bed material particle size on the benzene and tar compounds production per kg of d.a.f. ExR feed for steam/air gasification with $\lambda = 0.04$ and STBR = 1.2 in the IHBFSR. Corresponding experimental indexes: 8, 9, 10, 11 and 12 (SP2).

As it was also the case for the HT / PG and ExR steam/air gasification experiments, benzene was by far the most abundant condensable species detected. The injection of secondary air (4 kg/h) with F046 as a bed material led to benzene's yield reduction by 88 wt. % compared to the no secondary air case. With the increase to 8 kg/h for F046, a 17 wt. % reduction of benzene's yield was observed, with the corresponding decrease for F054 being almost three times higher. Naphthalene, acenaphthylene, anthracene and toluene were the most abundant tar species formed, with naphthalene presenting the higher concentrations by far. Its yield was reduced by 64 % with the increase of secondary air amounts from 4 to 8 kg/h for F054. For F046, the increase from 0 kg/h to 4 kg/h and finally to 8 kg/h led to a reduction by 87 wt. % and 28 wt. % of the naphthalene yield. In terms of tar classes, heterocyclic tars (phenol), were reduced by 92 % and 77 % for an increase of secondary air injection from 4 kg/h to 8 kg/h for F054 and F046, respectively. The amount of light aromatics and light polyaromatics also decreased with increasing amounts of secondary air. The latter effect was more pronounced for F054, where the anthracene yield was reduced by roughly 97 %, while phenanthrene disappeared completely absent from the 4 to 8 kg/h steam/air gasification experiment. The reduction especially of light aromatic and light PAH has also been reported in the literature for secondary air injection systems [66]. Considering heavy polyaromatic tars, while for the F054 experiments their yield dropped by 90 % from 4 kg/h to 8 kg/h of secondary air, in the case of F046, after an initial drop of 93 % from 0 to 4 kg/h, their yield increased by 60 % when the secondary air injection was further increased to 8 kg/h. This was mostly due to a steep increase of the pyrene yield by ~60 times. Such an observation for the effect of secondary air injection on heavy PAH was also made in [67] with no clear indication on the reasons behind it. Pyrene is a product of naphthalene decomposition and constitutes a stable PAH without substituent groups [50, 68]. Therefore the increase of its yield might be attributed to the decomposition of mainly naphthalene [69], which can be found among the gasification products in higher amounts for F046 rather than F054 bed material. It should be mentioned that the low amounts of heavy PAH detected, lead to a very high potential influence of an

experimental error on the values discussed here. Overall, it can be argued, that the injection of secondary air appears to be a very efficient method for tar removal in the context of the IHBFSR, regardless of the class.

5.4.3.5 Overview of the effect of secondary air injection

In general air injection, either primarily or secondarily, led to the increase of the bed temperature of the IHBFSR, due to increased char and biomass oxidation (Table 5.4). However, the effect of its addition on the average TC06-TC07 temperature on the freeboard is negligible. Therefore, it can be argued that the difference in terms of the temperature profile between the two methods of supplying air, lies mostly on how wide the high temperature zone is and on the location of the maximum. However, another effect of the reduction of the primary air is the increased accumulation of char in the bed area. As it is evident by the readings of TC04, the temperature at this region is slightly above the average bed temperature. The reduction of primary air leads to lower CCE values, even though secondary air injection improves the secondary conversion of fine char particles in the freeboard. The effect of secondary air addition on the gas yield (dnf) is negative. Despite the fact that lower amounts of total air are introduced and therefore dilution by N₂ is reduced, the lower degree of char conversion plays a significant role on the amount of gas produced. For example, the carbon content in the product gas was 1.2 kg dry less for experiment 9 compared to 7. The negative effect of secondary air addition on the gas yield is also reflected on the OE values (Table 5.4). However, the LHV of the product gases can be viewed as comparable, between the cases of 4 kg/h secondary air injection and 11.3/0 kg/h of primary/secondary air. At this level, the effect of N₂ dilution is apparently evened out by the increased tar conversion due to the catalytic char bed and localised air supply. This “dedication” of the air supplied to the system to tar conversion along of course with the effect of the char bed, is reflected on tar content in the product gas. Even though less air is injected for experiment 9 (and of course 10), the tar content is significantly lower. Additionally, the H₂/CO ratio is improved by the reduction of the primary and the addition of secondary air. Conclusively, the negative effect of secondary air addition on the syngas quality, can be mitigated through the employment of moderate amounts of air ($\lambda_{\text{overall}} \approx 0.13$) and the catalytic effect of accumulating char, as it was previously suggested also in [66]. Furthermore, the results presented both here and Section 5.4.1, strongly suggest that the employment of smaller (F054) bed material particle size can lead to improved quality of the produced syngas.

Table 5.4: Comparison of the effect of the total amount of air introduced and the respective introduction method for steam/air gasification experiments in the IHBFSR, with a STBR of 1.2, ExR as a feedstock and corundum F046 as a bed material.

Index (#)	Primary/secondary air (kg/h)	Average bed temperature/TC04/Average TC06-TC07 (°C)	Overall λ (-)	CCE (-)	Gas Yield (Nm ³ dnf/kg daf)	LHV product gas dry (MJ/Nm ³ dry)	OE	H ₂ /CO	Tars in total gas (g/Nm ³)
7	11.3/0	833/865/859	0.23	0.89	0.99	4.90	0.33	1.2	17.6
9	1.9/8	704/745/857	0.21	0.88	0.87	3.96	0.26	1.7	3.9
10	1.9/4	710/731/857	0.13	0.83	0.92	4.86	0.26	2.3	4.9
8	1.9/0	711/775/818	0.04	0.82	1.01	6.44	0.31	2.2	45

5.4.4 Effect of steam/air gasification duration

For the experiments where tar sampling was performed twice, the first sampling point (SP1) was initiated after switching from the combustion/warming up regime, to steam/air gasification. The second sampling (SP2) was performed after a steady state was achieved. The main purpose of performing both samplings, is to investigate the effect of char accumulation in the bed. For HT experiments (5,6 and 7), the temperature of the entire system increased with time (Table 5.5). For HT experiments, char accumulation still occurs at the bed, however to a much lower extent compared to the LT experiments, due to its partial oxidation. On the contrary, for the LT experiments the average bed temperature decreases between SP1 and SP2. The behaviour for the TC04 – TC05 region was similar, with the temperature increasing with time for the HT experiments and decreasing for the LT ones. Increased char accumulation for the LT experiments leads to comparatively lower temperatures for TC04, which tends to become equal to the one of the corundum fluidized bed right below. Finally, regarding the TC06 – TC07 average temperature, its value increased in all cases, except for 8 kg/h of secondary air injection. In this case, the temperature in this region of the freeboard was at roughly the same levels throughout the entire the experiment.

5.4.4.1 Gas composition

Accumulation of char in the bed, appears to be beneficial for the gas yield, with the average increase, despite only marginal in some cases, being $\sim 0.15 \text{ Nm}^3 \text{ dnf/kg daf}$. The enhanced catalytic activity of the char bed for SP2 vs SP1, which promotes tar decomposition and permanent gases formation, potentially explains the observed behaviour. The increase of the gaseous yield appears to be more significant for LT experiments (average increase of 0.21 versus 0.05 $\text{Nm}^3 \text{ dnf/kg daf}$), further substantiating this conclusion (Table 5.5). Additionally, apart from HT experiment 5 with PG as a feedstock, the influence of extended duration of the experiment was beneficial for the H_2 yield, which increased by 4 vol. % on average for HT and 8 vol. % for LT experiments, between SP1 and SP2. Therefore, H_2 production is positively associated with tar catalytic conversion in the accumulated char bed [70]. In the previous section, it was argued that the effect of secondary air injection on tar reduction and therefore H_2 production for LT experiments, is more effective than the higher bed temperatures of the HT experiments in that regard. This is showcased again here, along with the also aforementioned positive impact of secondary air injection on the H_2 yield. Contrary to H_2 , the CO and CH_4 were lower for SP2. The effect of longer steam/air gasification duration was again more significant for the LT experiments regarding these two gases. For CO, its yields decreased by 7 vol. % for LT experiments versus less than 1 vol. % for HT on average, between SP1 and SP2. CH_4 yields decreased by 3 vol. % for HT experiments versus less than 1 vol. % for LT experiments between SP1 and SP2. Finally, the CO_2 yields presented a small increase (1 vol. % on average) for the LT experiments.

5.4.4.2 Tar and benzene composition

For HT experiments (5, 6 and 7), the tar content in the product gas increased between SP1 and SP2. The increase was marginal (3 wt. %) for the PG experiment, but quite substantial for the two HT / ExR experiments (53 wt. % and 68 wt. %, respectively). For the PG experiment, the marginal difference can be attributed to the minor temperature differences between the set points. In the two ExR experiments a higher λ was employed for SP1, which can explain the higher tar production presented for SP2. Furthermore, char accumulation does not take place on a large extent in HT experiments, preventing tar catalytic cracking at such levels as for the LT experiments. Regarding individual tar compounds, for both those experiments benzene production more than doubled, while phenol yield increased by one order of magnitude, between SP1 and SP2. Contrary to that however,

the tar yield increased between SP1 and SP2 for the LT experiment 8. Most of the tar species content doubled, as well as benzene's, between those two sampling points. Phenol concentration, in particular, increased by a factor of 74. The fact that char accumulation under these experimental conditions is not enough for tar catalytic cracking to an appreciable extent is showcased by phenol behaviour. In general, char promotes the decomposition of oxygenated compounds even at temperatures lower than the ones achieved in this case [71]. Even though lower temperatures were achieved for the LT experiments and thus the effect of thermal cracking of phenol was less than for the HT ones, the reduction of its yield between SP1 and SP2, further supports the argument. Additionally, heavy PAH production also increased significantly from SP1 to SP2, with the yields of benzo(k)fluoranthene, benzo(a)pyrene and benzo(b)fluoranthene, increasing by ~400, 200 and 250 times, respectively. The yields of those three species combined, contribute to ~1 wt. % of the overall tar and benzene yield, therefore the differences between the set points are subject to a thin margin of sampling error. However, heavy PAH species are of a high importance, since even in low concentrations they can influence the tar dew point greatly [72]. This behaviour of experiment 8, can be attributed to the different temperature between the two set points. Namely, the bed and TC04 – TC05 temperature decreased by approximately 30 °C for both regions. The increase of temperature in the TC06 – TC07 region from 803 °C to 818 °C, was not enough for sufficient thermal cracking of the produced tars. Therefore, despite the presence of the accumulated char bed, the temperature of the freeboard and the method of air supply are very critical for tar removal during steam/air gasification in the IHBFSR. This remark can be well established through the differences between SP1 and SP2 for LT experiments 9, 10, 11 and 12. Starting with the overall tar content of the product gas, its reduction was significant in all four experiments from SP1 to SP2 (Table 5.5). The light and heavy PAH yield decreased by approximately 56 wt. % on average, while the effect on benzene was similar but less pronounced. The catalytic effect of the char accumulated in the IHBFSR is showcased by the decrease by ~52 wt. % on average, of the naphthalene yield for these LT experiments, from SP1 to SP2. In general, naphthalene is stable up to temperatures around 900 °C in a steam/CO₂ environment [73]. Therefore, the reduction of its yield between SP1 and SP2 for the LT experiments with secondary air as shown here, can be partly attributed to the presence of char in the bed. The effect of the use of char as a catalyst for the conversion of tar and in particular naphthalene, which is also here the most abundant tar specie formed, has been well described by El-Rub in [74]. According to this work, tar is adsorbed on active sites of the surface of char particles and undergoes catalytic conversion through two parallel pathways. The first one involves steam and dry gasification reactions for the formation of CO and H₂, catalysed by the char's mineral content. The second path is centred around tar decomposition for the formation of free radicals, which polymerize and form coke deposits on the char surface. According to Burhenne et al. [75], the presence of CO₂ leads to further activation of the char bed which improves benzene removal, although the effect of steam is more pronounced, especially in the context of the hereby presented IHBFSR experiments. In general, it can be argued that despite that char accumulates continuously in the IHBFSR bed, the product yields do stabilize to the hereby presented values (SP2), signalling that tar conversion peaks, but also does not fall below that point. As it has been argued by El-Rub [74], char activity does not decrease with time since its micropores grow to meso and macro pores, which are more effective on tar removal and the accessible mineral content increases with the conversion of its carbon content. Lastly, for the IHBFSR, the char keeps accumulating in the bed as long as gasification continues. Thus it can be argued that the efficiency of the tar conversion process is capped from the process conditions (temperature, λ, method of air supply, bed material, etc.) rather than the char catalyst's activity, as it has also been shown in [76]. High temperatures in particular have been shown to favour tar decomposition over a char bed [77, 78]. Furthermore, as it has been suggested in [79] for the combined use of char and oxidation for tar removal, for high O₂ concentrations, char BET surface area can decrease significantly,

due to partial oxidation. The fact that air can be added above the accumulated char bed in the IHBFSR can address this problem and provide more flexibility on the amount of oxidizing agent added. Overall, the detailed analysis of the properties of the char derived from the IHBFSR experiments (e.g. BET analysis, SEM, XRD, etc.), despite being relevant, was outside the scope of the present study. The corresponding investigation will be presented by the authors in a future study.

Table 5.5: Effect of steam/air gasification duration in the IHBFSR on various process parameters and product yields (experiments 5 – 8)

Index (#)	5		6		7		8	
	SP1	SP2	SP1	SP2	SP1	SP2	SP1	SP2
Set Point	SP1	SP2	SP1	SP2	SP1	SP2	SP1	SP2
Bed Material	F046	F046	F054	F054	F046	F046	F046	F046
Biomass	PG	PG	ExR	ExR	ExR	ExR	ExR	ExR
$\lambda(-)$	0.20	0.20	0.23	0.20	0.23	0.20	0.04	0.04
STBR (-)	0.8	0.8	1.2	1.2	1.2	1.2	1.2	1.2
Sec. air (kg/h)	0	0	0	0	0	0	0	0
Average Bed T (°C)	831	832	826	839	816	833	740	711
Average TC04 - TC05 (°C)	876	875	851	864	853	872	823	790
Average TC06 - TC07 (°C)	838	857	818	855	819	859	803	818
Gas Yield (Nm³ dnf/kg daf)	1.19	1.23	0.87	0.88	0.88	0.99	0.61	1.01
LHV product gas (MJ/Nm³ dry)	5.50	5.47	4.20	4.59	4.25	4.90	5.12	6.44
H₂O (vol. %)	25.6	24.4	29.8	18.0	27.8	28.2	31.8	47.4
H₂ (vol. % dnf)	28.7(±0.2)	24.8(±0.1)	29.4(±0.7)	33.4(±0.7)	28.8(±0.6)	32.7(±0.4)	39.4(±1.2)	44.2(±1.4)
CO (vol. % dnf)	30.9(±0.3)	31.4(±0.2)	28.8(±1.1)	27.6(±0.6)	29.1(±0.8)	27.8(±0.7)	23.6(±1.8)	20.3(±1.6)
CH₄ (vol. % dnf)	9.9(±0.1)	10.5(±0.1)	9.5(±0.4)	9.3(±0.2)	9.7(±0.4)	9.3(±0.3)	10.9(±0.4)	9.3(±0.6)
CO₂ (vol. % dnf)	30.5(±0.3)	33.3(±0.3)	32.3(±1.1)	29.7(±1)	32.4(±0.8)	30.2(±0.8)	26.1(±1)	26.2(±0.3)
N₂ (vol. % db)	52.3(±1)	51.6(±0.5)	62.4(±1.4)	59.9(±1.4)	62.0(±1.3)	56.9(±1.3)	58.5(±1.4)	45.8(±3.5)
CGE (%)	74.7	75.4	52.3	54.2	53.3	60.9	40.4	65.1
OE (%)	41.3	43.1	27.9	28.8	28.4	32.8	19.3	31.0
Tars in total gas (g/Nm³)	21.2	21.8	8.3	12.8	10.5	17.6	22.8	45.0
Benzene (g/kg daf)	1.34	1.40	0.37	0.96	0.52	1.13	1.62	2.90
Heterocyclic (g/kg daf)	5.1E-03	2.9E-03	3.1E-04	5.2E-03	3.6E-04	3.7E-03	7.1E-04	5.3E-02
Light Aromatic (g/kg daf)	1.2E-01	9.3E-02	1.2E-01	1.0E-01	1.5E-01	1.0E-01	3.6E-01	6.5E-01
Light PAH (g/kg daf)	7.1E-01	7.3E-01	3.7E-01	2.7E-01	4.1E-01	6.1E-01	1.0E+00	2.3E+00
Heavy PAH (g/kg daf)	7.1E-02	8.3E-02	3.1E-02	1.4E-02	3.4E-02	2.7E-02	1.4E-02	9.0E-02

Table 5.5 (continued from previous page): Effect of steam/air gasification duration in the IHBFSR on various process parameters and product yields (experiments 9 – 12)

Index (#)	9		10		11		12	
	SP1	SP2	SP1	SP2	SP1	SP2	SP1	SP2
Set Point	SP1	SP2	SP1	SP2	SP1	SP2	SP1	SP2
Bed Material	F046	F046	F046	F046	F054	F054	F054	F054
Biomass	ExR							
λ(-)	0.04	0.04	0.04	0.04	0.04	0.04	0.04	0.04
STBR (-)	1.2	1.2	1.2	1.2	1.2	1.2	1.2	1.2
Sec. air (kg/h)	8	8	4	4	4	4	8	8
Average Bed T (°C)	733	704	702	710	717	715	727	722
Average TC04 - TC05 (°C)	828	770	792	757	794	745	808	754
Average TC06 - TC07 (°C)	860	857	839	857	828	848	859	856
Gas Yield (Nm³ dnf/kg daf)	0.86	0.87	0.77	0.92	0.69	0.94	0.85	1.05
LHV product gas (MJ/Nm³ dry)	4.26	3.96	4.79	4.86	4.65	5.00	4.16	4.32
H₂O (vol. %)	25.3	23.8	29.1	25.7	30.4	23.7	29.0	23.9
H₂ (vol. % dnf)	31.6(± 0.7)	38.2(± 0.7)	34.7(± 1.1)	44.2(± 0.5)	31.9(± 0.9)	43.2(± 0.6)	31.4(± 0.9)	41.3(± 0.4)
CO (vol. % dnf)	29.6(± 1.4)	22.5(± 0.4)	25.5(± 1.2)	19.3(± 0.3)	29.8(± 1.5)	20.3(± 0.8)	30.2(± 1.4)	21.6(± 0.4)
CH₄ (vol. % dnf)	10.1(± 0.4)	7.9(± 0.2)	11.4(± 0.4)	7.6(± 0.3)	11.9(± 0.3)	8.1(± 0.5)	9.6(± 0.4)	6.5(± 0.4)
CO₂ (vol. % dnf)	28.7(± 1)	31.4(± 0.8)	28.4(± 0.6)	28.9(± 0.3)	26.3(± 0.8)	28.5(± 1.1)	28.8(± 0.8)	30.6(± 0.5)
N₂ (vol. % db)	63.9(± 1.3)	63.5(± 6)	60.7(± 0.8)	56.3(± 1.5)	63.1(± 1.1)	55.7(± 1.7)	64.2(± 1.4)	59.1(± 1.2)
CGE (%)	54.6	51.1	50.6	55.3	47.2	57.4	53.1	59.9
OE (%)	27.0	26.2	24.1	26.3	22.5	27.4	25.9	30.0
Tars in total gas (g/Nm³)	13.3	3.9	7.7	4.9	8.1	5.1	3.0	1.9
Benzene (g/kg daf)	0.84	0.29	0.43	0.36	0.47	0.43	0.22	0.18
Heterocyclic (g/kg daf)	4.1E-04	1.1E-03	5.9E-03	4.8E-03	6.9E-03	1.5E-03	4.6E-03	1.3E-04
Light Aromatic (g/kg daf)	1.9E-01	1.5E-02	4.9E-02	3.4E-02	4.1E-02	2.5E-02	1.1E-02	4.3E-03
Light PAH (g/kg daf)	5.8E-01	1.8E-01	5.1E-01	2.5E-01	4.8E-01	2.2E-01	1.3E-01	6.4E-02
Heavy PAH (g/kg daf)	2.6E-02	1.6E-02	1.8E-02	6.5E-03	2.3E-02	1.1E-02	4.4E-03	1.1E-03

5.4.5 Comparison of IHBFBRSR with other allothermal gasification concepts

As can be seen in **Table 5.6**, the overall performance of the IHBFBRSR during these commissioning experiments, compares well with other established allothermal gasification systems, some of which were already discussed in the introduction section. This is mainly in terms of cold gas efficiency and gas composition. The carbon conversion of the IHBFBRSR was lower compared to the other systems except for the HPR, which is also the most similar concept to the one employed here. Furthermore, it presented higher H₂:CO ratios among the non-pressurized systems (thus excluding the HPR). Overall, the hereby presented allothermal gasification concept is still in an early developmental stage and no extensive process optimization has yet been performed. Therefore, further comparison with these established technologies would not be meaningful. However, these initial results and comparison provide an important benchmark for future investigation and showcase the potential of the IHBFBRSR concept.

Table 5.6: Process conditions, working principles, performances and main gas compositions of Milena (ECN part of TNO), FICFB (TU Vienna), SilvaGas, Battelle (USA) and HPR (TU Munich) allothermal gasifiers

	MILENA [80-85]	FICFB [86-88]	SilvaGas [89, 90]	HPR [22, 29, 91]	IHBFBRSR [this study]
Reformer					
Type	CFB	BFB	CFB	FBR	BFB
Agent	Steam	Steam	Steam	Steam	Steam/air
Pressure	atm	atm	atm	2-10 bar	atm
Temperature (°C)	>700	850-900	800-1000	700-800	700-850
Combustor					
Type	BFB	CFB	CFB	FBR	Burner
Performance					
Carbon Conversion (%)	100	100	100	86	82 - 95
Cold Gas Efficiency (%)	80*	80**	70	70	51 - 84
Product gas composition (vol. % dnf)					
H₂	20	34	19	45	36
CO	50	24	54	21	26
CO₂	13	30	10	24	30
CH₄	17	12	17	10	9
Ratios (-)					
H₂:CO	0.4	1.4	0.4	2.2	1.5
H₂:CO₂	1.6	1.1	1.9	1.9	1.2
CO:CO₂	4.0	0.8	5.3	0.9	0.9
CH₄:H₂	0.8	0.4	0.9	0.2	0.3

*Taking into account gas cleaning

** Total efficiency Güssing plant

5.5 Conclusions

In this work, the results from the commissioning experiments on the novel IHBFSR were presented, along with a description of its operational characteristics for a wide range of experimental conditions. During the investigation, the importance of the char accumulating in the bed area for the overall process was highlighted, since it appeared to promote H₂ production and in-situ tar destruction especially for smaller bed material particle sizes. Furthermore, it was found that the injection of moderate amounts of air in the freeboard can improve tar reduction and to a lesser extent CCE without negatively impacting H₂ production, even when compared to the introduction of larger amounts as a fluidization agent. Overall, the present study offers a thorough presentation of the IHBFSR attributes for a variety of process conditions, allowing its use as a benchmark for similar systems and future works.

The product gas composition and CGE obtained from the IHBFSR is favourably compared to some similar allothermal gasification systems, while carbon conversion can still be improved. Although the presence of the accumulated char bed can have a positive effect on syngas composition in terms of quality and tar content, a compromise between this effect and the increase of carbon conversion must be found. Additionally, the in-depth investigation of process hydrodynamics and heat/mass transfer characteristics through e.g. computational fluid dynamics, can provide important insights as to the improvement of the IHBFSR's operation. The overall efficiency of the system can also be improved through for example, the increase of the burners output and efficiency and better insulation. Especially in the freeboard, with the addition of secondary air, lower temperatures and/or burner outputs could suffice for the required levels of tar removal. In general, the investigation of more tar reduction methods either in-situ (e.g. tar reducing bed material like olivine) or ex-situ (gas cleaning) should also be performed. Conclusively, despite the initial results being quite promising in terms of the scale-up potential of the IHBFSR, significant reactor development work remains to be done.

Bibliography

1. Wang, S., et al., *Lignocellulosic biomass pyrolysis mechanism: A state-of-the-art review*. Progress in Energy and Combustion Science, 2017. **62**: p. 33-86.
2. Basu, P., *Biomass Gasification and Pyrolysis Practical Design and Theory*. 2010: Elsevier Inc.
3. Sikarwar, V.S., et al., *An overview of advances in biomass gasification*. Energy & Environmental Science, 2016. **9**(10): p. 2939-2977.
4. Belgiorno, V., et al., *Energy from gasification of solid wastes*. Waste Management, 2003. **23**(1): p. 1-15.
5. Gómez-Barea, A., M. Suárez-Almeida, and A. Ghoniem, *Analysis of fluidized bed gasification of biomass assisted by solar-heated particles*. Biomass Conversion and Biorefinery, 2021. **11**(1): p. 143-158.
6. Levenspiel, O., *What Will Come after Petroleum?* Industrial & Engineering Chemistry Research, 2005. **44**(14): p. 5073-5078.
7. Karl, J. and T. Pröll, *Steam gasification of biomass in dual fluidized bed gasifiers: A review*. Renewable and Sustainable Energy Reviews, 2018. **98**: p. 64-78.
8. Fürsatz, K., et al., *Effect of biomass fuel ash and bed material on the product gas composition in DFB steam gasification*. Energy, 2021. **219**: p. 119650.
9. Schmid, J.C., et al., *Syngas for biorefineries from thermochemical gasification of lignocellulosic fuels and residues—5 years' experience with an advanced dual fluidized bed gasifier design*. Biomass Conversion and Biorefinery, 2019.
10. Mauerhofer, A.M., et al., *Influence of different bed material mixtures on dual fluidized bed steam gasification*. Energy, 2018. **157**: p. 957-968.
11. Thunman, H., et al., *Advanced biofuel production via gasification – lessons learned from 200 man-years of research activity with Chalmers' research gasifier and the GoBiGas demonstration plant*. Energy Science & Engineering, 2018. **6**(1): p. 6-34.
12. Anca-Couce, A., et al., *Kinetic scheme of biomass pyrolysis considering secondary charring reactions*. Energy Conversion and Management, 2014. **87**: p. 687-696.
13. Gussing Renewable Energy. 20/05/2021]; Available from: <http://www.gussingrenewable.com/>.
14. Project Gaya. 20/05/2021]; Available from: <https://www.projetgaya.com/>.
15. Martín-Gamboa, M., et al., *Delving into sensible measures to enhance the environmental performance of biohydrogen: A quantitative approach based on process simulation, life cycle assessment and data envelopment analysis*. Bioresource Technology, 2016. **214**: p. 376-385.
16. Liakakou, E.T., et al., *Gasification of lignin-rich residues for the production of biofuels via syngas fermentation: Comparison of gasification technologies*. Fuel, 2019. **251**: p. 580-592.
17. van der Meijden, C.M., H.J. Veringa, and L.P.L.M. Rabou, *The production of synthetic natural gas (SNG): A comparison of three wood gasification systems for energy balance and overall efficiency*. Biomass and Bioenergy, 2010. **34**(3): p. 302-311.
18. Liakakou, E.T., et al., *Connecting gasification with syngas fermentation: Comparison of the performance of lignin and beech wood*. Fuel, 2021. **290**: p. 120054.
19. Larsson, A., et al., *Steam gasification of biomass – Typical gas quality and operational strategies derived from industrial-scale plants*. Fuel Processing Technology, 2021. **212**: p. 106609.
20. Hanchate, N., et al., *Biomass gasification using dual fluidized bed gasification systems: A review*. Journal of Cleaner Production, 2021. **280**: p. 123148.
21. Jüntgen, H. and K.H. Van Heek, *Gasification of coal with steam using heat from HTRs*. Nuclear Engineering and Design, 1975. **34**(1): p. 59-63.
22. Karl, J., *Biomass heat pipe reformer—design and performance of an indirectly heated steam gasifier*. Biomass Conversion and Biorefinery, 2014. **4**(1): p. 1-14.

23. Inaba, Y., et al., *Coal gasification system using nuclear heat for ammonia production*. Applied Energy, 2000. **67**(4): p. 395-406.
24. Kubiak, H., et al., *Application of K₂CO₃ catalysts in the coal gasification process using nuclear heat*. Fuel, 1983. **62**(2): p. 242-245.
25. Lee, J.M., Y.J. Kim, and S.D. Kim, *Catalytic coal gasification in an internally circulating fluidized bed reactor with draft tube*. Applied Thermal Engineering, 1998. **18**(11): p. 1013-1024.
26. Naqvi, M., J. Yan, and E. Dahlquist, *Black liquor gasification integrated in pulp and paper mills: A critical review*. Bioresource Technology, 2010. **101**(21): p. 8001-8015.
27. Williams, R.H., et al., *Methanol and hydrogen from biomass for transportation*. Energy for Sustainable Development, 1995. **1**(5): p. 18-34.
28. Treiber, P. [26/01/2021]; Available from: <https://www.evt.tf.fau.eu/research/schwerpunkte/verbrennung-vergasung-von-biomasse/heatpipe-reformer/>.
29. Leimert, J.M., P. Treiber, and J. Karl, *The Heatpipe Reformer with optimized combustor design for enhanced cold gas efficiency*. Fuel Processing Technology, 2016. **141**: p. 68-73.
30. Gallmetzer, G., et al., *The Agnion Heatpipe-Reformer—operating experiences and evaluation of fuel conversion and syngas composition*. Biomass Conversion and Biorefinery, 2012. **2**(3): p. 207-215.
31. Karellas, S., J. Karl, and E. Kakaras, *An innovative biomass gasification process and its coupling with microturbine and fuel cell systems*. Energy, 2008. **33**(2): p. 284-291.
32. A. Sluiter, et al., *Biomass and Total Dissolved Solids in Liquid Process Samples*. 2008, National Renewable Energy Laboratory (NREL/TP-510-42621).
33. A. Sluiter, et al., *Determination of Ash in Biomass*. 2008, National Renewable Energy Laboratory (NREL/TP-510-42622).
34. Levenspiel, O., *Chemical Reaction Engineering*. 3d ed. 1998: John Wiley & Sons.
35. Siedlecki, M., *PhD Thesis: On the gasification of biomass in a steam-oxygen blown CFB gasifier with the focus on gas quality upgrading: technology background, experiments and mathematical modeling*. 2011, Delft University of Technology.
36. Di Marcello, M., et al., *Pilot scale steam-oxygen CFB gasification of commercial torrefied wood pellets. The effect of torrefaction on the gasification performance*. Biomass and Bioenergy, 2017. **105**: p. 411-420.
37. Siedlecki, M., W. De Jong, and A.H.M. Verkooijen, *Fluidized Bed Gasification as a Mature And Reliable Technology for the Production of Bio-Syngas and Applied in the Production of Liquid Transportation Fuels—A Review*. Energies, 2011. **4**(3): p. 389-434.
38. Kalinci, Y., A. Hepbasli, and I. Dincer, *Biomass-based hydrogen production: A review and analysis*. International Journal of Hydrogen Energy, 2009. **34**(21): p. 8799-8817.
39. de Lasa, H., et al., *Catalytic Steam Gasification of Biomass: Catalysts, Thermodynamics and Kinetics*. Chemical Reviews, 2011. **111**(9): p. 5404-5433.
40. Kumar, A., et al., *Steam-air fluidized bed gasification of distillers grains: Effects of steam to biomass ratio, equivalence ratio and gasification temperature*. Bioresource Technology, 2009. **100**(6): p. 2062-2068.
41. Kern, S., C. Pfeifer, and H. Hofbauer, *Gasification of lignite in a dual fluidized bed gasifier — Influence of bed material particle size and the amount of steam*. Fuel Processing Technology, 2013. **111**: p. 1-13.
42. Geldart, D., *The effect of particle size and size distribution on the behaviour of gas-fluidised beds*. Powder Technology, 1972. **6**(4): p. 201-215.
43. Turn, S., et al., *An experimental investigation of hydrogen production from biomass gasification*. International Journal of Hydrogen Energy, 1998. **23**(8): p. 641-648.
44. Klinghoffer, N.B., M.J. Castaldi, and A. Nzihou, *Influence of char composition and inorganics on catalytic activity of char from biomass gasification*. Fuel, 2015. **157**: p. 37-47.

45. Hosokai, S., et al., *Mechanism of decomposition of aromatics over charcoal and necessary condition for maintaining its activity*. Fuel, 2008. **87**(13): p. 2914-2922.
46. Abu El-Rub, Z., E.A. Bramer, and G. Brem, *Review of Catalysts for Tar Elimination in Biomass Gasification Processes*. Industrial & Engineering Chemistry Research, 2004. **43**(22): p. 6911-6919.
47. Devi, L., K.J. Ptasiński, and F.J.J.G. Janssen, *A review of the primary measures for tar elimination in biomass gasification processes*. Biomass and Bioenergy, 2003. **24**(2): p. 125-140.
48. Meng, X., et al., *Biomass gasification in a 100 kWth steam-oxygen blown circulating fluidized bed gasifier: Effects of operational conditions on product gas distribution and tar formation*. Biomass and Bioenergy, 2011. **35**(7): p. 2910-2924.
49. Devi, L., et al., *Catalytic decomposition of biomass tars: use of dolomite and untreated olivine*. Renewable Energy, 2005. **30**(4): p. 565-587.
50. Jess, A., *Mechanisms and kinetics of thermal reactions of aromatic hydrocarbons from pyrolysis of solid fuels*. Fuel, 1996. **75**(12): p. 1441-1448.
51. Zhang, Z. and S. Pang, *Experimental investigation of tar formation and producer gas composition in biomass steam gasification in a 100 kW dual fluidised bed gasifier*. Renewable Energy, 2019. **132**: p. 416-424.
52. Vreugdenhil, B.J. and R.W.R. Zwart, *Tar formation in pyrolysis and gasification in ECN-E--08-087*. 2009, ECN - Energy Research Centre of the Netherlands
53. Mayerhofer, M., et al., *Influence of pressure, temperature and steam on tar and gas in allothermal fluidized bed gasification*. Fuel, 2012. **99**: p. 204-209.
54. Fuentes-Cano, D., et al., *The influence of temperature and steam on the yields of tar and light hydrocarbon compounds during devolatilization of dried sewage sludge in a fluidized bed*. Fuel, 2013. **108**: p. 341-350.
55. Simell, P.A., et al., *Steam Reforming of Gasification Gas Tar over Dolomite with Benzene as a Model Compound*. Industrial & Engineering Chemistry Research, 1999. **38**(4): p. 1250-1257.
56. Qin, Y.H., J. Feng, and W.Y. Li, *Formation of tar and its characterization during air-steam gasification of sawdust in a fluidized bed reactor*. Fuel, 2010. **89**(7): p. 1344-1347.
57. Lv, P.M., et al., *An experimental study on biomass air-steam gasification in a fluidized bed*. Bioresource Technology, 2004. **95**(1): p. 95-101.
58. Kinoshita, C.M., Y. Wang, and J. Zhou, *Tar formation under different biomass gasification conditions*. Journal of Analytical and Applied Pyrolysis, 1994. **29**(2): p. 169-181.
59. Hernández, J.J., R. Ballesteros, and G. Aranda, *Characterisation of tars from biomass gasification: Effect of the operating conditions*. Energy, 2013. **50**: p. 333-342.
60. Morf, P., P. Hasler, and T. Nussbaumer, *Mechanisms and kinetics of homogeneous secondary reactions of tar from continuous pyrolysis of wood chips*. Fuel, 2002. **81**(7): p. 843-853.
61. Milne, T.A., R.J. Evans, and N. Abatzoglou, *Biomass Gasifier "Tars": Their Nature, Formation, and Conversion*. 1998, National Renewable Energy Laboratory (NREL) (NREL/TP-570-25357).
62. Gil, J., et al., *Biomass gasification in atmospheric and bubbling fluidized bed: Effect of the type of gasifying agent on the product distribution*. Biomass and Bioenergy, 1999. **17**(5): p. 389-403.
63. Pan, Y.G., et al., *Removal of tar by secondary air in fluidised bed gasification of residual biomass and coal*. Fuel, 1999. **78**(14): p. 1703-1709.
64. Robinson, T., et al., *Comparison of the air-blown bubbling fluidized bed gasification of wood and wood-PET pellets*. Fuel, 2016. **178**: p. 263-271.
65. Cao, Y., et al., *A novel biomass air gasification process for producing tar-free higher heating value fuel gas*. Fuel Processing Technology, 2006. **87**(4): p. 343-353.
66. Gómez-Barea, A., et al., *Improving the performance of fluidized bed biomass/waste gasifiers for distributed electricity: A new three-stage gasification system*. Applied Thermal Engineering, 2013. **50**(2): p. 1453-1462.

67. Campoy, M., et al., *Tar Reduction by Primary Measures in an Autothermal Air-Blown Fluidized Bed Biomass Gasifier*. Industrial & Engineering Chemistry Research, 2010. **49**(22): p. 11294-11301.
68. Zhang, Y., et al., *Tar destruction and coke formation during rapid pyrolysis and gasification of biomass in a drop-tube furnace*. Fuel, 2010. **89**(2): p. 302-309.
69. Tsalidis, G.A., et al., *The impact of dry torrefaction on the fast pyrolysis behavior of ash wood and commercial Dutch mixed wood in a pyroprobe*. Fuel Processing Technology, 2018. **177**: p. 255-265.
70. Ravenni, G., et al., *Adsorption and decomposition of tar model compounds over the surface of gasification char and active carbon within the temperature range 250–800 °C*. Applied Energy, 2019. **241**: p. 139-151.
71. Sun, Q., et al., *Decomposition and gasification of pyrolysis volatiles from pine wood through a bed of hot char*. Fuel, 2011. **90**(3): p. 1041-1048.
72. Li, C. and K. Suzuki, *Tar property, analysis, reforming mechanism and model for biomass gasification—An overview*. Renewable and Sustainable Energy Reviews, 2009. **13**(3): p. 594-604.
73. Abu El-Rub, Z., E.A. Bramer, and G. Brem, *Experimental comparison of biomass chars with other catalysts for tar reduction*. Fuel, 2008. **87**(10): p. 2243-2252.
74. Abu El-Rub, Z., *Biomass char as an in-situ catalyst for tar removal in gasification systems*. 2008, University of Twente: Enschede.
75. Burhenne, L. and T. Aicher, *Benzene removal over a fixed bed of wood char: The effect of pyrolysis temperature and activation with CO₂ on the char reactivity*. Fuel Processing Technology, 2014. **127**: p. 140-148.
76. Gilbert, P., et al., *Tar reduction in pyrolysis vapours from biomass over a hot char bed*. Bioresource Technology, 2009. **100**(23): p. 6045-6051.
77. Park, J., Y. Lee, and C. Ryu, *Reduction of primary tar vapor from biomass by hot char particles in fixed bed gasification*. Biomass and Bioenergy, 2016. **90**: p. 114-121.
78. Dabai, F., et al., *Tar Formation and Destruction in a Fixed-Bed Reactor Simulating Downdraft Gasification: Equipment Development and Characterization of Tar-Cracking Products*. Energy & Fuels, 2010. **24**(8): p. 4560-4570.
79. Zhao, S., et al., *Experimental investigation of the synergy effect of partial oxidation and bio-char on biomass tar reduction*. Journal of Analytical and Applied Pyrolysis, 2015. **112**: p. 262-269.
80. Drift, B., C. Meijden, and M. Boerrigter, *MILENA gasification technology for high efficient SNG production from biomass*, in ECN-RX-05-183. 2005, ECN - Energy Research Centre of the Netherlands
81. Meijden, C. and B. Drift, *Waste wood fueled gasification demonstration project*, in ECN-M--11-066. 2011, ECN - Energy Research Centre of the Netherlands
82. Meijden, C., B. Vreugdenhil, and B. Drift, *Experimental results from the allothermal biomass gasifier Milena*, in 15th European Biomass Conference & Exhibition. 2008: Berlin, Germany.
83. Meijden, C., et al., *Production of Bio Methane from wood using the MILENA gasification technology*, in ECN-M--15-044. 2014, ECN - Energy Research Centre of the Netherlands
84. Meijden, C., *Development of the MILENA gasification technology for the production of Bio-SNG*, in Chemical Engineering and Chemistry. 2010, Technische Universiteit Eindhoven: Eindhoven.
85. Meijden, C., et al., *The 800 kWth allothermal biomass gasifier MILENA*, in 16th European Biomass Conference & Exhibition. 2008: Valencia, Spain.
86. Hofbauer, H., et al., *The FICFB — Gasification Process*, in Developments in Thermochemical Biomass Conversion: Volume 1 / Volume 2, A.V. Bridgwater and D.G.B. Boocock, Editors. 1997, Springer Netherlands: Dordrecht. p. 1016-1025.

87. Rauch, R., et al., *Steam gasification of biomass at CHP plant in guessing - status of the demonstration plant*. Second world conference and technology exhibition, 2004: p. 1-4.
88. Pröll, T., et al., *Fluidized Bed Steam Gasification of Solid Biomass - Performance Characteristics of an 8 MWth Combined Heat and Power Plant*. International Journal of Chemical Reactor Engineering, 2007. **5**(1).
89. Paisley, M.A. and R. Overend. *Verification of the Performance of Future Energy Resources' SilvaGas Biomass Gasifier - Operating Experience in the Vermont Gasifier*. in *Pittsburgh Coal Conference*. 2002.
90. Babu, S., *Biomass gasification for hydrogen production—process description and research needs*. 2005, Gas Technology Institute: Des Plaines, Illinois, USA.
91. Leimert, J.M., et al., *Performance of a 100 kW Heatpipe Reformer Operating on Lignite*. Energy & Fuels, 2017. **31**(5): p. 4939-4950.

6. Two phase modelling of Geldart B particles in a novel indirectly heated bubbling fluidized bed biomass steam reformer

Chapter published in:
Chemical Engineering Journal, Volume 439, 1 July 2022, 135681

6.1 Introduction

Heat required for the operation of allothermal gasifiers can be provided through discontinuous intermittent operation of a single fluidized bed, through the circulation of particles between two interconnected fluidized beds, or finally by employing heat transfer surfaces [1]. The first category includes mainly Winkler's fluidized bed gasifier (1922) where air (or later O₂) blown combustion up to 1100-1200 °C was employed, repeatedly followed by steam gasification. In recent years the focus of the scientific community has been mostly on the other two technologies. The interconnected fluidized beds gasification technology, or Dual Fluidized Bed (DFB) gasification, utilizes two separate gasification and combustion reactors [2, 3]. A thorough literature review and technical analysis of the DFB gasification technology can be found in [1] and even more recent ones in [4] and [5]. In heat exchanger configurations, one concept completely separates the gasification area from the "heat provision reactor" to allow the application of a variety of fuels and/or processes. Juentgen and van Heek suggested such a concept in 1975 [6], incorporating helium produced from nuclear reactors at high temperatures (HTR), which was however abandoned due the poor heat transfer [7]. Another concept was the MTCI gasifier, where a pulse combustor fed the heat exchanger tubes located in the main steam blown atmospheric fluidized bed reactor, using the gasification product gas. Turbulent flue gas flow and low frequency acoustic oscillations from pulse combustion can lead to improved heat transfer compared to conventional heat exchangers [1, 8]. The most recent concept in this category is the Biomass Heatpipe Reformer. In this case gasification takes place in a pressurized chamber and the required heat is generated in a combustion chamber below it and exchanged through several heat pipes. Both the gasifier and the combustor are fluidized bed reactors, while for the heat pipes the working fluid (Na, K, etc.) evaporates on the combustor side and condenses on the gasifier one [9-11]. The use of this particular concept is claimed to increase heat transfer coefficients and reduce the required heat transfer areas 10 to 20 times [7].

In general, gas-solid fluidized beds are widely used in process industries and biomass gasification in particular, due to their ability to combine reactor and mixer capabilities and facilitate continuous operation [12]. Compared to other gas-solid reactor types, fluidized bed gasifiers offer significant advantages, such as rapid mixing and consequently almost isothermal conditions, high heat and mass transfer rates between gas and particles also leading to smaller required surface area of heat exchangers within the bed, suitability for large-scale operations and more [13]. Due to their importance for the process industry, fluidized beds have been widely studied, to better describe fluidization phenomena both experimentally and computationally. However, the lack of understanding of dense gas-particle flow fundamentals creates difficulties in designing and scaling-up such systems. Therefore, designing a fluidized bed reactor often becomes an empirical process, requiring expensive and time consuming preliminary pilot-scale experiments [14]. This task becomes even more challenging when non-standard or complex reactor geometries are employed. Therefore, the development of numerical models for the simulation of fluidized beds hydrodynamics with such geometries is of the outmost importance for the corresponding scientific community.

Complex fluidized bed geometries have been thoroughly studied in the literature in terms of numerical models development, however almost solely in the form of horizontally immersed tubes in a fluidized bed reactor. Most commonly, Eulerian-Lagrangian methods have been employed in their study. The CFD-DEM (Computational Fluid Dynamics-Discrete Element Method) has been widely applied [15-19], also coupled with various methods, such as the coarse grain (CG) model [20], the immersed boundary method (IBM) [21-23], the virtual dual-grid model (VDGM) [24, 25], the cut cell technique in a MFIx (Multiphase Flow with Interphase Exchange) solver [26, 27], the fictitious domain (FD) method [28, 29], LES (large eddy simulation) [30, 31], as well as with a combination of the signed distancing function (SDF) with the IBM and CG models [32]. Hard sphere, CFD-DPM (Computational Fluid Dynamics-Discrete Particle Method) models have also been employed for the simulation of complex geometries [33, 34]. Furthermore, Córcoles et al. [35] presented the simulation of a bubbling fluidized bed with immersed surfaces, using a Computational Particle Fluid Dynamics (CPFD) model,

based on the multiphase particle-in-cell (MP-PIC) method. Eulerian – Eulerian two-fluid models (TFM) have also been employed for the simulation of similar geometries, however to a lesser extent [36-44]. In a conceptually different approach than for the cases described above, Jašo et al. [45], investigated a fluidized bed membrane reactor for oxidative methane coupling via CFD simulations. In an effort to investigate the effect of distributed oxygen feed on the reactor performance several symmetrically arranged vertical tubes were placed in a cylindrical reactor geometry. A Eulerian–Eulerian granular kinetic flow model was used for the simulation of the fluidized bed, coupled with reaction kinetics, while a lab scale reactor with a diameter of 40 mm was used for experimental validation. The analysis of the results showed that certain vertical tube configurations influence hydrodynamics in such a way that the bottom-fed gas preferably follows a path near the walls of the reactor. A similar reactor concept was simulated by de Jong et al. [46], employing a hybrid DPM-IBM method, however without experimental validation. From their findings it became apparent that horizontal membrane tubes lead to reduced bubble size compared to vertical ones. Finally, Verma et al. [47] employed a TFM coupled with the cut-cell method in MFIX, to investigate the hydrodynamics of 3D fluidized beds containing vertical U-tubes banks, inspired from the design of carbon capture units. According to the authors, the presence of the vertical tubes leads to decreased bubble diameter, while their presence divides the bed into smaller, parallel gas-solid flow chambers.

The focus of this work lies on the numerical modelling and experimental validation, of the hydrodynamic behaviour of a novel 50 kW_{th} indirectly heated bubbling fluidized bed steam reformer (IHFBSR). This pilot-scale reactor was designed, built and commissioned by the Dutch company Petrogas - Gas Systems together with the Process and Energy Department of Delft University of Technology. In this novel reactor concept two radiant tube natural gas burners, one in the bottom (bed area) and one in the top (freeboard) of the reactor, provide the heat necessary for gasification (Figure 6.1). Its design aims at the reduction of heat losses, the provision of enough heat for the realization of the biomass steam reforming and cracking reactions and the exploration of scale-up possibilities to an industrial scale process. The IHFBSR concept proposes a novel approach on indirect gasification technology, with its unique reactor design. More details regarding this novel reactor's positioning among similar technologies as well as the results of its commissioning gasification experiments can be found in [48]. Overall, studying this complex geometry by employing a narrower cylindrical fluidized bed of equivalent hydrodynamic radius would constitute an oversimplification which would lead to the loss of information and not allow the representation of flow patterns critical to both the present operation and the scale-up of this novel reactor. As it became apparent from the previous discussion, the hydrodynamic behaviour of fluidized beds with immersed vertical tubes has not been thoroughly reported in literature. Furthermore, complex fluidized bed geometries in general have not been thoroughly investigated in terms of numerical modelling coupled with experimental validation for pilot scale reactors. Therefore, it can be argued that the present study, apart from investigating a novel reactor concept, adds also to the field of fluidized bed hydrodynamics numerical modelling. According to the knowledge of the authors, the combination of CFD simulations and experiments on the hydrodynamics of a pilot scale bubbling fluidized bed with an immersed vertical tube (complex geometry) has not been previously reported in the literature.

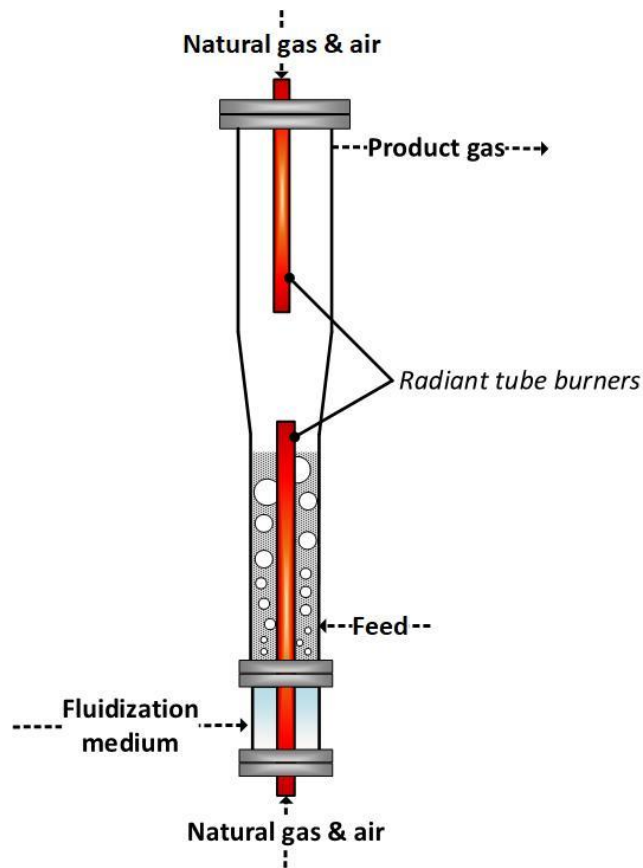


Figure 6.1: Conceptual design of the indirectly heated bubbling fluidized bed steam reformer (IHFBSR).

The numerical simulation of the fluidized bed's hydrodynamic behaviour was performed employing the Eulerian-Eulerian TFM approach. This choice was made with the large scale of the modelled fluidized bed in mind, due to the relatively lower computational costs of TFM versus DPM [49]. Conventional Eulerian-Lagrangian methods (DPM or DEM) which track individual particles, or even CG models which track particle "clusters" which are in general more favourable for large-scale systems modelling [50], would require the tracking of approximately 10^8 particles given the scale of the setup, even in a reduced simulation domain. Finally, it should be mentioned that in the context of this work the TFM model was used as a tool for studying the hydrodynamic behaviour of the IHFBSR. Focusing on TFM method development was outside the scope of the present work.

6.2 Experimental setup

6.2.1 Reactor description

In the 50 kW_{th} IHFBSR, biomass gasification experiments with air, nitrogen, steam or combinations of the above as fluidization media can be performed. However, for the hydrodynamic study performed within this work only air and N₂ were employed. A detailed presentation of steam/air gasification experiments in the IHFBSR can be found in [48]. The reactor was manufactured out of 310S (AISI) steel with a wall thickness of 4.78 mm and a height of ~3 m. It is insulated with a 200 mm three-layer mattress material. The dimensions of the reactor, along with the location of instrumentation equipment (thermocouples and pressure gauges) are presented in Figure 6.2. Data from the various instruments were recorded through a SCADA/PLC coupling employing a LabVIEW interface, every 10 s.

Before the test, 75 kg of bed material was inserted in the bed area of the IHBFBRS. The bed material employed was corundum, an aluminium oxide (Al_2O_3) containing also traces of iron oxide, titanium oxide and silica. This material, supplied by Unicorn ICS B.V., has a density of 3940 kg/m^3 , a hardness of 9 Mohs and its melting point is $1950 \text{ }^\circ\text{C}$. The mean particle diameter of the bed material was $543 \text{ }\mu\text{m}$, which classifies it in the Geldart B category (sand-like) of solids in bubbling fluidized beds [51]. The particle size distribution of the corundum bed material was determined using a Microtrac FLEX 10.6.2. Corundum has a very high hardness, thus the probability of fines production due to attrition of the particles is reduced. Furthermore, depending on the fluidization conditions, it has very good heat distribution properties [52].

Two self-recuperative ceramic burners supplied by WS – Wärmeprozessstechnik GmbH were used for the provision of heat in the IHBFBRS. Both were placed inside metal radiant tubes for protection from bed material blasting. Both burners operate in an on/off mode, with the bottom burner being controlled by the average values of thermocouples TC01 – TC05 and the top burner by TC07. The set point of the two burners in the context of the present work was $640 \text{ }^\circ\text{C}$, which was the maximum achievable temperature without the employment of in-bed combustion. The burners operate at a constant capacity of $20 \text{ kW}_{\text{th}}$ and $12 \text{ kW}_{\text{th}}$ for the bottom (REKUMAT C100) and top one (REKUMAT C80), respectively. The total main body length of the bottom radiant tube is $\sim 1.7 \text{ m}$, and 1.2 m of this is situated in the bed area. The bottom part of the radiant tube also warmed up the windbox, as shown in Figure 6.2. The top radiant tube is smaller, both in terms of diameter (0.1 m) and of total main body length (1.3 m).

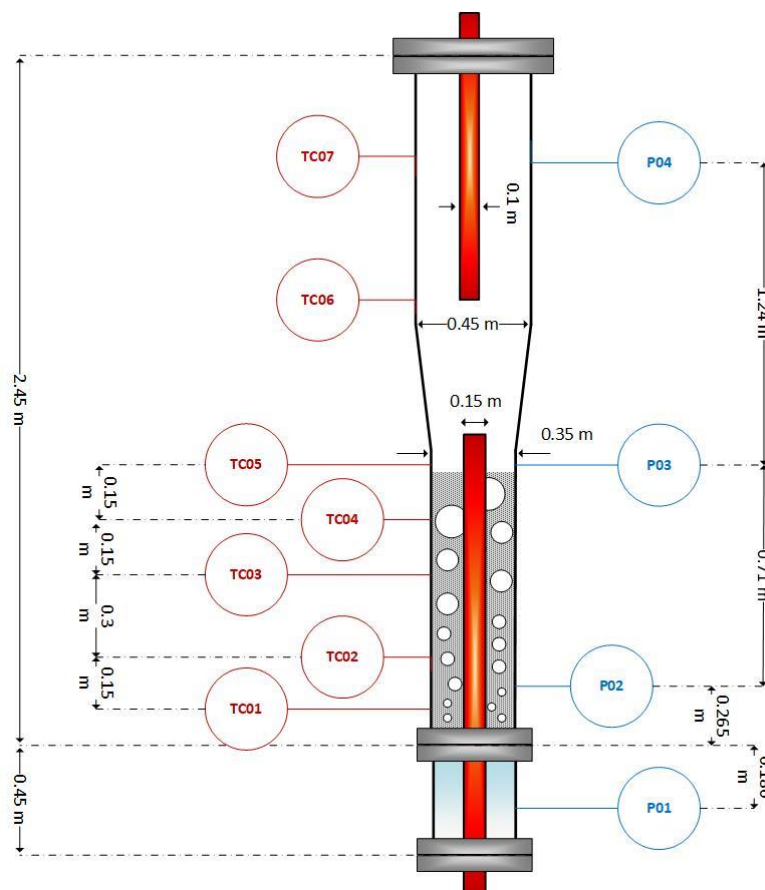


Figure 6.2: Basic dimensions of IHBFBRS and instrumentation (thermocouples – TC and pressure gauges – P locations)

The fluidization media employed in the present study (air and N_2) were introduced in the reactor through a distributor plate, after passing through a 6 kW preheater. Depending on the total amount of gases introduced, their inlet temperature ranged between 515 and $620 \text{ }^\circ\text{C}$. The distributor plate consisted of 50 tuyeres, each with 2 mm holes drilled in a 20° downwards angle. Nitrogen was also

employed to pressurize the feeding system and to prevent obstruction of the pressure gauge in the reactor. For the latter, for each pressure gauge, a 5 ml/min N₂ flow was introduced, while approximately 4 kg/h of N₂ was introduced in the reactor through the feeding system for the aforementioned purpose. The biomass feeder outlet in the reactor was located 170 mm above the distributor plate and its inside diameter was 50 mm. As can be observed in Figure 6.2, pressure gauges located in four spots within the reactor, along with their respective pressure transmitters, were used to record the pressure drops over the distributor plate, the bed zone and the freeboard.

6.2.2 Hydrodynamics experiments

The main purpose of the experiment presented in this section, was to determine the fluidization characteristics of the IHBFSR. Since visual observation is not possible in the IHBFSR, the variation of the bed height during an experiment can be deduced from the thermocouple readings. An example is shown in Figure 6.3, where fluidization apparently occurs after roughly 58 min. After this point, the reading of TC01, TC02 and TC03 begin to coincide, with the last one joining this group approximately 10 min later. From this behaviour, it can be safely deduced that the top of the particle bed is located between TC03 and TC04. Air and N₂ were introduced through the distributor plate at 22 and 26 kg/h, respectively, and the total mass flow remained unchanged until the temperature set point (640 °C average temperature) was achieved and the system was stabilized (234 min). The secondary N₂ side-flow through the feeder was stable at 4.11 kg/h during the experiment. After the previously mentioned point, the fluidization media flow was gradually reduced in steps of 1 kg/h. The first bed height reduction (1st BHR) point was observed when the total flow was firstly reduced to 22 and 25 kg/h of air and N₂, respectively. After reducing the flow of N₂, the temperature recorded by TC03 started to increase compared to TC01 and TC02. This observation suggests that TC03, no longer “insulated” by the fluidized bed material, experiences the heat produced by the burner unobstructed. By continuing the reduction of the gas flows, such an observation will however no longer be possible. This is because the de-fluidized bed height is 0.591 m and thus located above the location of TC02. Consequently, the only other variation that can be observed is the de-fluidization of the bed, in the 2nd bed height reduction point. At this point, which was achieved for 14 kg/h of air only, the temperatures of TC01 and TC02 started to diverge. Additionally, the de-fluidization was also observed from Figure 6.3, where for 14 kg/h of air only, the pressure difference dipped dramatically. To ensure that this was indeed the flow rate corresponding to the minimum fluidization velocity (u_{mf}), the flow was gradually zeroed. Finally, in the subsequent gradual increase of the air flow, fluidization was reinstated at 15 kg/h, which was observed both by the thermocouple and the pressured drop readings.

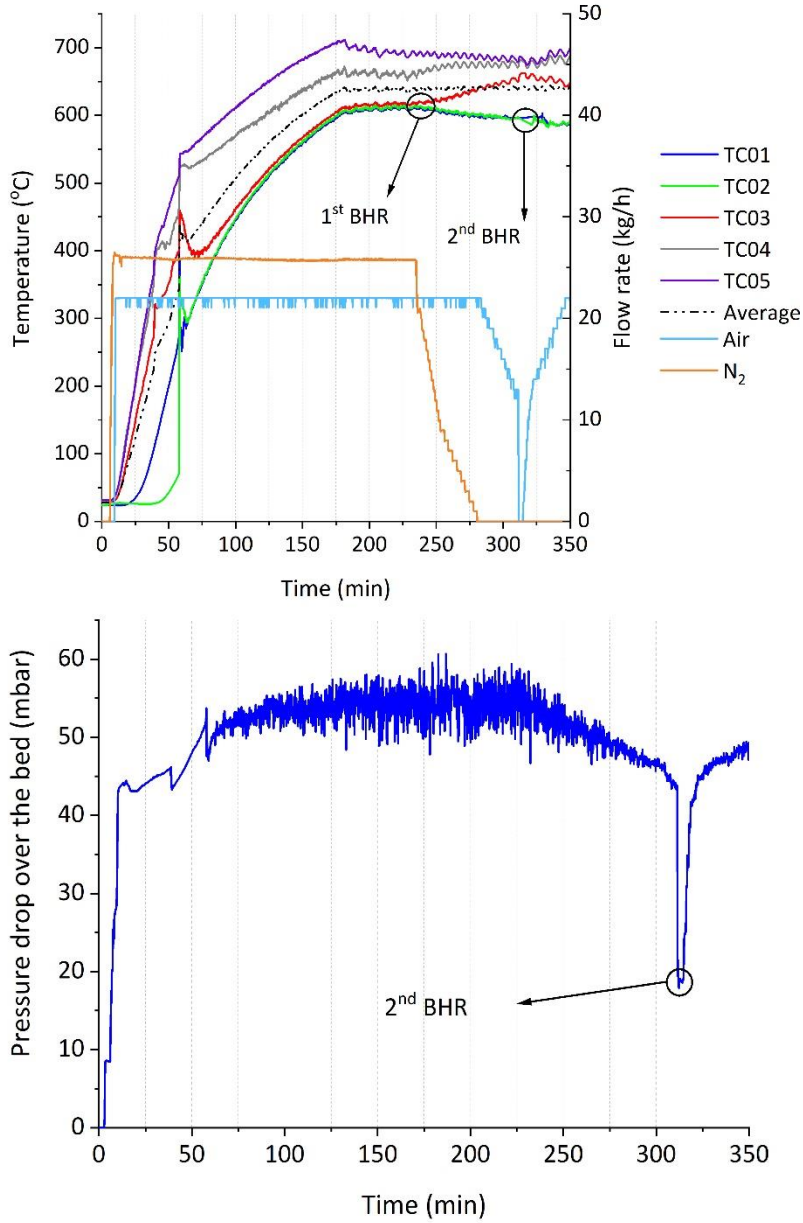


Figure 6.3: Top: Air and N₂ flow rates and temperature profile of the IHBFSR bed zone (TC01-TC05) with the bed height reduction (BHR) points marked during the fluidization experiment conducted in the IHBFSR. Bottom: Pressure drop over the bed during the fluidization experiment conducted in the IHBFSR.

From the aforementioned analysis of the experiment conducted in the IHBFSR, the data included in Table 6.1 was used as input for the model developed within this work. The packing limit was estimated as the ratio of the bulk density and the actual density of corundum ($1636/3950 = 0.414$) and therefore the void fraction at minimum fluidization conditions was calculated ($\alpha_{mf} = 1 - 0.414 = 0.586$). Subsequently, the void fraction (α) at the 1st BHR point was estimated by the following formula [13]:

$$\frac{H_{mf}}{H} = \frac{(1 - \alpha)}{(1 - \alpha_{mf})}$$

where H_{mf} is the minimum fluidization bed height and α_{mf} the void fraction at minimum fluidization conditions. For the numerical model developed within this work and which will be presented in the

following section, the 53 minutes of steady state before the 1st BHR point were used for validation. The data obtained regarding the minimum fluidization conditions were used as inputs for the Adjusted Syamlal model. The temperature throughout the bed area for the validation BHR point, as measured by TC01, TC02 and TC03, was assumed to be at a constant value of 600 °C. The temperature of the main gases (air, N₂) and the side-flow (N₂) entering the reactor was also assumed to be 600 °C. As mentioned in Section 2.1, this is very close to the actual value for the main gases. For the side-flow, its small amount relative to the reactor's size, permits this simplification. The average pressure drop over the bed at this point was 55 mbar, while the corresponding bed height was between 0.67 m (TC03) and 0.82 m (TC04). The reason for choosing this interval for the validation, was that after the 1st BHR point the bed area enters a transient state due to a variation in the flow rate. The time spent at each subsequent set point (~3 min) did not suffice for a steady state to be re-established. It should also be mentioned that given the location of P02, which is not at zero height with respect to the distributor plate, the pressure drop between P02 and P03 does not correspond to the pressure drop across the entirety of the bed material, but rather approximately 60 % of the overall bed mass. This will be considered in the model validation.

Table 6.1: Fluidization data obtained from the corresponding experiment in the IHBFSR

	Air	N ₂	Secondary N ₂	Total volumetric flow rate	Height	Void fraction
	(kg/h)	(kg/h)	(kg/h)	(m ³ /h)	(m)	(-)
1st BHR	22	26	4	136	0.67	0.63
2nd BHR	14	0	4	52	0.59	0.59

6.3 Numerical model

In the two-fluid continuum model (TFM), both gas and solid phases are described as fully interpenetrating continua using a generalized form of the Navier-Stokes equations. The accumulation of mass in each phase is balanced by the convective mass fluxes, while the sum of all fractions in a cell is equal to unity. The non-steady continuity equations for the gas (g) and solid (s) phases are given below [53],

$$\begin{aligned} \frac{\partial}{\partial t}(a_g \rho_g) + \nabla \cdot (a_g \rho_g \vec{u}_g) &= 0 \\ \frac{\partial}{\partial t}(a_s \rho_s) + \nabla \cdot (a_s \rho_s \vec{u}_s) &= 0 \end{aligned} \quad \text{Eq. 1}$$

where α is the volume fraction, ρ is the density and u is the velocity of the corresponding phase. According to Newton's second law of motion, momentum change equals to the sum of forces in a domain. The momentum equations for the gas and the solid phase are:

$$\begin{aligned} \frac{\partial}{\partial t}(a_g \rho_g \vec{u}_g) + \nabla \cdot (a_g \rho_g \vec{u}_g \vec{u}_g) &= -a_g \nabla p_g - \nabla \cdot \bar{\tau}_g + a_g \rho_g \vec{g} + K_{gs}(\vec{u}_s - \vec{u}_g) \\ \frac{\partial}{\partial t}(a_s \rho_s \vec{u}_s) + \nabla \cdot (a_s \rho_s \vec{u}_s \vec{u}_s) &= -a_s \nabla p_s - \nabla p_s - \nabla \cdot \bar{\tau}_s + a_s \rho_s \vec{g} + K_{gs}(\vec{u}_g - \vec{u}_s) \end{aligned} \quad \text{Eq. 2}$$

where $\bar{\tau}$ is the stress tensor and p is the pressure of the corresponding phase, and K_{gs} is the interphase exchange coefficient. To account for the particle-particle interactions, the kinetic theory of granular flow (KTGF) was employed to predict the solid's fluctuation energy. The granular temperature θ_s ,

which represents the energy associated with the particles' fluctuating velocity is given by the following formula [54]:

$$\frac{3}{2} \left[\frac{\partial}{\partial t} (\rho_s a_s \theta_s) + \nabla \cdot (\rho_s a_s \vec{u}_s \theta_s) \right] = - (p_s \vec{I} + \vec{\tau}_s) : \nabla \vec{u}_s + \nabla \cdot (k_{\theta_s} \nabla \theta_s) - \gamma + \varphi_{gs} \quad \text{Eq. 3}$$

The collisional dissipation of energy fluctuations γ represents the energy loss due to particle collisions and is derived from [55]:

$$\gamma = \frac{12(1-e^2)g_0}{d_s \sqrt{\pi}} \rho_s a_s^2 \theta_s^{\frac{3}{2}} \quad \text{Eq. 4}$$

In the above formula, g_0 is the radial distribution coefficient at contact and e is the restitution coefficient. The radial distribution coefficient at contact describes the increased probability of collisions between particles, caused by structure formation in dense suspensions of particles, and is given by [56]:

$$g_0 = \left[1 - \left(\frac{a_s}{a_{smax}} \right)^{\frac{1}{3}} \right]^{-1} \quad \text{Eq. 5}$$

The diffusion coefficient for granular temperature k_{θ_s} was calculated using the Syamlal-O'Brien formulation [57]:

$$k_{\theta_s} = \frac{15d_s \rho \sqrt{\theta_s \pi}}{4(41-33\eta)} \left[1 + \frac{12}{5} \eta^2 (4\eta-3) a_s g_0 + \frac{16}{15\pi} (41-33\eta) \eta a_s g_0 \right] \quad \text{Eq. 6}$$

$$\eta = \frac{1}{2} (1+e) \quad \text{Eq. 7}$$

The term φ_{gs} describes the damping of the particles' fluctuating velocities caused by the drag forces between the gas and solid phase. The solids pressure p_s represents the normal force due to particle interactions. The solid-phase stress tensor demands for its calculation the employment of the solid bulk viscosity λ_s , which is the measure of a fluid's dissipative resistance to compression, and the solids shear viscosity, which is the summation of dissipative tangential forces due to shearing particle interactions (collisions, kinetic and frictional viscosity). In this work the Syamlal expression for the kinetic solid viscosity was employed. The formulas that correspond to the aforementioned values are as follows [54, 57]:

$$\varphi_{gs} = -3K_{gs}\theta_s \quad \text{Eq. 8}$$

$$p_s = \theta_s \rho_s a_s + 2\rho_s (1+e) a_s^2 g_0 \theta_s \quad \text{Eq. 9}$$

$$\vec{\tau}_s = [\lambda_s \nabla \cdot \vec{u}_s] \vec{I} + 2\mu_s \vec{S}_s \quad \text{Eq. 10}$$

$$\vec{S}_s = \frac{1}{2} [(\nabla \vec{u}_s) + (\nabla \vec{u}_s)^T] - \frac{1}{3} \nabla \cdot \vec{u}_s \vec{I} \quad \text{Eq. 11}$$

$$\lambda_s = \frac{4}{3} a_s \rho_s d_s g_0 (1+e) \left(\frac{\theta}{\pi} \right)^{\frac{1}{2}} \quad \text{Eq. 12}$$

$$\mu_s = \mu_{s,coll} + \mu_{s,kin} + \mu_{s,fr} \quad \text{Eq. 13}$$

$$\mu_{s,coll} = \frac{4}{5} a_s^2 \rho_s d_s g_0 (1+e) \left(\frac{\theta}{\pi} \right)^{\frac{1}{2}} \quad \text{Eq. 14}$$

$$\mu_{s,fr} = \frac{p_s \sin(\gamma)}{2\sqrt{I_{2D}}} \quad \text{Eq. 15}$$

$$\mu_{s,kin} = \frac{a_s \rho_s d_p \sqrt{\pi \theta}}{6(3-e)} \left[1 + \frac{2}{5}(1+e)(3e-1)g_0 a_s \right] \quad \text{Eq. 16}$$

With regards to the drag function, the Adjusted Syamlal-O'Brien model was employed. Therefore, the following expression was used for the derivation of the interphase exchange coefficient K_{gs} [57]:

$$K_{gs} = \frac{3a_s a_g \rho_g}{4u_{r,s}^2 d_s} C_D \left(\frac{Re_s}{u_{r,s}} \right) |\vec{u}_s - \vec{u}_g| \quad \text{Eq. 17}$$

where the drag coefficient C_D and the solids terminal velocity $u_{r,s}$ are expressed as:

$$C_D = \left(0.63 + \frac{4.8}{\sqrt{Re_s/u_{r,s}}} \right)^2 \quad \text{Eq. 18}$$

$$u_{r,s} = 0.5 \left(A - 0.06Re_s + \sqrt{(0.06Re_s)^2 + 0.12Re_s(2B - A) + A^2} \right) \quad \text{Eq. 19}$$

$$A = a_g^{4.14} \quad \text{Eq. 20}$$

$$B = \begin{cases} 0.8a_g^{1.28} & (a_g \leq 0.85) \\ a_g^{2.65} & (a_g > 0.85) \end{cases} \quad \text{Eq. 21}$$

6.4 Computational Fluid Dynamics

Within this work, 3D simulations of the IHBFSR fluidization behaviour were performed. Simulations were performed in Ansys Fluent 19.2 on a computational cluster (28 cores, 56 threads, 2.40 – 3.30 GHz frequency). Except for the biomass feeding inlet, the reactor can be considered as almost axisymmetric, except for the two rings of 25 tuyeres at the bottom of the reactor. This allows for simulation using a periodically repeating “wedge” of either $360/25 = 14.4^\circ$ or $360/5 = 72^\circ$. The 72° wedge offers a good compromise between reducing the domain as much as possible and at the same time ensuring that the biomass feeder’s side flow does not propagate outside the selected region and influence the hydrodynamics outside the selected domain. Selecting the even smaller wedge would require less computational resources and would have proven to be a much faster option, however would also entail the risk of not properly encapsulating the side-flow’s effect on its entirety. It should also be mentioned that the bottom radiant tube burner constituted the “inner wall” of the aforementioned domain, with the actual reactor wall constituting its “outer wall”. Therefore, the bottom radiant tube burner is considered in the simulations through the effects of its boundaries on the hydrodynamic behaviour. The assumption that the biomass feeder side-flow’s effect does not propagate out of its section will be evaluated from the simulation results. The simulations presented within this work were performed with and without the presence of this side-flow. Another assumption was made with regards to the modelling of the flow entering the reactor through the tuyeres. As mentioned in Section 0, the tuyeres openings are pointed downwards at an angle of 20° and their very small diameter leads to an individual inlet velocity which is many orders of magnitude higher (450 m/s) than the dispersed bulk velocity, leading to a time step in the order of 10^{-5} s being required to meet the Courant-Friedrichs-Lewy (CFL) condition. To achieve reasonable time steps for the subsequent simulations, the plane corresponding to the top of the tuyeres (height of 33 mm) was assumed to be the bottom of the simulation domain. In this plane the whole cross-sectional area, except for the tops of the tuyeres, was considered to be gas flow inlet. The inlet velocity was assumed to be uniform due to the strong dispersing effect of the granular particles around and below this plane.

The total simulation height was 1 m, the width was 97.72 cm and the side-flow inlet was approximated with 16 points. Finally, regarding meshing, polyhedrons were used and all meshes had a maximum aspect ratio of 10. Grid independency tests were performed with 15, 20 and 30 times the bed particle diameter (d_p) grid sizes and are presented in the following section.

An overview of the species property settings is presented in Appendix D. The time step was calculated using the approximation presented in Eq. 22:

$$\Delta t \approx \frac{CFL \cdot \Delta z}{u_z} \quad \text{Eq. 22}$$

where Δz was approximated based on the grid density, u_z was assumed to be equal to the bottom inlet velocity and CFL values of 0.2 and 0.4 were selected. The effect of the CFL values on the simulation's behaviour is discussed in the following section. An overview of the simulation settings employed is presented in Appendix D. Within the system, all temperatures for the boundary conditions were assumed to be stable at 600 °C, while a no-slip condition was assumed for the burner walls, the reactor wall and the tuyeres. The inlet was modelled as a velocity inlet and the outlet as a pressure outlet. A symmetry boundary condition was also enforced in the azimuthal direction. For the flux of granular temperature at the wall, the Johnson and Jackson boundary condition was employed [58] as shown in Eq. 23.

$$q_s = \frac{\pi}{6} \sqrt{3} \phi \frac{a_s}{a_{s,max}} \rho_s g_0 \sqrt{\theta} u_{wall} - \frac{\pi}{4} \sqrt{3} \frac{a_s}{a_{s,max}} (1 - e_{s-wall}^2) \rho_s g_0 \theta^{\frac{3}{2}} \quad \text{Eq. 23}$$

Since the Johnson and Jackson condition is used in combination with the no-slip condition, the specular coefficient ϕ becomes equal to 1. The particle – wall restitution coefficient e_{s-wall} was assumed equal to 0.2 for this study. With regards to the particle – particle restitution coefficient, values between 0.8 and 0.99 were examined.

The determination of the bed height from the simulations was performed by locating the maximum in the gradient of the averaged solid volume fraction. The location of this gradient was approximated by employing an adaptation of the methodology described by Mahajan et. al. [59]. In particular, the height of the mesh was divided in 1 cm slices and for each slice the average void fraction was calculated. Subsequently, the derivative of the void fraction versus the height was calculated using linear interpolation and finally the bed height was derived as the height corresponding to the maximum gradient.

6.5 Results

6.5.1 Mesh and time step independence (without side-flow)

The mesh and time independence of the developed model was examined based on the pressure drop over the bed area and the fluidized bed height. The pressure drop is measured over the reactor volume between the heights of the two pressure gauges P02 and P03, as described in Section 0. The mesh and time step independence tests were performed for combinations of CFL equal to 0.2 and 0.4 and grid sizes 15, 20 and 30 times the bed material particle diameter (d_p). The results of the tests in regard to the pressure drop over the bed area are presented in Figure 6.4. The average values obtained from the mesh and time step independence tests are presented in Appendix D.

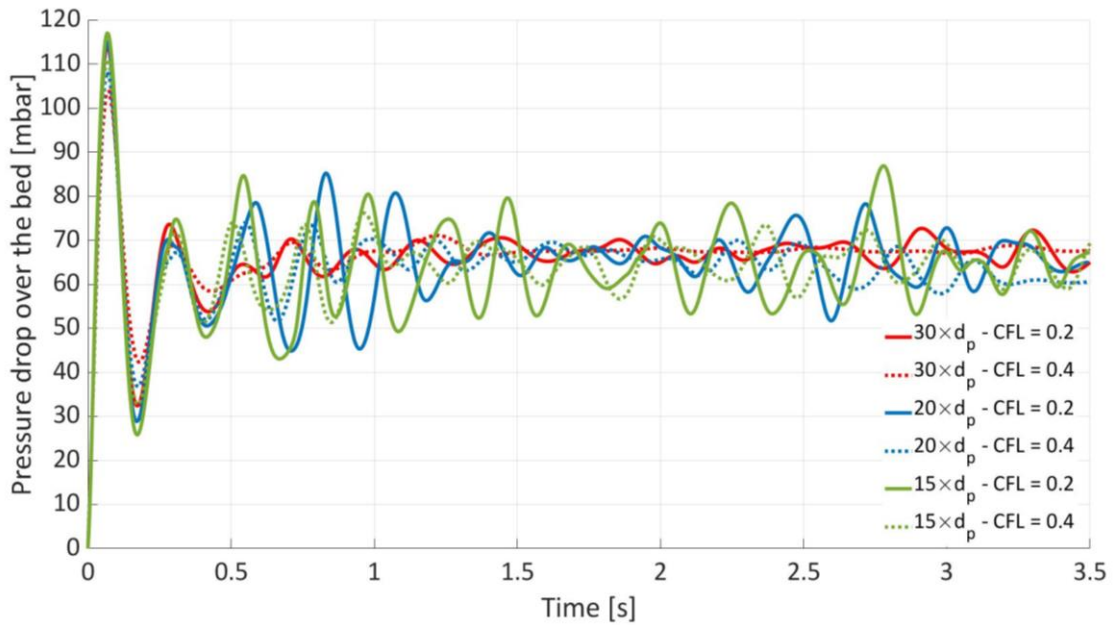


Figure 6.4: Pressure drop over the bed area for different grid size and CFL combinations from the IHBBFBSR hydrodynamics simulations without a side-flow.

In Figure 6.4, an initial spike in the pressure drop over the bed was observed in all cases, corresponding to the initial bed expansion and the subsequent collapse. After this point, the observed pressure fluctuations can be connected to bubble eruption at the top of the bed and its implosion thereafter. Overall, the magnitude of the fluctuations decreased for coarser meshes, leading to the potential loss of information for meshes larger than $30 \times d_p$. Regarding the effect of CFL variation for a specific mesh size, only a minor effect was apparent in the pressure drop behaviour. In particular, the average difference between the mean pressure drop, calculated between 1 and 3 s, ranged between 0.5 and 1.5 mbar (Appendix D). However, it can also be noted that the magnitude of the fluctuations was slightly smaller for higher CFL values, especially for the case of CFL=0.4. As mentioned before, for the latter case a loss of information due to the coarser mesh size employed exacerbates the much smaller effect of the time step increase. In general, it can be argued that an increase of CFL leads to minor accuracy losses, significantly lower than the effect of a mesh size increase. Therefore, no firm indication exists that a further decrease of the CFL and therefore the time step, would lead to significantly improved accuracy.

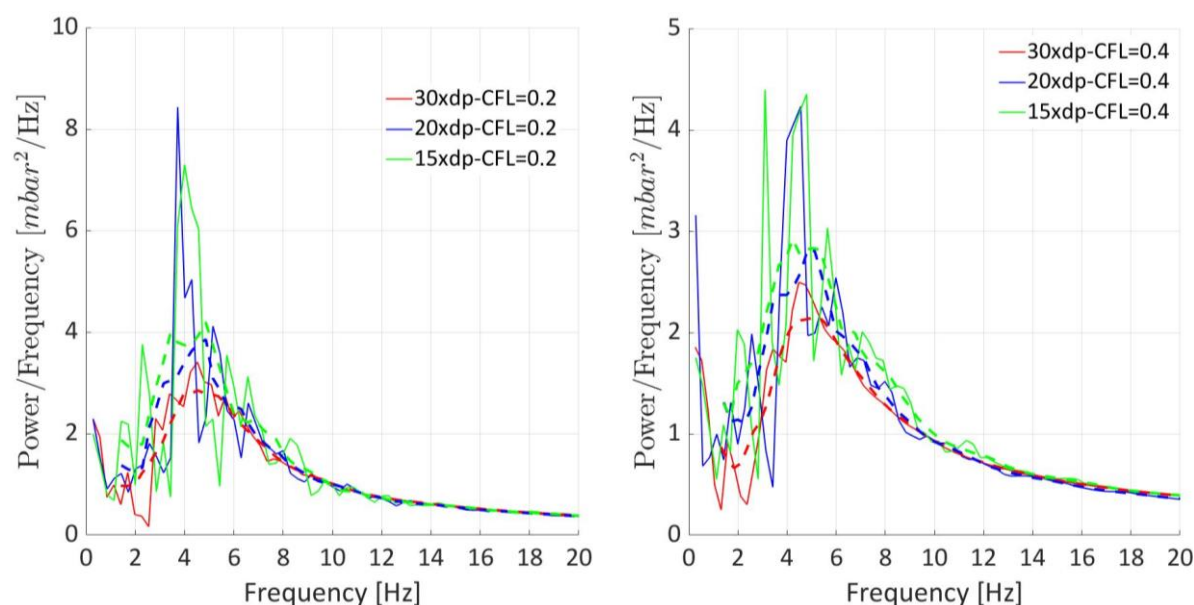
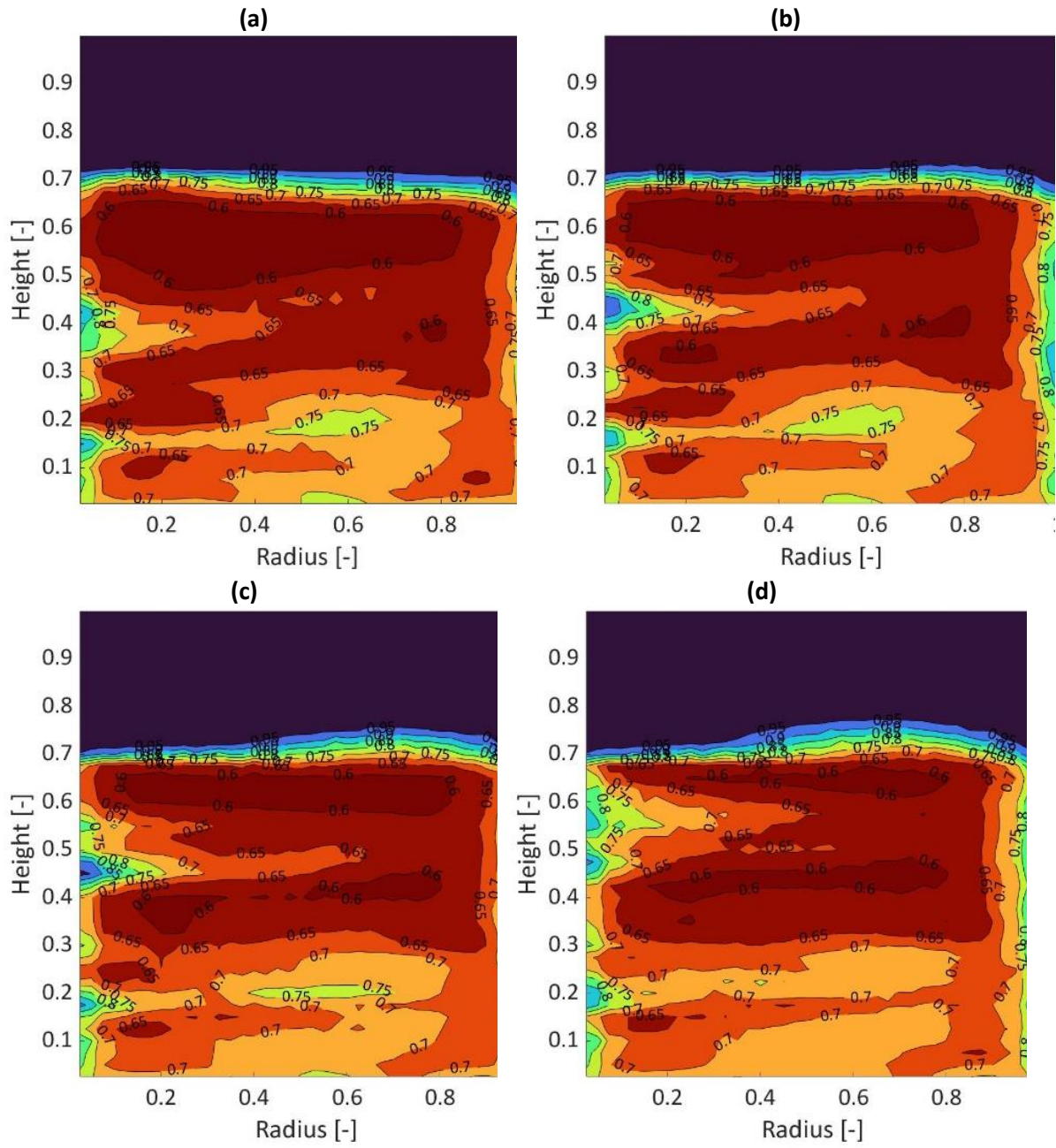


Figure 6.5: Power spectrum of pressure drop over the bed area for the simulations of the IHBFSR without side-flow for different mesh densities and CFL = 0.2 (left) and CFL = 0.4 (right). With the dotted line, the corresponding Savitzky – Golay filtered spectrum (polynomial order: 1, frame length: 9).

To determine the dominant pressure drop fluctuation frequency for the aforementioned simulations, fast Fourier transform (FFT) analysis was performed. This can provide an insight in the bubble frequency and associated particle mixing in a fluidized bed [59]. The resulting power spectra are presented in Figure 6.5, along with the Savitzky – Golay filtered spectra, for noise elimination purposes. The dominant frequency values for the unfiltered spectra obtained from the different mesh density/CFL combination simulations ranged between 3.1 and 4.6 Hz. The observed difference in terms of dominant frequency is small between the various combinations and it can be even smaller qualitatively, if the case of $15 \times d_p$ is considered. Figure 6.5 shows that the dominant frequency of 3.1 Hz for the $15 \times d_p$ – CFL=0.4 case is followed by a peak at ~ 4.6 Hz with a slightly lower magnitude. Overall, the behaviour in terms of bubble formation, as can be derived from the power spectrum of the pressure drop over the bed, was similar for the $20 \times d_p$ and $15 \times d_p$ simulations. For the $30 \times d_p$ cases, despite the qualitative agreement in terms of the location of the dominant frequency, less and broader peaks could be identified. This is indicative of the more gradual eruptions of the bubbles as they break up into the freeboard region, resulting from less sharply defined bubble edges due to the lower mesh density employed. Regarding the effect of CFL on the dominant power frequency, no clear trend could be derived also for this case. The void fraction contours corresponding to the dominant frequency for the $15 \times d_p$ – CFL = 0.2 case are presented in Figure 6.6. There, the movement of bubbles (light orange) that tend to emerge at the inner wall of the reactor can be clearly observed. In Figure 6.6, the x – axis denotes the dimensionless radius (0 corresponds to the inner-burner wall and 1 to the outer-reactor wall), while the y – axis shows the dimensionless height of the simulated domain, as they were introduced in the previous section.



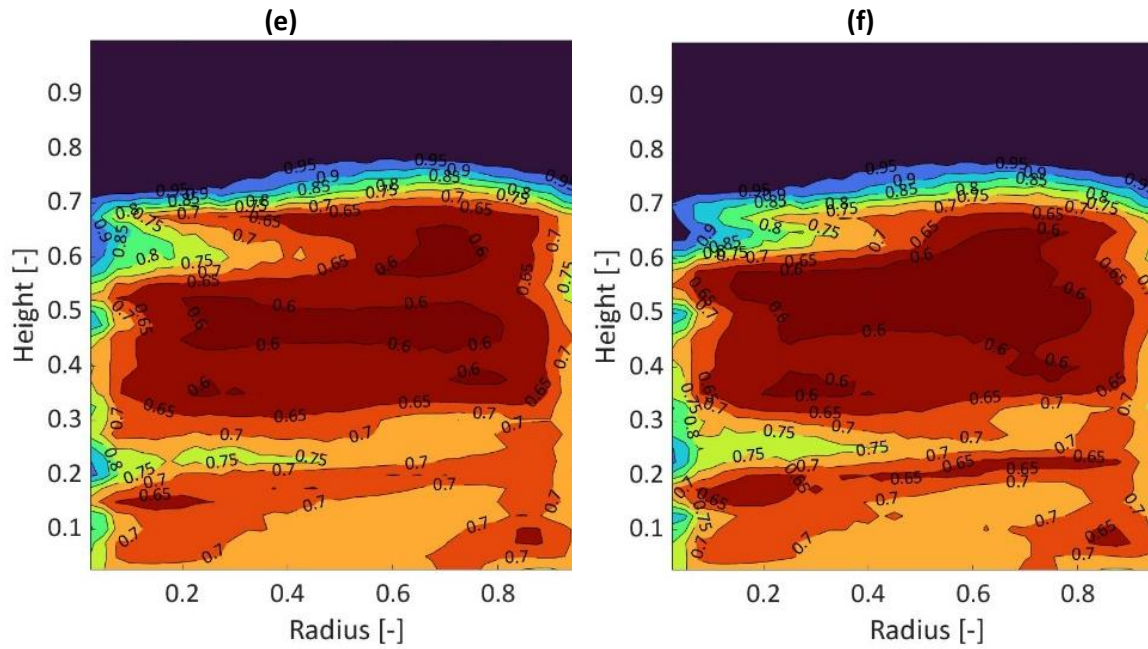


Figure 6.6: Instantaneous void fraction contours, showing the movement of bubbles (light orange) that tend to emerge at the inner wall at a dominant frequency of 4 Hz for the $15 \times d_p - CFL = 0.2$ case. Time starts at 2.25 s at a step of 0.0317 s moving from (a) to (f).

The determination of the bed height for the mesh and time step independence tests was performed using the method described in Section 6.4 and the results are presented in Figure 6.7. Focusing on the bed height after stabilization, i.e. after 2.5 s of simulation time, it is clear that a decrease of the mesh size from $30 \times d_p$ to $15 \times d_p$, led to a decrease of the bed height. Nevertheless, the difference between the $20 \times d_p$ and $15 \times d_p$ cases was only 0.03 and 0.04 m, for CFL values of 0.2 and 0.4, respectively. The reduction of the time step from CFL = 0.4 to CFL = 0.2, led to a 4.8, 2.6 and 1.4 % reduction of the bed height for the cases of $30 \times d_p$, $20 \times d_p$ and $15 \times d_p$, respectively.

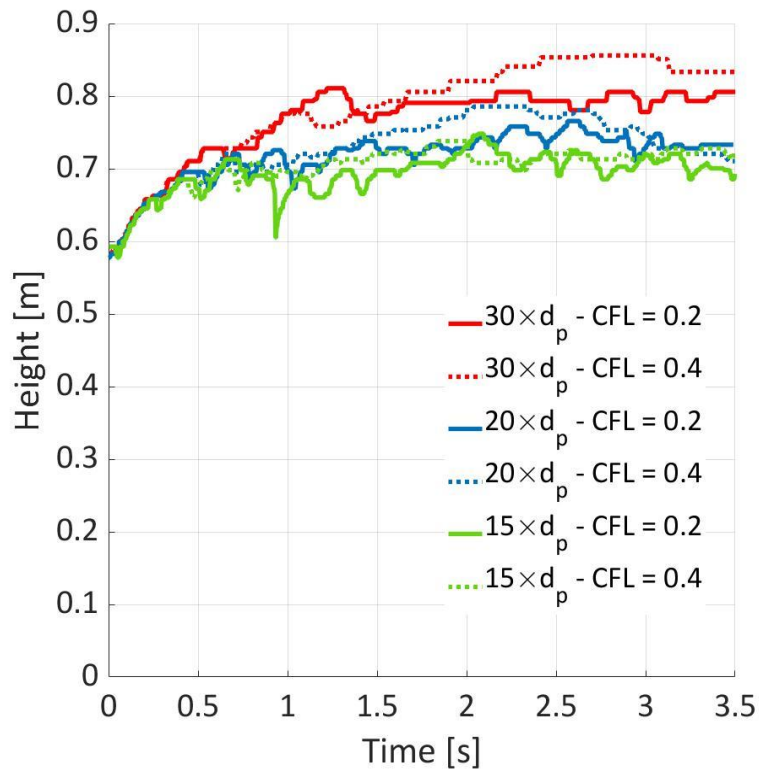


Figure 6.7: Bed height for different mesh density and CFL combinations for the simulations of the IHBFSR without side-flow.

Overall, the bed height derived from all simulations is well within the range deduced from the experimental results (0.67-0.82 m), except for the $30 \times d_p - CFL=0.4$ case. Furthermore, the aforementioned bed height reduction for decreasing CFL values becomes less significant for coarser mesh size. In addition, smaller differences were observed between the $20 \times d_p$ and $15 \times d_p$ cases in that regard. When the pressure drop dominant frequency is considered, the $20 \times d_p$ and $15 \times d_p$ cases again presented similar behaviour, in slight contrast with the $30 \times d_p$ case, where the observed peaks were broader. Considering these conclusions from the analysis of the simulations performed, as well as the lack of any useful ones from the pressure drop analysis, the $15 \times d_p$ mesh size was employed in the subsequent simulations. From the analysis performed, it became apparent that the simulation results were more sensitive towards variations of the grid size, rather than the time step size, a conclusion also derived in [60]. Therefore, both CFL values of 0.2 and 0.4 were employed in the following analysis.

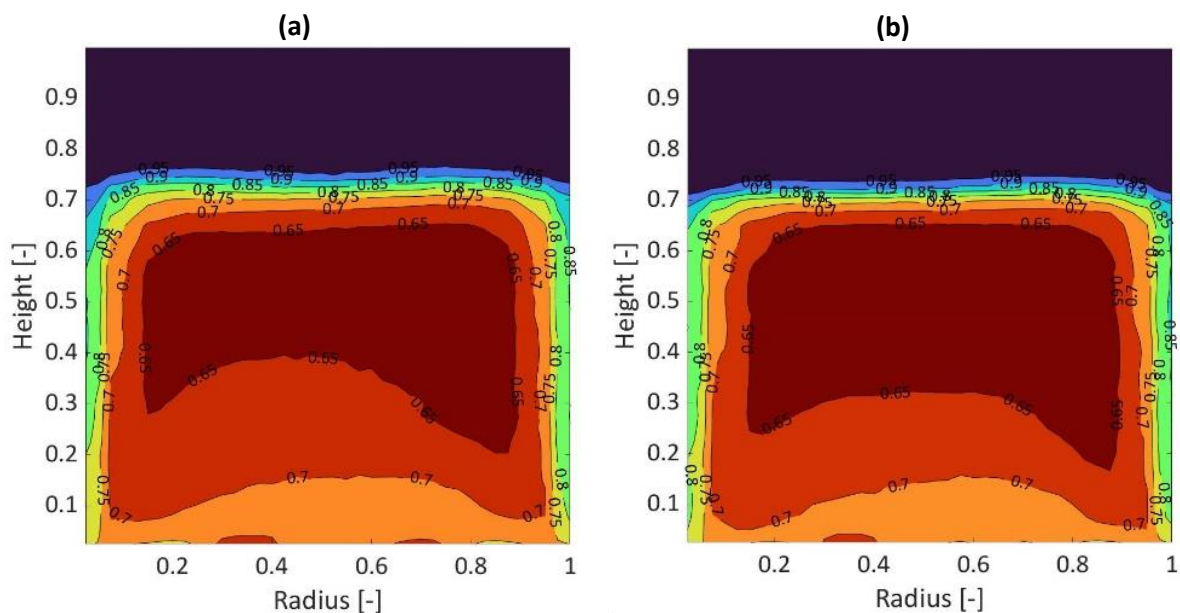
6.5.2 Restitution coefficient (without side-flow)

The restitution coefficient determines the degree of exchange of energy and momentum during particle collisions. A restitution coefficient of 1 corresponds to perfectly elastic collisions, while 0 corresponds to inelastic collisions. For sand-like material such as corundum, the typical range of values for the restitution coefficient employed in similar studies is between 0.9 and 0.99 [61-64]. However, in the context of this work, values of restitution coefficient between 0.8 and 0.99 were investigated. It should be mentioned that a restitution coefficient of 0.9 was employed in the simulations presented in the previous section. The average pressure drop, the dominant frequency and the bed height derived from the restitution coefficient simulations, are presented in Table 6.2. The simulations were performed with a $15 \times d_p$ grid and a CFL of 0.4.

Table 6.2: Average pressure drop (Δp), dominant frequency (Savitzky-Golay filter) and bed height derived from simulations with different values of the restitution coefficient. The average pressure drop was calculated in the 0.75 – 3.5 s interval and the bed height from 2.5 to 3.5 s, both after stabilization.

Restitution coefficient (-)	Average Δp (mbar)	Dominant frequency (Hz)	Bed height (m)
0.8	65.5	5.1	0.72
0.85	64.1	4.8	0.71
0.9	64.4	4.2	0.71
0.95	65.3	4.0	0.73
0.99	66.2	5.1	0.76

From Table 6.2, the minor influence of the restitution coefficient on the main simulation performance metrics employed in this work, can be clearly seen. For the average pressure drop, a standard deviation of 1 % was obtained for the five values investigated, while for the bed height the corresponding value was 3 %. Regarding the bed height, a slight increase was observed for higher values of restitution coefficient of 0.95 and 0.99. In the case of the dominant frequency, due to the presence of significant amount of noise in the data (especially in the $e = 0.85$ case), a Savitzky-Golay filter of 1st polynomial order and a frame length of 9 was applied. From this analysis, a 11 % standard deviation between the five values of restitution coefficient was obtained. The dominant frequency values, ranging between 4 and 5.1 Hz, showcased the small influence of restitution coefficient also in this regard. From these findings, it can be derived that the selection of the restitution coefficient value within this range, does not influence the three main metrics considered significantly, as has also been observed in literature [62]. Therefore, a value of 0.9 for the restitution coefficient was selected for the subsequent simulations. However, it remains valuable to examine its effect on the fluidization behaviour of the IHBFSR. In Figure 6.8, the time averaged void fraction contours for all investigated restitution coefficient values are presented.



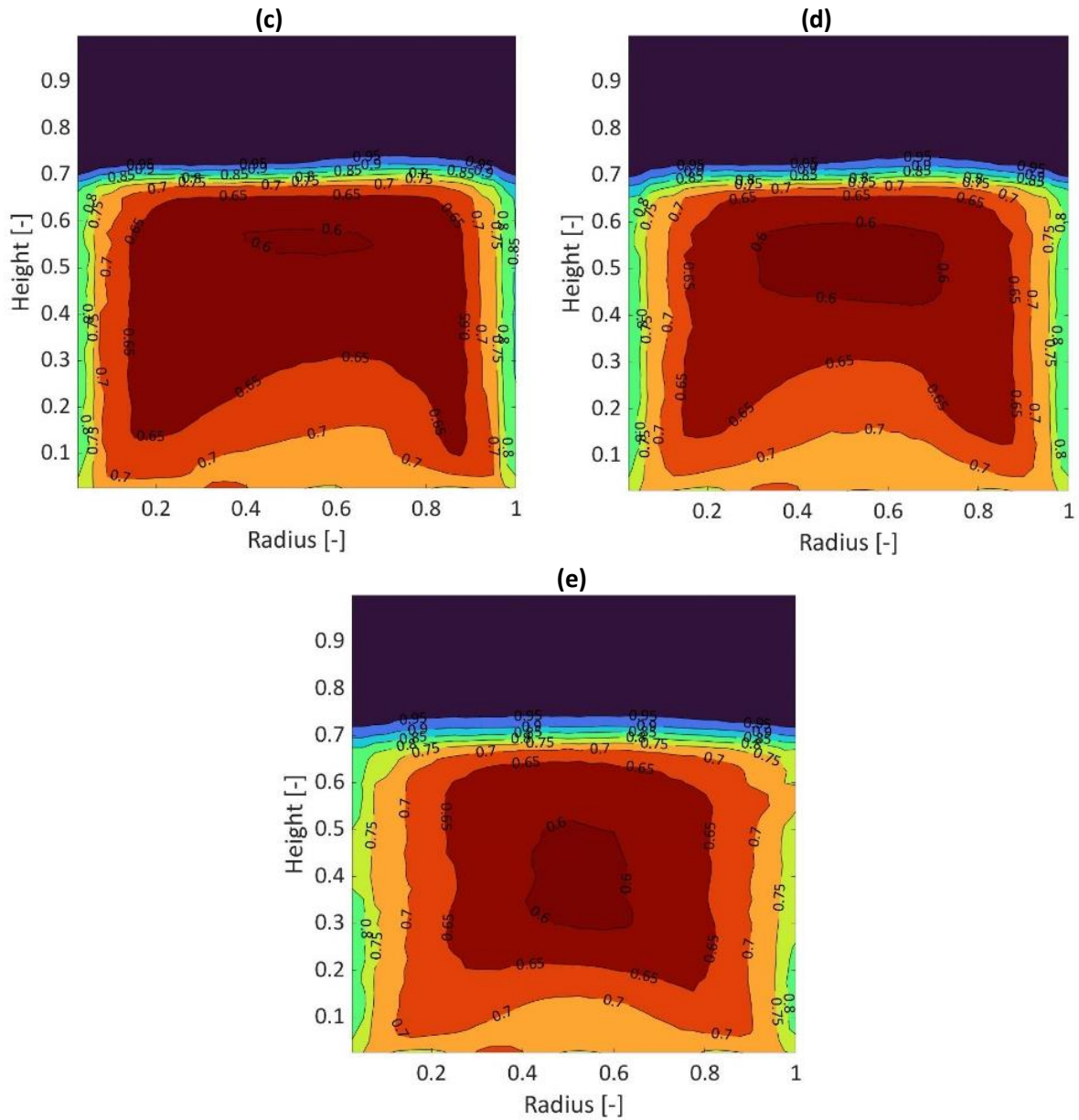


Figure 6.8: Time averaged void fraction contours of the IHBFSR bed area for different values of the restitution coefficient: (a) $e=0.8$, (b) $e=0.85$, (c) $e=0.9$, (d) $e=0.95$ and (e) $e=0.99$. The simulations were performed with a $15 \times d_p$ grid and a CFL of 0.4.

From Figure 6.8, it can be readily derived that the bubbles tend to move towards the inner and outer wall, leaving the highest solids density in the centre of the bed. With decreasing restitution coefficient values, the lowest void fraction area (voidage lower than 0.6), clearly observable at the centre of the bed for 0.99, becomes wider and thinner for values of 0.95 and 0.9, before disappearing completely for 0.85. This could be an indication of improved mixing of the bed for lower values of restitution coefficient, something that has also been reported in the literature [64]. Finally, the void fraction in the area between 0.15 – 0.4 radius and 0.15 – 0.35 height, presents higher void fraction values for restitution coefficient values decreasing from 0.9 to 0.85 to 0.8. Therefore, it can be concluded, that a further reduction of the restitution coefficient enhances the already significant channelling behaviour of the gas flow near the inner wall of the IHBFSR. Similar behaviour can also be observed at the outer wall, where areas with void fraction above 0.8 start to appear for restitution coefficient values lower than 0.95. These trends suggest that for decreasing values of restitution

coefficient, most of the particles tend to cluster towards the top of the bed area forcing the gas to flow along the inner and outer walls.

6.5.3 IHBFSR simulation results (without side-flow)

The previous subsection focused on time-averaged voidages. We now aim to get more insight in the bubble behaviour by focusing on the evolution of the instantaneous voidage distribution for a fixed restitution coefficient of $e=0.9$ in Figure 6.9. The lack of bubble formation in the middle of the reactor becomes readily apparent, since the area between 0.25 and 0.9 radius is dominated by the presence of solid clusters, which become more compact with increasing height. As can be deduced by studying Figure 6.9, the few bubbles that are formed in the middle of the reactor, do not seem to be able to penetrate the low void fraction area above them. This conclusion is derived by considering the high void fraction areas, corresponding to bubbles, noted in the general area between 0.5 and 0.8 radius. By piecing together the information provided by the contours in Figure 6.9, it can be argued that some bubbles formed in the middle of the reactor, after initially traversing through the bed material particles (a to c), reach a point where they are forced to move towards the side of the reactor (d), unable to pass through the dense top part residing in the middle. Connected to this, the gas flow appears to prefer the pathway along the inner (burner) and outer walls of the reactor. This becomes even more apparent by studying the time averaged void fraction contour in Figure 6.8 (c). The presence of the relatively thin high void fraction layers at the sides, indicate that the bubbles are moving up the sides of the reactor, behaving like a slug flow (channelling). This means that a significant amount of particles are trickling down the reactor walls, as large slow-moving bubbles are being formed. Again from Figure 6.8 (c), these high void fraction layers seem rather similar in terms of thickness. This, along with the fact that the outer wall area is significantly larger than the inner one, leads to the conclusion that the bubbles at the outer wall of the reactor are larger than the ones near the burner. Furthermore, the lower void fraction zones at the bottom of the reactor, clearly observable in Figure 6.9 (a) – (d), are most probably due to the walls corresponding to the tuyeres heads. Finally, note that the low void fraction area at the middle of the reactor appears to tilt towards the right side (outer reactor wall). This could be an indication of a circulating particle flow along the horizontal direction of the reactor, caused by the slug flow along the walls of the reactor (channelling).

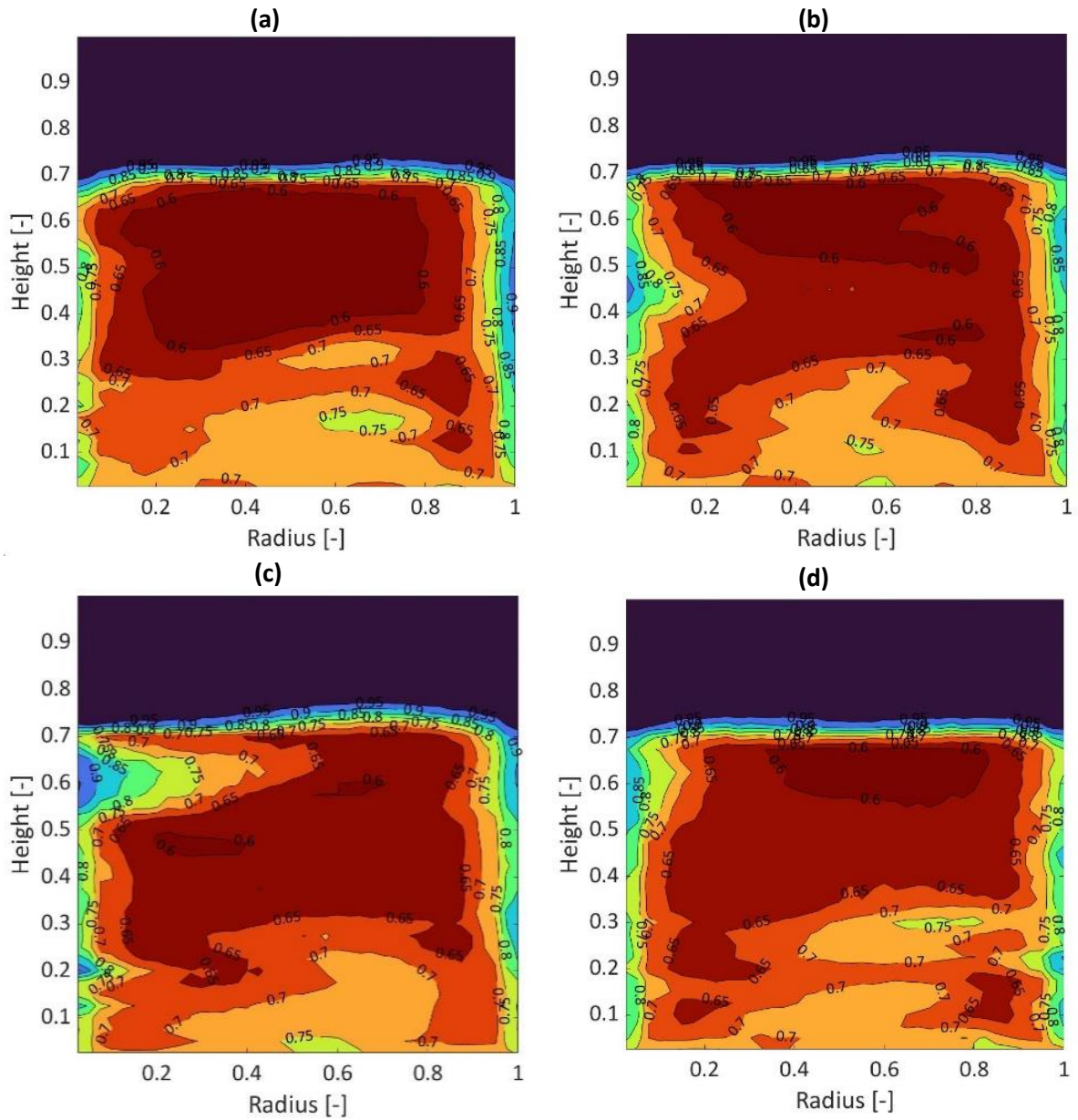


Figure 6.9: Void fraction contours of the IHBFSR bed area at $t = 1.26$ s (a), $t = 1.89$ s (b), $t = 2.52$ s (c), and $t = 3.16$ s (d). The simulation was performed with a $15 \times d_p$ grid and a CFL of 0.4.

The gas volume fraction and velocity vector field at the last time step of the simulation are presented in Figure 6.10. The selected time step corresponds to a stabilized state of the bed and therefore can be considered representative of the overall fluidization behaviour of the IHBFSR. From this figure the previously derived conclusions are verified, since the higher velocities in the system (which correspond to bubbles [13]) as well as the higher void fraction areas, are located mainly in the upper part of the outer and inner walls of the reactor.

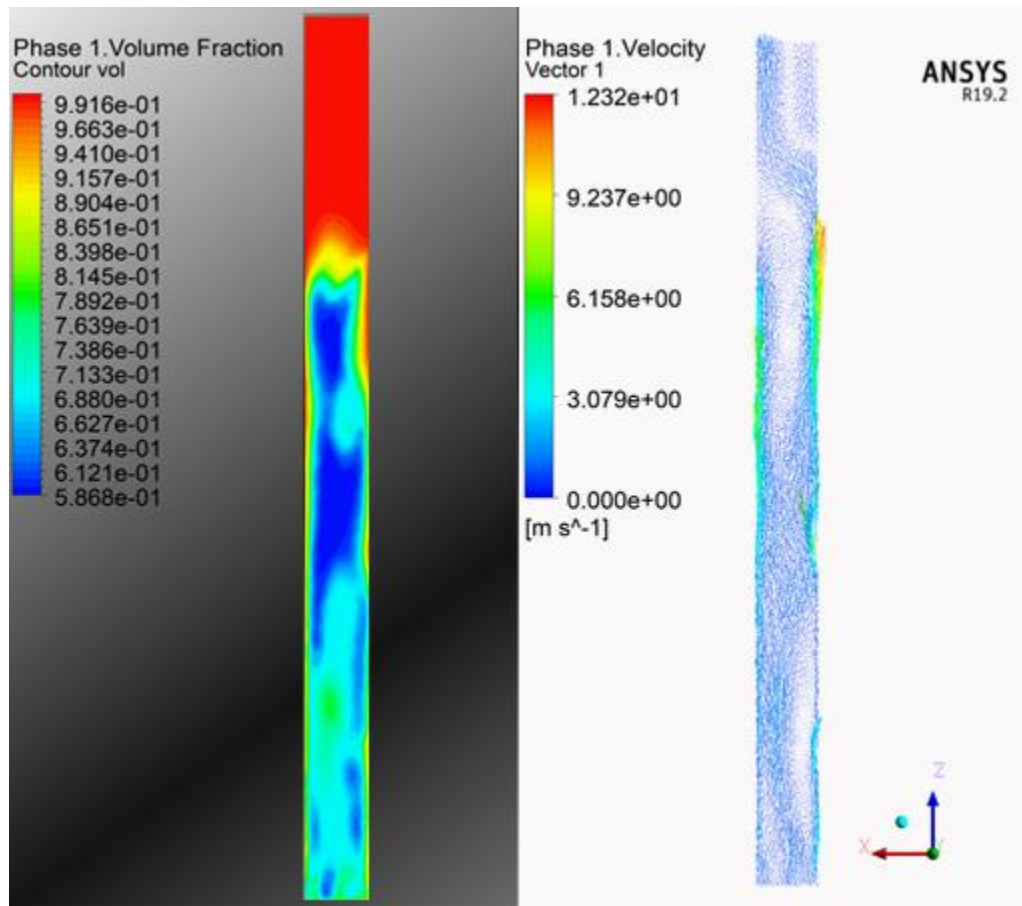
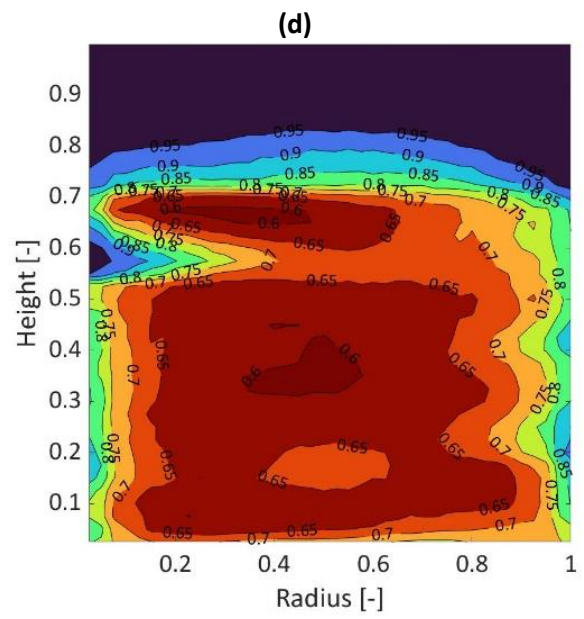
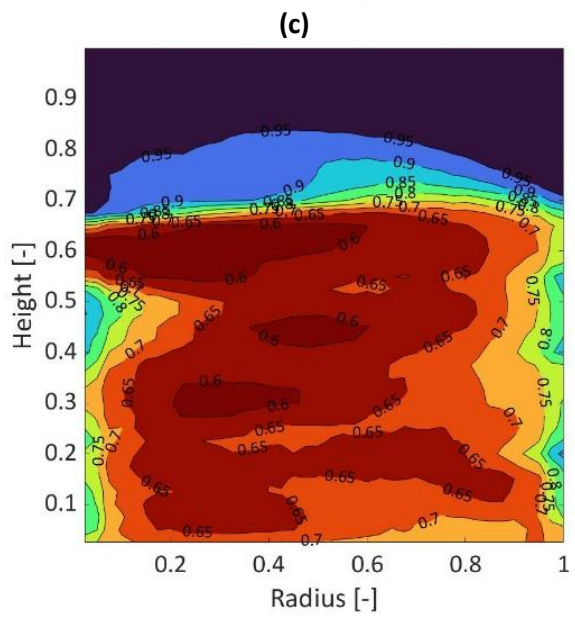
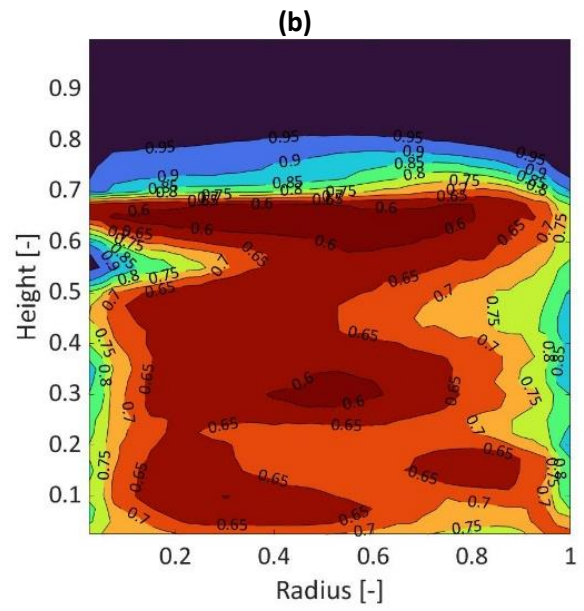
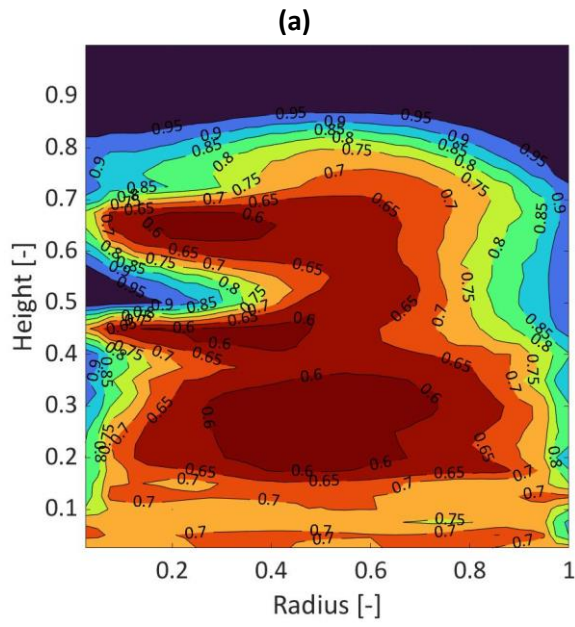


Figure 6.10: Gas volume fraction (left) and velocity vector field (right) from the final time step of the IHBFSR bed area simulation without side-flow. The simulation was performed with a $15 \times d_p$ grid and a CFL of 0.4.

6.5.4 Effect of the N_2 purge side-flow on the IHBFSR fluidization behaviour

In the previous section, the simulation of the fluidization behaviour of the IHBFSR bed area for a 72° “wedge” was presented. However, as was discussed in Section Reactor description, in the experimental system an additional N_2 feed is employed for the pressurization of the feeding system, preventing the back-flow of gases from the main reactor. As a result, a stream of N_2 enters the reactor through the feeder located at the outer wall. The effect of this flow was assumed to be local, within the 72° partition including the feeder outlet. In this section, the testing of this assumption is presented, along with the overall fluidization behaviour including this side-flow. The simulations were performed with a mesh size of $15 \times d_p$, as in the previous cases. Nevertheless, due to the higher gas velocities in the system due to the introduction of the side-flow, the CFL had to be reduced to 0.2. According to the time step independence analysis presented in 6.5.1, this is not expected to jeopardize the comparability with the previously conducted simulations with CFL = 0.4. The void fraction contours at four different time-steps of the simulation and the time averaged one are presented in Figure 6.11.



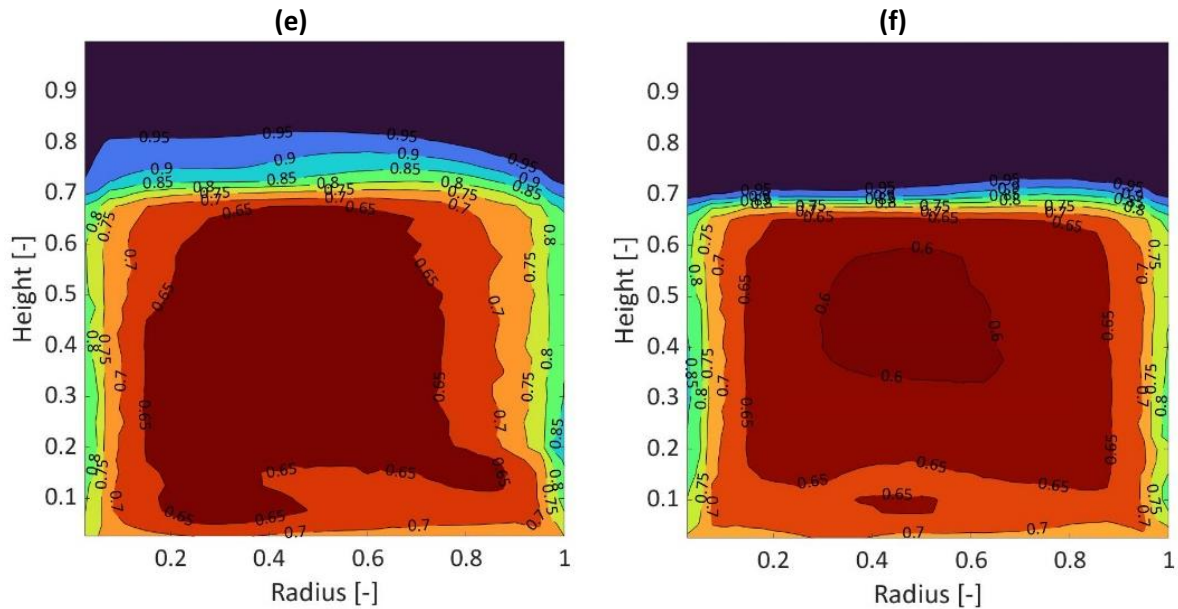


Figure 6.11: Void fraction contours of the IHBFSR bed area at $t = 0.92$ s (a), $t = 1.84$ s (b), $t = 2.76$ s (c) and $t = 3.69$ s (d). In (e) and (f) the time averaged void fraction contours for the side-flow and no side-flow cases, respectively. The simulation was performed with a $15 \times d_p$ grid and a CFL of 0.2. The feeder side-flow is located at the outer wall at a dimensionless height of 0.2025.

As it was also the case for the no side-flow simulations presented in a previous section, the formation of bubbles at the inner (burner) wall of the reactor can be clearly observed in Figure 6.11 (a) – (d). On the contrary, the formation of bubbles near the outer radius of the reactor is not as apparent as in the previous case. It appears that the side-flow behaves almost like a stream on the reactor wall, as it passes through the bed area. This particular behaviour also prevents the formation of bubbles near the outer wall of the reactor. This is also noticeable in the comparison of the time averaged void fraction contours of the side-flow and no side-flow simulations presented in Figure 6.11 (e) and (f), showing that the inner radius void fraction layers are similar in both cases. Regarding the outer radius, the high void fraction layer (above 0.7) becomes thicker (roughly from 0.85 to 1 radius, versus 0.95 to 1) for the side-flow case. Additionally, sub-layers with void-fraction of 0.8 and 0.85 which were marginally present or not present at all, respectively, for the no side-flow case, are clearly observable in Figure 6.11 (e). Another observation can be made in regard to the low void fraction area in the centre of the reactor. As was discussed in the previous section, the central low void fraction area for the case of no side-flow, presented a tilt towards the outer radius of the reactor. This tilt, which is also observable in Figure 6.11 (f), is reversed for the case of the side-flow inclusion, due to the aforementioned stream-like flow pattern with which this flow is introduced in the reactor. It appears that bed particles tend to concentrate more towards the burner wall, hinting towards an increased channelling of the flow towards the outer reactor wall. Another difference between the two cases lies in the presence of low void fraction areas in the centre of the reactor. For the side-flow case, even though the different void fraction zones present more complex morphologies, mostly 0.6 and 0.65 void fraction zones can be observed. On the other hand, as was discussed for Figure 6.9, bubbles appear to form also in the middle of the reactor, although to a much smaller extent. Nevertheless, the lack of void fraction zones lower than 0.65 and the aforementioned complex shapes formed in the centre of the reactor for the side-flow case, can indicate better mixing for this particular case throughout the height of the reactor. It should be reminded, that in the no side-flow case, the 0.25 - 0.9 radius area was dominated by particle clusters, which became more compact for increasing height.

The method for the determination of the bed height from the simulations performed was described in Section 6.4. For the simulations with the inclusion of the N_2 purge side-flow, the algorithm had a difficulty in determining the bed height for the first 2 s of the simulations. This phenomenon

occurred due to the presence of height layers with a high void fraction. These layers are visible in Figure 6.11 approximately from 0.7 to 0.8 height, something that was not the case for the no side-flow simulations. The abovementioned fact, along with the more intense bubble formation at the burner wall of the reactor, can lead the algorithm to identify the void fraction gradient caused by the bubble's presence as the bed height. This phenomenon can be observed in Figure 6.12 until roughly 2 s. After this point the behaviour stabilizes and the corresponding bed height is comparable to the case without the side-flow, albeit a little bit higher (0.72 versus 0.71 m). In regard to the average pressure drop over the bed, the inclusion of the side-flow to the simulations did not lead to a differentiation to its values. This could be attributed to the extreme channelling behaviour as observed in the void fraction contours, since the side-flow passes through the bed without effective obstacles. However, the pressure drop oscillations' magnitude was marginally higher for the case of the side-flow. This can be attributed to the more intense fluidization due to the larger amount of fluidization media and thus higher fluidization velocities employed. Finally, in regard to the dominant frequency, the corresponding values for the unfiltered spectra were 4 and 2.7 Hz for the cases without and with the side-flow, respectively (Figure 6.12). The corresponding values for the Savitzky – Golay filtered spectra were similar both in terms of magnitude and difference between the two cases (4.5 and 3.2 Hz, respectively). While it was expected that an increase in the overall fluidization velocity would lead to an increase of the dominant frequency, this was not observed. However, with the increase of the fluidization velocity imposed by the inclusion of the side-flow in the simulations, the number and height of the peaks observed increased. This observation, as it was for the more intense pressure oscillations noted before, is a result of the increased amount of fluidization media in the reactor.

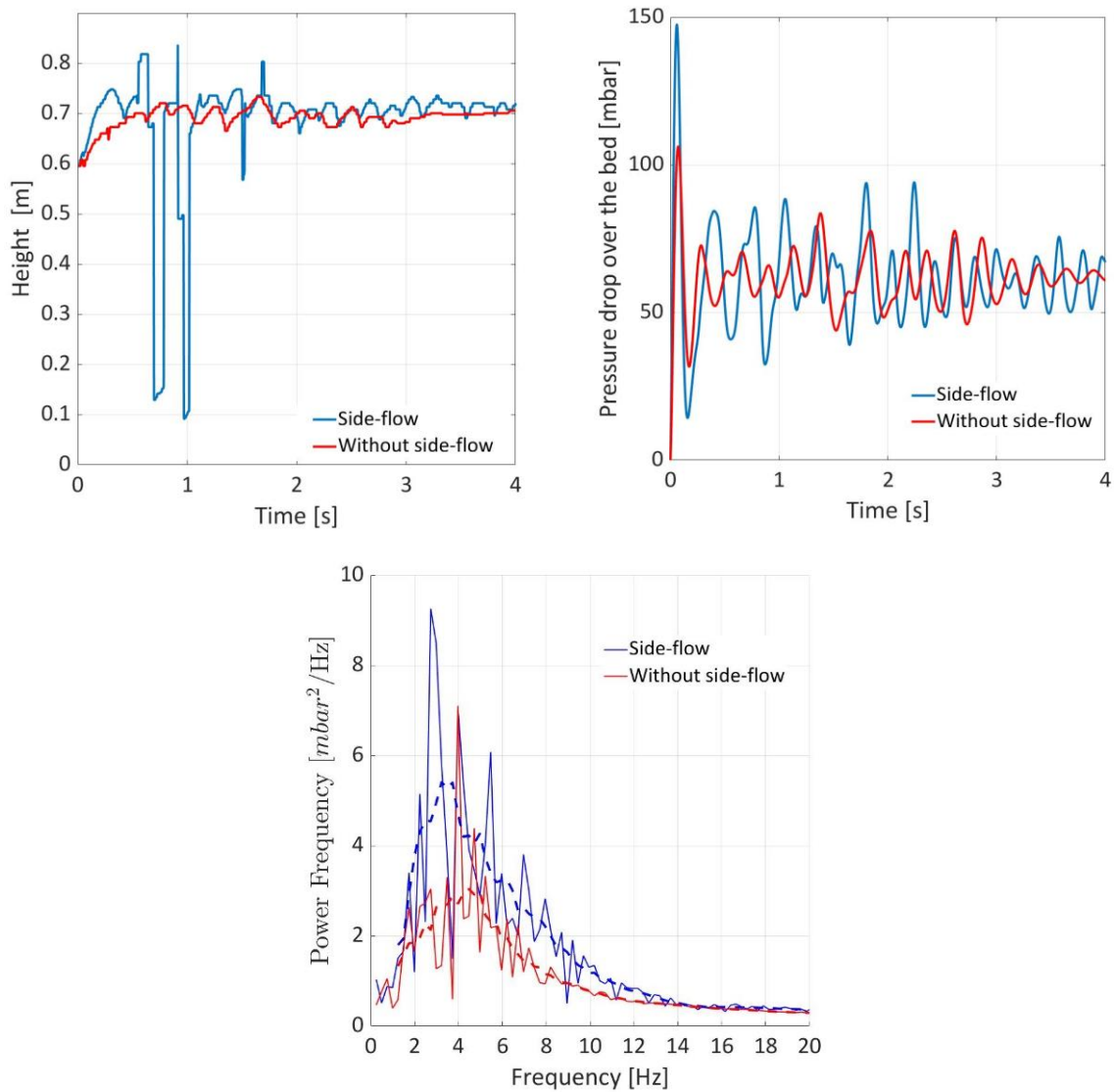


Figure 6.12: Comparison of the bed height (left), pressure drop over the bed (right) and power spectrum of pressure drop over the bed area (bottom) from the simulations of the IHBFSR with (blue) and without (red lines) side-flow. The simulation was performed with a $15 \times d_p$ grid and a CFL of 0.2. In the power spectrum graph (bottom), with the dotted line, the corresponding Savitzky – Golay filtered spectra (polynomial order: 1, frame length: 9).

As was mentioned in the beginning of this section, the validity of the reduction of the reactor's geometry to 72° partitions is assured as long as the side-flow does not propagate out of the respective domain. To investigate the validity of this assumption, the velocity vectors of the gas phase were computed and subsequently visualised in Figure 6.13. Depending on the time step, the flow moves slightly right or left from the feeder inlet, staying always far away enough from the symmetry boundary condition side walls to validate the aforementioned assumption. It can even be argued that the geometry domain could be further reduced to 36° , although at the loss of the observation of the waving effect in the radial direction of the side-flow stream. Such a decrease of the geometry's size would improve the computational requirements, allowing further decrease of the time step or mesh size.

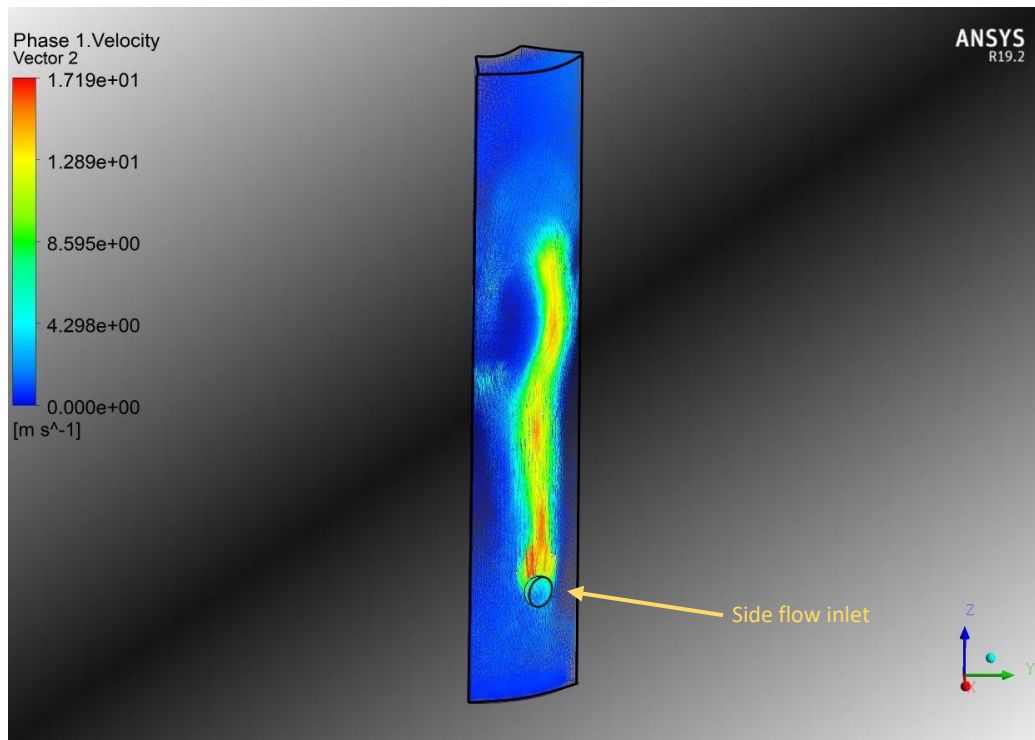


Figure 6.13: Velocity vectors of the gas phase from the simulations of the IHBFSR with side-flow. The simulation was performed with a $15 \times dp$ grid and a CFL of 0.2.

Overall, our results show that the side-flow is not well mixed in the reactor. Therefore, there is a possibility that in practice a cold spot is formed at the feeder inlet. The presence of such a cold spot, would render the assumption that the N_2 side-flow is at the same temperature as the rest of the reactor at this point ($600\text{ }^\circ\text{C}$) incorrect. In this case, the volume expansion of the N_2 gas caused by the temperature increase would also affect the internal flow field in ways not covered by the present simulations. Furthermore, as was also shown by Ostermeier et al. [65], the gas inlet geometry does not influence the global properties of bed height and pressure drop greatly. However, our work shows that it has a big influence on the gas and particle flow fields and solids distribution. The implementation of heat and mass transfer modelling in future simulations by the authors will allow the more in-depth investigation of this particular effect. Finally, regarding the bed height (0.72 with side-flow and 0.71 without side-flow) derived from the simulations, it was always within the limits imposed by the experiments (0.67 – 0.82 m). However, given the fact that for setting up of the Syamlal model, a minimum fluidization velocity including the side-flow was employed, the overall height computed might be over-predicted. Considering the behaviour of the side-flow presented in this work, it might be more appropriate to exclude it from the calculation of the minimum fluidization velocity of the corundum bed, since its effect appears to be insignificant. This conclusion is also supported by the clear over-prediction that can be observed for the pressure drop over the bed area. In particular, the experimentally derived average pressure drop of 55 mbar is over-predicted by 12.5 % in the side-flow simulations.

6.6 Conclusions

In this work, CFD – TFM simulations of a novel 50 kW_{th} indirectly heated bubbling fluidized bed steam reformer (IHFBSR) were performed to investigate its hydrodynamic behaviour. The results were verified with the employment of corresponding experimental results obtained from fluidization experiments conducted in a pilot-scale reactor. The hydrodynamic behaviour of the reactor was simulated successfully, as evident by the small deviations observed between the experimental and computational values obtained for the global hydrodynamic metrics (bed height and pressure drop). It was shown that for realistic values of the particle restitution coefficient channelling of the gas flow occurs near the reactor walls. This channelling was present for both the side-flow and no side-flow simulations. However, larger bubbles appeared to be forming near the outer wall of the reactor for the no side-flow simulations, while the opposite behaviour was encountered for the side-flow simulations. This was due to the stream-like behaviour of the side-flow moving against the outer wall of the reactor, thus preventing the formation of bubbles locally. Additionally, limiting the simulations to a 72° symmetry “wedge” was validated by the model findings, which indicated that even further reduction is possible. Overall, it can be argued that an increase of the reactor’s diameter could potentially lead to a reduction of the observed channelling of the fluidization media and improve the mixing achieved in the reactor. This could in turn improve the heat and mass transfer in the system and thus also increase the conversion efficiency of the IHFBSR during gasification experiments.

Overall, the present work constitutes the first step to study the fluidization behaviour of the novel IHFBSR reactor of TU Delft. This investigation of this geometrically unique fluidized bed hydrodynamics lays the groundwork for future heat and mass transfer, as well as chemical reaction modelling which will allow the introduction and exploration of more experimental variables in conjunction with the simulation work. Apart from further verifying the simulation work performed so far, such an approach will allow the utilization of the entire spectrum of the IHFBSR’s analytical/instrumentation capabilities, something that was practically impossible within the context of the present work.

Bibliography

1. Karl, J. and T. Pröll, *Steam gasification of biomass in dual fluidized bed gasifiers: A review*. Renewable and Sustainable Energy Reviews, 2018. **98**: p. 64-78.
2. Schmid, J.C., et al., *Syngas for biorefineries from thermochemical gasification of lignocellulosic fuels and residues—5 years' experience with an advanced dual fluidized bed gasifier design*. Biomass Conversion and Biorefinery, 2019.
3. Fürsatz, K., et al., *Effect of biomass fuel ash and bed material on the product gas composition in DFB steam gasification*. Energy, 2021. **219**: p. 119650.
4. Larsson, A., et al., *Steam gasification of biomass – Typical gas quality and operational strategies derived from industrial-scale plants*. Fuel Processing Technology, 2021. **212**: p. 106609.
5. Hanchate, N., et al., *Biomass gasification using dual fluidized bed gasification systems: A review*. Journal of Cleaner Production, 2021. **280**: p. 123148.
6. Jüntgen, H. and K.H. Van Heek, *Gasification of coal with steam using heat from HTRs*. Nuclear Engineering and Design, 1975. **34**(1): p. 59-63.
7. Karl, J., *Biomass heat pipe reformer—design and performance of an indirectly heated steam gasifier*. Biomass Conversion and Biorefinery, 2014. **4**(1): p. 1-14.
8. Williams, R.H., et al., *Methanol and hydrogen from biomass for transportation*. Energy for Sustainable Development, 1995. **1**(5): p. 18-34.
9. Gallmetzer, G., et al., *The Agnion Heatpipe-Reformer—operating experiences and evaluation of fuel conversion and syngas composition*. Biomass Conversion and Biorefinery, 2012. **2**(3): p. 207-215.
10. Leimert, J.M., P. Treiber, and J. Karl, *The Heatpipe Reformer with optimized combustor design for enhanced cold gas efficiency*. Fuel Processing Technology, 2016. **141**: p. 68-73.
11. Karellas, S., J. Karl, and E. Kakaras, *An innovative biomass gasification process and its coupling with microturbine and fuel cell systems*. Energy, 2008. **33**(2): p. 284-291.
12. Verma, V., et al., *Numerical Investigation on the Effect of Pressure on Fluidization in a 3D Fluidized Bed*. Industrial & Engineering Chemistry Research, 2014. **53**(44): p. 17487-17498.
13. Kunii, D. and O. Levenspiel, *Fluidization Engineering*. 2nd ed. 1991: Butterworth-Heinemann.
14. van der Hoef, M.A., et al., *Multiscale Modeling of Gas-Fluidized Beds*, in *Advances in Chemical Engineering*, G.B. Marin, Editor. 2006, Academic Press. p. 65-149.
15. Qiu, K., et al., *Heat transfer and erosion mechanisms of an immersed tube in a bubbling fluidized bed: A LES-DEM approach*. International Journal of Thermal Sciences, 2016. **100**: p. 357-371.
16. Wahyudi, H., K. Chu, and A. Yu, *3D particle-scale modeling of gas-solids flow and heat transfer in fluidized beds with an immersed tube*. International Journal of Heat and Mass Transfer, 2016. **97**: p. 521-537.
17. Zhao, Y., et al., *Particle-scale simulation of the flow and heat transfer behaviors in fluidized bed with immersed tube*. AIChE Journal, 2009. **55**(12): p. 3109-3124.
18. Ma, H., Y. Zhao, and Y. Cheng, *CFD-DEM modeling of rod-like particles in a fluidized bed with complex geometry*. Powder Technology, 2019. **344**: p. 673-683.
19. Yang, S., et al., *Particle-Scale Investigation of the Hydrodynamics and Tube Erosion Property in a Three-Dimensional (3-D) Bubbling Fluidized Bed with Immersed Tubes*. Industrial & Engineering Chemistry Research, 2014. **53**(17): p. 6896-6912.
20. Zhou, L. and Y. Zhao, *CFD-DEM simulation of fluidized bed with an immersed tube using a coarse-grain model*. Chemical Engineering Science, 2021. **231**: p. 116290.
21. PengZhao, et al., *A computational fluid dynamics-discrete element-immersed boundary method for Cartesian grid simulation of heat transfer in compressible gas-solid flow with complex geometries*. Physics of Fluids, 2020. **32**(10): p. 103306.

22. Zhao, P., et al., *A CFD-DEM-IBM method for Cartesian grid simulation of gas-solid flow in complex geometries*. Chemical Engineering Journal, 2020. **389**: p. 124343.
23. Guo, Y., C.-Y. Wu, and C. Thornton, *Modeling gas-particle two-phase flows with complex and moving boundaries using DEM-CFD with an immersed boundary method*. AIChE Journal, 2013. **59**(4): p. 1075-1087.
24. Chen, M., et al., *CFD-DEM-VDGM method for simulation of particle fluidization behavior in multi-ring inclined-hole spouted fluidized bed*. Particuology, 2021. **57**: p. 112-126.
25. Su, J., Z. Gu, and X.Y. Xu, *Discrete element simulation of particle flow in arbitrarily complex geometries*. Chemical Engineering Science, 2011. **66**(23): p. 6069-6088.
26. Dietiker, J.-F., et al., *Cartesian grid simulations of gas-solids flow systems with complex geometry*. Powder Technology, 2013. **235**: p. 696-705.
27. Li, T., et al., *Cartesian grid simulations of bubbling fluidized beds with a horizontal tube bundle*. Chemical Engineering Science, 2011. **66**(23): p. 6220-6231.
28. Cheng, K., Y. Wang, and Q. Yang, *A semi-resolved CFD-DEM model for seepage-induced fine particle migration in gap-graded soils*. Computers and Geotechnics, 2018. **100**: p. 30-51.
29. Yang, Q., et al., *Improvement of semi-resolved CFD-DEM model for seepage-induced fine-particle migration: Eliminate limitation on mesh refinement*. Computers and Geotechnics, 2019. **110**: p. 1-18.
30. Gui, N., J.R. Fan, and K. Luo, *DEM-LES study of 3-D bubbling fluidized bed with immersed tubes*. Chemical Engineering Science, 2008. **63**(14): p. 3654-3663.
31. Gui, N. and J. Fan, *Numerical simulation of pulsed fluidized bed with immersed tubes using DEM-LES coupling method*. Chemical Engineering Science, 2009. **64**(11): p. 2590-2598.
32. Mori, Y., C.-Y. Wu, and M. Sakai, *Validation study on a scaling law model of the DEM in industrial gas-solid flows*. Powder Technology, 2019. **343**: p. 101-112.
33. Wu, C.L., A.S. Berrouk, and K. Nandakumar, *Three-dimensional discrete particle model for gas-solid fluidized beds on unstructured mesh*. Chemical Engineering Journal, 2009. **152**(2): p. 514-529.
34. Wu, C.L., et al., *Dense particulate flow model on unstructured mesh*. Chemical Engineering Science, 2006. **61**(17): p. 5726-5741.
35. Córcoles, J.I., A. Acosta-Iborra, and J.A. Almendros-Ibáñez, *Influence of immersed surface shape on the heat transfer process and flow pattern in a fluidized bed using numerical simulation*. International Journal of Heat and Mass Transfer, 2021. **178**: p. 121621.
36. Fattahi, M., et al., *Numerical simulation of heat transfer coefficient around different immersed bodies in a fluidized bed containing Geldart B particles*. International Journal of Heat and Mass Transfer, 2019. **141**: p. 353-366.
37. Hau, Z. and E.W.C. Lim, *Heat Transfer from an Immersed Tube in a Bubbling Fluidized Bed*. Industrial & Engineering Chemistry Research, 2016. **55**(33): p. 9040-9053.
38. Ngo, S.I., et al., *Flow behavior and heat transfer in bubbling fluidized-bed with immersed heat exchange tubes for CO₂ methanation*. Powder Technology, 2021. **380**: p. 462-474.
39. Sin, E.M.L. and E.W.C. Lim, *Heat transfer from immersed tubes in a pulsating fluidized bed*. Powder Technology, 2018. **327**: p. 500-511.
40. He, Y., et al., *Prediction on immersed tubes erosion using two-fluid model in a bubbling fluidized bed*. Chemical Engineering Science, 2009. **64**(13): p. 3072-3082.
41. Dong, N.H., et al., *Effect of tube shape on the hydrodynamics and tube-to-bed heat transfer in fluidized beds*. Applied Thermal Engineering, 2013. **60**(1): p. 472-479.
42. Armstrong, L.M., S. Gu, and K.H. Luo, *The influence of multiple tubes on the tube-to-bed heat transfer in a fluidised bed*. International Journal of Multiphase Flow, 2010. **36**(11): p. 916-929.
43. Vogtenhuber, H., D. Pernsteiner, and R. Hofmann, *Experimental and Numerical Investigations on Heat Transfer of Bare Tubes in a Bubbling Fluidized Bed with Respect to Better Heat Integration in Temperature Swing Adsorption Systems*. Energies, 2019. **12**(14): p. 2646.

44. Schreiber, M., T.W. Asegehegn, and H.J. Krautz, *Numerical and Experimental Investigation of Bubbling Gas–Solid Fluidized Beds with Dense Immersed Tube Bundles*. Industrial & Engineering Chemistry Research, 2011. **50**(12): p. 7653-7666.
45. Jašo, S., H. Arellano-Garcia, and G. Wozny, *Oxidative coupling of methane in a fluidized bed reactor: Influence of feeding policy, hydrodynamics, and reactor geometry*. Chemical Engineering Journal, 2011. **171**(1): p. 255-271.
46. de Jong, J.F., M. van Sint Annaland, and J.A.M. Kuipers, *Membrane-assisted fluidized beds—Part 2: Numerical study on the hydrodynamics around immersed gas-permeating membrane tubes*. Chemical Engineering Science, 2012. **84**: p. 822-833.
47. Verma, V., et al., *Hydrodynamics of gas–solids flow in a bubbling fluidized bed with immersed vertical U-tube banks*. Chemical Engineering Journal, 2016. **287**: p. 727-743.
48. Tsekos, C., M. del Grosso, and W. de Jong, *Gasification of woody biomass in a novel indirectly heated bubbling fluidized bed steam reformer*. Fuel Processing Technology, 2021. **224**: p. 107003.
49. Uddin, M.H. and C.J. Coronella, *Effects of grid size on predictions of bed expansion in bubbling fluidized beds of Geldart B particles: A generalized rule for a grid-independent solution of TFM simulations*. Particuology, 2017. **34**: p. 61-69.
50. Adnan, M., et al., *Multiscale modeling of bubbling fluidized bed reactors using a hybrid Eulerian-Lagrangian dense discrete phase approach*. Powder Technology, 2020. **376**: p. 296-319.
51. Levenspiel, O., *Chemical Reaction Engineering*. 3d ed. 1998: John Wiley & Sons.
52. Siedlecki, M., *PhD Thesis: On the gasification of biomass in a steam-oxygen blown CFB gasifier with the focus on gas quality upgrading: technology background, experiments and mathematical modeling*. 2011, Delft University of Technology.
53. Ding, J. and D. Gidaspow, *A bubbling fluidization model using kinetic theory of granular flow*. AIChE Journal, 1990. **36**(4): p. 523-538.
54. Gidaspow, D., *Multiphase Flow and Fluidization: Continuum and Kinetic Theory Descriptions*. 1994, New York: Academic Press.
55. Lun, C.K.K., et al., *Kinetic theories for granular flow: inelastic particles in Couette flow and slightly inelastic particles in a general flowfield*. Journal of Fluid Mechanics, 1984. **140**: p. 223-256.
56. Ogawa, S., A. Umemura, and N. Oshima, *On the equations of fully fluidized granular materials*. Zeitschrift für angewandte Mathematik und Physik ZAMP, 1980. **31**(4): p. 483-493.
57. Syamlal, M. and T.J. O'Brien, *Computer simulation of bubbles in a fluidized bed*. A.I.Ch.E. Symposium Series, 1989. **85**: p. 22-31.
58. Johnson, P.C. and R. Jackson, *Frictional–collisional constitutive relations for granular materials, with application to plane shearing*. Journal of Fluid Mechanics, 1987. **176**: p. 67-93.
59. Mahajan, V.V., et al., *Nonspherical particles in a pseudo-2D fluidized bed: Experimental study*. AIChE Journal, 2018. **64**(5): p. 1573-1590.
60. Ostermeier, P., et al., *Comprehensive investigation and comparison of TFM, DenseDPM and CFD-DEM for dense fluidized beds*. Chemical Engineering Science, 2019. **196**: p. 291-309.
61. Wang, J., M.A. van der Hoef, and J.A.M. Kuipers, *Comparison of Two-Fluid and Discrete Particle Modeling of Dense Gas-Particle Flows in Gas-Fluidized Beds*. Chemie Ingenieur Technik, 2013. **85**(3): p. 290-298.
62. Adnan, M., et al., *Comparative CFD modeling of a bubbling bed using a Eulerian–Eulerian two-fluid model (TFM) and a Eulerian-Lagrangian dense discrete phase model (DDPM)*. Powder Technology, 2021. **383**: p. 418-442.
63. Almohammed, N., et al., *A comparative study on the influence of the gas flow rate on the hydrodynamics of a gas–solid spouted fluidized bed using Euler–Euler and Euler–Lagrange/DEM models*. Powder Technology, 2014. **264**: p. 343-364.

64. Wang, T., et al., *Experimental and numerical investigations on the particle behaviours in a bubbling fluidized bed with binary solids*. Powder Technology, 2020. **362**: p. 436-449.
65. Ostermeier, P., et al., *Three dimensional multi fluid modeling of Geldart B bubbling fluidized bed with complex inlet geometries*. Powder Technology, 2017. **312**: p. 89-102.

7. Conclusions & Recommendations

7.1 Conclusions

In this dissertation, experimental, analytical and modelling methods were developed in order to study biomass pyrolysis. In particular, the experimental and analytical efforts were mostly focused on the development of accurate methods for the characterization of biomass feedstocks by means of fast (Pyroprobe) or slow (Thermogravimetric Analysis – TGA) pyrolysis. This work was complemented and expanded with the development of kinetic and Artificial Neural Network (ANN) models, for the investigation of biomass mass loss behaviour in a pyrolysis environment and the prediction of the pyrolytic product yields, respectively. Furthermore, the novel Indirectly Heated Bubbling Fluidized Bed Steam Reformer (IHBFSR) commissioning experiments were presented and the reactor's operational characteristics, occurring phenomena, performance metrics and product attributes were showcased. Finally, the hydrodynamic performance of the IHBFSR was investigated in a combination of experimental and numerical modelling efforts.

In Chapter 2, the fast pyrolysis of woody biomass in a Pyroprobe (PP) reactor was examined. The main purpose was to study PAH formation at high pyrolysis temperatures, thus relevant also to gasification processes, in an efficient, accurate and user – friendly manner. The comparison of the results to experiments conducted with a similar type of system (heated foil), showed a definite improvement in terms of PAH capture. The PP reactor was also more efficient with respect to the total yields determination, due to the absence of thermal lag at lower temperatures, that leads to higher char yields for reactors such as the heated foil. Overall, it was also concluded that reactors with configurations similar to the heated foil are not applicable for PAH quantification, due to their inherent process limitations and the inability to properly sample the produced tars. Overall, the PAH yields showed an increasing trend for increasing pyrolysis temperature in the PP, reaching a maximum of 0.2 wt.% of the overall yield at 1000 °C. Naphthalene and acenaphthylene and phenanthrene were the main compounds detected. The evolution of PAHs coincided with the increase of the CO, H₂ and CH₄ yields, the stabilization of the char yield and the decrease of the total liquid yield, suggesting that it is mainly a product of secondary decomposition. Overall, the hereby proposed method was successful in quantifying PAH produced from biomass fast pyrolysis experiments, with high reproducibility. The flexibility of the system allows the fast conduction of multiple experiments, with minimal complexity in terms of sampling, while specific tar compounds can be targeted (PAH, sugars, acids, phenolics, etc.), depending on the experimental conditions.

In Chapter 3, the general confusion that exists in the field of determination of mass loss kinetics for biomass pyrolysis, due to the broad range of values reported, was showcased. For this purpose, an international round robin of TGA pyrolysis experiments with pure cellulose and beech wood was conducted with 7 participants. Cellulose pyrolysis was modelled as a singular first order reaction and beech wood pyrolysis through 3 parallel reactions, using a fitting routine. The isoconversional KAS method was used to complement and enhance beech wood pyrolysis kinetic analysis. In terms of the devolatilization behaviour, deviations were observed of around 10 °C in the position of the peak at 5 K/min and 20 – 30 kJ/mol in the predicted activation energies for cellulose, hemicellulose and conversions up to 90 % for beech wood. Higher deviations were obtained for higher conversions and for lignin. To increase the reliability of the determination of biomass pyrolysis kinetics, a method was developed and is hereby recommended. The first step includes the conduction of pure cellulose pyrolysis experiments at 5 K/min, to assess the employed TGA device and methods in comparison to relevant literature. The present work highlighted that when discrepancies were seen at this step, this led to further ones when other biomass feedstocks were examined. For example, in two cases where an initial mass of over 10 mg was employed, a significantly higher char yield was obtained. In general, lower initial mass samples are recommended to avoid thermal lag. The second step of the proposed method includes the conduction of the biomass pyrolysis experiments at various heating rates and the

utilization of isoconversional methods in order to validate the reliability of the experiments and the derived kinetic parameters. This study shows that high R-squared values (over 0.99), except for very low and high conversions, are to be expected from isoconversional methods. When this criterion was not fulfilled, the corresponding measurements were disregarded for the rest of the study. Finally, isoconversional methods can support the determination of the activation energies for cellulose and hemicellulose using a fitting method, however certain deviations are expected for lignin. Within the context of the round robin presented in this work, the employment of the above-described method, led to the dismissal of the data of three out of seven cases, while for a fourth one the data at one heating rate were disregarded. The deviations in activation energy for these cases were less than 10 kJ/mol (less than half than when considering all experiments), except for lignin. An activation energy of around 180 kJ/mol was obtained for the cellulose component in beech wood, a value of 150 kJ/mol was derived for hemicellulose while for lignin the value was above 200 kJ/mol. While this method does not completely guarantee the derivation of optimal kinetics, it ensures that they are chemically meaningful. Such an approach can assist the reduction of the variability in biomass kinetics determination, which can be attributed significantly to the lack of consistency in data acquisition and kinetic analysis of TGA experiments.

The ANN models proposed in Chapter 4 for the prediction of the pyrolysis product yields focus on generalizability, to achieve the best possible results for a variety of biomass feedstocks, reactor types and process conditions. With this in mind, a large database consisting of a variety of small-scale experimental pyrolysis studies was built. This effort constituted a first-of-its-kind attempt in terms of employing ANN models for such a wide range of literature data. Overall, while the implementation of the ANN models was successful (reasonable prediction of RMSE values), they cannot be compared to ones obtained from single or in general more limited studies. The derived models were able to reproduce the expected trends in relation to temperature variation but at the same time other parameters such as residence and holding time did not appear to have any effect. Reducing the input led to increased generalization capabilities (prediction quality improvement) for the char and gas ANNs, while in the case of the liquid ANN the loss of information was not beneficial (RMSE of 9.3 wt.% ar. versus 6.9 wt.% ar.). An important finding was that by adding the char yield as an input parameter in the ANN models, can lead to improved predictive capabilities. For the cases of the char and gas ANNs, the reduced input networks performance was only slightly better compared to the full ones. Among the three product classes, the char models were the best performing ones, largely due to the higher accuracy of char yield experimental measurements. The liquid product ANN was the worst performing one, most likely due to the wide variety of methods employed for pyrolysis liquid product measurement or determination (e.g. calculation by difference). The reason for the significantly better performance of the gas models can be attributed to the lower standard deviation of the gas yield values (10.9 wt% ar), compared to the ones of the char (15 wt% ar) and liquid (14.7 wt% ar).

The results from the commissioning experiments on the novel IHBFBRS were presented, along with a description of its operational characteristics for a wide range of experimental conditions in Chapter 5. Through the conduction of these experimental campaigns, it was found that char accumulating in the bed area for the overall process, appeared to promote H₂ formation and in-situ tar destruction, especially when smaller bed material particle sizes were employed. Furthermore, it was found that by injecting moderate amounts of air in the freeboard, tar reduction and (to a lesser extent) CCE can be improved without compromising H₂ production, even when compared to the introduction of larger amounts as a fluidization agent. Finally, the product gas composition and CGE obtained, compares favourably to similar allothermal gasification systems, while carbon conversion can still be improved. Overall, the present study offers a thorough presentation of the IHBFBRS attributes for a variety of process conditions, allowing its use as a benchmark for similar systems and future works.

Finally, in Chapter 6, the CFD-TFM simulations of the IHBFSR for the investigation of its hydrodynamic behaviour were presented. The results of the simulations were successfully verified with the corresponding experimental results obtained from fluidization experiments. The simulation of the reactor's hydrodynamic behaviour showcased small deviations compared to the experimental and computational values of the global hydrodynamic metrics (bed height and pressure drop). Through the simulations, it was observed that for realistic values of the particle restitution coefficient the gas flow forms channels near the reactor walls, regardless of the presence of a side flow from the reactor's feeding system. However, when no side-flow was implemented, larger bubbles appeared to be forming near the outer wall of the reactor, with the opposite behaviour being evident for the side-flow simulations. This can be attributed to the stream-like behaviour of the side-flow, which moves against the outer wall of the reactor without forming bubbles locally. Overall, the present work constitutes the first step to study the fluidization behaviour of the novel IHBFSR reactor of TU Delft.

7.2 Recommendations

In Chapter 2, it was seen that the PP system produced reasonably satisfactory mass balance closure values (80 wt% on average). Char and gas yields were determined with high accuracy, however gravimetric liquid analysis was lacking. This was mostly due to the inability to properly quantify the condensable products in the impinger bottle. Often, a trade-off exists between the gravimetric determination of the total pyrolysis liquid yield and the quantification of its constituents. For example, adding a solvent evaporation step might improve the mass balance closure values, but at the same time it would hamper the efficiency of determination of the liquid compounds. In this work, it was shown, that while a single cold trap is sufficient for comparatively lower PAH condensation at low pyrolysis temperatures concentrations, the same does not hold for higher temperatures. For this purpose, more research effort is required in regard to the development of an improved condensation/trapping system combined to a PP system or the exploration of alternative experimental strategies that can combine the two targets. An initial attempt to improve the mass balance closure values of the PP reactor is presented in Appendix A.

The TGA-based round robin work described in Chapter 3, was later expanded with the conduction of additional campaigns on *Miscanthus* pyrolysis and *Miscanthus* char oxidation/gasification. The results of this endeavour were reported within the context of the European project BRISK II (grant agreement number: 731101). Overall, the conduction of similar studies using the proposed methodology, could enhance its usefulness, by further corroborating its results and highlighting potential shortcomings. Additionally, the further expansion of this methodology and its adaptation to be implementable for a variety of biomass feedstocks and thermochemical conversion processes (pyrolysis, gasification), could be similarly beneficial. The coupling of kinetic data obtained through this method, with more generalized models of biomass pyrolysis or gasification (e.g. ASPEN+), could improve their reliability and completeness. As described in the relevant chapter, the chaos surrounding the biomass thermochemical conversion kinetics literature highly due to the lack of standardization, constitutes an important short-coming of the field and leads to the perpetuation of scientifically inaccurate and therefore inconsequential practices. The relative ease with which TGA data can be generated and the simplicity with which basic (and often inaccurate) kinetics can be derived, has saturated the field and reduced the perceived importance and impact of such studies. While it is not claimed that the proposed method is the final answer to issue of biomass pyrolysis kinetics, it showcases a scientifically sound and well-rounded attempt. Scientists in the field should respond to this work by testing its boundaries and limitations, expanding it, enhancing it, or even potentially replacing it. Overall, the recommendation of the author is that the community should strive

to produce less, but more meaningful kinetic data on biomass thermochemical conversion, focusing on the development and employment of specific standards.

In regards to the ANN models developed within Chapter 4, the results could be improved by the further optimization of the ANNs, the inclusion of continuous reactors in the database and necessary models adaptations, the reduction of the scope (e.g. focus on specific pyrolysis regime) or by imposing more stringent criteria for the induction of data in the database. Additionally, the feature reduction method, could be further refined through hypothesis – testing methods for obtaining correlations within the dataset. The lack of relevant fast pyrolysis samples could be addressed by the removal of some input parameters and/or by focusing on specific regimes, that would allow the expansion of the database to include omitted studies. However, the limitations imposed due to the presence of discrepancies in the literature are still significant. Firstly, even though the composition of biomass samples can be measured using different methodologies with varying results, the employed standards are often not mentioned in the literature. Furthermore, during the literature research, it was often seen that fundamental parameters are also regularly ill-reported (e.g. lignocellulosic composition, gas residence time, heating rate). As it was also discussed in the relevant chapter, those significant ambiguities exist in the literature due to the employment of different methods for products measurement and yields calculation and presentation. It was often encountered that different bases of yield expressions (ar., db., daf.) were incorrectly employed or converted, with the effect of this error often masked by the incomplete mass balance closure values, or the calculation of a product class by difference. Such ambiguities can be easily surpassed by explicitly referring to the calculation procedure and the provision of the moisture and ash values necessary for the attempted conversion. Nevertheless, it was found in multiple studies that such basic requirements were not met. Furthermore, closing the mass balances by difference often covers intrinsic mass losses of the experimental setup and can therefore lead to incorrect conclusions and misplaced amounts of mass in certain product yields. This particular practice constitutes a gross simplification of the pyrolysis process studies and limits the scientific importance of the data. In a world that is rapidly shifting its focus towards the realm of big data, it is essential to provide large amounts of high-quality data that can be easily used and compared by these types of models. Therefore, the pyrolysis scientific community needs to be aware of using higher standards in terms of reported data quality.

Concerning the work performed surrounding the IHBFSR presented in Chapter 5, it should be mentioned that despite the fact that the presence of the accumulated char bed can have a positive effect on syngas quality and tar content, a compromise between this effect and the increase of carbon conversion must be found. Furthermore, increasing burners output and efficiency as well as better insulation, could improve the overall efficiency of the system. In particular for the freeboard, when adding secondary air, lower temperatures and/or burner outputs could suffice to achieve the desired levels of tar removal. However, the investigation of alternative tar reduction methods either in-situ (e.g. tar reducing bed material like olivine) or ex-situ (gas cleaning) is also essential in order to compare the performance. In terms of alternative feedstocks, already experiments with Miscanthus and plastic waste have been conducted in the setup. Despite the results being promising, important adaptations need to be made to the setup to facilitate the conduction of experiments with such feedstocks. For biomass feedstocks with elevated ash content, special consideration of the process parameters should be made in view of agglomeration challenges. Additionally, the utilization of additives (e.g. Kaolin) could also assist to the suppression of agglomeration phenomena. In regard to plastic feedstocks, the adaptation of the feeding system to avoid melting of the feed and subsequent blockage is of the essence, as well as the optimization of the sampling system to avoid blockages. Finally, the extensive characterization of the system's char product as well as the applicability of the produced syngas in industrial applications should be investigated. Conclusively, while the initial results are quite promising

in terms of the scale-up potential of the IHBFSR, significant reactor development work remains to be done.

Finally, from the simulations presented in Chapter 6, it was shown that limiting the simulations to a 72° symmetry “wedge” was validated by the model findings. This also indicates that even further reduction is possible, which could reduce the computational time significantly. However, most importantly, the results of this study suggest that an increase of the reactor’s diameter could potentially lead to a reduction of the observed channelling of the fluidization media and improve the reactor’s mixing capabilities. In its turn this would improve the heat and mass transfer in the system and consequently benefit the conversion efficiency of the IHBFSR. Overall, further experimental and simulation work should be performed to validate and enhance the results of this study, by exploring different operational parameters of the reactor. This investigation of this geometrically unique fluidized bed’s hydrodynamics can be utilized in future heat/mass transfer and chemical reaction modelling, which will allow the employment of additional experimental variables and data. Apart from further verifying the simulation work performed so far, such an approach will allow the utilization of the entire spectrum of the IHBFSR’s analytical/instrumentation capabilities, something that was practically impossible within the context of the present work.

A. Appendix – Tar sampling in a Pyroprobe reactor

Temperature calibration

As it was mentioned in a previous section, the actual temperature inside the quartz tube differs from the set temperature of the coil by 100 °C according to the manufacturer. However, previous measurements on the instrument showed that this difference may be higher. For this reason, a calibration campaign was performed for finding the correlation between the set temperature and the actual temperature inside the holder. The probe was removed from the furnace and an empty holder was placed in the coil. For the measurement of the temperature inside the coil, a 0.2mm Pt-PtRh (13 %) type R thermocouple was used, connected to an Omega device for the reading of the values at a frequency of 500 Hz. Such a thermocouple was selected due to the increased sensitivity required, imposed by the fact that a very high heating rate (600 °C/s) and short pyrolysis duration (10 s) are employed in the experiments. The results of these measurements may differ a little from reality, since during the experiments the probe is placed inside the pyrolysis chamber which is heated up to 300 °C. However, it is hypothesized that these conditions may have a more significant effect on the heat transfer phenomena than the actual temperature experienced by the sample during pyrolysis. Measurements were performed between 500 °C and 1300 °C at increments of 100 °C. For each temperature point, three measurements were performed and then the average values were taken. From them, the maximum temperature observed was the final output for each set temperature point. The results of the measurements are presented in Figure A.1. It can be observed that the relationship between the measured and set temperature values is linear with $R = 0.9938$.

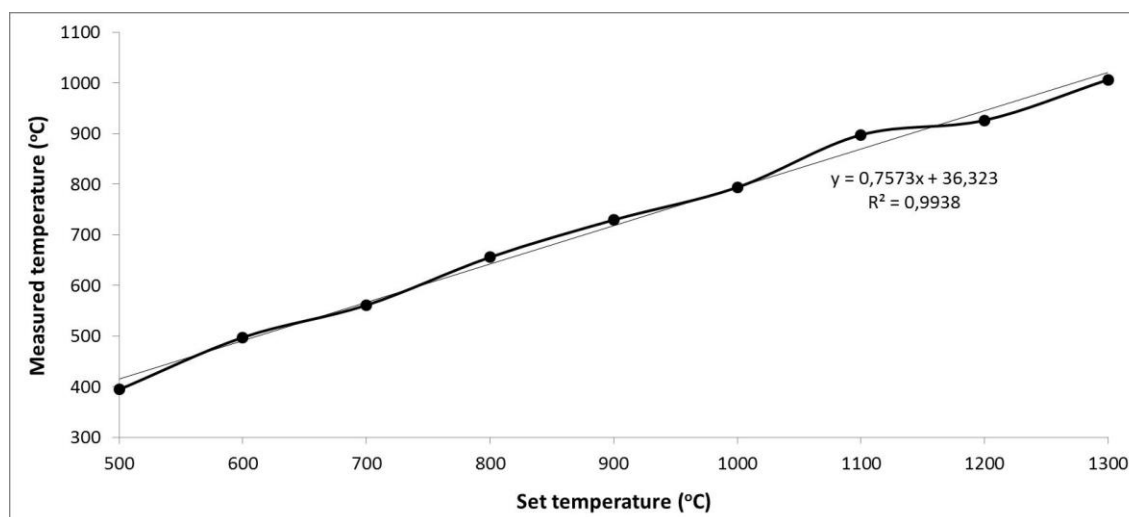


Figure A.1: Plot of the measured temperature inside the holder versus the set temperature of the filament coil.

The linear expression derived was used for the determination of the required set temperature for achieving a corresponding pyrolysis temperature and the results are presented in Figure A.1. It should be mentioned that the correspondence derived through this campaign was very similar to the one obtained from the calibration campaign for the previous filament coil. It should also be noted that the temperature correction regards only the quartz tube effect and not the effect of the sample's presence in the tube, since such measurements cannot be conducted in the current setup. Furthermore, due to

the low thermal conductivity of the quartz tube, the actual heating rate that the sample experienced is also expected to be lower than the imposed 600 °C/s heating rate of the probe coil (approximately 450 °C/min). Finally, the required holding time for the experiment is also adapted to also include the required time for the sample to reach the final pyrolysis temperature. For the reasons described before, the actual heating rate also differs slightly from the one actually achieved. The required holding times to achieve 10 s of pyrolysis regardless of the temperature for a set heating rate of 600 °C/s are presented in Table A.1.

Table A.1: Correspondence between set filament temperature, actual sample temperature and holding time.

Filament Temperature (°C)	Sample Temperature (°C)	Adjusted Holding Time (s)
500	612	11.2
600	744	11.5
700	876	11.9
800	1008	12.5
900	1141	12.9
1000	1273	13.5

Further optimization of tar sampling

Overall, as it was mentioned in the corresponding section, the mass balance closure values of fast pyrolysis experiments conducted in the Pyroprobe reactor, fail to reach 100 %. First of all, as it has been observed during Pyroprobe maintenance, there is the possibility of tar condensation before the trap, namely in the oven. Furthermore, some losses can occur by the evaporation of very volatile compounds, during the time between the removal of the trap from the reactor until the gravimetric measurement. Another reason that leads to an unclosed mass balance originates from the micro GC limitations, since higher hydrocarbons such as C₂H₄, C₂H₆, C₃H₆ and C₃H₈ cannot be detected. According to Hajaligol et al. [1], these gaseous products are derived from secondary decomposition of tar and therefore their yield is increased with temperature. It is indicated in literature [2, 3] that the total yield of these products can sum up to a 2 % wt. - 5 % wt. for lignocellulosic species. Additionally, the water produced, included both in the liquid and gaseous product is also unaccounted for. Pyrolytic water can account for 10 % wt. - 12 % wt. [4]. Furthermore, light tars that escape the trap and condense in the isopropanol filled impinger bottle also cannot be measured gravimetrically. Finally, there is always the possibility of error during the gravimetric measurements of the liquid and solid product as well as in the determination of the gaseous products through the micro GC and the ideal gas law implementation.

Table A.2: Proximate, ultimate, elemental analysis and LHV of Miscanthus feedstock utilized in the fast pyrolysis experimental campaign.

Proximate analysis	
Moisture (wt%, a.r.)	10.4
Volatiles (wt%, a.r.)	70.7
Fixed carbon (wt%, a.r.) ^a	17
Ash (wt%, a.r.)	1.9
Ultimate analysis	
C (wt%, d.b.)	49.05

H (wt%, d.b.)	6.03
N (wt%, d.b.)	0.88
S (wt%, d.b.)	0.06
Cl (wt%, d.b.)	0.04
O (wt%, d.b.) ^a	43.98
Elemental Analysis	
Al (ppm, d.b.)	44.03
Ca (ppm, d.b.)	1745.72
Fe (ppm, d.b.)	103.99
K (ppm, d.b.)	4214.93
Mg (ppm, d.b.)	799.59
Na (ppm, d.b.)	80.75
Si (ppm, d.b.)	2252.09
Zn (ppm, d.b.)	4.30
LHV (MJ/kg, d.b.)	17.79

During a fast pyrolysis experimental campaign with Miscanthus as the feedstock (composition described in Table A.2), a significant amount of liquid products appeared to condense in the condenser assembly, right after the pyroprobe trap. At this point, it should be reminded to the reader, that the trap's weight measurement before and after the experiment produces the liquid product yield presented in this work. As it can be observed in Figure A.2, the colour of the isopropanol filled condenser changed after the experiment from transparent to yellowish. This phenomenon has not been presented before in the long experience of the operator with this apparatus, even though a wide range of products has been studied (lignocellulosic biomass, marine biomass, sludge, etc.). In an older study performed using the same Pyroprobe reactor [5], it was determined that volatile compounds including benzene and toluene mainly condense in the condenser. The same was also the case for a fraction of the PAHs produced. Therefore, it can be safely hypothesized that a significant amount of liquid products that fail to condense in the trap, end up in the condenser, significantly affecting the mass balance closure values and leading to an underestimation of the total liquid product yield. To tackle this issue, two approaches were examined. The first one was to identify the amount of liquid products that remain in the condenser, either by removal of the IPA impinger and the employment of a second trap, or by evaporating the IPA. The latter approach can lead to the evaporation of significant amounts of the liquid products collected. The losses included in this approach can jeopardize the gravimetric measurement of the liquid products but also the individual compounds detection and quantification through the subsequent analysis. The second approach, was the reduction of the nitrogen flow rate. In the aforementioned campaign with Miscanthus, a N₂ flow rate between 15 and 20 ml/min was employed. This range of values was established as a good experimental point since very high flow rates can lead to flying char particles inside the apparatus and low liquid product condensation in the trap. On the other hand, low flow rates may result to tar condensation in the tubes in the reactor's oven due to the increased gas residence time.



Figure A.2: On the left the isopropanol filled condenser before the initiation of a Miscanthus fast pyrolysis experiment at 900 °C. On the right the condenser after the completion of the same experiment

Starting with the gravimetric measurement of the liquid products that condense downstream the trap, when no IPA condenser is employed, fast pyrolysis experiments with Miscanthus were conducted at 600 °C and 700 °C at a heating rate of 600 °C/min and a holding time of 10 s, using both configurations. The only difference between the two sets of experiments was the use of the impinger condenser in one and the employment of a second trap in the other. All the experiments were performed in duplicate and the comparison of the results of these different tar sampling schemes is presented in Figure A.3. As it can be observed, the char and gas yields were not affected by the change, as it was expected in particular for the char. Char formation cannot be influenced by such changes downstream the pyrolysis chamber, unless they lead to an increase in the system's pressure for example. For the liquid product, at 600 °C its total yield was roughly 46.2 wt. % which consisted of 45.9 wt. % collected in the first trap and 0.3 wt. % in the second, when no condenser was employed. The difference with the original setup's tar sampling configuration was less than 1 wt. %. At 700 °C, for the no-condenser configuration the total amount of liquid products was approximately 4.2 wt. % higher than the corresponding value for the original setup. However, this difference was mostly due to a 3.1 wt. % increase in the liquid collected in the first trap. Overall, it was shown, that such a modification of the sampling system provides only incremental improvements on the mass balance closure values. Furthermore, this improvement, potentially comes in the expense of the subsequent tar analysis due to the lack of the use of a solvent like IPA, to assist in tar condensation.

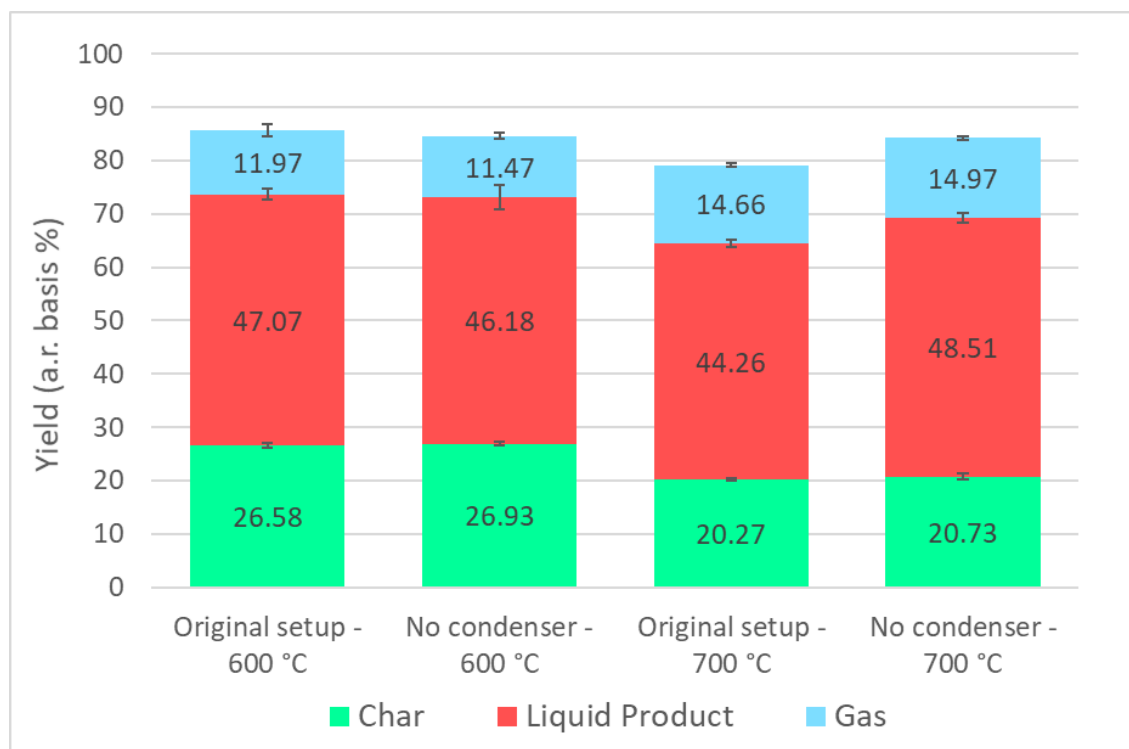


Figure A.3: Product yields from fast pyrolysis of Miscanthus in Pyroprobe for different liquid product sampling configurations

The second approach on gravimetric measurement of the liquid product downstream the first trap, included the employment of the original sampling configuration. However, after the completion of the experiment, the 2 ml of IPA/liquid product solution of the condenser were emptied on a glass petri dish. After approximately 2 h, the IPA was evaporated and the dish was weighed for the determination of the tar product left behind. For this purpose, fast pyrolysis experiments with Miscanthus were conducted at 600 °C, 700 °C, 800 °C, 900 °C and 1000 °C at a heating rate of 600 °C/min and a holding time of 10 s. A wide temperature range was employed, to examine whether the products variation with temperatures influences the process. The amount of tar yields measured only in the petri dish with this configuration for each of the duplicate experiments performed are presented in Figure A.4. As can be seen, the variability between the experiments is high. The overall increasing trend implies a preference for the collection of heavier tars using this method, since those are favoured in high temperatures as discussed in the previous section and they are also more difficult to evaporate. However, the low overall yields (below 2 wt. %) and the observed differences between the experiments indicate that this method lacks the required precision. It is important to consider that, as it will be shown in the experiments presented in the following section, the overall yields measured are within the usually acceptable error margin of the gravimetric measurements. Finally, this method is destructive for the sample collected, which therefore cannot be analysed further. Thus, it is difficult to determine which species actually remain in the dish and make the comparison with the original sampling method.

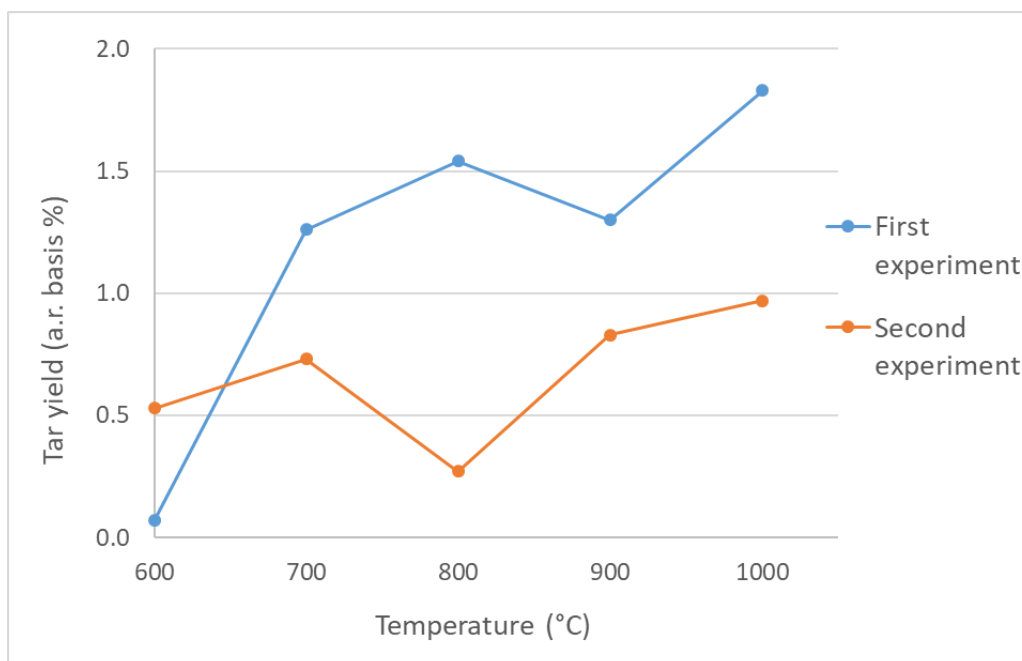


Figure A.4: Tar yield of impinger condenser after the evaporation of IPA, collected from fast pyrolysis of Miscanthus at 600 °C/min in the Pyroprobe

Another attempt to improve the gravimetric liquid product measurement and therefore the mass balance closure of the fast pyrolysis experiments in pyroprobe, included the analysis of the effect of the N₂ purge mass flow rate. For this purpose, Miscanthus experiments were conducted at 1000 °C, with a heating rate of 600 °C/min and a holding time of 10 s, employing three different mass flow rates of N₂. These mass flow rates were 20-15 ml/min, 10 ml/min and 5 ml/min. The temperature of 1000 °C was selected in order to test the effect of the N₂ flow rate for the maximum possible amount of volatiles in the system. The results are presented in Figure A.5. From the results, it can be clearly derived that with the reduction of the flow rate to 10 ml/min, the liquid product was sampled much more effectively, while the gas product was not influenced at all. With the further decrease of the flow rate to 5 ml/min, the liquid yield continued to decrease. However, the simultaneous decrease of the gas product by roughly 10 wt. %, indicates that the increased residence time imposed by the lower flow rate influences it negatively. In particular, it is possible that the increased residence time leads to more secondary reactions that hinder the formation of permanent gases, since with the exception of H₂ which is produced at amounts less than 1 wt. %, all the product gases yields measured were lower in this case. Overall, since the purpose of the Pyroprobe is to limit secondary reactions to a minimum level and the mass balance closure values were not improved with a flow rate of 5 ml/min, the 10 ml/min flow rate was selected for the continuation of the fast pyrolysis experiments. Additionally, employing low mass flow rates, can lead to tar condensation in the tube located in the Pyroprobe oven or the exit of the pyrolysis chamber. Finally, the addition of ice around the impinger bottle, did not influence the gravimetric results at all, however its employment was also chosen, in an effort to facilitate tar and moisture condensation.

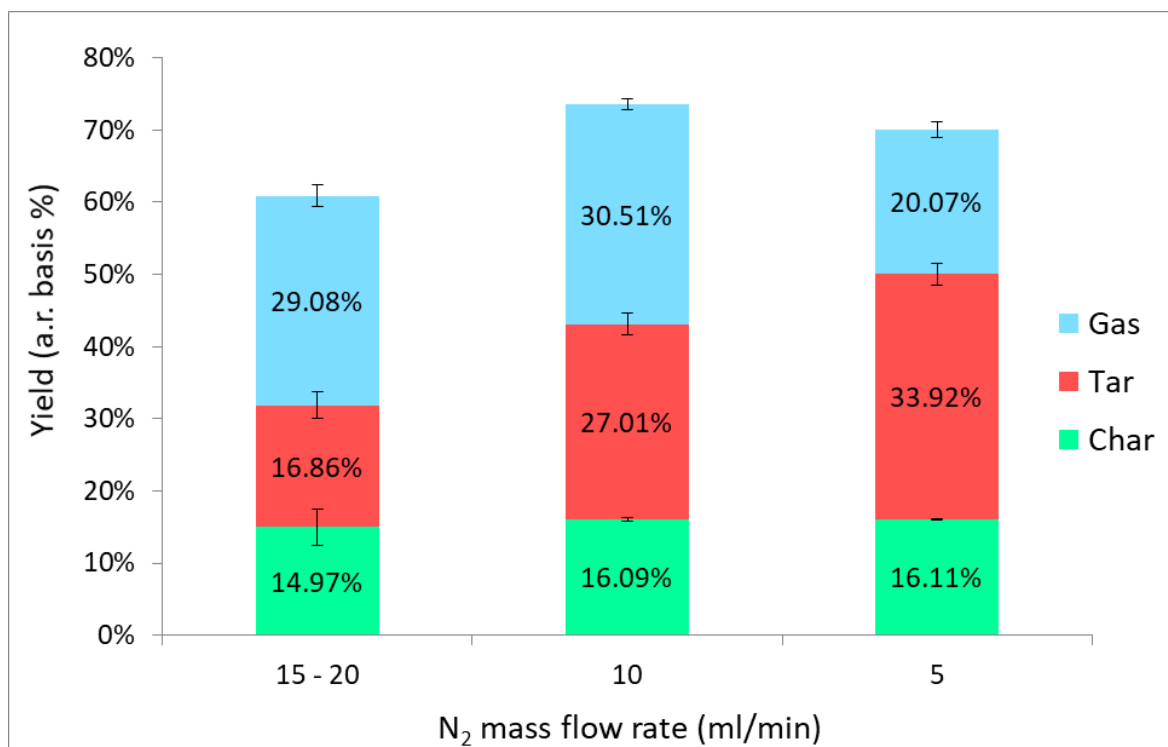


Figure A.5: Miscanthus fast pyrolysis product yields for different N₂ purge mass flow rates (600 °C/s heating rate, 10 s holding time)

Bibliography

1. Hajaligol, M.R., et al., *Product compositions and kinetics for rapid pyrolysis of cellulose*. Industrial & Engineering Chemistry Process Design and Development, 1982. **21**(3): p. 457-465.
2. Bridgwater, A.V. and G.V.C. Peacocke, *Fast pyrolysis processes for biomass*. Renewable and Sustainable Energy Reviews, 2000. **4**(1): p. 1-73.
3. Nunn, T.R., et al., *Product compositions and kinetics in the rapid pyrolysis of sweet gum hardwood*. Industrial & Engineering Chemistry Process Design and Development, 1985. **24**(3): p. 836-844.
4. Mohan, D., C.U. Pittman, and P.H. Steele, *Pyrolysis of Wood/Biomass for Bio-oil: A Critical Review*. Energy & Fuels, 2006. **20**(3): p. 848-889.
5. Schoenmakers, P.L., *Fast pyrolysis of wood and reed in the pyroprobe: Studying a new method for examination of the devolatilization behavior of biomass*. 2016, Delft University of Technology

B. Appendix - Estimation of lignocellulosic biomass pyrolysis product yields using artificial neural networks

Table B.1: Studies from literature included in the database, along with the amount of data points

ID	Biomass Type	Data points	Reference
2	Wood mixture, reed	12	[1]
3	Hazelnut, almond, walnut and sunflower shells	32	[2]
4	Cotton cocoon shell, tea factory waste, olive husk	12	[3]
5	Torrefied and non – torrefied ash wood	25	[4]
6	Leucaena leucocephala	1	[5]
7	Coffee waste	6	[6]
10	Switchgrass	12	[7, 8]
11	Pine needles	23	[9]
12	Giant fennel	27	[10]
13	Laurel extraction residue	23	[11]
14	Safflower seed cake	19	[12]
15	Hazelnut cupula	12	[13]
16	Euphorbia rigida, sesame stalk	4	[14]
17	Rice straw	3	[15]
18	Maple fruit	12	[16]
19	Miscanthus X Giganteus	27	[17]
22	Rice straw	5	[18]
23	Geodae – Uksae 1	7	[19]
24	Bagasse, coco peat, paddy straw, palm kernel shell, umbrella tree stem, umbrella tree bark	6	[20]
26	Sugarcane bagasse	15	[21]
27	Rice husk	18	[22]
28	Spruce wood	4	[23]
29	Xylan, cellulose, hemicellulose and mixtures	6	[24]
30	Xylan, cellulose and hemicellulose	3	[25]
31	Lignin	7	[26]
33	Cotton seed cake	12	[27]
34	Beech wood	97	[28]
35	Beech and fir wood, agricultural residues	18	[29]
36	Beech wood	10	[30]
37	Wheat straw, almond shell, olive stone, grape refuse	20	[31]
38	Pine wood	4	[32]

Table B.2: Hyperparameter values used in the powerset and sequential tests

Parameter	Powerset test	Sequential test
Hidden layers	1	1
Neurons in hidden layers	15	15
Batch size	30	30
Epochs	1250	1500
Learning rate	0.001	0.001
Noise (σ)	0	0.02
Dropout probability	0	0.2

Table B.3: Hyperparameter values for the ANN models developed in the present study

Parameter	Full char	Reduced Char	Full liquid	Reduced liquid	Full gas	Reduced gas	Full liquid with char input	Reduced gas with char input
Hidden layers	1	1	1	1	1	1	1	1
Neurons in hidden layers	9	9	18	9	9	9	18	9
Batch size	30	30	30	30	30	30	30	30
Epochs	500	750	1500	1500	750	1500	750	750
Learning rate	0.01	0.0001	0.001	0.01	0.01	0.001	0.003	0.003
Noise (σ)	0.3	0.2	0.3	0.3	0.1	0.2	0.3	0.2
Dropout probability	0.2	0	0.2	0.2	0.2	0	0.2	0

Table B.4: Correspondence between RMSE and R^2 values for the ANN models developed within the present study

ANN	RMSE (wt% ar)	R^2
Reduced Char	5.1	0.75
Reduced Gas	5.6	0.86
Full Liquid	6.9	0.7
Full Liquid w/ char	5.5	0.81
Reduced Gas w/ char	4.9	0.89
Full Char	5.9	0.66
Reduced Liquid	9.3	0.47
Full Gas	6	0.84
Char ID 34	1.9	1
Liquid ID 34	1.5	0.99
Char ID 12	0.43	0.91
Gas ID 12	0.63	0.62

A) Full char ANN

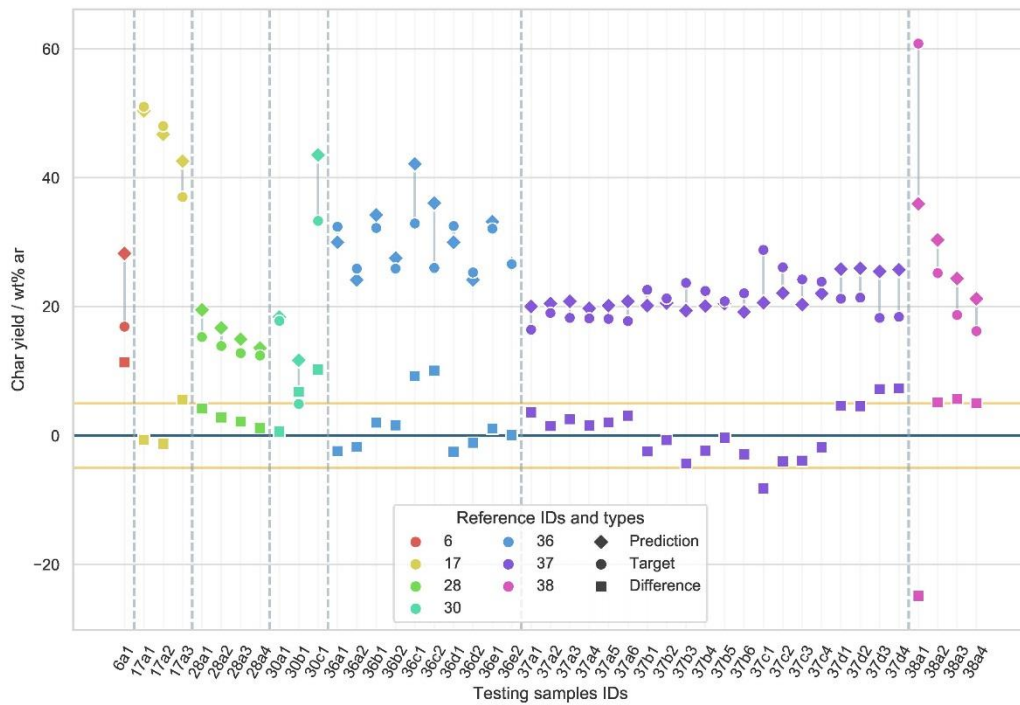


Figure B.1: Performance of the full char ANN over the test set. Predictions of the networks are shown alongside the targets for each single sample in the test set. Indicative boundary lines are shown ± 5 wt% ar around the zero line.

B) Reduced liquid ANN

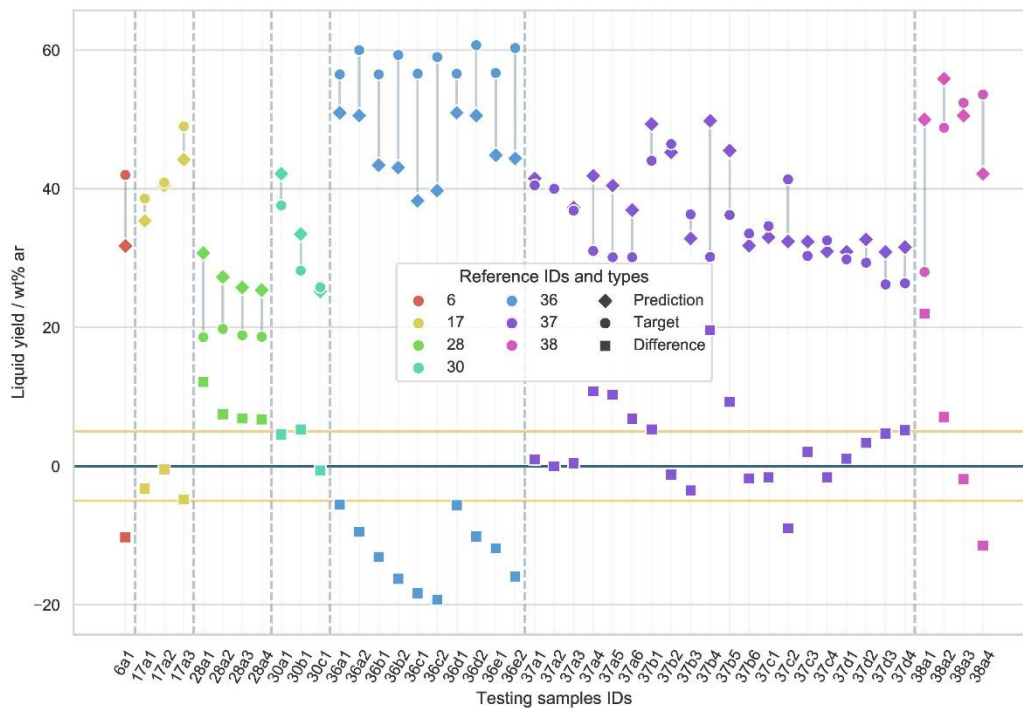


Figure B.2: Performance of the reduced liquid ANN over the test set. Predictions of the networks are shown alongside the targets for each single sample in the test set. Indicative boundary lines are shown ± 5 wt% ar around the zero line.

C) Full gas ANN

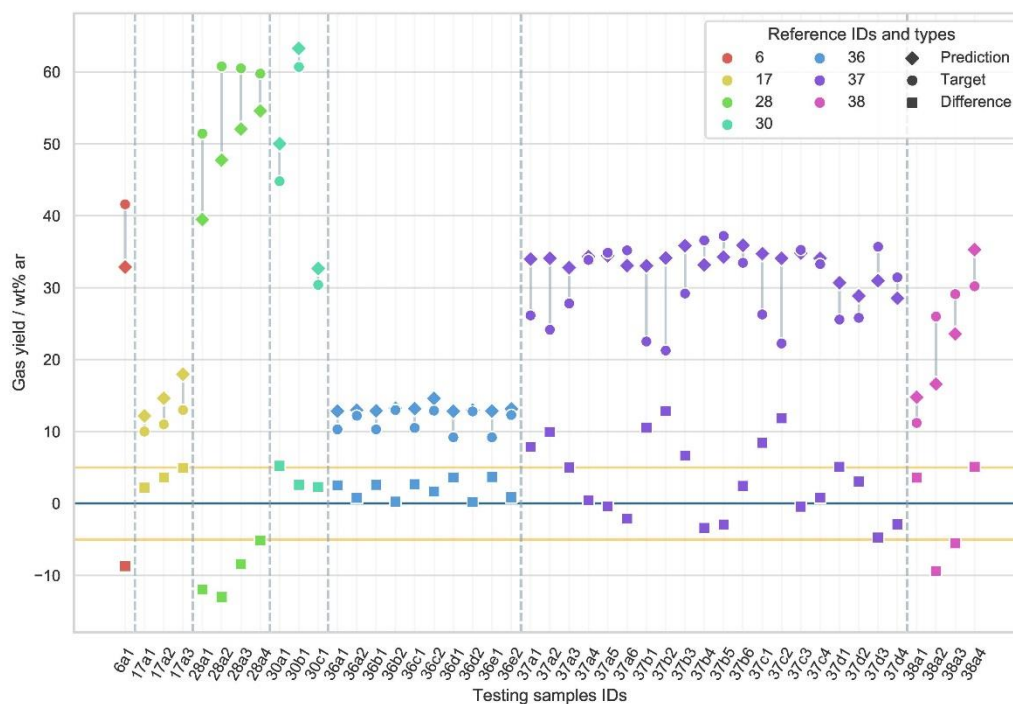


Figure B.3: Performance of the full gas ANN over the test set. Predictions of the networks are shown alongside the targets for each single sample in the test set. Indicative boundary lines are shown ± 5 wt% ar around the zero line.

D) Full liquid with char as an input ANN

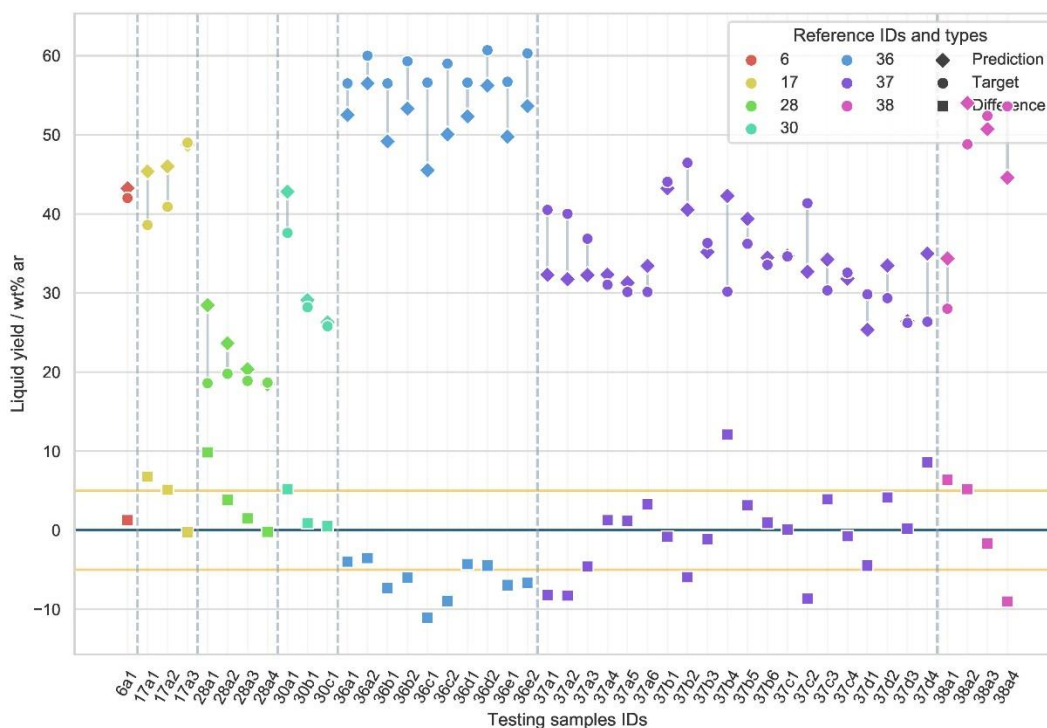


Figure B.4: Performance of the full liquid ANN with char as an input over the test set. Predictions of the networks are shown alongside the targets for each single sample in the test set. Indicative boundary lines are shown ± 5 wt% ar around the zero line.

E) Reduced gas with char as an input ANN

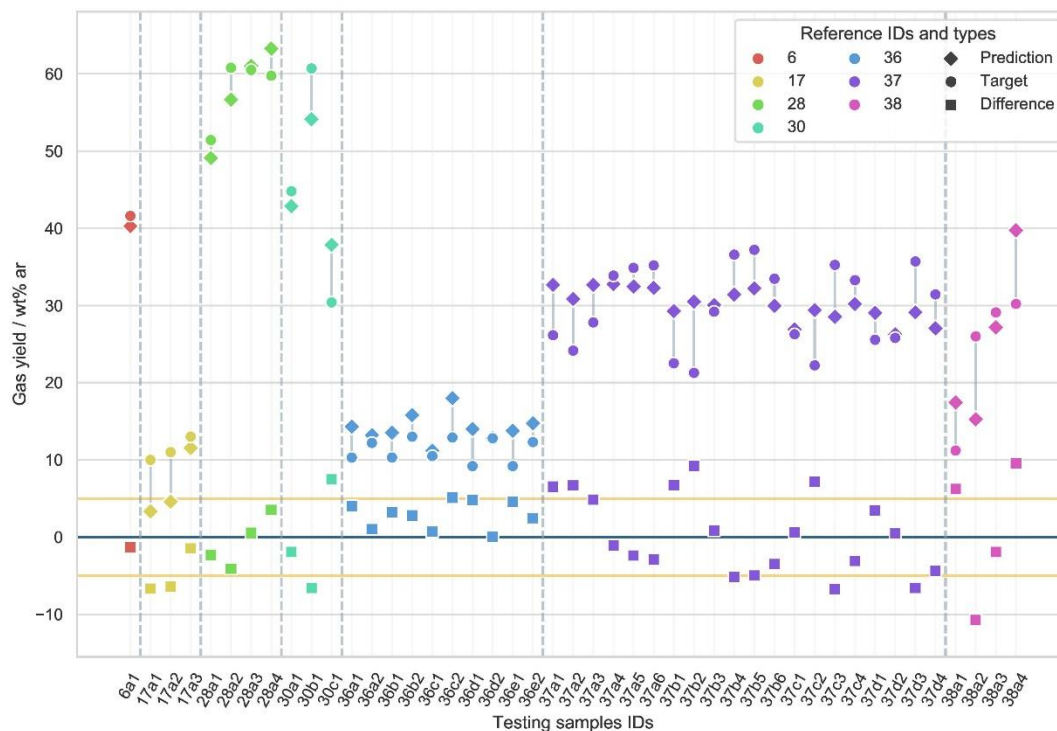


Figure B.5: Performance of the reduced gas ANN with char as an input over the test set. Predictions of the networks are shown alongside the targets for each single sample in the test set. Indicative boundary lines are shown ± 5 wt% ar around the zero line.

F) Single study ANNs

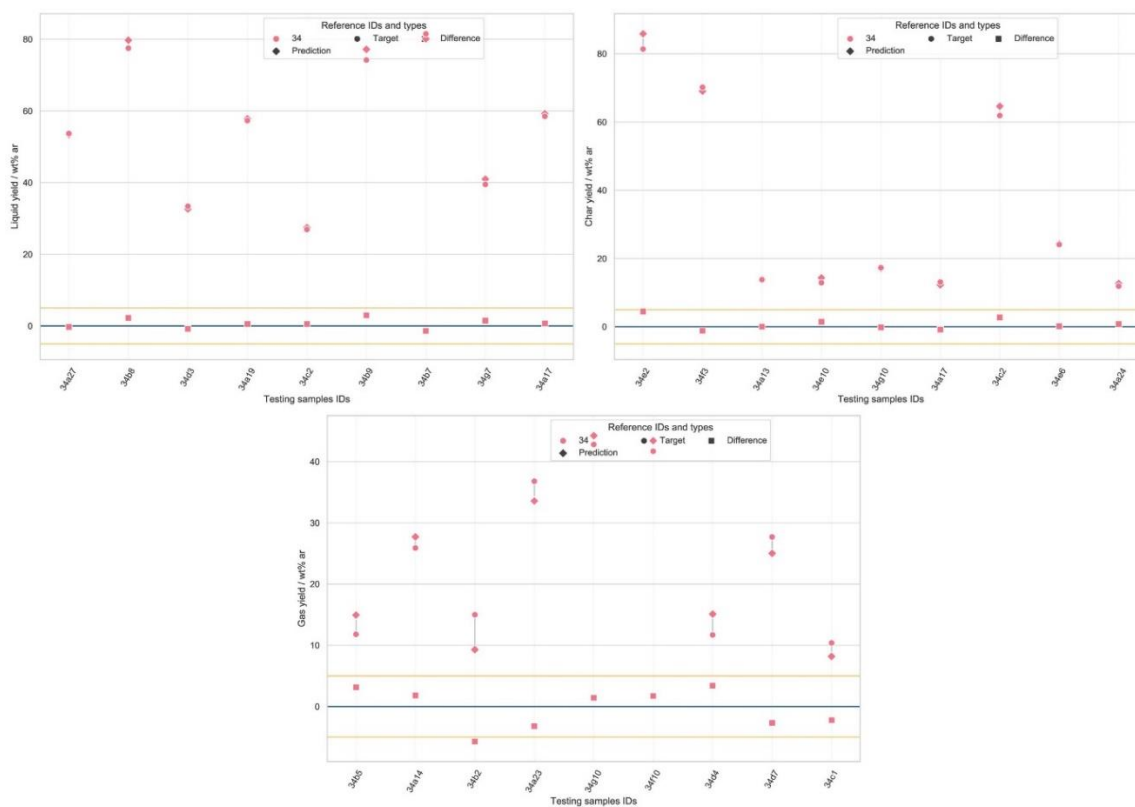


Figure B.6: Performance of the liquid, char and gas ANN over the test set for reference 34. Predictions of the networks are shown alongside the targets for each single sample in the test set. Indicative boundary lines are shown ± 5 wt% ar around the zero line.

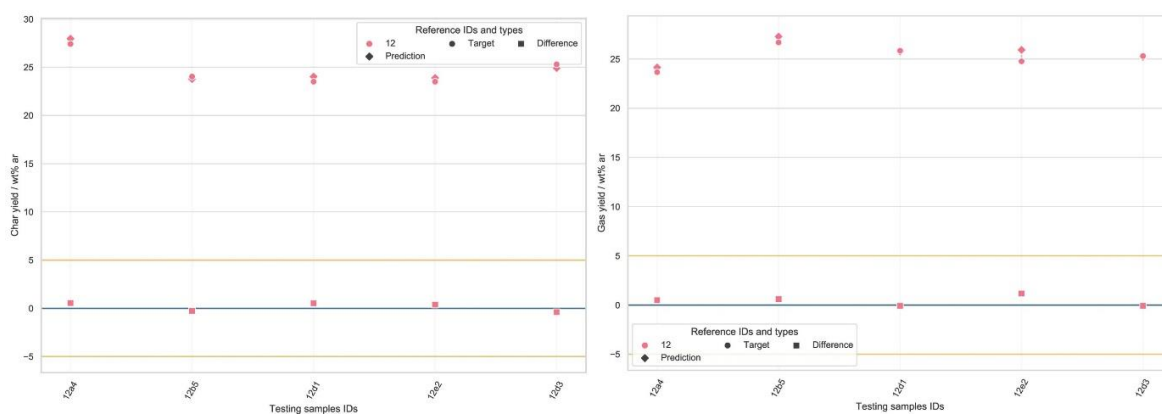


Figure B.7: Performance of the char and gas ANN over the test set for reference 12. Predictions of the networks are shown alongside the targets for each single sample in the test set. Indicative boundary lines are shown ± 5 wt% ar around the zero line.

Bibliography

1. Anastasakis, K., I. Kitsiou, and W. de Jong, *Fast devolatilization characteristics of 'low cost' biomass fuels, wood and reed. Potential feedstock for gasification*. Fuel Processing Technology, 2016. **142**: p. 157-166.
2. Demirbas, A., *Effect of temperature on pyrolysis products from four nut shells*. Journal of Analytical and Applied Pyrolysis, 2006. **76**(1): p. 285-289.
3. Demirbaş, A., *Yields of hydrogen-rich gaseous products via pyrolysis from selected biomass samples*. Fuel, 2001. **80**(13): p. 1885-1891.
4. Tsalidis, G.A., et al., *The impact of dry torrefaction on the fast pyrolysis behavior of ash wood and commercial Dutch mixed wood in a pyroprobe*. Fuel Processing Technology, 2018. **177**: p. 255-265.
5. Wannapeera, J., B. Fungtammasan, and N. Worasuwanarak, *Effects of temperature and holding time during torrefaction on the pyrolysis behaviors of woody biomass*. Journal of Analytical and Applied Pyrolysis, 2011. **92**(1): p. 99-105.
6. Becidan, M., Ø. Skreiberg, and J.E. Hustad, *Products distribution and gas release in pyrolysis of thermally thick biomass residues samples*. Journal of Analytical and Applied Pyrolysis, 2007. **78**(1): p. 207-213.
7. Boateng, A.A., K.B. Hicks, and K.P. Vogel, *Pyrolysis of switchgrass (Panicum virgatum) harvested at several stages of maturity*. Journal of Analytical and Applied Pyrolysis, 2006. **75**(2): p. 55-64.
8. Dien, B.S., et al., *Chemical composition and response to dilute-acid pretreatment and enzymatic saccharification of alfalfa, reed canarygrass, and switchgrass*. Biomass and Bioenergy, 2006. **30**(10): p. 880-891.
9. Varma, A.K. and P. Mondal, *Pyrolysis of pine needles: effects of process parameters on products yield and analysis of products*. Journal of Thermal Analysis and Calorimetry, 2018. **131**(3): p. 2057-2072.
10. Aysu, T. and M.M. Küçük, *Biomass pyrolysis in a fixed-bed reactor: Effects of pyrolysis parameters on product yields and characterization of products*. Energy, 2014. **64**: p. 1002-1025.
11. Ertaş, M. and M. Hakkı Alma, *Pyrolysis of laurel (Laurus nobilis L.) extraction residues in a fixed-bed reactor: Characterization of bio-oil and bio-char*. Journal of Analytical and Applied Pyrolysis, 2010. **88**(1): p. 22-29.
12. Şensöz, S. and D. Angın, *Pyrolysis of safflower (Charthamus tinctorius L.) seed press cake: Part 1. The effects of pyrolysis parameters on the product yields*. Bioresource Technology, 2008. **99**(13): p. 5492-5497.
13. Keleş, S., K. Kaygusuz, and M. Akgün, *Pyrolysis of Woody Biomass for Sustainable Bio-oil*. Energy Sources, Part A: Recovery, Utilization, and Environmental Effects, 2011. **33**(9): p. 879-889.
14. Ateş, F., A.E. Pütün, and E. Pütün, *Pyrolysis of two different biomass samples in a fixed-bed reactor combined with two different catalysts*. Fuel, 2006. **85**(12): p. 1851-1859.
15. Ukaew, S., et al., *Effects of torrefaction temperature and acid pretreatment on the yield and quality of fast pyrolysis bio-oil from rice straw*. Journal of Analytical and Applied Pyrolysis, 2018. **129**: p. 112-122.
16. Bahadır, A., et al., *Bio-oil production from fast pyrolysis of maple fruit (acer platanoides samaras): product yields*. World Journal of Engineering, 2017. **14**(1): p. 55-59.
17. Yorgun, S., *Fixed-Bed Pyrolysis of Miscanthus x giganteus: Product Yields and Bio-Oil Characterization*. Energy Sources, 2003. **25**(8): p. 779-790.
18. Park, J., et al., *Slow pyrolysis of rice straw: Analysis of products properties, carbon and energy yields*. Bioresource Technology, 2014. **155**: p. 63-70.

19. Lee, Y., et al., *Characteristics of biochar produced from slow pyrolysis of Geodae-Uksae 1*. Bioresource Technology, 2013. **130**: p. 345-350.
20. Lee, Y., et al., *Comparison of biochar properties from biomass residues produced by slow pyrolysis at 500°C*. Bioresource Technology, 2013. **148**: p. 196-201.
21. Al Arni, S., *Comparison of slow and fast pyrolysis for converting biomass into fuel*. Renewable Energy, 2018. **124**: p. 197-201.
22. Tsai, W.T., M.K. Lee, and Y.M. Chang, *Fast pyrolysis of rice husk: Product yields and compositions*. Bioresource Technology, 2007. **98**(1): p. 22-28.
23. Dufour, A., et al., *Synthesis gas production by biomass pyrolysis: Effect of reactor temperature on product distribution*. International Journal of Hydrogen Energy, 2009. **34**(4): p. 1726-1734.
24. Zhou, H., et al., *Effect of interactions of biomass constituents on polycyclic aromatic hydrocarbons (PAH) formation during fast pyrolysis*. Journal of Analytical and Applied Pyrolysis, 2014. **110**: p. 264-269.
25. Zhou, H., et al., *Polycyclic aromatic hydrocarbons (PAH) formation from the pyrolysis of different municipal solid waste fractions*. Waste Management, 2015. **36**: p. 136-146.
26. Zhou, H., et al., *Polycyclic Aromatic Hydrocarbon Formation from the Pyrolysis/Gasification of Lignin at Different Reaction Conditions*. Energy & Fuels, 2014. **28**(10): p. 6371-6379.
27. Ozbay, N., A.E. Pütün, and E. Pütün, *Bio-oil production from rapid pyrolysis of cottonseed cake: product yields and compositions*. International Journal of Energy Research, 2006. **30**(7): p. 501-510.
28. Nik-Azar, M., et al., *EFFECTS OF HEATING RATE AND PARTICLE SIZE ON THE PRODUCTS YIELDS FROM RAPID PYROLYSIS OF BEECH-WOOD*. Fuel Science and Technology International, 1996. **14**(4): p. 479-502.
29. Di Blasi, C., C. Branca, and A. Galgano, *Biomass Screening for the Production of Furfural via Thermal Decomposition*. Industrial & Engineering Chemistry Research, 2010. **49**(6): p. 2658-2671.
30. Di Blasi, C., et al., *Effects of Particle Size and Density on the Packed-Bed Pyrolysis of Wood*. Energy & Fuels, 2013. **27**(11): p. 6781-6791.
31. Manyà, J.J., J. Ruiz, and J. Arauzo, *Some Peculiarities of Conventional Pyrolysis of Several Agricultural Residues in a Packed Bed Reactor*. Industrial & Engineering Chemistry Research, 2007. **46**(26): p. 9061-9070.
32. Williams, P.T. and S. Besler, *The influence of temperature and heating rate on the slow pyrolysis of biomass*. Renewable Energy, 1996. **7**(3): p. 233-250.

C. Appendix - Indirectly heated bubbling fluidized bed steam reformer

Setup presentation

In this section, the novel indirectly heated biomass gasification concept is presented along with the respective commissioning experiments. It constitutes an atmospheric pressure 50 kW_{th} indirectly heated bubbling fluidized bed steam reformer (IHBFSR) which was designed, built and commissioned by the Dutch company Petrogas - Gas Systems in collaboration with the Process and Energy Department of the Delft University of Technology. The novelty of the reactor lies within the method of heat provision for the gasification reactions. In this reactor concept two radiant tube natural gas burners, one in the bottom (bed area) and one in the top (freeboard) of the reactor, are employed (Figure C.1). Its design aims at the reduction of heat losses, the provision of enough heat for the realization of the biomass steam reforming and cracking reactions and the exploration of scale-up possibilities to an industrial scale process. The commissioning experiments presented in this work are aimed at obtaining understanding of the operation characteristics, fuel conversion and raw product gas composition.

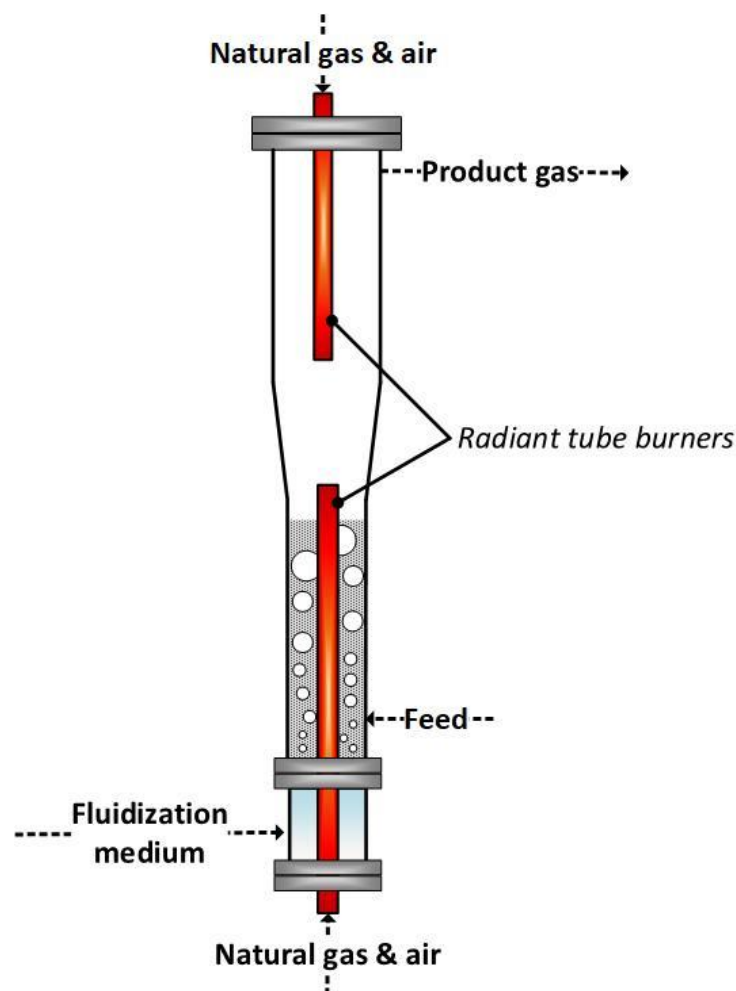


Figure C.1: Conceptual design of the indirectly heated bubbling fluidized bed steam reformer (IHBFSR)

A simplified process flow chart of the reactor is presented in Figure C.2. As mentioned earlier, the novelty in this reactor concept lies within the provision of heat by two burners placed vertically at both ends of the gasifier. This way combustion and gasification reactions remain separated to a great extent, thus avoiding the dilution of the product gas. In the following paragraphs the main sections of the IHBFBRS system are going to be discussed.

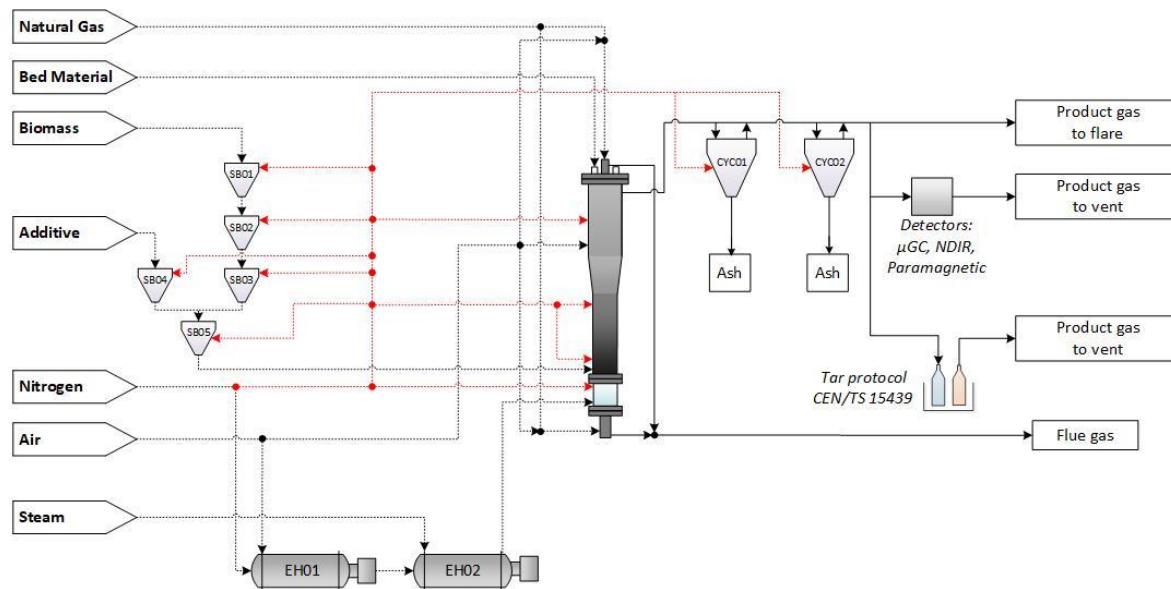


Figure C.2: IHBFBRS simplified process flow chart

Starting from the biomass and additive feeding section, this part of the setup consists of a funnel (SB01) and four bunkers, two for biomass (SB02 and SB03) and one for the additive (SB04). The biomass feeding system is designed for pelletized feedstocks. The additive bunker (SB04) and the bottom biomass bunker (SB03) are connected through two separate volumetric screw feeders to the main bunker (SB05) where the additive and the biomass are mixed. At this point it should be mentioned that the use of an additive depends on the experiment to be conducted. The conceptual design of the IHBFBRS process, includes the use of additives such as Kaolin ($\text{Al}_2\text{Si}_2\text{O}_5(\text{OH})_4$) for the reduction of the probability of agglomerate formation. By using alumina – rich compounds like kaolin, alkali – aluminum silicates can be formed. These silicates have a much higher melting temperature than the alkali silicates that are formed from biomass ash melting when no additive is used [1]. However, the use of additives is not required for example when low ash content biomass feedstocks, such as wood, are employed. The maximum feeding rate for the additives is 1 kg/h for clay – like materials such as kaolin and can also be used for feeding materials with similar bulk densities (e.g. char). From the main bunker (SB05), the main volumetric screw feeder leads the biomass into the reactor, just above the distributor plate. The nominal maximum fuel thermal power input for the reactor is 50 kW, which decides the maximum biomass feeding rate depending on the biomass type. The SB02 bunker is pressurized with N_2 and biomass is fed in and through it using ball valves. A constant N_2 flow of 4.11 kg/h is fed through the remaining bunkers, as well as the hoppers and main screw feeder, towards the reactor to avoid product gases back-flowing in the feeding system. To avoid pyrolysis reactions in the screw feeder due to elevated temperatures, the screw feeder is cooled down using a water-cooled jacket. The biomass/additive feeding system was supplied by Gericke B.V.

The gases that can be employed as fluidization agents in the IHBFBRS are N_2 (purity 99.999 %), air and steam. Steam is produced using a dedicated CERTUSS steam generator with a working pressure between 3.5 and 5 bar at temperatures between 103 °C and 105 °C, depending on the supply. The

steam line is insulated with a 2 mm layer of BCTEX fabric tape (GCC-1000 °C) provided by Horst GmbH and a 50 mm layer of Rockwool 810 provided by Rockwool B.V. Air (7 barg, 20 °C) and/or nitrogen (11 barg, 20 °C), which is mainly used during heating up, first pass through a 4.5 kW preheater (EH01), where they are heated up to 150 °C. The steam, along with the gases (if any) that are preheated by EH01, are fed to a second 6 kW preheater (EH02), which according to the throughput, heats up the gaseous mixture (set point: 650 °C). The gasification media are fed to the reactor at a pressure in the order of magnitude of 200 mbarg, again depending on the throughput. Air can also be directly fed into the freeboard, to assist with tar cracking, directly from the main supply. The secondary air injection point is located roughly 90 cm below TC06 (Figure C.3). In regard to the radiant tube burners, air and natural gas are supplied to them at 80 mbar and 60 mbar respectively. As mentioned in the previous paragraph, roughly 4 kg/h of N₂ flow into the reactor from the feeding system along with an extra 2.6 kg/h of N₂. This extra amount of N₂ is equally distributed (5 ml/min flows) between the pressure gauges in the reactor (Figure C.3) and the two cyclones. In the case of the pressure gauges the N₂ flow helps to prevent blockages and thus false readings, while for the cyclones, the N₂ flow rate assists with reducing ash accumulation. In both cases, the N₂ flow is added to the total produced gas flow. In general, all the pipes and both electrical heaters are insulated by a 100 mm Superwool plus blanket layer finished with isolation sealing rope and aluminium foil.

The reactor is manufactured out of 310S (AISI) steel with a wall thickness of 4.78 mm and a height of roughly 3 m. The reactor vessel is insulated with a 200 mm three-layer matras, provided by Thermoheat B.V. The first layer consisted of Thermoseal CH84, the second from Superwool plus bulk and the third one from Thermoseal RC materials. Gases are fed in the windbox and from there in the reactor, through a distributor plate. The distributor plate consists of 50 tuyeres each with two 2 mm holes drilled in a 25° angle (downwards). The area above the distributor plate occupied by the bed material constitutes the bed zone and its height is determined by both the amount of bed material employed and the fluidization agent flow rate. As presented in Figure C.3, the temperature in the reactor is monitored by thermocouples located in and near the bed zone. The first five thermocouples start 220 mm above the distributor plate and are located 150 mm apart from each other. The last thermocouple (TC07) is located at almost the same height as the product gas outlet which is on the reactor wall. Pressure gauges are located in four spots within the IHBFSR along with differential pressure transmitters, that allow the recording of the pressure drop over the distributor plate, the bed zone and the freeboard. In general, data from the various instruments are recorded through a SCADA/PLC coupling employing a LabVIEW interface. The system reads and records data every 10 s.

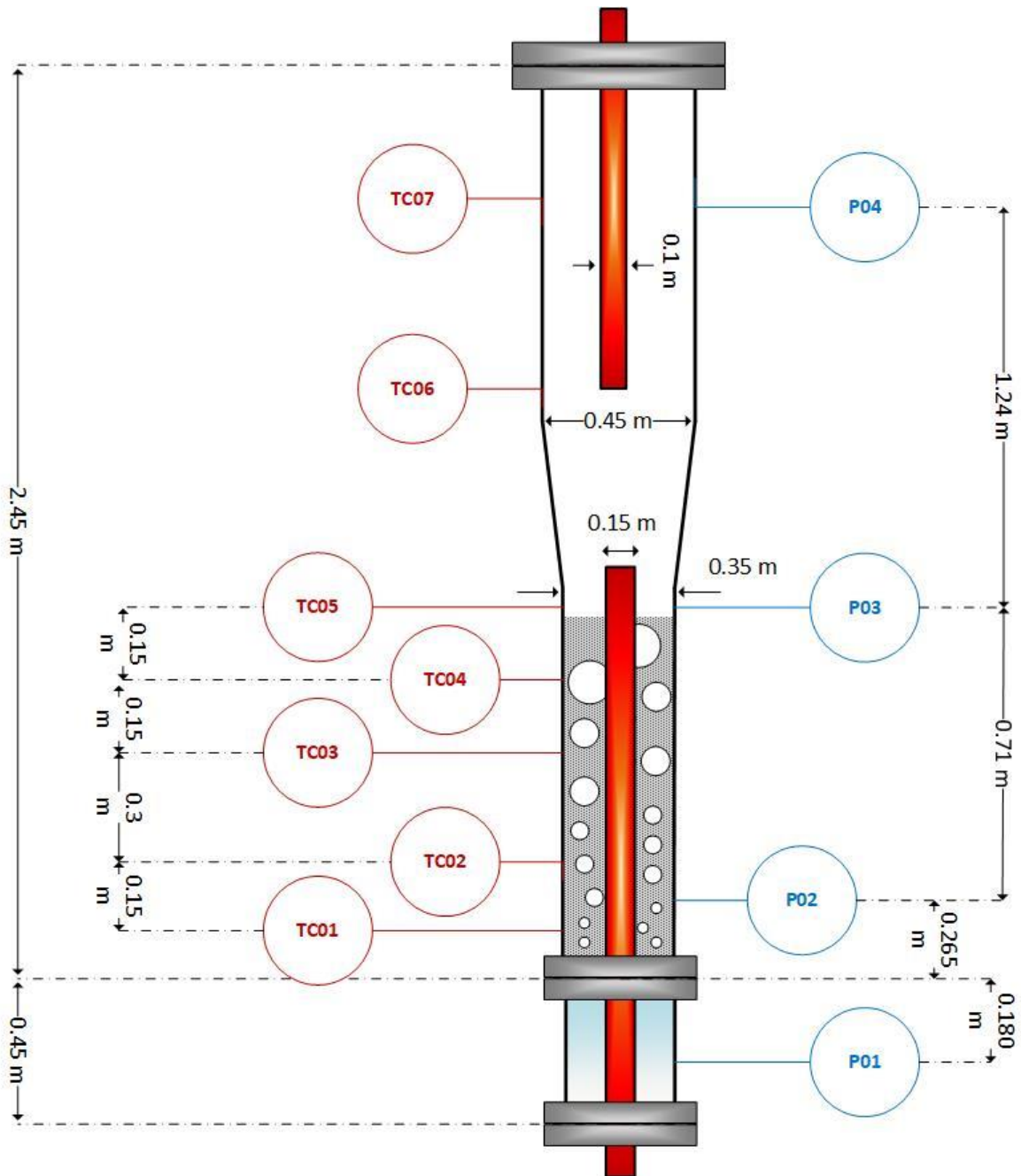


Figure C.3: Basic dimensions and main sensors location in the IHBFSR reactor chamber. PG: pressure gauge, TC: thermocouple

The two self-recuperative ceramic burners utilized for gasification heat provision were supplied from WS – Wärmeprozessstechnik GmbH and operate in a high velocity combustion mode. Both burners operate in an on/off mode; the bottom burner is controlled by the average values of thermocouples TC01 – TC05 and the top burner by thermocouple TC07. For both burners the maximum allowable set point was set at 850 °C according to the safety regulations. The burners operate at a constant capacity of 20 kW and 12 kW for the bottom (REKUMAT C100) and top one (REKUMAT C80), respectively. Regarding the bottom radiant tube, its total main body length is approximately 1.7 m and 1.2 m of this are in the bed area. Its bottom part is heating up the windbox, as shown in Figure C.3. The top radiant tube is smaller both in terms of diameter (0.1 m versus 0.15 m) and total main body length (1.3 m versus 1.7 m). As mentioned before, both burners operate at a constant capacity on/off mode. Thus, after a certain point of continuous operation, the temperature

on the burners and the radiant tube becomes stable. To determine this temperature during an actual experiment, K-type thermocouples were placed on four heights of the bottom burner and two of the top one. At each height three thermocouples were placed in its circumference. It should be clarified, that for the bottom burner, the thermocouples were placed in the part of the burner within the bed area, thus above the distributor plate. In the part of the burner within the windbox, thermocouples were not placed due to practical limitations having to do with the installation of the burner. Less, thermocouples were placed on the top radiant tube, due to its similarity with the bottom one and practical limitations of the employed devices (Omega) and software. All the thermocouples were placed on the burner rather on the radiant tube, since the fluidization of the bed could either cause mechanical damage on the thermocouple and most likely move its position on the tube, thus affecting the reading. The aforementioned temperature readings are presented in Table C.1.

Table C.1: Temperature at the circumference of various heights of the bottom and top radiant tube burners.

Bottom Burner			
Thermocouple (#)	Temperature (°C)	Average Temperature at a certain height (°C)	Height – Distance from distributor plate (m)
1	1109		
2	1094	1104	1.18
3	1108		
4	985		
5	1006	983	0.88
6	959		
7	969		
8	979	972	0.48
9	967		
10	915		
11	930	924	0.05
12	928		
Top Burner			
13	1122		
14	1108	1106	n.a.
15	1089		
16	978		
17	983	983	n.a.
18	988		

The product gas, after passing through the cyclones, which were insulated using a 100 mm layer of Superwool Plus blankets, isolation sealing rope and aluminium foil, is led in its majority to the flare. The rest of the product gas is led to the gas analysis section. The sampling of the gas is initiated with the opening of a needle valve, which allows the product gas to pass to the gas analysis system. Then follows a quartz fibre candle filter, employed for the removal of char and ash particles that can lead to clogging of lines and damage the analytical equipment. The gas analysis line until this point is traced at 400 °C and the filter is heated at 350 °C by means of a heating cable (HS-450 °C) provided by Horst GmbH and a Tyco IJ-GL glad silk heated jacket respectively. After this point, part of the gas is channelled to the tar sampling system, where tars are sampled according to the Tar Protocol CEN/TS 15439 [2]. The tar sampling system consists out of 6 impinger bottles, out of which the 2nd, 3rd, 4th and 5th are equipped with a quartz filter and all five first are filled with 100 ml of isopropanol. The first, second and fourth bottle are submerged in a water bath (25 °C – 40 °C) and the rest in an ice bath.

Downstream the tar protocol lies a pump used to assist with maintaining a steady flow and afterwards a flowmeter and a gas meter. Continuing with the gas analysis part, after the junction with the tar protocol section, the gas passes through a water-cooled condenser. In this condenser ends up the larger part of the water contained in the product gas in steam gasification experiments. Downstream lies a series of four bottles, three of them filled with isopropanol and one filled with silica gel. The isopropanol filled bottles are mainly used for tar removal from the gas stream, while the silica gel bottle assures the non-presence of water in the gas stream that passes through the detectors. Subsequently follow a Whatman 55 mm paper filter and the pump and from there the gas flows towards the detectors. A u-GC, samples from the product gas stream every 4 minutes, measuring CO, CO₂, H₂, CH₄ and N₂. Then the gas flow splits into two streams each passing through the O₂ detector and the Non-Dispersive Infrared Detector (NDIR), for the measurement of CO and CO₂. The use of these two detectors, might appear redundant due to the presence of the u-GC. However, the presence of the O₂ detector allows the operator to: a) verify that there is not an excess of O₂ when the reactor is in combustion mode, b) ensure good operation while in air gasification mode, c) ensure that not an excessive amount of secondary air is used, and most importantly d) signal potential leakages in the gas analysis system. The NDIR detector, despite being able to detect less permanent gases than the u-GC, has the advantage that it yields the results in real time during the experiments, while the u-GC has a 4 min lag. Thus, it assists significantly with the monitoring of the experiments. Finally, the product gas streams coming out of the two detectors are joined again before passing through a gas meter and fed into the vent.

Experimental procedure and overview

Before each test, 75 kg of bed material (corundum) were loaded in the reactor using a flange located at its top. This amount of bed material corresponds to a stationary bed height of roughly 0.59 m according to the reactor geometry and bed material properties.

The experiment is initialized by warming up the reactor to an average bed temperature of 850 °C. The average bed temperature is defined as the average values of thermocouples TC01 – TC05. This process, which includes two separate steps, was repeated with negligible variations for all the experiments described within this work. The first step starts by introducing the maximum fluidization media flow, which corresponds to 30 kg/h of N₂ and 22 kg/h of air. At the same time, both burners are turned on with a set point of 850 °C, while the two preheaters are also turned on (set points 150 °C and 650 °C respectively). The choice to introduce the maximum available gas input was made to achieve fluidization as quickly as possible, in order to improve heat transfer and consequently reduce the time required for heating up the reactor. In order to reach the designated temperature set point the heat provided by the radiant tube burners does not suffice. Therefore, a biomass combustion step is added to the warming up process. Combustion is performed with 22 kg/h and the appropriate amount of biomass feedstock to achieve a lambda (λ) of 1, that corresponds to stoichiometric combustion. The biomass flow rate for stoichiometric combustion is approximately 4 kg/h for both PG and ExR, since the two species have similar compositions.

Regarding the preheaters, the first one (EH01) achieves heating up the N₂ and air mixture (30 kg/h and 22 kg/h respectively) at 150 °C. The same stands also for the pure air flow for the combustion step and the flow employed for the gasification step. The behaviour of the second preheater, whose set point is always 650 °C, can be observed in Figure C.4, through a representative example. The process of warming up the reactor was the same for each experiment conducted. During this flow regime, the second preheater (EH02) achieves to heat up the gaseous mixture to a maximum temperature of 490 °C after roughly 3 h. However, after around 90 min (463 °C), the heating rate was below 1 °C/min and dropping. Furthermore, as it can also be seen in Figure C.4, the gaseous mixture suffers significant

heat losses on the way to and in the windbox. In particular, the average temperature difference is 130 °C and the heat losses at steady state conditions (after roughly 3 h) are roughly 1.7 kW. The heat losses were calculated using the following formula:

$$\dot{Q}(kW) = (\dot{m}_{N_2} \cdot c_{p_{N_2}} + \dot{m}_{air} \cdot c_{p_{air}}) \cdot \Delta T \quad (\text{Eq. 8})$$

where, \dot{m} is the flowrate of N_2 (kg/s) and air respectively, the specific heat c_p (J/kgK) for both gases was obtained for the average value of the temperatures after EH02 and the windbox according to [3], and ΔT (K) is the corresponding temperature difference.

After the initiation of combustion, as is also visible in Figure C.4, the preheater is able to achieve higher temperatures, due to the reduction of its throughput to 22 kg/h of air. However, this reduction of the total flow has a negative effect on the windbox temperature which effectively decreases. In total, the average temperature difference between the two points was approximately 204 °C and the average heat loss was calculated at 1.35 kW, using the same procedure as mentioned earlier.

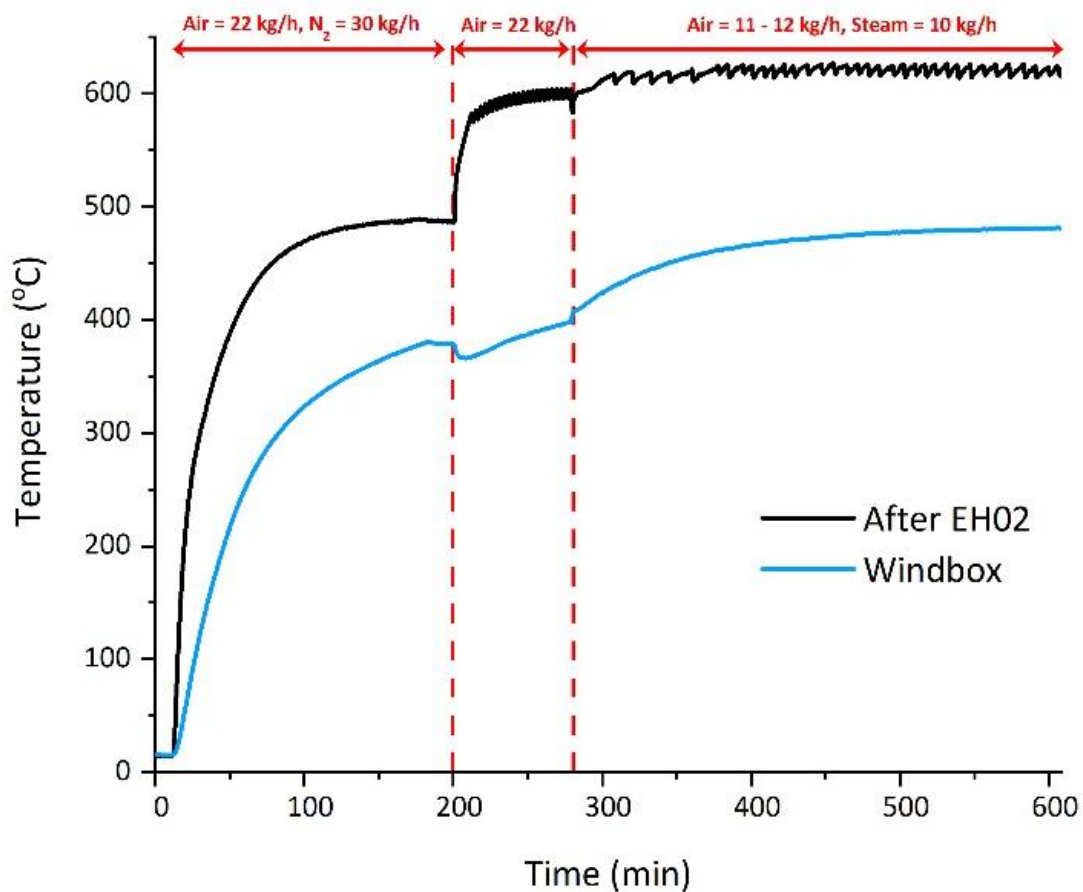


Figure C.4: Temperature of the N_2 – air flow after the second preheater and in the windbox for three different experimental regimes.

The last part of Figure C.4 (air = 11 - 12 kg/h and steam = 10 kg/h), corresponds to the steam/air gasification part of the experiment. The purpose behind the selection of this particular combination of steam and air will be discussed later. At this point, in order to showcase the second preheater's behaviour as well as the conditions in which the fluidization media enter the reactor, this experiment will be compared to one where roughly 1.9 kg/h of air and 8.7 kg/h of steam were used. In Figure C.5, the high and low total flowrate experiments are compared, in terms of the aforementioned criteria.

The same observation made earlier, can also be repeated here. Namely, the reduction of the total air and steam flowrate leads to better performance of the preheater, however this reduction leads to increased heat losses in the windbox. Overall, due to the significant reduction of the total flow rate, the heat losses from the EH02 to the windbox, were 1.5 kW for the high flow rate case versus 0.9 kW for the low one, with the corresponding entry temperatures in the main reactor being 480 °C and 430 °C respectively. It should be mentioned that the average windbox temperature was 480 °C for high flowrate experiments (air \geq 11 kg/h and steam = 10 kg/h) and 440 °C for the low flowrate ones (air = 1.9 kg/h and steam \approx 8.5 kg/h) for the experiments examined within this work. Therefore, the behaviour presented through this particular experiment is representable of the gasification media inlet conditions within the context of the present work, considering the main gasification experiment (thus excluding warming up). Conclusively, as the installation currently stands, a clear trade-off exists between the reduction of heat losses and the gasification inlet temperature.

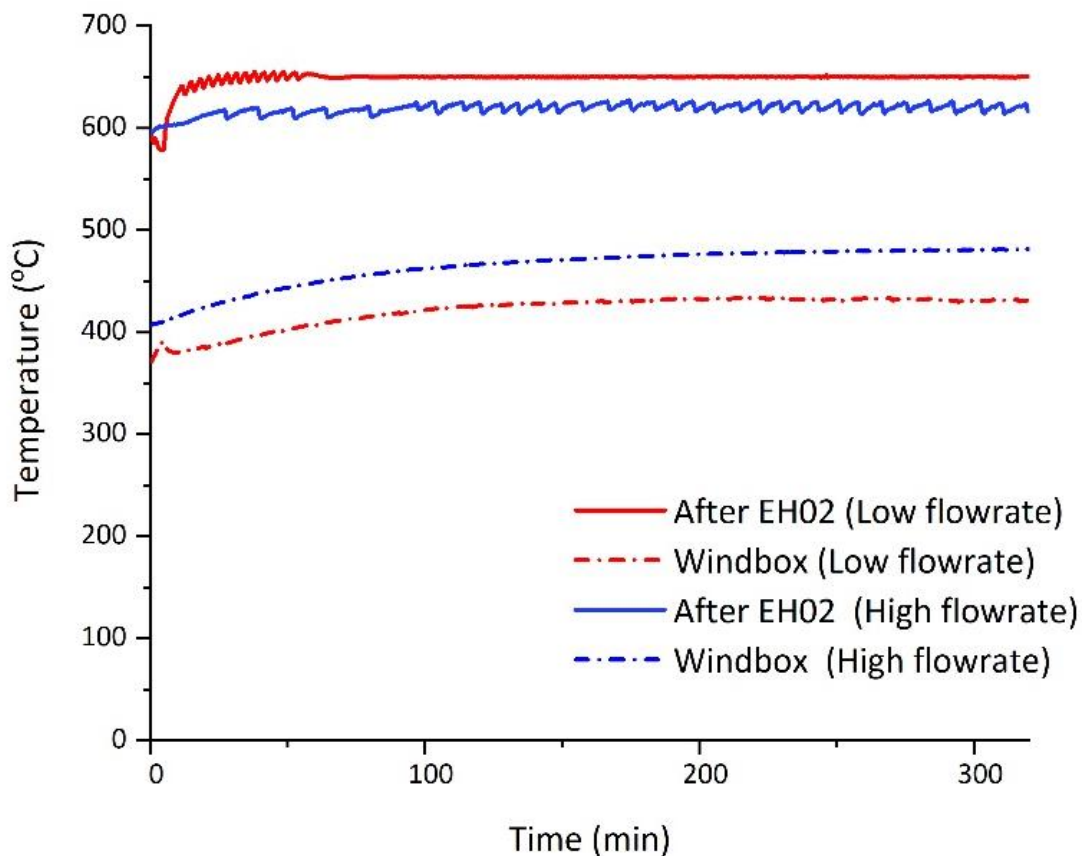


Figure C.5: Temperature of the air – steam flow after the second preheater (EH02) and in the windbox for a high total flowrate (air = 11 kg/h and steam = 10 kg/h) and a low total flowrate (air = 1.9 kg/h and steam = 8.7 kg/h).

The experimental campaign presented hereby, is focused on biomass steam reforming. Therefore, as explained earlier, conceptually the presence of air in the process is not desired, since it leads to the dilution of the product gas. However, through experimentation, it was observed that the heat provided from the burners did not suffice for maintaining high enough temperatures for the conduction of gasification experiments ($>$ 700 °C). To achieve meaningfully high temperatures, different amounts of air were introduced along with steam. The presence of O₂ in the reactor, led to exothermal combustion reactions of either biomass and/or its char, that initially led to a temperature increase and eventually stabilization. In the following paragraphs, the necessity of this approach as well as its application are going to be presented through experimental examples.

A representative example of the temperature profile of the bed zone (TC01 – TC05) is presented in Figure C.6. In the context of this work, this particular experiment can be characterized as a high temperature (HT) experiment, since the average temperature of the bed area during gasification (last two regions) is around 850 °C. Experiments where the average bed temperature during gasification is lower than 850°C will be referred to as low temperature (LT) experiments. This categorization concerns only experiments with PG, since all the ExR experiments were conducted at high temperatures. In the experiment presented in Figure C.6, the first two regions correspond to the warming up of the reactor, firstly with the air/N₂ combination and subsequently with combustion of biomass (ExR in particular). The different regimes can be marked very clearly by the changes observed in the thermocouples readings. To begin with, just before 50 min, TC02 which until this point was stabilizing at room temperature, jumped to temperatures above 200 °C and started coinciding with TC01 which also jumped at the same time. This point marks the start of fluidization and the thermocouples temperature serves as a rough indicator of the bed's height. For example, after roughly 65 min TC03 value, which until this point was rising steadily, slightly dropped and started coinciding with the TC01 and TC02 ones. Therefore, it can be safely surmised that the bed height ranges between the locations of TC03 and TC04. As time goes by, it can be observed that TC04 temperature increase starts stagnating and most importantly small oscillations in the readings begin to appear. The appearance of these oscillations can be linked to acoustic vibrations caused by the bubbling fluidized bed which height is approaching TC04 location. In general, it should be reminded, that the increasing temperature's effect on the gases properties (density, viscosity) leads to an simultaneous increase of the fluidization velocity and therefore of the corresponding bed height [4]. Due to the overall stagnation of the bed temperatures increase, combustion of biomass was initiated to expedite the process. In this particular experiment for example, the average bed temperature heating rate moving average dropped from 4 °C/min to below 2 °C/min within the approximately 100 min duration of the first warming up region. Switching to a combustion regime, expectedly led to the increase of the heating rate and the set point of the system (Average temperature of TC01 – TC05) was reached within approximately 40 min. This increase is at a certain degree "artificial" and it does not only concern the actual bed region. The latter is now comprised only by TC01 and TC02 as seen in Figure C.6. The reduction of the total flow, led to a decrease of the bed height, thus TC03 either came out of the bed area or is marginally in. The second seems as the most likely option, since the recorded temperature values are not as high as in the cases of TC04 and TC05. It is apparent that the bed material prevents the effective heat transfer from the radiant tube to the thermocouples. When the thermocouples depart the fluidization region and are therefore "revealed" to the radiant tube, their temperature rises fast. Overall, switching to combustion mode, apart from the temperature gain due to the exothermicity of the process, mainly evident by the temperature increase in the fluidization region (TC01-TC02), has also an indirect effect leading to the desired result which is to increase the temperature of the bed area. Namely, the reduction of the total flow, firstly reduces the total amount of flow needed to be heated up by the system and secondly "reveals" TC03 to the radiant tube burner.

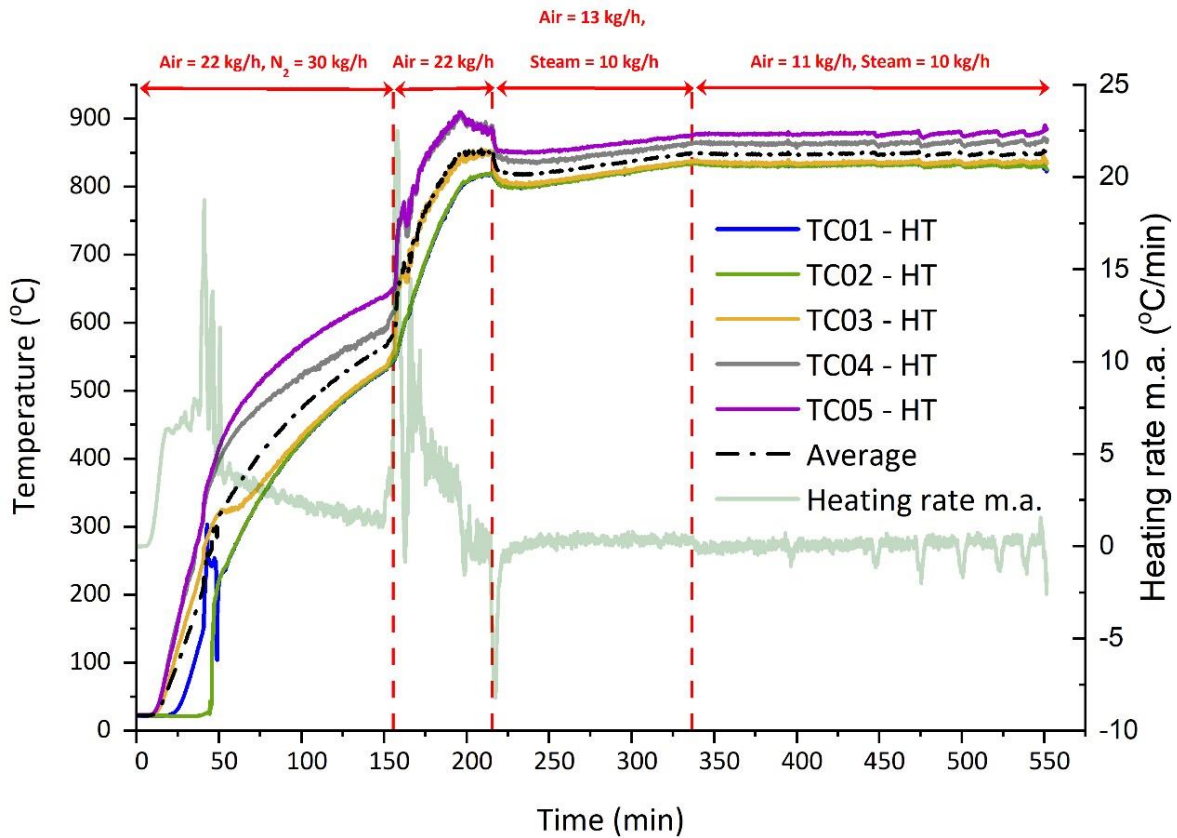


Figure C.6: Temperature profile of the IHBFSR bed zone (thermocouples: TC01-TC05) for a high temperature (HT) steam gasification experiment with ExR as a feedstock and corundum F046 as bed material. The heating rate moving average refers to the average bed temperature heating rate with a period of 20.

At this point it should be mentioned, that when the set point for a burner is reached, the burners switches off. According to the temperature hysteresis selected, which in this case is 1 °C for the bottom burner and 5 °C for the top one, the burner will switch on and off. As it is shown in Figure C.6, when this set point is reached and as long as the average temperature does not fall below 849 °C, the burner (bottom) will not turn back on. As a result, the temperature in the actual fluidization area (TC01 – TC03) is maintained due to the exothermicity of combustion. However, the temperature for the two thermocouples above is dropping, since the burner is now off. In any case, the target, which was to reach the certain temperature for the initiation of steam gasification is reached this way. After this point and some minutes of the stabilization and preparation, steam was fed into the system. As can be seen in Figure C.7 and the first two regions, the behaviour of the system during warming up is fairly repeatable for the different experiments, so the remarks made here can be generalised for all the experiments conducted.

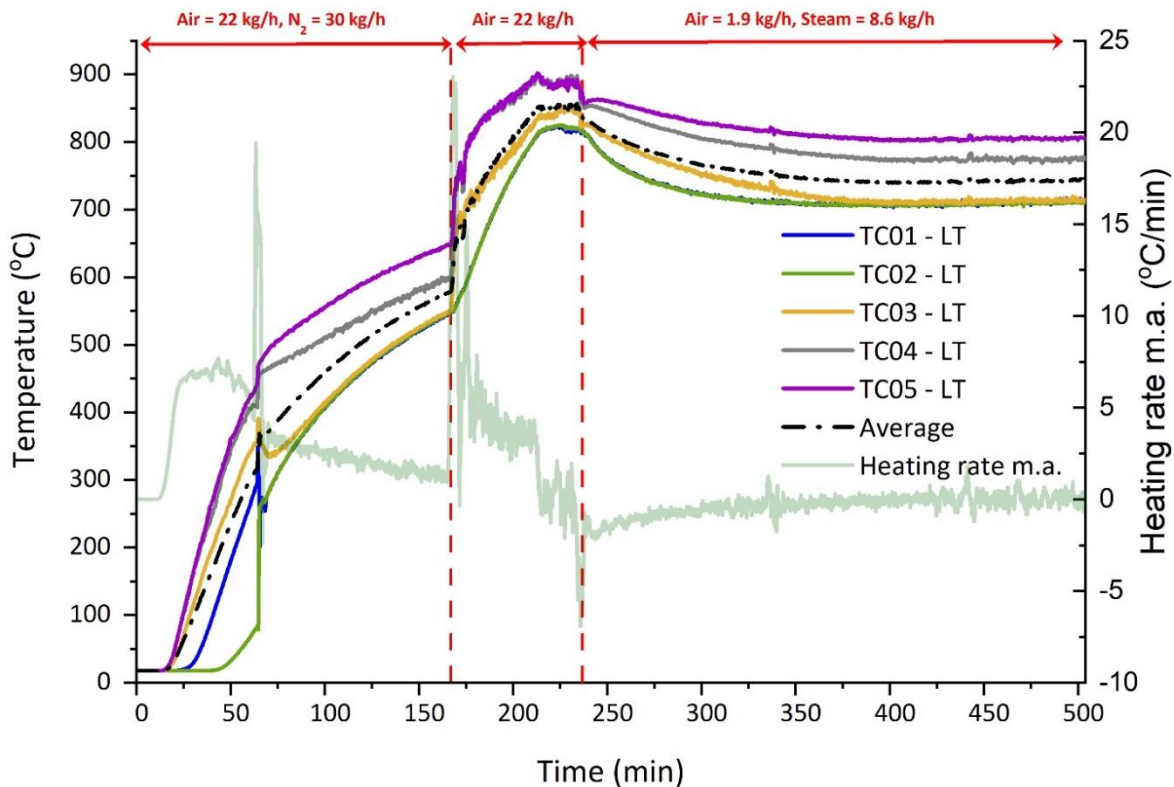


Figure C.7: Temperature profile of the IHBFSR bed zone (thermocouples: TC01-TC05) for a low temperature (LT) steam gasification experiment with ExR as a feedstock and corundum F046 as bed material. The heating rate moving average refers to the average bed temperature heating rate with a period of 20.

Figure C.6 and Figure C.7, provide the opportunity for a direct comparison of a HT and a LT experiment in terms of the temperatures in the bed area. Starting from the same initial point, namely an average temperature of 850 °C, the switch from combustion to steam gasification mode was performed. For the HT experiment (Figure C.6), the incoming 22 kg/h air flow was substituted initially with 13 kg/h ($\lambda = 0.23$) of air plus 10 kg/h of steam. The air input was later changed to 11 kg/h ($\lambda = 0.196$). In the case of the LT experiment, combustion air was substituted with 1.9 kg/h ($\lambda = 0.04$) of air plus 8.6 kg/h of steam. As mentioned before, the combustion part of the experiment is always performed with a PG or ExR feed of 4 kg/h, corresponding to a $\lambda = 1$. For the gasification phase and the two experiments presented in Figure C.6 (HT) and Figure C.7 (LT), the biomass feed (ExR) was 10 kg/h and 8 kg/h respectively. These values correspond to a STBR of approximately 1.2 for both cases. It should be mentioned that the combination of 8 kg/h feed and $\lambda = 0.04$, corresponded to the lower limit of the system. This means, that this was the minimum amount of ExR feed and the minimum amount of air that were required to maintain a bed temperature above 700 °C.

It is interesting to note the differences in the heating behaviour between the two systems for the respective gasification regimes, starting with the bed height, as it is observed through the thermocouples values. In the case of the HT experiment, which corresponds to the higher total fluidization flow (Figure C.6), TC03 is part of the actual bed zone, something that is not the case in the LT experiment (Figure C.7). In the LT experiment, the reduction of the total air flow led to the reduction of the bed height. In the HT case, even the incremental increase in terms of total flow compared to the combustion interval, led to an increase in the bed height as it is evident by the similar values of TC01 – TC03. On the contrary, for the LT case, TC03 was outside the bed area initially, as the actual bed temperature (TC01 – TC02) was dropping. As mentioned earlier, the employment of the different lambdas (λ), leads to different operational temperatures throughout the system, due to the varying degree of char and/or biomass oxidation reactions. This reduction of the extent of oxidation reactions

in the case of the LT (and thus low λ), leads however to increased char accumulation in the bed. That is evident by the fact that in Figure C.7, the value of TC03 over time becomes equal to the TC01 – TC02 values. Without the addition of more bed material or the increase of the flow rate due to an operational intervention or through the increase of the produced gas amount somehow, char accumulation in the bed area is the only plausible reason for the observed behaviour. The char accumulated in the bed after a certain gasification interval becomes part of the reactor's solid inventory. Of course, it is being consumed at the same time by gasification and oxidation reactions, but it is also being replenished by the continuous biomass feed and subsequent char production. This particular phenomenon, as well as its effect on the produced syngas is going to be discussed in a later section. In this section, its effect is discussed only in terms of its effect on the system's operation. It can be argued that char is also accumulated at HT experiments, which is the case of course. Nevertheless, the increased air presence, leads to lower amounts of it compared to the LT experiments. Furthermore, as it has been shown in the discussion for the heating behaviour for the other operational regimes, it is often the case that TC03, falls in and out of the actual bed area. This is because the distance between the stationary bed height (~ 0.6 m for 75 kg of F046) and TC03 is only 0.07 m. For the HT experiments, TC03 is as mentioned before, barely in the actual bed area and its distance from TC04 is 0.15 m. Therefore, with the lower degree of char accumulation, it is difficult to see its effect on the system, at least through this approach. Finally, it should be added that the amount of char recovered from LT experiments was significantly higher compared to the HT cases as it will be discussed in following sections.

At this point, it is important to explain the reason behind the employment of 13 kg/h of air for the initial gasification stage in the case of the HT experiment presented in Figure C.6, since later the flow is reduced to 11 kg/h. This particular experiment concerns the gasification of ExR, as mentioned before. The goal was to perform the ExR gasification experiments with similar STBR and λ as with the PG experiments that were conducted earlier. Such an experiment with PG is presented in Figure C.8 and the differences with the ExR experiment in Figure C.6 are minimal for what the two initial warming up regions are concerned. The differences were observed with the initiation of steam/air gasification. Namely, in the case of the PG experiment (Figure C.8), the average temperature of TC01 – TC03 dropped to 813 °C before stabilizing at roughly 833 °C after 60 min. For the ExR experiment (Figure C.6), the average temperature of TC01 – TC03 fell initially from 830 °C below 810 °C within 2 min since the switch to air/steam gasification. This steep drop led to the decision, at this particular moment, to increase the air supply to 13 kg/h in order to maintain an overall actual bed temperature comparable to the PG experiment. Thereafter, the drop continued until 800 °C, for roughly 15 min. After this point, the TC01 – TC03 average temperature started increasing until the desired point (between 830 and 840 °C) for roughly 120 min, when the amount of air was set again at 11 kg/h. To explain this difference noted between the two biomass feedstocks one can look at their compositional characteristics (Table 5.1). Even though the LHV values are slightly higher for PG (19 MJ/kg versus 19.5 MJ/kg), the difference between the values is too small. On the contrary, the much lower fixed carbon content of ExR (15 wt % versus 20 wt %), can presumably lead to less char formation, mainly from the initial pyrolysis part of the gasification process. The subsequent, char oxidation is assumed to be the main reason for maintaining the desired gasification temperature, since the LHV of biomass char is in general much higher compared to the parent biomass [5].

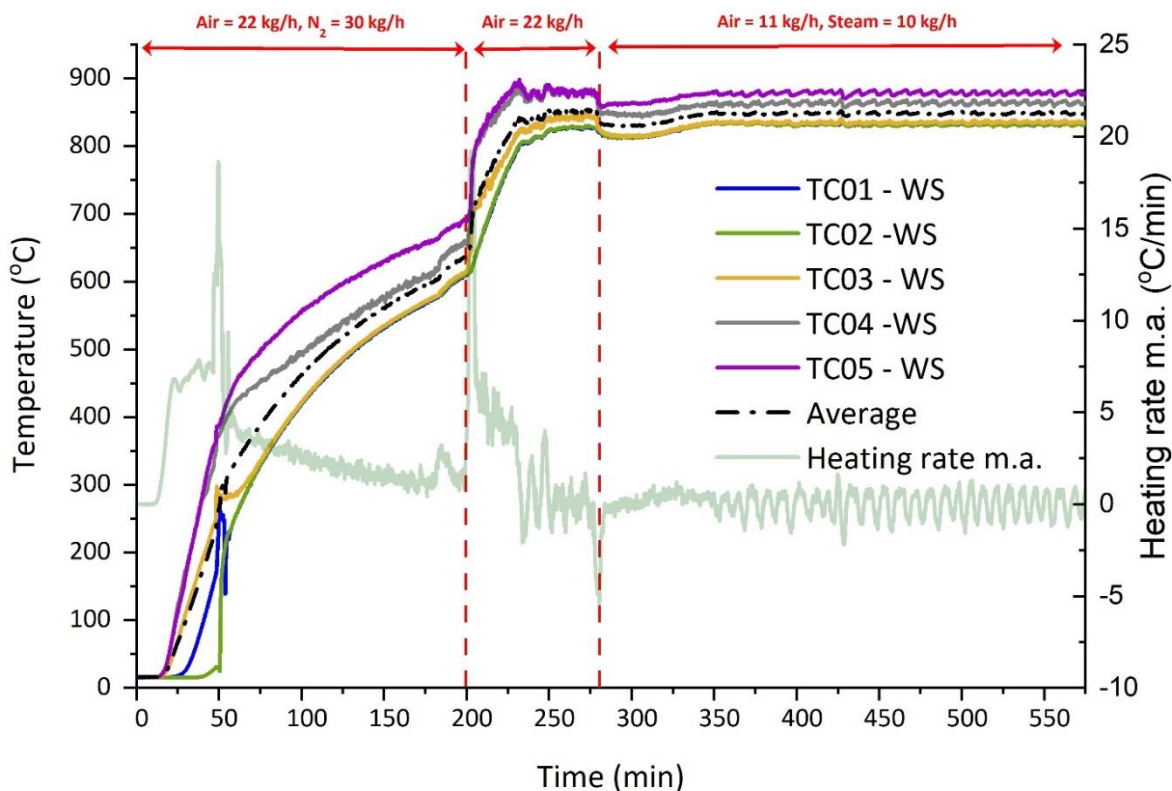


Figure C.8 Temperature profile of the IHBFSR bed zone (thermocouples: TC01-TC05) for a high temperature (HT) steam gasification experiment with PG as a feedstock and corundum F046 as bed material. The heating rate moving average refers to the average bed temperature heating rate with a period of 20.

The values from the thermocouples located at the freeboard part of the setup are of course very significant in the overall process. However, their behaviour depends on significantly less factors than the corresponding bed area thermocouples. In particular, since the O_2 supplied with air is mostly consumed by the time the total flow reaches this part of the system and the rest of the cracking and reforming reactions taking place are endothermic, the temperature of this area is mainly influenced by the top radiant tube burner. However, the fact that oxidative reactions take place in the bed zone, alone with the fact that the bottom burner has a higher capacity (20 kW versus 12 kW), leads to higher temperatures in the thermocouples TC04 and TC05 compared to TC06 and TC07. As a result, the flow incoming to the TC06-7 area also heats up this part of the reactor, with TC05 consistently presenting the higher temperature in the reactor. This argument is further backed by the values in Table C.1, which show that the temperature of the burner increases as we move towards its tip. Conclusively, the top part of the reactor is heated from the top burner and the incoming flow from the bottom. However, this is mostly the case in HT experiments, since in LT experiments the temperature of the bed area is significantly lower than the one that can be achieved in the top part with only the burner contributing. Thus, this part of the heating process of the freeboard is no longer valid. This leads to significantly lower temperatures throughout the system, top part included, with TC06 becoming the highest temperature point of the reactor. As mentioned in the description of the setup, there is also the possibility of feeding air on the top part of the reactor (approximately 1.5 m higher than the distributor plate, just below TC06). Such secondary air injection can lead to higher temperatures and thus significant tar reduction and it is considered as a valid gasifier modification for tar reduction from the literature [6]. The effect of air injection on the composition of the product gas and the final tar yield will be further analysed on the experimental results section. However, in the context of the present analysis, it can be mentioned that the exothermal oxidation reaction that occur lead to significant increase of the local temperature. It should also be mentioned that this measure was

applied only for the case of LT and thus ExR experiments, which facilitate the investigation of this process effect due to the low temperatures employed. All the different behaviours of the freeboard area encountered in this specific experimental campaign are depicted in the two graphs of Figure C.9.

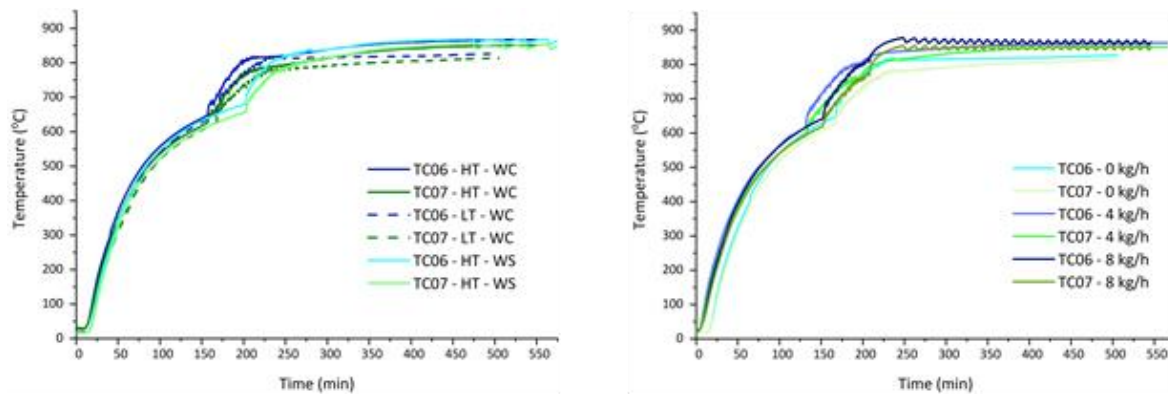


Figure C.9: Temperature profile of the freeboard zone of the IHBFSR (TC06 – TC07) for a high (HT) and a low (LT) temperature steam gasification experiment with ExR and a HT with PG as a feedstock and corundum F046 as bed material (left) with STBR = 1.2. On the right, again the temperature profile of the freeboard zone of the IHBFSR (TC06 – TC07) for LT experiments in which various amounts of secondary air were injected (0, 4 and 8 kg/h) with ExR as a feedstock and corundum F046 as bed material under $\lambda = 0.04$ and STBR = 1.2. The LT experiment on the left is the same as the 0 kg/h one on the right.

Overall, it can be concluded by studying Figure C.9 that the warming up regions behaviour leads to the same results for all the different experiments presented. At this point it should be reminded that the top burner set point is 850 °C (controlled by TC06) and its hysteresis ± 5 °C. The differences between the experiments in terms of the duration of each stage, which was not specifically set, do not allow a comparison based on time. Nevertheless, for all the experiments with ExR the temperature of the two thermocouples arrived at similar values before the initiation of gasification (approximately 815 °C for TC06 and 780 °C for TC07). For PG the corresponding values were significantly higher, namely 836 °C for TC06 and 810 °C for TC07. For both feedstocks though, the same pattern was noted, with the switching from the initial warming up stage to the combustion one, leading to a significant increase of the heating rate. This is attributed to both the heat produced from the combustion and the reduction of the total flow as it was discussed in the previous paragraph. However, in continuation of the previous remark about the TC06 and TC07 peak values from warming up for ExR and PG, it is interesting to note the shape of their temperature profile in steady state gasification conditions. For the HT experiments with PG, the burner switches on and off, which means that the designated temperature for TC06 was exceeded for 5 °C and subsequently went below 845 °C. Despite the fact that for the ExR – HT experiments the temperature was similar on average, the burner remains continuously on. This is perhaps a minor difference, however it is consistent with the previously mentioned difficulty of achieving the required bed temperature for the ExR experiments which led to the increase of the air flow for the first part of the gasification stage. Furthermore, regarding the HT and LT – ExR experiments, the main differences are again apparent at the tail of the graphs were the difference in terms of the average temperature achieved is approximately 40 °C for both TC06 and TC07. In the graph on the right of Figure C.9 though, it can be readily observed that the injection of even 4 kg/h of air in the freeboard is enough to push the TC values towards their maximum achievable set points. With the further increase of the flow rate to 8 kg/h, the burner starts to switch on and off, which indicates the ease with which the set point is reached. The frequency of the temperature oscillations caused by the on/off operation of the burner, is indicative of this ease and can be favourably compared to the HT – PG case depicted on the left of Figure C.9.

Finally, another operational parameter that should be discussed, despite not being controlled directly by the operators, is pressure. The pressure of the system can be measured in terms of the pressure differential as described in Figure C.3, since the four pressure gauges installed allow the recording of the pressure drop over the distributor plate, the bed zone and the freeboard. The pressure is also recorded at the system's exit, right after the second cyclone. This value, however, is highly dependent on the condition of the flare line in general. In particular, the flare line of the IHBFSR setup is several meters long since it has to reach a certain point outside the building where the product gas can be safely combusted by the flame. Before this flame, a flame-retardant mesh is placed which helps with the trapping of tar and char particles that could damage the equipment downstream. However, this mesh remains open in certain percentages according to the level of impurities collected, causing significant variations in the pressure of the system. Even though this mesh is cleaned on a regular basis, it is difficult to assess its condition after one or two experiments. This particular characteristic of the setup does not allow the direct comparison of the pressure values obtained from the various experiments. Regarding singular experiments however, some interesting observations can be extracted, in particular from the differential pressure readings. These observations, that will be discussed in the following paragraph, were consistent among the different experiments as trends rather than as pure values.

In Figure C.10, an example of the behaviour of the pressure drop over the system is presented. From this figure, it can be readily observed, that the pressure drop over the freeboard is constantly zero as expected, since no obstructions to the flow are encountered in this region of the reactor. The largest pressured drop initially, is observed for the distributor plate. That can be explained by the presence of the bed material, which prior the fluidization rests on top of the plate. The introduction of air and N_2 initially, lead to a steep increase of the pressure drop over the distributor plate and to a less degree over the bed area. At this stage, the passing fluids (air and N_2) percolate through the void spaces between the stationary bed material particles and the whole system is essentially a fixed bed. When the minimum fluidization velocity is reached for a specific set of conditions, the pressure drop decreases immediately, since after this point, the fluidization of the bed material allows for the easier passage of the gases. This initial drop in the pressure difference over the distributor plate, coincided for all the experiments conducted with the thermocouple readings of the actual bed area coming together as described for Figure C.6. Afterwards, the pressure drop over the distributor plate increases along with temperature as the reactor is heating up, before dropping to much lower values with the reduction of the total flow for the combustion stage. From that it becomes obvious, that the main reason for this high pressure drop after fluidization is the distributor plate itself and the tuyeres employed, rather than the bed material itself. After this point the pressure drop over the distributor plate becomes similar to the one over the bed area, albeit a little lower. Switching to the various steam and air combinations, did not appear to have significant effect on the pressure drops, as long as the total amount of flow introduced remained similar. Finally, as it can be derived from the interval directly after the initiation of fluidization, the magnitude of the oscillations of the readings increases slightly with time and thus intensification of fluidization. This stands for both the distributor plate and the bed area pressure differentials.

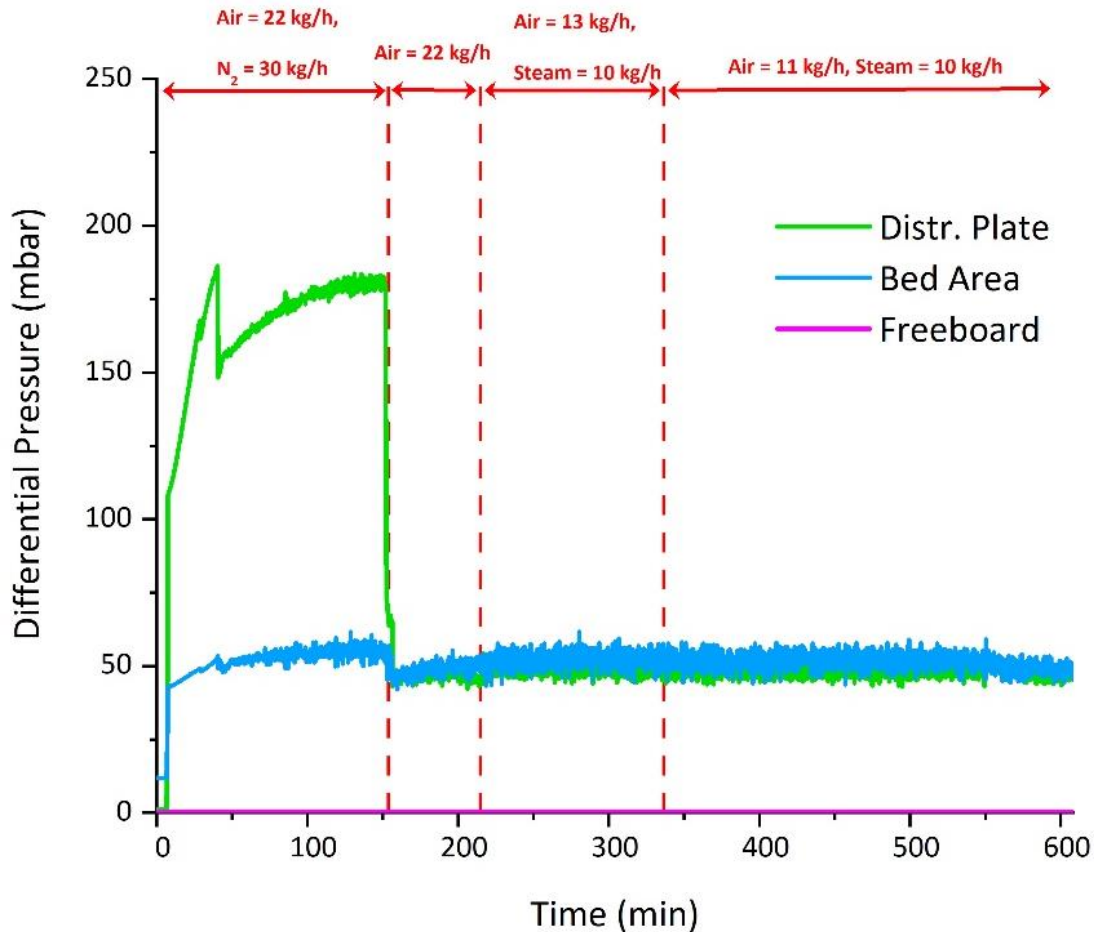


Figure C.10: Differential pressure drops over the distributor plate, the bed area and the freeboard during a HT steam gasification experiment with ExR as a feedstock and corundum F046 as bed material.

In Figure C.11 and Figure C.10, two LT experiments with and without secondary air injection are presented. The reason was to illustrate the similarities between experiments performed under similar conditions. Firstly, it should be mentioned that, as it was expected, secondary air injection did not influence the differential pressure readings. Regarding the distributor plate pressure differential one interesting remark can be made, however. The switch from combustion (22 kg/h of air) to steam gasification (1.9 kg/h of air and 8.6 kg/h of steam) mode is denoted by the green and the black dashed lines for the 0 and 8 kg/h air injection experiments respectively. Through pure chance, the switching from the initial warming up part to the combustion one, coincided for the two experiments in terms of time, and it is thus denoted by the red dashed line. At around 107 min, a very big drop of the distributor plate pressure differential is noted for the 8 kg/h secondary air experiment. This drop did not coincide with any other external or internal events in the system. This drop was followed by the expected drop after the reduction of the total flow through switching to the steam gasification regime. Additionally, a similar observation can be made for the 0 kg/h secondary air experiment. In particular, after switching to the combustion mode, the pressure differential dropped to approximately 68 mbar, which is higher as a value compared to the 8 kg/h experiment. In principle the pressure differential between the two experiments should be the same since the exact same operational parameters are employed. At 220 min however, a drop on the differential pressure values is also noted for the 0 kg/h experiment, again with no other event coinciding. As it can be deduced from Figure C.11, the two experiments are exact duplicates in terms of both the differential pressures examined after these two sudden drops. This particular behaviour, since it is limited to the distributor plate, can be attributed to blocked tuyeres. Bed material particles, can block some of the tuyeres of the distributor plate which

are later unblocked at random moments, causing the observed pressure differential drop in the distributor plate. However, as it was evident in Figure C.10, these blockages do not occur for every experiment. Finally, it can be concluded that the behaviour of the LT experiments is similar to the one described for the HT experiments in Figure C.10.

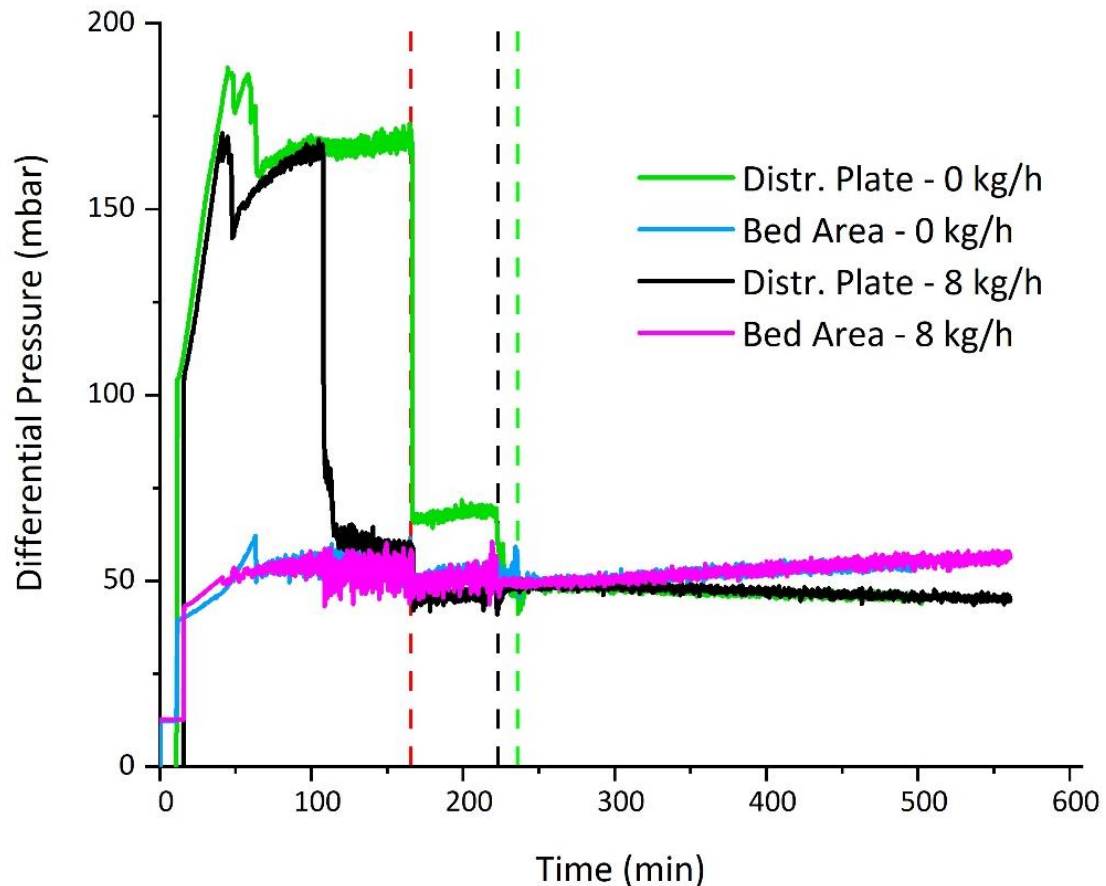


Figure C.11: Differential pressure drops over the distributor plate and the bed area during two LT steam gasification experiments with different amounts of secondary air injected (0 and 8 kg/h). ExR was employed as a feedstock and corundum F046 as the bed material. The red dotted line denotes the time where combustion was initiated for both experiments. The initiation of the steam gasification regime is marked with the green and the black line for the 0 kg/h and 8 kg/h experiments respectively.

As was presented with the use of the previous graphs, the behaviour of the differential pressure build-up throughout the system, is consistent between the various experiments and only subject to major differentiations in terms of the total flow introduced to the system. Therefore, a final factor that needs to be examined in terms of its effect on the pressure differential in the system, is the bed material employed, in terms of total amount and particle size. The total amount of bed material certainly influences directly the pressure differential of the bed, however in the context of the present work this parameter was not changed. However, from preliminary experiments that were conducted and are not presented here for brevity, it was shown that, as it is expected, the increase of the amount of bed material introduced, leads to a higher pressure differential in the bed area. In regard to the distributor plate, increasing amount of bed material leads to a decreasing pressure differential, but to a lesser extent than the bed area. These findings can explain the behaviour noted at the tail of Figure C.12, where a slow but steady increase of the bed area differential pressure and a similar decrease of the distributor plate differential pressure is noted. Such an observation is not possible for HT experiments as it is also evident in Figure C.11. Therefore, this particular observation can be linked to the aforementioned char accumulation in the bed area. For the LT experiments the less degree of

oxidation reactions due to the lower amounts of air introduced, leads to higher char amounts in the bed area compared to the HT experiments. Conclusively, it can be argued that the increasing bed inventory through char accumulation for the LT experiments leads to this particular behaviour of the differential pressures of the system.

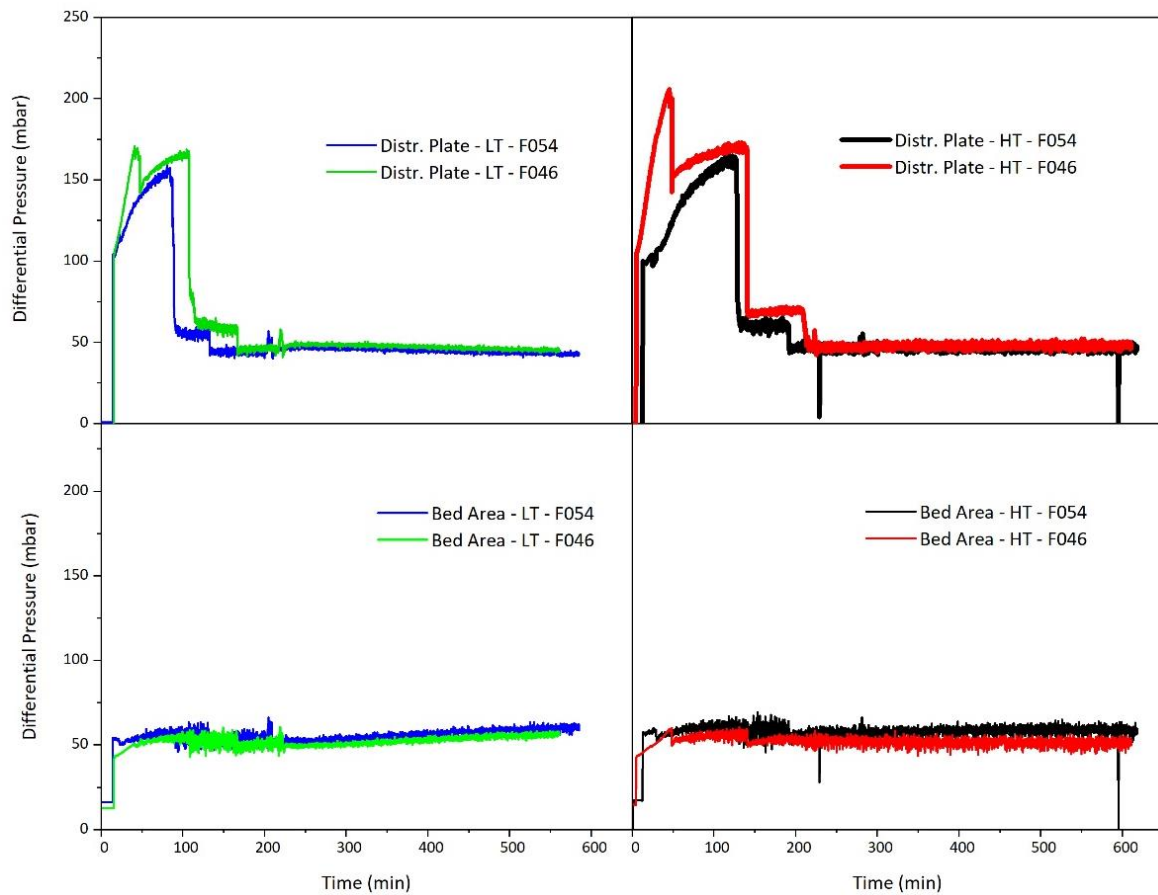


Figure C.12: Differential pressure drops over the distributor plate and the bed area during LT (left) and HT (right) steam gasification experiments with corundum F054 and F046 used as bed material. ExR (left) and PG (right) was used as feedstock for the LT and HT respectively.

In regard to the effect of the bed material particle size, the differences between the two particle sizes in terms of the bed area and distributor plate differential pressure are presented in Figure C.12 for both HT and LT experiments. As it can be readily observed, the most important remarks regard the mostly steady steam gasification region approximately after 250 min for both the graphs on the right and left. Observations regarding the switching between regimes and the char accumulation for LT experiments that are noted here, were discussed in the previous paragraphs and are therefore omitted here. For the LT experiments the average pressure drop over the distributor plate after 250 min was 45 mbar and 47 mbar for F054 and F046 respectively. The corresponding pressured drops for the bed area were 57 mbar for F054 and 53 mbar for F046. For the HT experiments the results were somewhat similar. In particular, the average pressure drop over the distributor plate after 250 min was 46 mbar for F054 and 48 mbar for F046, while the corresponding values for the bed area were 58 mbar and 51 mbar. In an initial minor remark, it should be mentioned, that the HT and LT experiments present very similar behaviours, also in terms of numerical results, except for the effect of char accumulation. This is despite the fact that HT experiments with PG and LT experiments with ExR were used. Concerning, the bed particle size comparison, it was proven consistently that with larger particle sizes ($F054 < F046$), lower pressure drops over the bed area are expected. This behaviour is consistent also with fluidization theory, since though Ergun's equation, the frictional pressure drop has a negative

relationship with particle size [4]. The opposite was observed for the distributor plate pressure drop but at a lower extent.

Overall, the experimental procedure followed for each experiment is summarised in the following bullet points. It should be mentioned that this is a generalization of the process, since significant differences exist between each experiment as discussed in the previous paragraphs.

- The bed material (corundum F046 or F054) was inserted from a flange located on the top of the reactor. In the context of the present work, 75 kg were used for each experiment.
- Air (22 kg/h) and N₂ (30 kg/h) start being fed in the reactor.
- Preheaters are turned on. The set points are 150 °C and 650 °C for the first and the second one respectively.
- The cyclone automatic system is turned on. This practically means that every four minutes the cyclones are emptied through an automatic valve system.
- The flare line tracing and the actual flare are turned on. This regards the part of the product gas line downstream the cyclones.
- The main feeder is initiated at 100 %, although no biomass is being fed yet. This is done in order to avoid bed material accumulating at the front part of the screw. This way blockages can be avoided.
- Both burners are turned on, with the set point temperature at 850 °C.
- The tracing of the gas sampling system is turned on.
- When the heating rate of the system drops and the temperatures start to stagnate (usually around 550 °C), combustion mode is initiated. For both PG and ExR, the biomass feeder is set at 11 % (corresponds to 4 kg/h of feed) and N₂ flow is set to zero. Air is kept at 22 kg/h. At this point it should be clarified that the main feeder considers feeding material from the main bunker (SB05) to the reactor bed area. The biomass feeder feeds from the biomass bunker (SB03) to the main bunker (SB05).
- It should be mentioned at this point, that biomass is fed at a one 20 kg bag per time rate on SB01, which is a funnel and subsequently to SB02 bunker. The whole bunker system is pressurized from and including bunker SB02. A sensor placed on the main bunker (SB05) notifies the operator with a red light when the total amount of biomass in the bunker is getting low. In practice, for ExR and PG feeds this corresponds to approximately 3 kg of biomass.
- After this point gas analysis is also started. That concerns the O₂ detector and the NDIR which are measuring gas composition online, as well as the u-GC which has a delay of 4 min as described earlier. Minor supervision of the sampling line is required, since the amount of tar produced is minimal in this stage (combustion).
- When the set point for the bottom burner is reached, meaning the average (TC01 – TC05) bed temperature becomes 850 °C, the cyclone bins are emptied. This is done in attempt to separate the ash and char particles produced during the combustion phase from the subsequent gasification one. In practice however, part of the ash that is on the cyclone main body is not removed at this point. This is a certain limitation for the system, mostly in the determination of the final ash yield but also for the amount of char that is collected through this process. This particular effect is mitigated through the use of low ash content biomass such as PG and ExR. Furthermore, the amount of char produced through the combustion process can be considered as negligible.

- At the same time, the CERTUSS boiler is turned on. Approximately 15 min are required for the boiler to warm up and build up the required pressure to be ready to supply the steam.
- When the above steps are completed, gasification may be initiated. Steam and air are supplied to the system according to the STBR and λ required. The biomass feeder is set to the required percentage. The amount of biomass fed to the reactor is actually controlled through the biomass feeder, since the main feeder is operating constantly at 100 %. The biomass feeder is calibrated prior to the conduction of each experimental campaign employing a new type of feedstock.
- Since steam gasification is initiated, the goal is to achieve steady state operation. This practically means that the temperature throughout the reactor stabilizes, as well as the values obtained from the u-GC regarding the gas composition. When steady state is achieved, tar sampling using the tar protocol is initiated. According to this protocol, tar sampling should be performed for at least 30 min with a gas flow rate between 0.1 and 0.6 Nm³/h. The latter is monitored through a gas meter placed downstream the impinger bottles. Practically, the duration of the sampling depended on the amount of tar produced as a result of the experimental conditions employed. For experiments with high amounts of tar produced, the tar sampling system had to be unblocked, so the process might be interrupted. In particular, even though gas is sampled downstream the cyclones, it was observed that char particles, along with tars, blocked the frit of the impinger bottles. In this case, tar sampling was paused and the blocked frits were replaced. In any case, especially for LT experiments, constant monitoring of the tar sampling system was required. Of course, multiple samplings can be performed during an experiment. For example, in the LT experiments, tar sampling was also performed in the start of gasification mode.
- The gas sampling system is in operation since the start of the gasification process, to monitor the produced syngas. This can also serve as an indication of the performance of the system. During the experiment, the operators monitor the CO and CO₂ values from the NDIR, the O₂ levels from the O₂ detector and the H₂ and CH₄ values from the u-GC. For example, very low levels of H₂ are expected during the combustion process, where mostly CO₂ and to a lesser extent CO are produced. Furthermore, the O₂ value can serve as an indicator on whether stoichiometric combustion is achieved during that stage. During the gasification stage, the values of those gases are also monitored and the quality of the sampling is evaluated according to the expectations from the respective experimental conditions. In particular regarding the O₂ though, its detection during the gasification interval can be either due to an excess amount of secondary air or due to blockages/leakages in the gas sampling system. The latter is the most common reason for the detection of O₂. If there is severe blockage in a certain point of the gas sampling train the flow will be interrupted and that will be immediately obvious from all the measurements. However, the present of smaller blockages, can allow part of the flow to pass by. However, due to the pressure increase downstream the blockage, atmospheric air is sucked into the sampling system through tiny holes in the tubing, impinger caps, etc.
- After the finalization of the experiment, the reactor is shut down and cooling down is initiated. That includes turning of both preheaters, both burners and the gas sampling tracing. The flare and the corresponding line tracing stay open a little longer, since reactions continue to take place in the reactor where biomass char is still present. The biomass feeder is also turned off, with the main feeder remaining open a little longer, to ensure that the main bunker (SB05) is

completely empty. To preserve the char in the reactor for weighing and future analysis, only N₂ is fed in the reactor at its maximum amount. This way oxidation reactions can be avoided. Oxidation reactions would firstly consume the char and secondly lead to an increase of the reactor's temperature. Secondary air however is employed to expedite the cooling down of the freeboard. The N₂ flow is maintained at high levels until the bed area temperatures fall below 500 °C at least. After this point, the N₂ flow is reduced to 5 kg/h and is kept constant overnight. The automatic cyclone cleaning system also operates overnight to ensure that the cyclones are emptied.

- The tar samples from the tar protocol(s) measurements performed are collected in bottles and refrigerated at ~5 °C. Two samples of each tar protocol are taken in HPLC vials for the subsequent tar analysis (GC-FID) and Karl Fischer titration.
- When the bed temperature falls below 50 °C, which is something that happens overnight, the bed material can be removed from the reactor. This is done through a flange located roughly at the height of the feeder, approximately 90° from it.
- The bed material is collected and subsequently sieved to separate the bed material from the larger char particles. This is done with the use of a 500 or 600 µm sieve, depending on the bed material used, in combination with a Retsch AS300 sieve shaker. The char is weighed and stored, while the bed material is also weighed and five samples from it are introduced in a muffle furnace (Nabetherm 30). In the muffle furnace, the bed material samples are combusted at 600 °C for 4 h, under an air environment. This process is performed as many times as required in order to achieve a constant weight (± 0.3 mg). The difference in weight is assumed to correspond to the amount of smaller char particles that remained in the bed from the sieving process. The combustion process is also performed for the material removed from the cyclones, which contains both ashes and char particles. Through these three processes, the char yield and therefore also the ash yield, of each experiment is determined.

Bibliography

1. Siedlecki, M., *PhD Thesis: On the gasification of biomass in a steam-oxygen blown CFB gasifier with the focus on gas quality upgrading: technology background, experiments and mathematical modeling*. 2011, Delft University of Technology.
2. Neeft, J.P.A., et al., *Guideline for Sampling and Analysis of Tars and Particles in Biomass Producer Gases*. Progress in Thermochemical Biomass Conversion, 2001: p. 162-175.
3. Perry, R.H. and D.W. Green, *Perry's Chemical Engineers' Handbook*. 1997: McGraw-Hill.
4. Kunii, D. and O. Levenspiel, *Fluidization Engineering*. 2nd ed. 1991: Butterworth-Heinemann.
5. Basu, P., *Biomass Gasification and Pyrolysis Practical Design and Theory*. 2010: Elsevier Inc.
6. Devi, L., K.J. Ptasinski, and F.J.J.G. Janssen, *A review of the primary measures for tar elimination in biomass gasification processes*. Biomass and Bioenergy, 2003. **24**(2): p. 125-140.

D. Appendix - Two phase modelling of Geldart B particles in the IHBFSR

Table D.1: Ansys Fluent species property settings

Parameter	Input
Air	
Phase type	Eulerian
Density	Ideal Gas Law
Viscosity	Kinetic Theory
Molecular Weight (kg/kmol)	28.966
Corundum	
Phase type	Granular
Density	3950
Bulk density (kg/m ³)	1636
Particle diameter	543 μm
Granular temperature model	PDE
Granular viscosity	Syamlal O'Brien
Granular bulk viscosity	Lun et. al [1] (kg/ms)
Granular conductivity	Syamlal O'Brien
Solids pressure	Lun et. al [1]
Elasticity modulus	Derived
Packing limit (-)	0.4141
Wall	
Fluent database	Default settings
Roughness constant (-)	0.5
Granular condition	Johnson – Jackson
Wall restitution coefficient (-)	0.2

Table D.2: Ansys Fluent simulations settings

Parameter	Input
Model	TFM
Volume fraction parameter formulation	Implicit
Simulation dimension	3D
Drag model	Adjusted Syamlal
Restitution coefficient	0.8 – 0.99
Convergence continuity	10 ⁻⁴
Convergence (remaining)	Default
Turbulence model settings	
K – epsilon model	Realizable
Near – wall treatment	Standard wall functions
Turbulence multiphase model	Mixture
Model constants	Default
Run conditions	
Grid size	Variable
Time steps	Variable
Max iterations	2000 – 3000
Data frequency	Variable

Table D.3: Pressure drop over the bed (d_p) (mean, maximum and minimum) and dominant frequency values calculated between 1 and 3 s of the simulation and bed height (from 2.5 to 3.5 s) for the mesh density/CFL combinations used in the independence tests without side-flow.

Mesh size	CFL	Mean d_p (mbar)	Max d_p (mbar)	Min d_p (mbar)	Dominant frequency (Hz)	Bed height (m)
30× d_p	0.2	67.3	72.7	61.7	4.5	0.79
30× d_p	0.4	67.8	71.0	63.3	4.5	0.83
20× d_p	0.2	66.1	85.2	45.3	3.7	0.74
20× d_p	0.4	64.6	73.3	57.8	4.6	0.76
15× d_p	0.2	64.4	86.9	49.2	4.0	0.71
15× d_p	0.4	65.0	76.1	51.3	3.1	0.72
Experimental		55.0	60.7	46.7	n.a.	0.67-0.82

Bibliography

1. Lun, C.K.K., et al., *Kinetic theories for granular flow: inelastic particles in Couette flow and slightly inelastic particles in a general flowfield*. Journal of Fluid Mechanics, 1984. **140**: p. 223-256.

Curriculum Vitae

Christos Tsekos was born in Athens, Greece and studied Mechanical Engineering in the National Technical University of Athens, specializing in Energy Engineering. After receiving his diploma, he worked as an intern Researcher for the Centre for Research and Technology Hellas. During this internship he worked on pilot scale gasification experiments as well as on experimental data fitting, using evolutionary algorithms. In 2014 he moved to the Netherlands, to study in the Sustainable Energy Technology MSc. Programme offered by TU Delft. His specialization was on Energy from biomass and his master thesis was focused on the effect of biomass torrefaction as a pretreatment for a pyrolysis process.

After the completion of his studies in 2017, he started a PhD in the Process and Energy department of the Mechanical, Maritime and Materials Engineering Faculty of TU Delft. His PhD project was focused on the development of experimental and analytical/modelling methods for the investigation of biomass pyrolysis and gasification in a novel indirect fluidized bed reactor. This project was conducted within the framework of the BRISK 2 Horizon 2020 EU project.

Following the conclusion of his PhD work in 2021, he moved to the Netherlands Organisation for Applied Scientific Research (TNO) and in particular in the Energy Transition Unit – Biobased and Circular Technologies group in Petten, the Netherlands. There, he worked as a Lead Scientist on biomass and plastic waste pyrolysis projects for sustainable energy and chemicals production and as the Program Manager of the Biorizon Shared Research Center – Horizon 1, focused on the production of bio-aromatics through thermochemical conversion.

In September 2023, he joined Technip Energies in Zoetermeer, the Netherlands as a Product Development Engineer for sustainable pyrolysis and gasification technologies.

List of Publications

Journal Articles:

- Christos Tsekos, Duncan de Voogt, Wiebren de Jong, Johan Padding, *Two phase modelling of Geldart B particles in a novel indirectly heated bubbling fluidized bed biomass steam reformer*, Chemical Engineering Journal, Volume 439, 1 July 2022, 135681
- Christos Tsekos, Mara del Grosso, Wiebren de Jong, *Gasification of woody biomass in a novel indirectly heated bubbling fluidized bed steam reformer*, Fuel Processing Technology, Volume 224, 15 December 2021, 107003
- Christos Tsekos, Simone Tandurella, Wiebren de Jong, *Estimation of lignocellulosic biomass pyrolysis product yields using artificial neural networks*, Journal of Analytical and Applied Pyrolysis, Volume 157, August 2021, 105180
- Andrés Anca-Couce, Christos Tsekos, Stefan Retschitzegger, Francesco Zimbardi, Axel Funke, Scott Banks, Tzouliana Kraia, Paula Marques, Robert Scharler, Wiebren de Jong, Norbert Kienzl, *Biomass pyrolysis TGA assessment with an international round robin*, Fuel, Volume 276, 15 September 2020, 118002
- Christos Tsekos, Konstantinos Anastasakis, Paul Schoenmakers, Wiebren de Jong, *PAH sampling and quantification from woody biomass fast pyrolysis in a pyroprobe reactor with a modified tar sampling system*, Journal of Analytical and Applied Pyrolysis, Volume 147, May 2020, 104802
- Georgios Archimidis Tsalidis, Christos Tsekos, Konstantinos Anastasakis, Wiebren de Jong, *The impact of dry torrefaction on the fast pyrolysis behavior of ash wood and commercial Dutch mixed wood in a pyroprobe*, Fuel Processing Technology, Volume 177, August 2018, Pages 255-265
- Wijittra Poomsawat, George Tsalidis, Christos Tsekos, Wiebren de Jong, *Experimental studies of furfural production from water hyacinth (Eichhornia Crassipes)*, Energy Science & Engineering, Volume 7, Issue 5 p. 2155-2164
- Mara Del Grosso, Luis Cutz, Urša Tiringer, Christos Tsekos, Peyman Taheri, Wiebren de Jong, *Influence of indirectly heated steam-blown gasification process conditions on biochar physico-chemical properties*, Fuel Processing Technology, Volume 235, October 2022, 107347
- Christos Christodoulou, Christos Tsekos, Georgios Tsalidis, M. Fantini, Kyriakos Panopoulos, Wiebren de Jong, Emmanuel Kakaras, *Attempts on cardoon gasification in two different circulating fluidized beds*, Case Studies in Thermal Engineering, Volume 4, November 2014, Pages 42-52
- Mara Del Grosso, Balaji Sridharan, Christos Tsekos, Sikke Klein, Wiebren de Jong, *A modelling based study on the integration of 10 MWth indirect torrefied biomass gasification, methanol and power production*, Biomass and Bioenergy, Volume 136, May 2020, 105529

Conference Proceedings:

- Christos Tsekos, Despina Vamvuka, Stelios Sfakiotakis, Christos Mihailof, Angeliki Lemonidou, Kyriakos Panopoulos, Despina Pentari., *Kinetic Modelling for the Pyrolysis of Biomass Fuels derived from Oil Crops*, Proceedings European Combustion Meeting 2015;1.
- Luga Simbolon, Daya Pandey, Christos Tsekos, Wiebren de Jong and Savvas Tassou, *Investigation of poultry litter conversion into useful energy resources using fast pyrolysis*, 27th European Biomass Conference and Exhibition, 27-30 May 2019, Lisbon, Portugal